THE UNIVERSITY
of ADELAIDE

INSTITUTE FOR PHOTONICS
& ADVANCED SENSING

A Whispering Gallery Mode Microlaser Biosensor

by

Tess Reynolds

A thesis submitted for the degree of
Doctor of Philosophy

In the

Faculty of Science
School of Physical Sciences

February 2017

To Natalka, Edwin and Scott

Risk something or forever sit with your dreams
– Herb Brooks

Contents

Abstract

A biological sensor, commonly referred to simply as a biosensor, is a transducing device that allows quantitative information about specific interactions, analytes or other biological parameters to be monitored and recorded. The development of biosensors that are low-cost, reliable and simple to use stand to facilitate fundamental breakthroughs and revolutionize current medial diagnostic methods. Notably, there remains an unmet need for developing *in-vivo* biosensors, allowing insights to be directly gained from the precise location of biological interactions within the human body.

Over the last two decades, whispering gallery modes (WGM) within microresonators have emerged as a promising technology for developing highly sensitive and selective biosensors, among many other applications. However, significant work remains to allow WGM sensors to make the transition from primarily being used within purely research environments to real-world applications. Specifically, one of the key limiting factors is the requirement of an external phase-matched coupling scheme (such as a tapered or angle polished optical fiber, prism or waveguide) to excite the WGMs, despite these devices displaying tremendous sensing performance. One way to lift this dependency on complex interrogation schemes is introduce a gain medium, such as a fluorescent dye or coating the resonator with quantum dots for example, thereby rendering it active and allowing remote excitation and collection of the WGM spectrum. Using active WGM resonators has allows the creation of novel sensing opportunities such as tagging, tracking and monitoring forces from insides living cells. Applications like these could not have been realized using external phase-matched coupling schemes.

The biosensing platform presented here is based on combining WGM within active microspherical resonators with microstructured optical fibers (MOF). The MOF enables both the excitation and collection method for the WGM spectrum while simultaneously providing a robust and easy to manipulate dip sensing architecture that has the potential to address the unmet need for real time label-free *in-vivo* sensing by combining with a catheter.

The platform is investigated fundamentally as well as experimentally, beginning with the development of an analytical model that is able to generate the WGM spectrum of active microspherical resonators. This provides the opportunity to pinpoint the optimal choice of resonator to be used for undertaking refractive index based biosensing. Specifically by being able to extract the quality (Q) factor, a measure of the resonance linewidth, and refractive index sensitivity from the WGM spectrum, the optimal combination of resonator parameters (diameter and resonator refractive index) can be identified for optimizing the resonators sensing performance. Further, the availability, biocompatibility and cost, as well as fabrication requirements can be also considered when selecting the ideal resonator.

Next, the inherently lower Q-factors observed in active resonators compared to their passive counterparts (i.e. resonators without a gain medium) is examined using a combination of theoretical, experimental and imaging methods. Through this examination process, the inherent asphericity of the

resonator is identified as being the limiting factor on the Q-factor of active resonators, with its effect most notably being observed for measurements made in the far field.

Experimentally, the first demonstration of this platform operating as a biosensor is presented by monitoring the well-documented specific interaction of Biotin/neutravidin in pure solutions. Including identifying ways to improve sensing performance and lower the detection limit, such as operating the resonator above its lasing threshold. Although, it is noted that in its current form, this platform is best suited for the monitoring of protein, preferably occurring in higher concentrations, until further improvements to the sensing performance can be implemented. However, the robust design coupled with its ability to provide access to previously difficult to obtain locations provides an insight into its potential future application capabilities.

Finally, the extension of the platform to operating in complex samples, namely undiluted human serum, is outlined. By self-referencing the platform, through the addition of a second, almost identical resonator (only varying in its surface functionalization) into one of the remaining vacant holes on the tip of the fiber, the effects of non-specific binding as well as changes in local environmental conditions (i.e. temperature fluctuations), can be eliminated.

Declaration

I confirm that this work contains no material which has been accepted for the award of any other degree or diploma in any university or other tertiary institution to Tess Reynolds and, to the best of my knowledge and belief, contains no material previously published or written by another person, except where due reference has been made in the text.

I give consent to this copy of my thesis when deposited in the University Library, being made available for loan and photocopying, subject to the provisions of the Copyright Act 1968.

The author acknowledges that copyright of published works contained with this these resides with the copyright holder(s) of those works.

I also give permission for the digital version of my thesis to be made available on the web, via the University's digital research repository, the Library catalogue, the Australasian Digital These Program (ADTP) and also through web search engines, unless permission has been granted by the University to restrict access for a period of time.

Signed:

Date:

Acknowledgements

Firstly, acknowledgments must go to my supervisors, Tanya Monro, Stephen Nicholls and Alexandre François. Without their guidance, support and passion this thesis would not be what it is today. Tanya, your ability to provide insight and guidance, coupled with your undeniable enthusiasm has made this journey a privilege and one I will remember. Alex, you have been nothing short of an outstanding mentor, and I am sincerely grateful for every opportunity you afforded me, including the immense patience, support and understanding you always showed.

Gratitude must also be extended to the current and former members of Tanya Monro's Laureate Fellowship Group including Jonathan Hall, Mathew Henderson, Nicholas Riesen, Shahraam Afshar and Alexandre François for constant support, countless insightful discussions, collaborations, work ethic and dedication to research.

I also would like to acknowledge the support of the Optofab node of the Australian National Fabrication Facility, along with Heike Ebendorff-Heidepreim, Roman Kostecki, Erik Schartner, Tony Leggatt, Peter Henry and Alastair Dowler for their patience and assistance through out the almost year long silica microstructured fiber fabrication process.

On a more personal note I would like to begin with a heartfelt thank you to Erik Schartner, Georgios Tsiminis and Maximus Malacari. Max, I would not have believed that 9 years ago when we first met that we would both be where we are today. Thank you for all the adventures, outrageous stories, laughs and tears we have shared. Erik and Georgios, I am not even sure where to begin with you two, but I know that I am forever thankful for the hours spent listening to me complain about failed experiments, anything and everything related to hockey and the scandalous stories that came from my comically poor choices in housemates. Further, to my closest friends and sisters I never had, Jane Claxton, Diana Glass, Astrid Mark and Sophie Calabretto. Thank you for never giving up on me, especially on the days I gave up on myself. Without your encouragement, inspiration, guidance and reality checks when needed, I would not have made it through. I cannot wait to celebrate with you all.

Lastly, I would like to thank my parents, Nat and Ed, and brother, Scott, for their undeniable love, support and advice throughout my entire academic journey. Thank you for always encouraging me to purse my dreams and providing every single opportunity to do so, especially when that includes putting everything else on hold and travelling all over the world for ice hockey.

If I have seen further it is by standing on the shoulders of giants

- Sir Isaac Newton

Publications Contained Within Thesis

P1. **T. Reynolds**, N. Riesen, A. Meldrum, X. Fan, J. M. M. Hall, T. M. Monro, and A. François, "Fluorescent and lasing whispering gallery mode microresonators: an emerging paradigm for sensing application", Submitted to Laser Photonics Review (October 2016)

P2. **T. Reynolds**, M. R. Henderson, A. François, J. M. M. Hall, S. Afshar V., S. J. Nicholls, and T. M Monro, "Optimization of whispering gallery resonator design for biosensing applications ", Opt. Express, 23(13), 17067-17076, 2015.

P3. N. Riesen, **T. Reynolds**, A. François, M. R. Henderson and T. M. Monro, "Q-Factor limits for far-field detection of whispering gallery modes in active microspheres", Opt. Express, 23(22), 28896-28904, 2015.

P4. A. François, **T. Reynolds** and T. M. Monro, "A fiber-tip label free biological sensing platform: a practical approach toward *in-vivo* sensing", Sensors (Basel), 15(1), 1168-1181, 2015.

P5. **T. Reynolds**, A. François, N. Riesen, M. E. Turvey, S. J. Nicholls, P. Hoffman and T. M. Monro, "Dynamic self-referencing approach to whispering gallery mode biosensing and its application to measurement within undiluted serum" Analytical Chemistry, 88(7), 4036-4040, 2016.

The following paper was prepared after the drafting of this thesis and thus is included in Appendix C.

C1. J. M. M. Hall, **T. Reynolds**, M. R. Henderson, N. Riesen, T. M. Monro and S. Afshar V., "A unified theory of multilayer microspheres with single or active layer source," submitted to Optics Express (In Press – January 2017).

Other Publications

The following papers, which were published during the candidature but not included in this thesis, are listed here.

1. A. François, **T. Reynolds**, N. Riesen, J. M. M. Hall, M. R. Henderson, E. Zhao, S. Afshar V., and T. M. Monro, "Combining whispering gallery mode lasers and microstructured optical fibers: limitations, applications and perspectives for *in-vivo* biosensing," MRS Advances 2016, Available on CJO2016. doi: 10.1557/adv.2016.342

2. A. François, **T. Reynolds**, N. Riesen, J. M. M. Hall, S. Afshar V., and T. M. Monrno, "Whispering gallery mode laser at the tip of a fiber for biomedical applications," Optics and Photonics News, p. 58, December 2015.

3. E. Shartner, G. Tsiminis, A. François, R. Kostecki, S. C. Warren-Smith, L. V. Nguyen, S. Heng, **T. Reynolds**, E. Klantsataya, K. J. Rowland, A. Abell, H. Ebendorff-Heidepriem and T. M. Monro, "Taming the light in microstructured optical fibers for sensing," Int. J. Applied Glass Sciences 6, 229-239, 2015.

4. J. M. M. Hall, S. A. Vahid, A. François, **T. Reynolds**, N. Riesen, and T. M. Monro, "Method for predicting whispering gallery mode spectra of spherical microresonators," Opt. Express. 23(8), 9924-9937, 2015.

5. J. M. M. Hall, A. François, S. Afshar V., N. Riesen, M. R. Henderson, **T. Reynolds** and T. M. Monro, "Determining the geometric parameters of microbubble resonators from their spectra," J. Opt. Soc. Am. B 34, 2699-2706, 2017.

Conference Proceedings During Candidature

1. A. François, K. J. Rowland, **T. Reynolds**, S. J. Nicholls, and T. M. Monro, "Combining whispering gallery mode laser and microstructured optical fibers for *in-vivo* biosensing applications", *Photonics North*, Ottawa, Canada (June 2013).

2. **T. Reynolds**, A. François, S. J. Nicholls, and T. M. Monro, "In-vivo measurement tools for applications in Cardiology", *Conference on Optics Atoms and Laser Applications (KOALA),* Sydney, Australia (November 2013).

3. **T. Reynolds**, A. François, S. J. Nicholls, and T. M. Monro, "A demonstration of multiplexed biosensing using whispering gallery mode microspheres positioned onto a microstructured optical fibre tip", *International Society for Optics and Photonics (SPIE) Photonics West*, San Francisco, United States of America, (February 2014).

4. **T. Reynolds**, A. François, S. J. Nicholls, and T.M. Monro, "Multiplexed biosensing using whispering gallery modes in complex media", *5th International Nano Medicine Conference,* Sydney, Australia (June 2014).

5. **T. Reynolds**, M. R. Henderson, A. François, T.M. Monro, "Whispering gallery mode biosensing – optimal sensor design", *Conference on Optics Atoms and Laser Applications (KOALA)*, Adelaide, Australia (November 2014).

6. **T. Reynolds**, M. R. Henderson, A. François, S. J. Nicholls, and T. M. Monro, "Optimization of Whispering gallery mode sensor design for applications in biosensing", *International Society for Optics and Photonics (SPIE) Photonics West,* San Francisco, United States of America, (February 2015).

7. J. M. M. Hall, S. Afshar V., M. R. Henderson, A. François, **T. Reynolds**, N. Riesen, T. M. Monro, "Predicting the whispering gallery mode spectra of microresonators," *International Society of Optics and Photonics (SPIE) Photonics West*, San Francisco, Unites States of America, (February 2015).

8. N. Riesen, **T. Reynolds**, A. François, T. M. Monro, "On the fundamental limits of far-field detection of active microsphere whispering gallery modes," *Frontiers in Optics,* San Jose, United States of America, (October 2015).

9. **T. Reynolds**, A. François, N. Riesen, J. M. M. Hall, S. Afshar V., S. J. Nicholls, and T. M. Monro, "A fibre tip whispering gallery mode biosensing platform," *Australian and New Zealand Conference on Optics and Photonics (ANZCOP),* Adelaide, Australia (December 2015).

10. A. François, N. Riesen, **T. Reynolds**, J. M. M. Hall, M. R. Henderson, E. Zhao, S. V. Afshar, and T. M. Monro, "Combining whispering gallery mode lasers and microstructured optical fibres for *in-vivo* biosensing applications," *Australian and New Zealand Conference on Optics and Photonics (ANZCOP)*, Adelaide, Australia (December 2015).

11. J. M. M. Hall, **T. Reynolds**, M. R. Henderson, and S. V. Afshar, "Multilayer microshell sensitivity analysis," *Australian and New Zealand Conference on Optics and Photonics (ANZCOP)*, Adelaide, Australia (December 2015).

12. N. Riesen, A. François, **T. Reynolds**, M. R. Henderson and T. M. Monro, "On the fundamental limits of far-field detection of the WGMs of active microspheres," *Australian and New Zealand Conference on Optics and Photonics (ANZCOP)*, Adelaide, Australia (December 2015).

13. J. M. M. Hall, S. Afshar, M. R. Henderson, A. François, N. Riesen, **T. Reynolds**, and T. M. Monro, "Microbubble resonator design using FDTD," *Australian and New Zealand Conference on Optics and Photonics (ANZCOP)*, Adelaide, Australia (December 2015).

14. A. François, **T. Reynolds**, N. Riesen, J. M. M. Hall, M. R. Henderson, E. Zhao, S. Afshar V., and T. M. Monro, "Combining whispering gallery mode lasers and microstructured optical fibers: limitations, applications and perspectives for *in-vivo* biosensing applications," *Material Research Society*, Phoenix, United States of America (April 2016).

15. S. Afshar V., J. M. M. Hall, **T. Reynolds**. M. R. Henderson, N. Riesen, and T. M. Monro, "A unified model for active multilayer microsphere resonators," *Australian Conference on Optical Fibre Technology (ACOFT)*, Sydney, Australia (September 2016).

16. **T. Reynolds**, A. François, N. Riesen, M. E. Turvery, S. J. Nicholls, P. Hoffmann, and T. M. Monro, "Using whispering gallery mode micro lasers for biosensing within undiluted serum," *International Society for Optics and Photonics (SPIE) Biophotonics Australasia,* Adelaide, Australia (October 2016).

17. A. François, N. Riesen, **T. Reynolds**, J.M. M. Hall, and T. M. Monro, "Whispering gallery mode lasers for biosensing applications," *Australian Physiological Society/Australian Society for Biophysics 2016 Symposia,* Adelaide, Australia (December 2016)

List of Figures

List of Tables

Abbreviations

ELIZA	**E**nzyme-**L**ined **I**mmunosorbent **A**ssay
FET	**F**ield **E**ffect **T**ransistors
FRET	**F**örester **R**esonance **E**nergy **T**ransfer
FOM	**F**igure **o**f **M**erit
LEP	**L**aser **E**igenvalue **P**roblem
MOF	**M**icrostructured **O**ptical **F**ibre
NSB	**N**on-**S**pecific **B**inding
PC	**P**hotonic **C**rystal
PCR	**P**olymerase **C**hain **R**eaction
PE	**P**oly**e**lectrolytes
PEG	**P**oly**e**thylene **G**lycol
QED	**Q**uantum **E**lectro**d**ynamics
QCM	**Q**uartz **C**rystal **M**icrobalance
RIU	**R**efractive **I**ndex **U**nit
SEM	**S**canning **E**lectron **M**icroscope
SNR	**S**ignal to **N**oise **R**atio
SPR	**S**urface **P**lasmon **R**esonance
TE	**T**ransverse **E**lectric
TIR	**T**otal **I**nternal **R**eflection
TIR	**T**otal **I**nternal **R**eflection **F**luorescence
TM	**T**ransverse **M**agnetic
WGM	**W**hispering **G**allery **M**ode

Chapter 1

Introduction

1 Motivation and Overview

The field of biological sensing has emerged as the result of the growing demand from a wide range of research areas spanning medicine [1], pharmacology [2], environmental studies [3], defense [4] and even food safety [5], to observe and monitor biological interactions rapidly, using compact and low cost technologies. Biosensors have been developed from a variety of different sensing architectures such as electrical [6], mechanical [7], magnetic [8, 9], thermometric [10] and optical [11]. All of these architectures operate on the same principle of translating biological interactions and information into observable analytical signals, allowing highly specific and sensitive information to be recorded. Further, biological sensing technologies can be categorized depending on whether the target analyte of interest requires a label, such as a fluorescent dye [12] or radioactive material [13], or can remain un-labeled, allowing real-time measurements along with acquiring additional information such as the binding kinetic of the analyte of interest.

Electrical

Electrical biosensors operate by monitoring changes in electrical properties such as current (amperometric [14]), potential (potentiometric [15]), conductive properties (conductometric [16]), capacitance (capacitative [17]) or resistance (impedimetric [18]) as the result of an interaction with the analyte of interest. Commonly, electrical interfaces such as field effect transistors (FET) [19], nanowire arrays [20], electrodes [21] or nanoparticles [22] are used. In the mid 1950s, Clark developed one of the most notable and pioneering electrochemical biosensors with the invention of the oxygen electrode [23] and then an electrode system for glucose detection a number of years later [24]. This work paved the way for the first commercially available biosensor purely for glucose detection in 1975 [25]. Since then, a significant portion of the commercial biosensing market has been dedicated to developing and improving glucose monitoring technology, enabling point-of-care as well as continuous monitoring systems to be developed [26]. However, the majority of other electrochemical sensors have been predominately limited to purely research applications with improvements in sensitivity, stability and response time required [27].

Mechanical

Monitoring changes in motion and mechanical forces have also been used to develop biosensing platforms, with two main architectures being utilized, namely microcantilevers [28-30] and Quartz Crystal Microbalances (QCM) [31-33]. In microcantilever based sensors, as the name suggests, the key element is the cantilever which acts as the force transducer. For example, deflections or oscillations in the frequency of the cantilever can occur due to the binding of the analyte of interest [34]. Deflection

based microcantilever sensors have been used for monitoring protein [28], DNA [29] and even drug interactions [30]. However, the cantilevers are susceptible to deflections due to changes in refractive index, temperature and sample flow rate, which are indistinguishable from binding events. Similar to the operating principle of oscillatory microcantilevers, QCMs rely on the oscillation of a crystal, monitoring fluctuations in the resonance frequency during interactions with the target analyte [35]. QCMs have found applications as humidity sensors [36], for studying atmosphere corrosion of metals [37], and cancer biomarker detectors [38].

Optical

Optical biosensors operate by monitoring light/matter interactions, positioning themselves as reliable analysis and detection tools for biosensing applications by providing robust architectures that are capable of continuous monitoring, remote sensing, working in complex solutions, and in some cases for conducting measurements in real time [11, 39-41]. The 3 main classes of optical biosensors are fluorescence, absorbance and label-free, which includes reflectance [42], light scattering [43], Raman spectroscopy [44] and refractive index detection [11]. Fluorescence-based sensors operate by monitoring the fluorescence signal, generated by the de-excitation of an electron to the ground state via displacement [45, 46], competitive [47, 48] or sandwich [49, 50] interactions with labeled analytes, Fig. 1.1. Commonly used fluorescence-based biosensors include those based on biochemical methods such as Western blots [51, 52] and Enzyme-Linked Immunosorbent Assay (ELISA) [53-55], along with newer technologies such as total internal reflection fluorescence (TIRF) [56] and polymerase chain reaction (PCR) [57, 58].

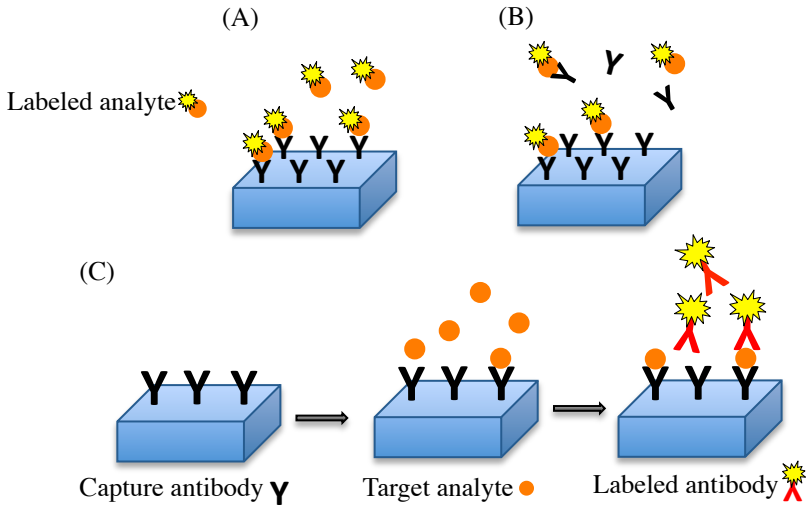

Figure 1.1 Fluorescence based optical biosensors, (A) direct, (B) competitive binding and (D) sandwich assays.

Despite the success and clinical usage of fluorescence-based techniques, there are notable drawbacks that continue to plague this class of technologies. Firstly, the labeling process can be time consuming and complex. Secondly, quantitative measurements can be difficult in both low and high analyte concentrations. In low concentrations, other background sources of light can overshadow the fluorescence from the target analyte, while at high concentrations, the proximity of the fluorophores has the potential to allow Förster resonance energy transfer (FRET). When FRET occurs, instead of radiating away the energy from an excited fluorophore, the energy is transferred to a neighboring fluorophore [59]. Further, the inability to precisely control the number of fluorophores present on each target analyte can introduce a signal bias [60]. Label-free methods on the other hand allow for detection of analytes in their natural state, unlabeled and unaltered. There are various detection methods employed by label-free optical biosensors however, the method of refractive index detection has emerged as the leading candidate for developing robust and promising optical biosensing technologies. Examples of some of the most commonly used refractive index based biosensing architectures and a sample of the corresponding applications are summarized in Table 1.1.

Each of these architectures has shown great sensing performance in their own regard. For example, Mach-Zender interferometers have demonstrated low refractometric detection limits (10^{-8} RIU) [61], while waveguide based sensors are easily multiplexed [62] and photonic crystal resonators provide a compact design [63]. However, it has been Surface Plasmon Resonance (SPR) based sensors that have become the benchmark for commercially available label-free refractive index based sensors with their ability to enable fast and reliable quantitative analysis of a broad range target analytes down to clinically relevant levels.

SPR technologies were first implemented as biosensors in 1983 [64], and since then have been a reliable and powerful sensing tool for monitoring biological interactions for both research and clinical applications [65, 66]. Surface plasmons are oscillations of free-electrons that reside at the interface of two mediums, with opposite dielectric constants, commonly observed in metal (typically silver/gold) and dielectric interfaces. The most common methods of interrogating SPRs include prisms [67], waveguides [68], optical fibers [69] and gratings [70]. Both the prism and waveguide configurations provide robust platforms, displaying low detection-limits [71, 72]. SPR biosensors became commercially available in 1990 thanks to Biacore International [73], and have continued to grow and be developed by a range of other companies. Some key features of commercial SPR sensors include the integration of flow systems along with automatic sampling mechanisms and multiple sample channels, including reference channels, allowing the effects of non-specific binding to be minimized and multiple analytes measured simultaneously.

Label Free Optical Sensing Architecture	**Application**	**Advantages (+)/ Disadvantages (-)**
Mach-Zehnder Interferometer	Refractive Index Sensing [74, 75] Protein Detection [76] Disease Diagnosis [77]	**+:** Low detection limits [61] **-:** Large size and small dynamic range
Waveguide	Pathogen Detection [78] Protein Detection [79, 80]	**+:** Ability to be highly multiplexed **-:** Difficult to fabricate
Photonic Crystal (PC)	Protein Detection [81, 82] Virus Detection [83] Cancer Cell Detection [84]	**+:** Small mode volumes, ability to be highly multiplexed, low detection limits [85, 86] **-:** Difficulties integrating some configurations with microfluidic systems
Surface Plasmon Resonance (SPR)	Protein Detection [87] Enzyme Detection [88] DNA Detection [89]	**+:** Fast and reliable quantitative analysis of multiple analytes **-:** Expensive and cumbersome, wide signal linewidths, not able to reach single molecule detection
Fibre Bragg Grating	DNA Detection [90] Refractive Index Sensing [91]	**+:** Highly sensitive, suited to distributed sensing **-:** Difficult to fabricate
Whispering Gallery Mode (WGM)	Refractive Index Sensing [92-94] Protein Detection [95, 96] DNA Detection [97, 98] Virus Detection [99, 100] Single Molecule Detection [101-103] *In-situ* Cell Monitoring [104-106]	**+:** Single molecule detection, narrow signal linewidths, compact design, ability to conduct *in-vivo* and remote sensing **-:** Some resonators can be expensive to fabricate and can have practical limitations that restrict use outside research environments

Table 1.1 Examples of commonly used label free refractive index based sensing architectures and a sample of corresponding biosensing applications.

However SPR sensors contain expensive components, complicated optics and are large in size. Optical fiber SPR sensors, on the other hand, remove some of these associated complexities, while also providing a straightforward route towards device miniaturization [107-109]. Despite the large amount of research focused on optical fiber SPR sensing platforms [110], there has been a notably absence of commercially available sensors. This is most likely due to their higher detection limits and lack of thorough demonstrations of sensor reliability and reusability.

Despite only being utilized for biological sensing applications over the last few decades, it is Whispering Gallery Mode (WGM) based sensors that have provided excellent sensitivity [111] and low detection limits [112, 113], allowing fundamental questions of biology to be examined. Further, by combining WGM sensors with other technologies such as plasmonic effects [101, 114] or using heterodyning techniques [115, 116], single molecule detection has become common. They have also been able to provide unprecedented access to previously unattainable locations, paving the way for *in-vivo* biological sensing in low-cost configurations to be realized [104-106]. Originally known as "Morphological Dependent Resonances" [117, 118], optical WGMs owe their name to the acoustic phenomenon that occurs within large domed structures, such as St Paul's Cathedral in London, as was famously observed by Lord Rayleigh in 1910 [119]. In such circular structures, acoustic modes propagate along the smooth, curved surfaces, efficiently guiding the sound to allow even whispers to be audible on the opposite side of the room. For optical WGMs, dielectric structures allow light travelling within them to be confined and circulated along the circumference due to total internal reflection (TIR) between the resonator and surrounding environment. The confinement can be considered spatially in terms of mode volume (V) or temporally in terms of the quality factor (Q) and is ensured through geometric design and material considerations, whereby one or more axis of revolution occurs within the resonator such as seen in spheres [120], capillaries [121], disks or toroids [122] and even polygons [123-125].

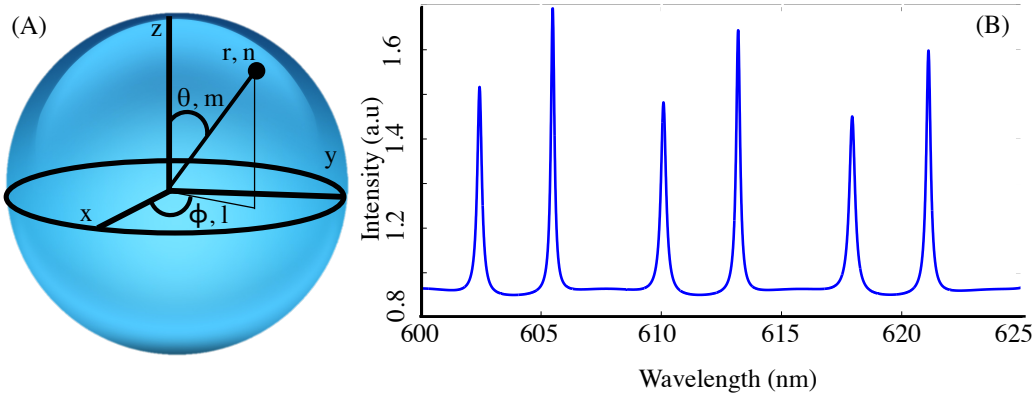

Fig.1.2 (A) The coordinates of a sphere, with corresponding eigenvalues, l, m, and n as marked. (B) An example WGM spectrum of a 10 μm polystyrene (n_1 = 1.59) microsphere in water (n_2 = 1.3325).

WGMs can be examined by solving Maxwell's Equations using the appropriate boundary conditions, and expanding the electric and magnetic fields of the transverse electric (TE) and transverse magnetic (TM) modes in terms of their eigenfunctions [126-128]. In the case of a microsphere resonator, the corresponding eigenvalues, typically denoted l (azimuthal), m (polar) and n (radial) represent the

quantization conditions for the waves within the resonator to return in phase after a round trip. An example of a microsphere resonator, indicating the spherical coordinates and the corresponding mode numbers is shown in Fig. 1.2 (A). The WGM spectrum of a resonator is recognizable by its relatively sharp, well-spaced peaks, corresponding to the WGM resonances, as depicted in Fig. 1.2 (B). The narrow line-widths observed is a consequence of the quantization conditions, with broadening of the line-widths occurring as a result of imperfections in the circular symmetry of the geometric cross-section [129, 130] as well as mode degeneration due to scattering [131], material losses [132] and weak confinement of the light [133].

The simplest geometry for WGM to propagate in is a sphere. Microscale spherical resonators can be fabricated from a diverse range of materials including liquids [134, 135] and polymers [136-140] to glass [93, 98, 141, 142] and crystalline materials [143-145]. Liquid droplets, for example, were first utilized as optical resonators in 1977 [146], with surface tension allowing extremely smooth boundaries to form, resulting in Q-factors as high as 10^9 being recorded in liquid hydrogen droplets [134]. However, mechanical instabilities and evaporation severely restricted the widespread usage of this particular system. Recently, liquid resonators have begun to resurface as novel microlaser sources [147, 148] and notably have found applications for biological sensing by allowing integration of biological molecules and live cells directly into the resonator [149, 150]. Today, silica remains one of the most commonly used materials for microspherical WGM resonators. Silica microspherical resonators are typically fabricated via melting the tip of a standard telecommunications optical fiber [101, 151], whereby surface tension allows almost perfect microspheres, with extremely low intrinsic surface imperfections, to be formed. Common tools used for melting the tip include CO_2 lasers [152, 153], electric arc discharge [154], commercial fiber slicers [155] or butane microtorches [156]. The first demonstration of WGMs within silica microspherical resonators occurred in 1987 [157], opening the door for a broad range of applications with the innovation of novel and efficient external near-field evanescent resonator-light coupling schemes such as angle-polished fibers [158], fiber tapers [159], waveguides [160] and prisms [161]. This has lead to unprecedented performance in terms of narrow signal line widths [162], allowing WGM resonators to be used in applications spanning lasers [163], quantum electrodynamics [164], non-linear optics [165], mechanical filters [166, 167] and label-free biosensors [96, 97, 168-170]. Resonators requiring the use of such external evanescent coupling schemes, as they do not contain a gain medium, can be classified as passive resonators. However, it is these external evanescent coupling schemes that ultimately restrict the practical application of passive resonators outside a research laboratory environment, as they demand precise alignment conditions to be maintained throughout the measurement [171] and are also susceptible to breakage and fowling [172].

Effort has been placed towards the development of novel approaches to alleviate the need for external couplers for passive resonators, such as deformed cavities [172, 173] or introducing scattering centers by immobilizing nanoparticles onto the resonators surface [174]. For the case of deformed cavities however, the requirement of precise alignment of the focused free-space light onto the resonator still restricts their possible use outside laboratory environments. Although immobilizing nanoparticles onto the surface of the resonator can remove this dependency, both configurations still suffer from notably wider signal linewidths, and therefore reduced performance, in comparison to evanescently coupled resonators. An alternative approach is to utilize resonators with a gain medium, classified as active resonators, enabling free space excitation and collection of the WGMs. These active resonators take advantage of the Purcell effect producing a WGM modulated fluorescence spectra (i.e. increasing the fluorescence intensity at the specific resonance wavelengths [174, 175]). This alleviates the need for precision near-field coupling strategies. Examples of active resonators include dye-doped polystyrene microspheres [176, 177], microdroplets [178], quantum dot [179, 180] or fluorescent nano-crystal [181] coated resonators and fluorescent capillaries [95]. Active resonators enable the use of smaller resonators, as the requirement of precise positioning near an evanescent coupling scheme has been mitigated, allowing greater refractive index sensitivities and high multiplexing capabilities [182, 183]. They also enabled novel biosensing applications including monitoring biomechanical forces from inside a cell [104], allowing individual cells to be tagged and tracked [105], as well as creating cellular lasers [106]. All of these applications would not be possible with current passive configurations.

A key drawback for free-space coupled resonators (either active or passive) is the notably wider signal linewidths displayed compared with their evanescently coupled counterparts [129, 184]. This restricts their potential for reaching single molecule detection, as well as widespread usage to other applications outside of sensing. However, single molecule detection has limited to no relevance in many standard biosensing applications, such as for food safety and medical diagnostics for example, where analytes are typically found in higher concentrations [185, 186]. Further, specifically for active resonators, techniques have been developed to decrease the signal linewidth. These include operating the resonator in the stimulated emission regime [187], enabling narrower linewidths to be realized upon reaching the lasing threshold or combining fluorescent microspheres with microstructured optical fibers (MOF) to break the symmetry of the resonator [188]. This latter technique has added advantage of developing a robust and easy to manipulate dip sensing architecture that could be utilized for biosensing applications [140, 189, 190], with the potential for future *in-vivo* sensing.

1.1 Whispering Gallery Mode Theory

1.1.1 Resonator Parameters

While there are many different parameters associated with WGM resonators, such as the finesse, mode volume, free-spectral range and visibility of the mode (i.e. intensity compared to the background), details of which can be located elsewhere [191], the key metrics for WGM biosensing are the Q-factor, refractive index sensitivity, signal to noise ratio (SNR) and limit of detection.

Q-Factor

The Q-factor describes the photon storage time within the resonator and can be expressed equivalently in a variety of forms, the most common of which include the resonance linewidth (Fig 1.3), cavity ring down time, steady-state energy balance as well as considering the individual loss mechanisms that are present in the resonator. The Q-factor can be extracted in terms of the resonance wavelength, λ, and the linewidth, Δλ, and expressed as,

$$Q = \frac{\lambda}{\Delta\lambda} \tag{1.1}$$

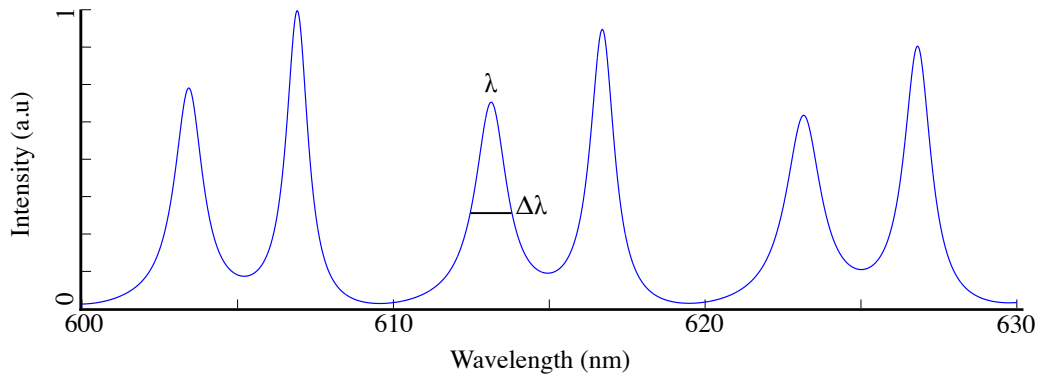

Fig. 1.3 A WGM emission spectrum depicting the resonance wavelength, λ, and linewidth, Δλ.

Alternatively, the cavity ring down time τ_{RD} can be used to define the Q-factor, where the rate at which the light leaves the cavity is measured, and hence the Q-factor can be expressed in terms of resonator frequency, ω_R and τ_{RD} [192],

$$Q = \omega_R \tau_{RD} \tag{1.2}$$

Equivalently, the Q-factor can also be expressed in terms of the individual loss mechanisms present in the resonator, namely,

$$\frac{1}{Q}=\frac{1}{Q_m}+\frac{1}{Q_s}+\frac{1}{Q_c} \tag{1.3}$$

where Q_m is the material loss, Q_S is the loss due to scattering from surface roughness and Q_R is the radiation loss. Material losses can be characterized by considering the absorption of light by both the resonator and the surrounding medium by using an absorption decay constant, α_m, as [132],

$$Q_m=\frac{2\pi n_1}{\lambda\alpha_m} \tag{1.4}$$

The individual contributions to the Q-factor from the resonator and surrounding medium are influenced by a range of factors including how tightly the light is confined within the resonator, the wavelength range being considered and the nature of the environment in which the measurement is taking place.

Scattering losses due to surface inhomogeneities can be described by modeling the surface roughness as a function of changing dielectric constant. An expression for the limit on the Q-factor due to surface scattering is,

$$Q_s\approx\frac{3\lambda^3 R}{8n_1\pi^2B^2\sigma^2} \tag{1.5}$$

Where B is the correlation length and σ is the variance of the surface roughness [131]. Scattering losses can be reduced in resonators made from materials such as silica, where, during the fabrication process the melting techniques used remove the majority of the inhomogeneities both inside and on the surface of the resonator. In comparison with material and scattering losses, there is no explicit formula for tunneling loss in a WGM resonator; however, the curvature of the resonator affects the condition for TIR, with confinement losses being higher in resonators with smaller radii. For large resonators, $R >$ 100 μm, the confinement loss becomes negligible and the Q-factor is predominately dictated by the material and scattering losses.

Refractive Index Sensitivity

As highlighted previously, there is a strong dependence on the resonance position of WGMs on the refractive index contrast of the resonator and surrounding environment, allowing WGM resonators to be exploited for a diverse range of sensing applications. The refractive index sensitivity of a resonator is defined as the change in the spectral position of a resonance due to a change in refractive index of

the surrounding medium (in refractive index units, RIU), with units of nm/RIU. Changes in the surrounding refractive index can occur due to changes in pressure [193-195], temperature [196], humidity [197], electric fields [198] and binding of molecules on the resonators surface [199]. However, it is impossible to identify the source of the refractive index change if measures are not taken to remove the influence from changes in environmental conditions. This is a key problem for conducting biosensing measurements outside controlled laboratory environments where external factors like temperature and pressure can fluctuate. One solution to this problem is to self-reference the sensor, allowing background fluctuations to be removed by comparing the spectral shifts of a sensing resonator and reference resonator. This has been demonstrated primarily for integrated WGM resonator configurations, such as microdisks [200], where there are multiple resonators residing on a single device. This technique is obviously harder to implement for single resonator sensors. However, one technique that is emerging to allow self-referencing within a single resonator is mode-splitting [116, 201].

The spectral shift, $\Delta\lambda$, as a result of a change in the surrounding refractive index, Δn_m, is determined by [202],

$$\Delta\lambda = \eta \Delta n_m \frac{\lambda}{n_e} \tag{1.6}$$

where η is the fraction of the evanescent field that extends into the surrounding medium n_m, and n_e, as previously defined, is the effective refractive index. From Eq. 1.6, it is clear that increasing the fraction of the evanescent field extending out into the surrounding medium will result in an increase in the refractive index sensitivity. This can done by either varying the refractive index contrast between the resonator and surrounding medium through the choice of material [93, 203] or decreasing the diameter of the resonator [204].

Utilizing novel resonator designs such as hollow resonators (microbubbles) [205-208] or coated capillaries [209, 210] and microspheres [211, 212] can also provide increased refractive index sensitivity. For example, Teraoka *et al*. [211, 212] showed that altering the thickness of the coated layer could maximize the sensitivity of a coated microsphere, thereby allowing more of the evanescent field to extend into the surround medium. Similarly, Lane *et al*. conducted an extensive investigation on coated fluorescent capillaries, also finding an optimal coating thickness for maximizing the reach of the evanescent field into the sample medium [210]. Finally, interest has also been generated by the possibility of hybrid sensing platforms for improving refractive index sensitive by increasing the local evanescent field intensity through plasmonics [114, 213-215].

Refractive Index Biosensing

Specifically for the detection of the binding of analytes to a resonators surface, whereby the interaction causes a change in the refractive index within the evanescent field of the WGM resonator, the corresponding wavelength shift is given by [151],

$$\frac{\delta\lambda}{\lambda} = \frac{\alpha_{ex}\sigma_S}{\varepsilon_0(n_1^2 - n_2^2)R} \tag{1.7}$$

where ε_0 is the vacuum permittivity, R is the radius of the resonators axis of symmetry, n_1 and n_2 are the refractive index of the resonator and surrounding medium respectively. The excess polarizability can be approximated by the polarizability given by the Clausius-Mossotti equation,

$$\alpha = \frac{\varepsilon_r - 1}{\varepsilon_r + 2}\frac{3M\varepsilon_0}{N_A\rho_m} \tag{1.8}$$

where N_A is Avogadro's number and ε_r, ρ_m and M are the dielectric function of the molecule of interest, with $\varepsilon_r = n^2$, its mass density, and molecular weight respectively.

Limit of Detection

Although individually the Q-factor and refractive index sensitivity can provide a wealth of information about the performance of the resonator, combining them together provides an indication of the resonators ability to detect and quantify the various properties of the target solution through the definition of the detection limit [202]. The detection limit indicates the smallest measureable refractive index change the resonator can accurately quantify,

$$DL = \frac{\delta\lambda}{S} \tag{1.9}$$

where $\delta\lambda$ is the sensor resolution [202]. The sensor resolution is influenced by the properties of the resonator (i.e. Q-factor) as well as the observing system (e.g. spectrometer or photodiode) and associated noise sources (e.g. variations in temperature and excitation laser intensity). For example, consider an active WGM sensor using a spectrometer to observe and track the wavelength shift of the resonance peaks. The first limit introduced on the sensor resolution is from the spectral resolution of the spectrometer, $\sigma_{\text{spect-res}}$, typically ranging from 200 pm as seen in common portable spectrometers up to 4 pm in laboratory grade spectrometers. The second limit arises from the noise associated with the detection system, which can be classified as either being amplitude or spectral noise. Amplitude noise, σ_{amp}, is defined as noise that contributes to the overall spectrum, such as variation in the intensity of the

excitation laser, while spectral noise, σ_{peak}, specifically covers noise that influences the position of the resonance peaks, such as temperature variations. Using Monte Carlo simulations, it has been shown that σ_{peak} can be approximated by [202, 216],

$$\sigma_{peak} \approx \frac{\Delta\lambda_{peak}}{4.59\left(SNR^{0.25}\right)} \tag{1.10}$$

where $\Delta\lambda_{peak}$ is the width of the WGM mode of interest in nm. The total sensor resolution, $\delta\lambda$, can then be quantified as the sum of all these individual noise sources [202], namely,

$$\delta\lambda = 3\sigma = 3\sqrt{\sigma^2_{spect-res} + \sigma^2_{amp} + \sigma^2_{peak}} \tag{1.11}$$

therefore, one way to improve the sensor resolution is to optimize the SNR of the sensor [217]. For active resonators, the SNR ratio can be improved by operating the resonator above its lasing threshold, resulting in an increase in both spectral intensity and Q-factor [188, 189]. While interferometric techniques and phase shift cavity ring down spectroscopy [218] have proven useful techniques for increasing the SNR of passive resonators.

1.1.2 Mode Positions of Spherical Resonators

Developing analytical and numerical tools that allow the mode positions, along with the WGM spectrum, to be produce represents important techniques for assisting in interpreting and predicting experimental observations as well as providing a way investigating novel resonator materials and geometries. The simulation of WGMs in spherical resonators began with the development of Mie scattering theory to extract wavelength positions of the modes [126, 128, 219]. The mode positions of WGMs in a spherical resonator can be estimated from purely geometric arguments as the result of constructive interference of the travelling wave satisfying the resonance condition,

$$\lambda_R = \frac{2\pi R n_e}{m} \tag{1.12}$$

Where R is the radius, n_e is the effective refractive index of the sphere and the surrounding medium and m is the mode number. More explicitly, by solving the boundary value equation of a spherical resonator, and enforcing continuity, the characteristic equations [220] as a function of the size parameter, $x = \pi D/\lambda$, can be established,

$$n_e^{1-2k}\frac{j_n'(n_e x)}{j_n(n_e x)} = \frac{h_n'(x)}{h_n(x)} \tag{1.13}$$

where $k = 0$ for TE and $k = 1$ for TM modes and j_n and h_n are the spherical Bessel and Hankel functions respectively. From this equation, both the TE and TM mode positions can be obtained. Furthermore, the Q-factor can be estimated using a model derived from the asymptotic analysis of the above characteristic equation, where solutions lie near a root, t_0, of the Airy Function, $A_i(t)$ [220, 221],

$$Q = \frac{\mathrm{Re}(\omega)}{\mathrm{Im}(\omega)} = \frac{1}{2} v n_e^{2k-1} \sqrt{n_e^2 - 1} e^{2T_l} \tag{1.14}$$

$$T_l = v[\eta_l - \tanh(\eta_l)] \tag{1.15}$$

$$\eta_l = ar\cosh\left\{ n_e \left[1 - \frac{1}{v} \left(t_0 \left[\frac{v}{2} \right]^{1/3} + \frac{n_e^{1-2k}}{\sqrt{n_e^2 - 1}} \right) \right]^{-1} \right\} \tag{1.16}$$

where $v = l + ½$. However, in order to determine the Q-factor more accurately, it is preferable to use one of the alternative methods for calculating the Q-factor instead of Eq. 1.14, such as using the resonance wavelength and linewidth obtained directly from the WGM spectrum or considering the loss mechanisms present (e.g. scattering, radiation, material) as previously outlined.

1.1.3 Generating WGM Spectra from Spherical Resonators

Progressing from simply being able to predict the location of the modes, the ability to generate the WGM spectrum enables greater insight into the performance of a resonator by allowing for comparison and interpretation of experimentally observed spectra. The WGM spectrum can be modeled numerically using approaches such as the Finite-element Method (FEM) [222] and Finite-Difference Time Domain (FDTD) [223, 224], or analytically. Different excitation scenarios can also be considered, such as plane-wave [223, 225] and dipole excitation [226-230]. Dipole source excitation is particularly interesting for active resonators, allowing analogous comparisons with experimental spectra from either quantum dot covered or fluorescent-doped resonators, as have been utilized for the experimental work contained in this thesis, for example.

There are both advantages and disadvantages to using either numerical or analytical approaches to examine and characterize the properties and performance of active WGM resonators. For example, numerical methods allow for the comprehensive treatment of the electromagnetic fields, including the ability to consider the effects of non-ideal shapes and surface roughness. In the case of FDTD, space and time are discretized on a grid. The electric field is evaluated in the center of each grid line, and the magnetic field in the center of each cell, in a construction known as the Yee Cell [231]. This allows access to the intermediate values in the fields, enabling transient or emergent optical phenomena to be

investigated, as the time is incremented slice-by-slice. While, FEM methods are better suited for investigating the steady-state behavior of the modes by approximating the resonator as a polygon, and solving the boundary differential equation at each interface. However, numerical methods are notoriously computationally intensive to run and therefore are not suited to being able to evaluate large numbers of resonators at once or provide real-time comparison with experimental data. Although analytical models can only consider ideal resonators (i.e. perfect and homogenous refractive index spheres) and the TE and TM mode profiles are generated independently from each other, analytical models are significantly faster to run and have been implemented for identifying resonator parameters (radius and refractive index) in real-time [232].

In 1988, Chew developed the first analytical model that allowed the generation of WGM from spherical resonators with first a single and then distribution of dipole sources [226, 228]. Beginning with a single dipole orientated either perpendicular or parallel to the surface tangent, the normalized power spectrum can be calculated from [227],

$$\frac{P^{\perp}}{P_0^{\perp}} = \frac{3}{2}\frac{\varepsilon_1 n_1}{x_1^2}\sqrt{\frac{\varepsilon_2}{\mu_2}}\sum_{n=1}^{\infty} n(n+1)\cdot(2n+1)\frac{j_n^2(x_1)}{x_1^2}|D_n|^2 \tag{1.17}$$

$$\frac{P^{\parallel}}{P_0^{\parallel}} = \frac{3}{4}\frac{\varepsilon_1 n_1}{x_1^2}\sqrt{\frac{\varepsilon_2}{\mu_2}}\sum_{n=1}^{\infty}(2n+1)\cdot\left(\left|\frac{[x_1 j_n(x_1)]'}{x_1 D_n}\right|^2 + \frac{\mu_1\mu_2}{\varepsilon_1\varepsilon_2}\frac{j_n^2(x_1)}{|D_n'|^2}\right) \tag{1.18}$$

where $n_i = \sqrt{\varepsilon_i \mu_i}$, for the resonator and surrounding medium corresponding to i = 1 and 2 respectively. The denominators, D_n and D_n' define the resonance positions, matching with the Mie Scattering coefficients[204],

$$D_n = \varepsilon_1 j_n(x_1)\left[x_2 h_n^{(1)}(x_2)\right]' - \varepsilon_2 h_n^{(1)}(x_2)\left[x_1 j_n(x_1)\right]' \tag{1.19}$$

$$D_n' = D_n(\varepsilon_{1,2} \to \mu_{1,2})$$

By considering a distribution of dipoles, representing a dye-doped polystyrene microsphere for example, within a resonator and averaging over the orientations of a random distribution of dipoles in the active region, the normalized power spectrum can be obtained [204, 233],

$$\left\langle \frac{P}{P_0} \right\rangle \equiv \left\langle \frac{P^{\perp}}{P_0^{\perp}} + 2\frac{P^{\parallel}}{P_0^{\parallel}} \right\rangle \frac{1}{3} \tag{1.20}$$

$$P = 2H\sum_{n=1}^{\infty}\frac{2n+1}{3}\left(\frac{J_n}{|D_n|^2} + \frac{GK_n}{|D_n'|^2}\right) \tag{1.21}$$

where

$$H = \frac{9\varepsilon_1}{4x_1^5}\sqrt{\frac{\varepsilon_1\varepsilon_2\mu_1}{\mu_2}},\ G = \frac{\mu_1\mu_2}{\varepsilon_1\varepsilon_2},$$

$$K_n = \left(\frac{x_1^3}{2}\right)\left[j_n^2(x_1) - j_{n+1}(x_1)j_{n-1}(x_1)\right],\ J_n = K_{n-1} - nx_1 j_n^2(x_1)$$

Examples of the resulting normalized power spectrum (Eq. 1.21) for active microspherical resonators (n_1 = 1.59) residing in water (n_2 = 1.33) with radii 4, 5, 6 and 7 μm are displayed in Fig. 1.4.

Examining Fig 1.4, as the radius is increased from 4 through to 7 μm there are significant changes in the mode profile, free spectral range (i.e. distance between two successive TE or TM modes) and Q-factor are observed. For example, as the radius is increased the Q-factor increases, reducing the chance of overlapping modes such as those in Fig. 1.4 (D), while the free spectral range decreases, allowing more modes to be observed over a given wavelength range, Fig. 1.4 (A). This highlights how changing the size of the resonator can be used to tailor the performance of the resonator (i.e. refractive index sensitivity and Q-factor), noting that varying the refractive index of the resonator has a similar affect. Therefore, using this theory and analytical model (corresponding MATLAB code in Appendix A), the problem of selecting the ideal active resonator for undertaking refractive index biosensing using active microspheres can be addressed by investigating the performance of resonators with varying size and refractive index [204].

1.1.4 Lasing Whispering Gallery Modes

Additionally, active WGM resonators have the ability to be turned into microscopic laser sources, as documented in a variety of configurations [106, 137, 148, 183, 209, 234-237]. Operating resonators in the stimulated emission regime increases the Q-factor, typically by a factor of approximately 4, which can lead to an increase in resolution and hence lower detection limits for biosensing applications. This has been demonstrated for both dye-doped polystyrene microspheres [189] and fluorescent polymer coated microcapillary resonators [209].

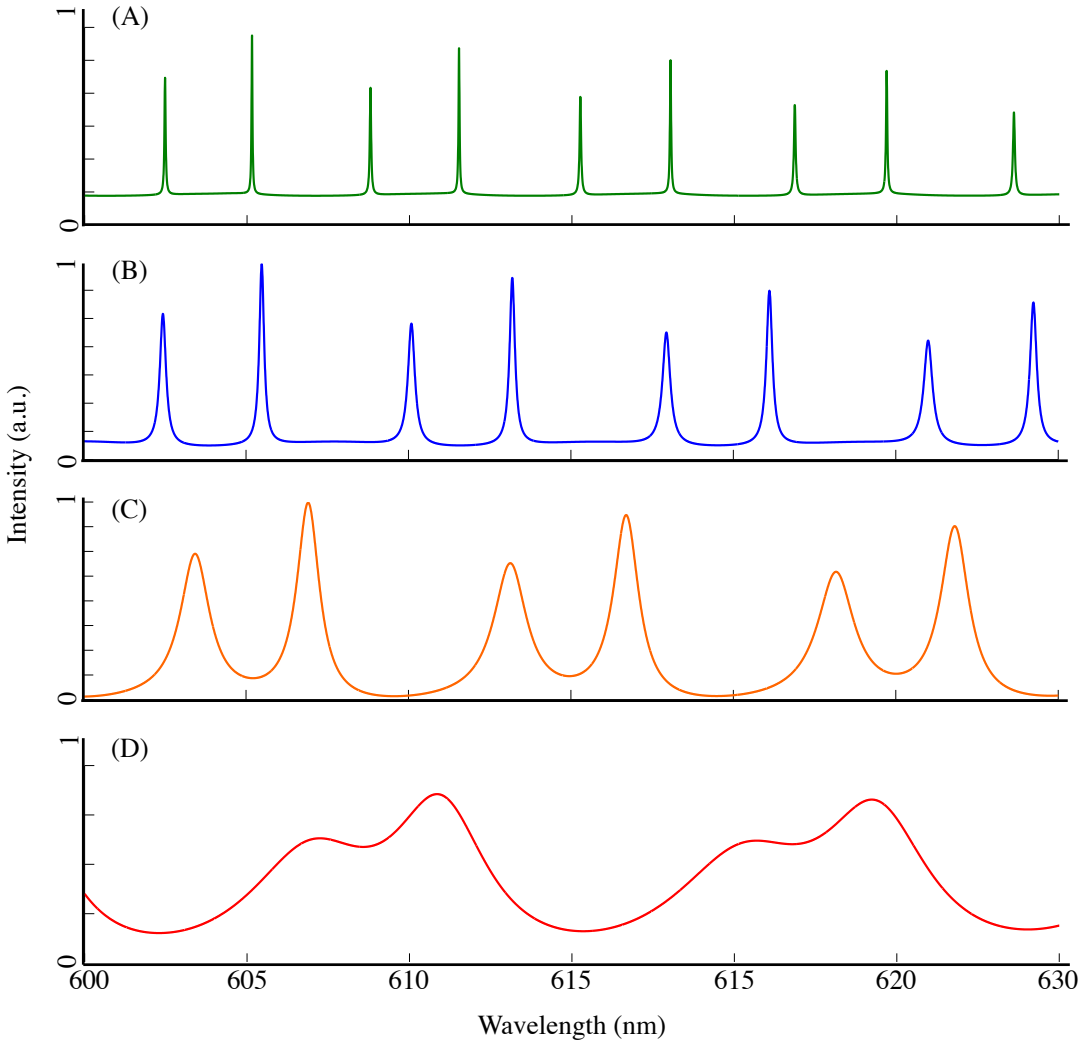

Figure 1.4. Examples of normalised WGM power spectra for active microspherical resonators with refractive index $n_1 = 1.59$ in water $n_2 = 1.33$ with radius (A) 7 μm (B) 6 μm (C) 5 μm (D) 4 μm

From a theoretical standpoint, describing the behavior and understanding the contributing factors for determining the lasing threshold of whispering gallery mode lasers remains challenging. Original formulations, such as cold-cavity modeling (i.e. with no consideration of gain effects) of microlasers used FDTD simulations [238], associating the modes with the largest Q-factors as lasing modes [239, 240]. Using approaches such as the Lasing Eigenvalue Problem (LEP) [241, 242] on the other hand, which introduces gain through the imaginary part of the refractive index, allows both the laser threshold and frequencies to be determined numerically. Similarly, by introducing an imaginary refractive index into Eq. 1.21, the laser threshold of the individual modes can be determined. However, this model is not able to provide information about the modes once they have surpassed their lasing threshold [243].

In terms of establishing a relationship for the laser threshold, there is also not yet a consensus in the literature. For example, a relationship has been established for the Raman lasing threshold of a fiber coupled microsphere, highlighting the dependency on the gain factor (A), effective mode volume (V_{eff}) and Q-factor [120],

$$I_{threshold} = A\frac{V_{eff}}{Q^2} \tag{1.22}$$

Here, A can be either the gain coefficient for a Raman laser [120], the gain medium concentration or quantum yield of a fluorescent dye [137]. In contrast, earlier work with neodymium doped silica microspheres [244] and more recent work with ZnO microdisks [245], reported a lasing threshold that had a linear dependency on the inverse of the Q-factor.

1.2 Resonators

Microscale WGM resonators have been fabricated from a diverse range of materials including liquids [134, 135] and polymers [136-140] to glass [93, 98, 141, 142] and crystalline materials [143-145] with geometries including simple microspheres and microbubbles [206, 246-248] through to capillaries [168, 169, 249], toroids [192] and disks [250, 251]. The resonator sizes encompass microns to millimeters in diameter. Every type of resonator geometry can be made active with the inclusion of an organic or inorganic gain medium. More detailed discussions specifically on active resonators, as well as highlighting some of the most commonly used and novel organic and inorganic gain mediums, are provided in Chapter 2. Here, the methods used to excited WGM resonators are briefly outlined, including near field evanescent coupling schemes for interrogating WGM within microresonators such as fiber taper [252], waveguide [160], prism [161] and angle-polished fibers [253], depicted in Fig. 1.5.

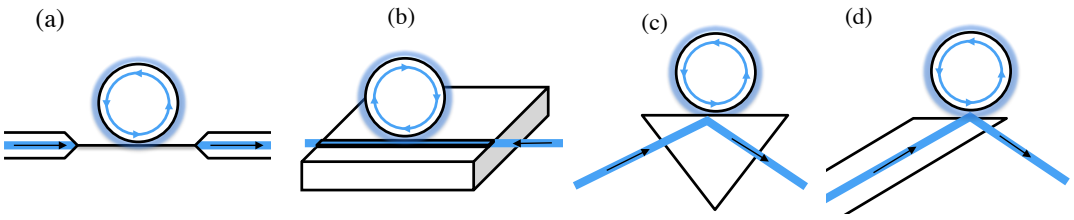

Figure 1.5 Depiction of commonly used evanescent wave coupling schemes for interrogating WGM. (a) Fibre taper, (b) waveguide, (c) prism and (d) angle polished-fiber

The basic principle of near field evanescent coupling schemes is to excite WGM resonances via efficient energy transfer from the evanescent field of the coupler to the resonator. This can occur if there is phase or mode matching as well as significant overlap between the evanescent fields of the coupler and the resonator [171, 254]. Phase matching occurs when the propagation constant of the resonator and coupler match. While the overlap of the two fields can be ensured by maintaining a precise gap between the resonator and coupler. Any changes in the resonators positioning can result in reduced Q-factor [255] or changes in resonance frequencies [256]. This leads to the definition of three coupling categories, under-coupled, critical coupled and over coupled, which depend on the relationship between the losses of the coupler and resonator [257]. Critical coupling occurs when the losses of the resonator and coupler are equal and therefore there is complete energy transfer from the coupler to the resonator, with no transmission at the output of the coupler. Under coupling occurs when the losses of the coupler (i.e. scattering) are greater than that of the resonator, resulting in significantly lower Q-factors compared to critically coupled resonators. In over coupled situations, the losses of the resonator are larger than those of the coupler, again reducing the Q-factor compared to a critically coupled configuration. Coupling efficiencies have reached as high as 99% with fiber tapers [258], 78% for prisms [254] and 28% with angle polished fibers [253].

Fiber Taper

Fiber tapers were originally used for interrogating WGM within silica microspherical resonators [97, 159, 259], and since then have been extended to other geometries including microdisks [250, 251], toroids [192], goblets [260], microbubbles [206, 246-248] and capillaries [168, 169, 249]. Phase-matching of the propagation constant of the resonator and the taper for critical coupling can be fine-tuned via varying the thickness of the fibre taper during fabrication [252]. Fiber taper coupled resonators, such as silica microspheres for example, have demonstrated tremendous performance including extremely high Q-factors [162], allowing them to be used as biosensors [96, 97, 199, 261, 262], filters [166, 167], force sensors [263] as well as nonlinear optics and QED applications [164, 165] to name a few. Fiber-tapers have also been used to interrogate active glass-based microspherical resonators, such as those formed through either direction fabrication of doped glasses or by the deposition of coatings and rare-earth ions to the resonators surface [141, 264-266]. However, the significant drawback to utilizing fiber taper interrogation systems specifically for biosensing experiments is the inherently small diameter of the taper, making it susceptible to damage and fowling [172].

Waveguide

Waveguide couples are commonly fabricated on top of a substrate using techniques such as molecular-beam epitaxy [267] or vapor deposition [268, 269] to form microstructures that are able to guide light through a refractive index contrast. This allows the evanescent field of the incident laser to overlap and couple into the resonator [270, 271], as depicted in Fig. 1.5 (B). Waveguides provide a robust platform for integrated sensing, allowing multiplexed [272-275] as well as self-referenced configurations to be constructed easily. For example, White *et al*. demonstrated how placing multiple anti-resonant reflecting optical waveguides onto a single chip allows multiple ring resonators to be excited within a single liquid core ring resonator [269]. While, the self-referenced configurations work by having one resonator that is not looking for a specific interaction and therefore can be used to subtract signal fluctuations from changing environmental conditions or non-specific binding in complex solutions. Notably, Genalyte Inc. have developed a multiplexed silicon ring resonator diagnostic platform, with capabilities for monitoring 32 biological analytes from a single sample [200], using the same approach.

Prism

TIR at the prisms surface allows incident laser light to be evanescently coupled into the resonator, with critical coupling being reached via varying the angel of incidence of the laser light [123, 276], as depicted in Fig. 1.5 (C). Similarly to waveguide couplers, prisms provide a more robust coupling scheme compared with fibre tapers and have found applications for nonlinear optics [277] and as tunable filters [278], for example. Although, achieving critical coupling through varying the incidence angle is both tedious and difficult. The prism surface is also susceptible to contamination from dust and water vapor, which can lead to degradation of the Q-factor of the coupled resonator [153].

Angle-polished fiber

Polishing the end of an optical fiber to a specific angle allows incident laser light guided through the fibre to undergo frustrated TIR at the fiber tip, resulting in evanescent coupling into the resonator [253, 279, 280], Fig. 1. 5 (D). This provides increased robustness compared to a fiber taper, but without the bulkiness of waveguides or prisms. Although the fiber can also be used to collect the transmitted light from the resonator, practical applications of angle-polished fiber systems outside a research environment are severely limited. For example, the specific angle the fiber must be polished to depends on the individual properties of the resonator (i.e. size, material), meaning a new fiber must be polished each time the resonator is changed. Finally, angle-polished fibers have highest coupling efficiency for larger resonators (i.e. > 1mm), with a significant drop off seen for smaller resonators.

1.3 Active Microsphere Preparation

Due to the low cost, commercial availability and practical advantages of free-space coupled active resonators, for all the experimental work considered in this thesis, the resonators used are dye-doped polystyrene microspheres (nominal diameter of 20 μm, $\Delta\emptyset$ = 0.8 μm and n = 1.59 for [189], nominal diameter of 15 μm, $\Delta\emptyset$ = 0.8 μm and n = 1.59 for [129, 140]), where the gain medium is provided by the laser dye Nile Red (λ_{abs} = 532 nm, λ_{em} = 590 nm) [281]. Here, a description of the doping procedure used and a brief overview of possible surface functionalization techniques for WGM resonators is provided.

1.3.1 Doping

The doping procedure begins by suspending the polystyrene microspheres in water, Fig. 1.6 (A), and then dissolving the laser dye Nile Red into xylene until the solubility limit is reached. Xylene is immiscible with water, therefore when the Nile Red/xylene solution is pipetted on top of the suspended microspheres, Fig. 1. 6 (B), there is no mixing between the liquids. By using a magnetic stirrer to provide agitation, the polystyrene microspheres are able to reach the interface between the two solutions, where the fluorescent dye can be transferred to the spheres.

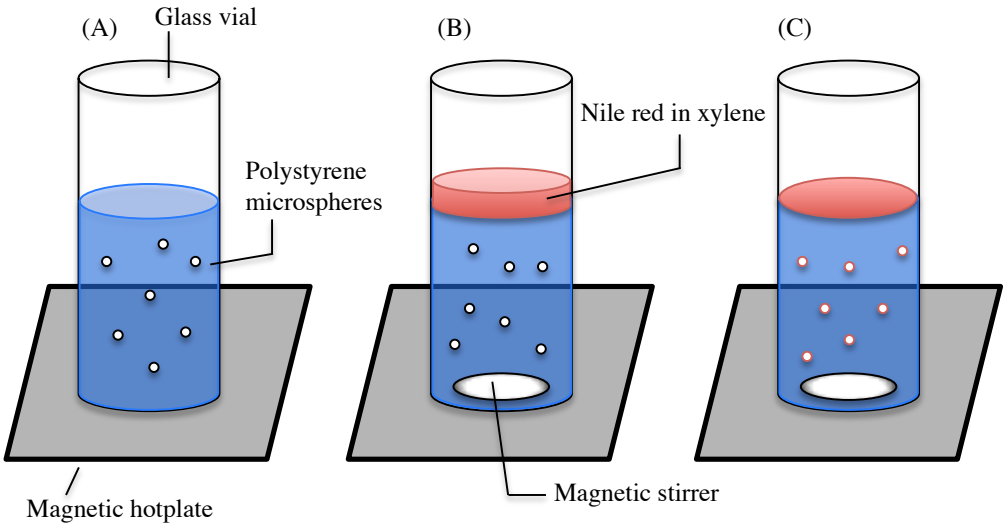

Fig.1.6 steps in the dye-doping process (A) Polystyrene microspheres are placed in water on top of a hot plate, (B) the fluorescent dye Nile Red, dissolved in xylene, is added to the vial (C) The fluorescent dye is transferred to the spheres as they come into contact with the xylene layer.

This process continues until all the xylene has been either transferred to the spheres or evaporated away, Fig. 1.6 (C). The low solubility of Nile Red and water ensures that once the dye has entered the sphere is will remain inside. Varying the amount of Nile Red/xylene solution used effects the lasing threshold of the microspheres [209].

1.3.2 Surface Functionalization

In order to enable highly sensitive, selective and label-free monitoring of specific interactions with analytes such as viruses [103], bacteria [272, 282], proteins [140, 189] or DNA strands [97], the resonators surface must first be functionalized, Fig 1.7. During the functionalization process considerations including the thickness of the functionalized layer, to ensure any interaction on the resonators surface occurs within the resonators evanescent field, and the orientation of the immobilized bioreceptors, to maximize the available binding sites [283-285], needs to be taken into account. Functionalization of a resonators surface typically occurs in three steps: preparing the surface, immobilization of the bioreceptor of interest, and pacifying active sites to reduce the effects of non-specific binding.

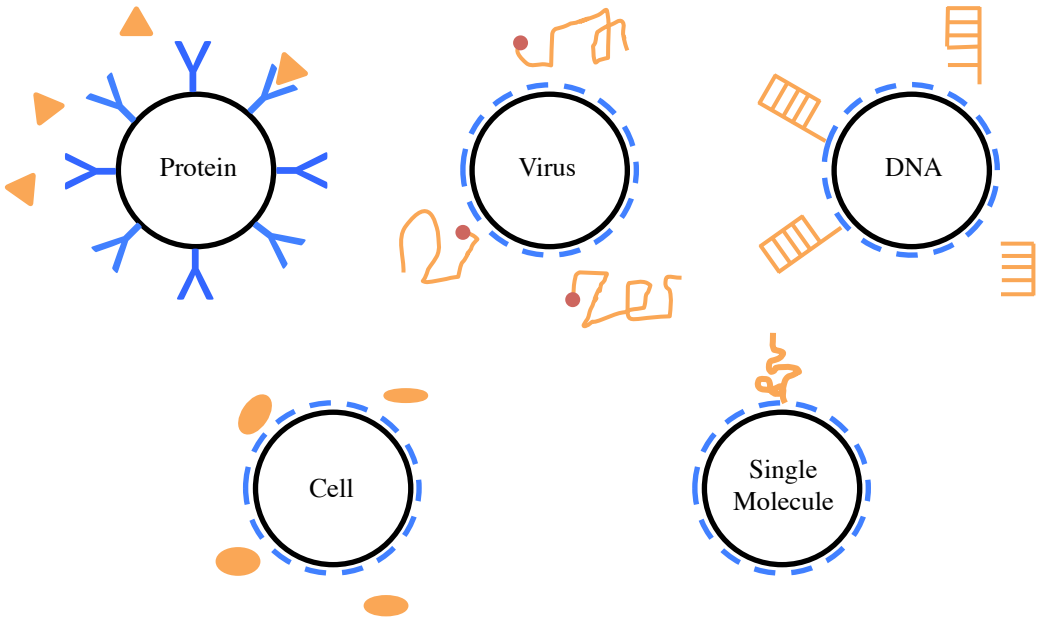

Fig. 1.7 Examples of functionalized WGM resonators.

A. Preparing the Surface

The first step in the surface functionalization process is to prepare the resonators surface with functional groups in order to facilitate the subsequent immobilization of the required bioreceptor. This

is typically achieved using either covalent binding or physiosorption techniques. Covalent binding techniques are approaches that create covalent bonds on the sensors surface and are known for their stability and durability [286-289]. The most commonly used covalent binding approaches involve the binding of silane groups, such as (3-aminopropyl)trimethoxysilane (APTMS) [290], 3-aminopropyldimethylethoxysilane (APDMES) [291], 3-glycidoxypropyl-trimethoxysilane (GOPTS) [292, 293] and 3-mercaptopropyltrimethoxysilane (MPTMS) [176] to the resonators surface. However, in order for the silane groups to bind to the resonator, the surface must first be activated with hydroxyl groups and is commonly achieved by either acid cleaning [294] or plasma activation [295]. Unfortunately, this process of activating the resonators surface is not applicable to all materials, including polymers, such as polystyrene, that have been utilized throughout this project.

Alternatively, physiosorption techniques such as depositing layers of alternating charge polyelectrolytes (PE) onto the resonators surface, can be applied to a range of materials [296-299], notably including polymers [177]. There are a variety of different PEs that can be used, however, polyallylamine hydrochloride (PAH) and polystyrene sulfonate (PSS), are two of the most widely implemented. For example, they have been successfully deposited on dye-dope polystyrene microspheres [177] (including for the work completed in this thesis [140, 189]), the core of a suspended core silica MOF [296, 297] as well as silver coated optical fibers for SPR biosensing [298, 299].

B. Bioreceptor Immobilization

Once the surface has been prepared with the appropriate functional group, further chemical interactions can be implemented to facilitate the immobilize of the bioreceptor of interest. Typically, cross-linkers such as hydrazine-nicotinamide (HyNic)/4-formylbenzaminde (4FB) [300], glutaradldehyde [301, 302] and coupling reagents carbodiimides such as 1-ethyl-3-(3-dimethylaminoropyl) carbodiimide (EDC) and N-hydroxysuccinimide (NHS) [140, 189] are used to enable covalent binding between the primary amine on the sensors prepared surface and the bioreceptor of interest. Commonly used bioreceptors include antibodies, complementary DNA, enzymes and aptamers. Sensors utilizing antibodies are known as immunosensors, and they take advantage of the high affinity and specificity between an antibody and its corresponding antigen. While aptasesnors (i.e. aptamer based sensors) use functional molecules that allow a wide range of target analytes spanning small molecules and proteins through to cells to be detected.

For the work completed here, covalent binding between the final PAH layer and Biotin-D is used to create a biotinylated surface and represents the end of the surface functionalization process. The

specific interaction between biotin and neutravidin is then used to demonstrate and characterize the sensors capabilities. However, the biotinylated surfaces can easily be further functionalized by coating with another layer of an avidin (i.e. neutravidin or streptavidin) and then a biotinylated antibody [293].

Regardless of the bioreceptor utilized, correctly immobilizing the bioreceptor to the resonators surface is as important as the resonators parameters (i.e. Q-factor and refractive index sensitivity) in determining the ultimate performance of the sensor [65]. For example, the ability to control the orientation of the bioreceptor is highly desirable in order to maximize the responsiveness and affinity of the sensor to the target analyte, especially in low concentrations [285]. In the case of immunosensors, one technique employed to ensure the correct orientation of the antibodies is to use protein A or G [303, 304]. These proteins form an anchor on the sensors surface through the F_c fragment, as shown in Fig. 1.8, allowing the epitopes, also known as the F_{ab} fragments, to face away from the surface and interact with the antigens in surrounding medium.

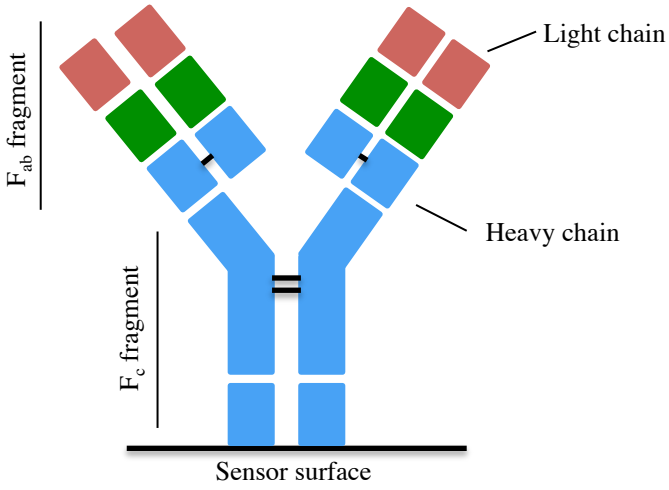

Fig. 1.8 Depiction of a protein G antibody structure.

Recently, techniques using selective UV photo-activated cross linkers have began to generate interest for functionalizing WGM resonators [112, 305]. Unlike other covalent or physiosorption techniques, using UV photo-activated cross linkers allows precise control and localization of the functionalization sites. Notably for example, this technique has been utilized for functionalizing microbubble resonators ensuring that only the hollow cavity is functionalized and not simply the entire capillary structure [306]. This is important, especially when dealing with low concentrations of analytes, to ensure that any interaction of the analyte of interest occurs within the evanescent field of the WGMs, and not further up in the capillary. Additionally, this technique has enabled multiple microbubbles residing along the same capillary to be individual functionalized to monitor different interactions [306].

C. Pacification

Non-specific binding (NSB) is the binding of other proteins or biomarkers present in a sample to the surface of the resonator, which can lead to increased spectral noise, false positive readings or degradation of the sensor [172]. Reducing the effects of NSB is one of the main challenges for WGM biosensing, as for all refractive indexed based biosensors, when undertaking measurements in complex solutions. For example, the ability of a sensor to distinguish or eliminate unwanted fluctuations in the signal due to variations in temperature, surrounding refractive index or NSB events is critical in transitioning from operating purely in controlled research environments to applications involving being able to assess real clinical samples.

The main methods developed for preventing NSB in label-free biosensing platforms containing a single resonators to date have focused primarily on improving surface functionalization techniques by trying to increase specificity through pacifying NSB sites on the sensor's surface. For example, successful reduction of the effects of NSB has been demonstrated on Surface Plasmon Resonance biosensors [65, 307] by using NHS esters [308], CM dextran [309] and polyethylene glycol (PEG) [310]. For WGM biosensors, PEG coatings have proven successful when integrated with silica microspheres [96, 311], with thrombin being detected in 10-fold diluted human serum samples using a flow cell [96], for example. Unfortunately, these surface functionalization processes require the initial production of hydroxyl groups on the sensors surface [294, 295], and as previously discussed is not possible on all surface types, specifically not being applicable for polystyrene resonators.

For the work completed here a Casein blocking agent is used to pacify the binding sites by "filling the gaps" between the antibodies bound to the surface. Casein is chosen in preference over other commonly used blocking agents such as BSA and gelatin as it provides a distribution of molecular weights, ensuring better coverage between the binding sites.

1.4 Project Aims

The primary aim of this thesis is to develop an efficient and simple biosensing platform that is able to conduct real-time label-free protein detection in complex solutions, with the potential for future *in-vivo* sensing, through the combination of the refractive index transducing mechanism of WGMs within fluorescent microspheres and a suspended core MOF.

Review of Active WGM Sensing

First, a review of WGM in fluorescent microresonators and their sensing applications is provided. This includes providing a theoretical background on fluorescent and lasing WGM resonators, strategies for

incorporating organic or inorganic gain medium and an overview of fluorescent resonator geometries, both commonly used and newer architectures, and their corresponding applications. Concluding remarks focus on future applications and possible improvements for fluorescent based WGM sensing technologies.

Resonator Selection

One of the initial steps in developing a WGM based biosensing platform is the selection of the resonator and maximizing its performance. For biosensing applications there are two key parameters commonly used for characterization sensing performance and they are the Q-factor and refractive index sensitivity. A higher Q-factor results in increased resolution, while higher refractive index sensitivity enables subtler changes in the surrounding environment to be monitored. As both these parameters can be extracted directly from the WGM spectrum, by developing an analytical tool that is able to efficiently generate the spectrum of any active microsphere resonator with radius, R, and refractive index, n, the characterization of a large number of resonators can take place. This process can be tailored for individual applications through restricting the types of materials, the wavelength range, sizes and surrounding environment, for example, that are considered, allowing the optimal resonator parameters in terms of refractive index and size to be identified. As an example of how this model can be used to provided guidelines for undertaking refractive index biosensing with active microspherical resonators, a subset of resonators is assessed. The set of resonators is selected based on previous experimental work with polystyrene microspheres doped with fluorescent organic dyes to determine the optical combination of resonator refractive index and radius to optimize sensing performance in water (the typical environment for biosensing applications). The results of this optimization process are then used to select the resonators for the fiber-tip sensing platform

Performance Limitations

The inherently lower Q-factors associated with active resonators, specifically those of fluorescent microspheres remains a limiting factor for lowering the detection limit of active resonators for biosensing applications. In order to investigate this further, dye-doped polystyrene microspheres are examined and compared under different excitation (free-space and fiber taper) and collection (far-field and fiber taper) methods. It is proposed that the intrinsic asphericity present in commonly used active resonator (such as dye-doped polystyrene microspheres) is responsible and therefore differences in the Q-factor would become apparent under the different excitation/collection situations. Along with the experimental data, theoretical modeling and imaging techniques are used to thoroughly investigate the resonators and identify the potential source for the lower Q-factors observed.

Platform Demonstration

An alternative approach to free-space excitation and collection the WGM modulated fluorescence spectrum that still enables flexibility and control over the measurement location, is to use a MOF. The core of the fiber acts like a fiber taper, allowing only a subset of modes to be excited, resulting in an increase in the Q-factor. Further, the MOF provides a robust and easy to manipulate dip-sensing architecture that bypasses the need for complex microfluidic sample delivery systems and has the potential to operate *in-vivo*. The first demonstration of such a platform based on the combination of a MOF and an active WGM resonator to be used for biosensing applications is performed using the well-known specific interaction model based on biotin-Neutravidin in unperturbed small volume samples. Further, ways to improve the sensing performance, specially the detection limit, are investigated by operating the resonator above its lasing threshold.

Measurements in Complex Solutions

Finally, as mentioned previously, the ability of a sensor to distinguish or eliminate unwanted fluctuations in the signal due to variations in, for example temperature, surrounding refractive index or NSB is critical in transitioning from operating purely in controlled research environments to applications involving being able to assess real clinical samples. A simpler approach, asides from using surface functionalization techniques to overcome to this problem, is to introduce a second resonator into the sensing system to act as a dynamic reference capable of compensating for both changes in the environmental conditions, such as temperature fluctuations, as well as NSB events. Previous demonstrations of multiplexing WGM sensors include a range of resonator types and geometries covering passive microspheres [97], liquid core ring resonators [269], microdisks [312] and even fluorescent microspheres for imaging techniques [313, 314]. Here, a self-referenced WGM biosensing platform is developed and demonstrated for the specific detection and quantification of biomolecules in undiluted human serum by extending on the work completed in [189], through the addition of a second almost identical fluorescent microsphere resonator to the MOF tip. In this configuration one resonator acts as a sensing resonator, being functionalized for monitoring of a specific interaction, while the second resonator is functionalized to act as a dynamic reference compensating for environmental changes and NSB. Again, to evaluate the sensing performance of the self-referenced platform in both pure and complex solutions, the well-known specific interaction model based on biotin-Neutravidin is used.

Flowchart showing the links between chapters, publications and appendices

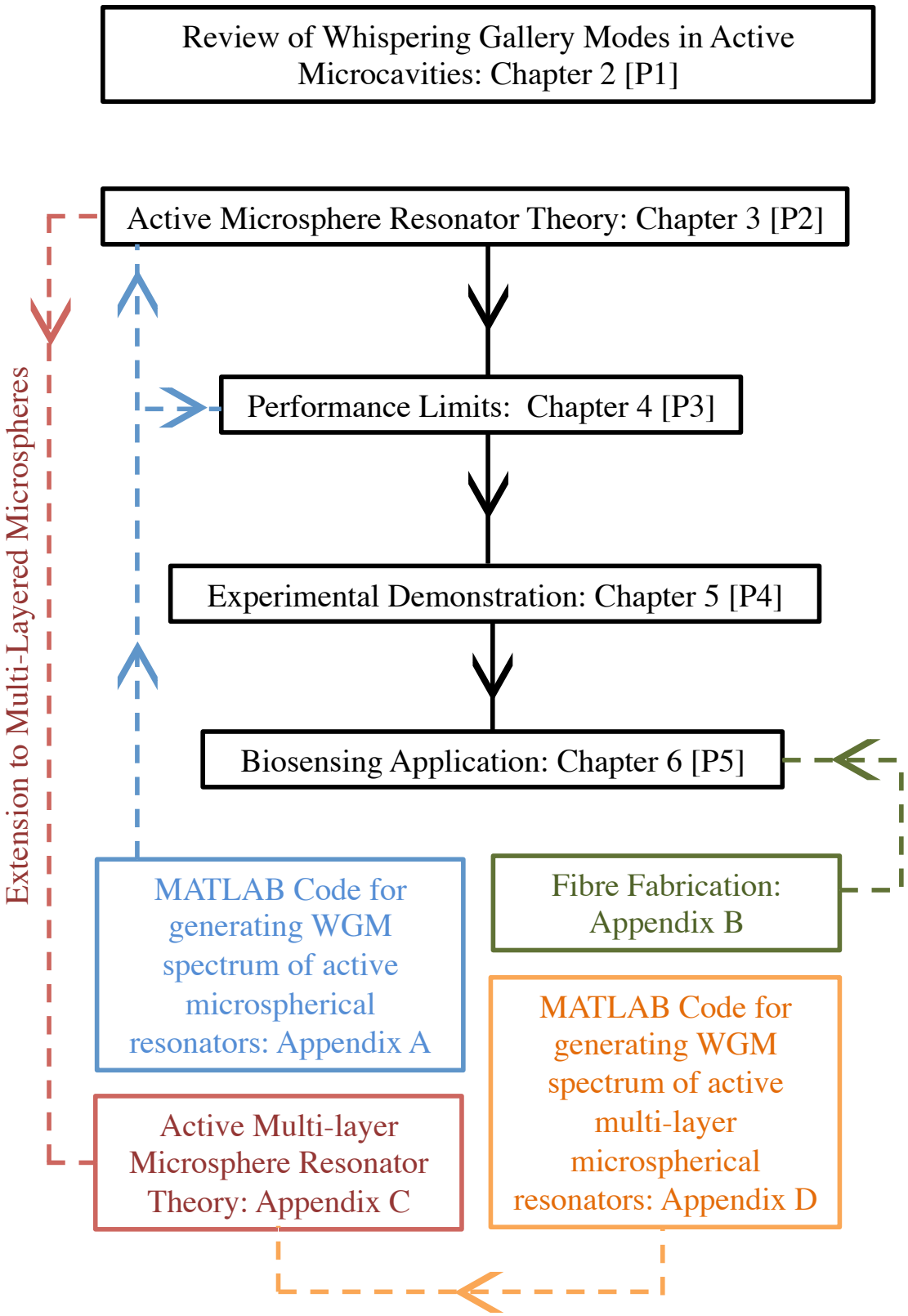

1.5 References

1. Tokel, O., F. Inci, and U. Demirci, *Advances in Plasmonic Technologies for Point of Care Applications*. Chemical Reviews, 2014. **114**(11): p. 5728-5752.
2. Cooper, M.A., *Biosensor profiling of molecular interactions in pharmacology*. Current Opinion in Pharmacology, 2003. **3**(5): p. 557-562.
3. Rodriguez-Mozaz, S., et al., *Biosensors for environmental monitoring of endocrine disruptors: a review article*. Analytical and Bioanalytical Chemistry, 2004. **378**(3): p. 588-598.
4. Paddle, B.M., *Biosensors for chemical and biological agents of defence interest*. Biosensors and Bioelectronics, 1996. **11**(11): p. 1079-1113.
5. Mello, L.D. and L.T. Kubota, *Review of the use of biosensors as analytical tools in the food and drink industries*. Food Chemistry, 2002. **77**(2): p. 237-256.
6. Luo, X. and J.J. Davis, *Electrical biosensors and the label free detection of protein disease biomarkers*. Chemical Society Reviews, 2013. **42**(13): p. 5944-5962.
7. Arlett, J.L., E.B. Myers, and M.L. Roukes, *Comparative advantages of mechanical biosensors*. Nat Nano, 2011. **6**(4): p. 203-215.
8. Perez, J.M., et al., *Magnetic relaxation switches capable of sensing molecular interactions*. Nat Biotech, 2002. **20**(8): p. 816-820.
9. Graham, D.L., H.A. Ferreira, and P.P. Freitas, *Magnetoresistive-based biosensors and biochips*. Trends in Biotechnology, 2004. **22**(9): p. 455-462.
10. Ramanathan, K. and B. Danielsson, *Principles and applications of thermal biosensors*. Biosensors and Bioelectronics, 2001. **16**(6): p. 417-423.
11. Fan, X., et al., *Sensitive optical biosensors for unlabeled targets: A review*. Analytica Chimica Acta, 2008. **620**(1–2): p. 8-26.
12. Ruan, Y., et al., *Antibody immobilization within glass microstructured fibers: a route to sensitive and selective biosensors*. Optics Express, 2008. **16**(22): p. 18514-18523.
13. Goldsmith, S.J., *Radioimmunoassay: Review of basic principles*. Seminars in Nuclear Medicine, 1975. **5**(2): p. 125-152.
14. Eggins, B.R., *Chemical sensors and biosensors*. Vol. 28. 2008: John Wiley & Sons.
15. Stepurska, K.V., et al., *Development of novel enzyme potentiometric biosensor based on pH-sensitive field-effect transistors for aflatoxin B1 analysis in real samples*. Talanta, 2015. **144**: p. 1079-1084.
16. Song, Y., et al., *A novel conductance glucose biosensor in ultra-low ionic strength solution triggered by the oxidation of Ag nanoparticles*. Analytica Chimica Acta, 2015. **891**: p. 144-150.

17. Mattiasson, B. and M. Hedström, *Capacitive biosensors for ultra-sensitive assays*. TrAC Trends in Analytical Chemistry, 2016. **79**: p. 233-238.

18. Pei, R., et al., *Amplification of antigen–antibody interactions based on biotin labeled protein–streptavidin network complex using impedance spectroscopy*. Biosensors and Bioelectronics, 2001. **16**(6): p. 355-361.

19. Aydemir, N., J. Malmstrom, and J. Travas-Sejdic, *Conducting polymer based electrochemical biosensors*. Physical Chemistry Chemical Physics, 2016. **18**(12): p. 8264-8277.

20. Patolsky, F., G. Zheng, and C.M. Lieber, *Nanowire-Based Biosensors*. Analytical Chemistry, 2006. **78**(13): p. 4260-4269.

21. Chaubey, A. and B.D. Malhotra, *Mediated biosensors*. Biosensors and Bioelectronics, 2002. **17**(6–7): p. 441-456.

22. Park, S.-J., T.A. Taton, and C.A. Mirkin, *Array-Based Electrical Detection of DNA with Nanoparticle Probes*. Science, 2002. **295**(5559): p. 1503-1506.

23. Clark, L.C.J., *MONITOR AND CONTROL OF BLOOD AND TISSUE OXYGEN TENSIONS*. ASAIO Journal, 1956. **2**(1): p. 41-48.

24. Clark, L.C. and C. Lyons, *ELECTRODE SYSTEMS FOR CONTINUOUS MONITORING IN CARDIOVASCULAR SURGERY*. Annals of the New York Academy of Sciences, 1962. **102**(1): p. 29-45.

25. Wang, J., *Glucose Biosensors: 40 Years of Advances and Challenges*. Electroanalysis, 2001. **13**(12): p. 983-988.

26. Yoo, E.-H. and S.-Y. Lee, *Glucose Biosensors: An Overview of Use in Clinical Practice*. Sensors (Basel, Switzerland), 2010. **10**(5): p. 4558-4576.

27. Sethi, R.S., *Transducer aspects of biosensors*. Biosensors and Bioelectronics, 1994. **9**(3): p. 243-264.

28. Backmann, N., et al., *A label-free immunosensor array using single-chain antibody fragments*. Proceedings of the National Academy of Sciences of the United States of America, 2005. **102**(41): p. 14587-14592.

29. Wu, G., et al., *Bioassay of prostate-specific antigen (PSA) using microcantilevers*. Nat Biotech, 2001. **19**(9): p. 856-860.

30. Ndieyira, J.W., et al., *Nanomechanical detection of antibiotic-mucopeptide binding in a model for superbug drug resistance*. Nat Nano, 2008. **3**(11): p. 691-696.

31. Kim, N., D.-K. Kim, and Y.-J. Cho, *Development of indirect-competitive quartz crystal microbalance immunosensor for C-reactive protein*. Sensors and Actuators B: Chemical, 2009. **143**(1): p. 444-448.

32. Kurosawa, S., et al., *Evaluation of a high-affinity QCM immunosensor using antibody fragmentation and 2-methacryloyloxyethyl phosphorylcholine (MPC) polymer*. Biosensors and Bioelectronics, 2004. **20**(6): p. 1134-1139.

33. Park, K., et al., *Measurement of adherent cell mass and growth*. Proceedings of the National Academy of Sciences of the United States of America, 2010. **107**(48): p. 20691-20696.

34. Gfeller, K.Y., N. Nugaeva, and M. Hegner, *Micromechanical oscillators as rapid biosensor for the detection of active growth of Escherichia coli*. Biosensors and Bioelectronics, 2005. **21**(3): p. 528-533.

35. Marx, K.A., *Quartz Crystal Microbalance: A Useful Tool for Studying Thin Polymer Films and Complex Biomolecular Systems at the Solution−Surface Interface*. Biomacromolecules, 2003. **4**(5): p. 1099-1120.

36. Zhu, Y., et al., *Synthesis of mesoporous SnO2–SiO2 composites and their application as quartz crystal microbalance humidity sensor*. Sensors and Actuators B: Chemical, 2014. **193**: p. 320-325.

37. Zakipour, S. and C. Leygraf, *Quartz crystal microbalance applied to studies of atmospheric corrosion of metals*. British Corrosion Journal, 1992. **27**(4): p. 295-298.

38. Uludag, Y. and I.E. Tothill, *Cancer Biomarker Detection in Serum Samples Using Surface Plasmon Resonance and Quartz Crystal Microbalance Sensors with Nanoparticle Signal Amplification*. Analytical Chemistry, 2012. **84**(14): p. 5898-5904.

39. Cooper, M.A., *Optical biosensors in drug discovery*. Nat Rev Drug Discov, 2002. **1**(7): p. 515-528.

40. Yoo, S.M. and S.Y. Lee, *Optical Biosensors for the Detection of Pathogenic Microorganisms*. Trends in Biotechnology. **34**(1): p. 7-25.

41. Narsaiah, K., et al., *Optical biosensors for food quality and safety assurance—a review*. Journal of Food Science and Technology, 2012. **49**(4): p. 383-406.

42. Chang, Y.-F., et al., *Use of liposomal amplifiers in total internal reflection fluorescence fiber-optic biosensors for protein detection*. Biosensors and Bioelectronics, 2016. **77**: p. 1201-1207.

43. Abdelhaseib, M.U., et al., *Fiber optic and light scattering sensors: Complimentary approaches to rapid detection of Salmonella enterica in food samples*. Food Control, 2016. **61**: p. 135-145.

44. Huh, Y.S., A.J. Chung, and D. Erickson, *Surface enhanced Raman spectroscopy and its application to molecular and cellular analysis*. Microfluidics and Nanofluidics, 2009. **6**(3): p. 285-297.

45. Meadows, D. and J.S. Schultz, *Fiber-optic biosensors based on fluorescence energy transfer*. Talanta, 1988. **35**(2): p. 145-150.

46. Russell, R.J., et al., *A Fluorescence-Based Glucose Biosensor Using Concanavalin A and Dextran Encapsulated in a Poly(ethylene glycol) Hydrogel*. Analytical Chemistry, 1999. **71**(15): p. 3126-3132.

47. Chinnayelka, S. and M.J. McShane, *Microcapsule Biosensors Using Competitive Binding Resonance Energy Transfer Assays Based on Apoenzymes*. Analytical Chemistry, 2005. **77**(17): p. 5501-5511.

48. Fabbrizzi, L., et al., *Pyrophosphate Detection in Water by Fluorescence Competition Assays: Inducing Selectivity through the Choice of the Indicator*. Angewandte Chemie International Edition, 2002. **41**(20): p. 3811-3814.

49. Huang, L., et al., *Prostate-specific antigen immunosensing based on mixed self-assembled monolayers, camel antibodies and colloidal gold enhanced sandwich assays*. Biosensors and Bioelectronics, 2005. **21**(3): p. 483-490.

50. Uotila, M., E. Ruoslahti, and E. Engvall, *Two-site sandwich enzyme immunoassay with monoclonal antibodies to human alpha-fetoprotein*. Journal of Immunological Methods, 1981. **42**(1): p. 11-15.

51. Oshannessy, D.J., et al., *Detection and Quantitation of Hexa-Histidine-Tagged Recombinant Proteins on Western Blots and by a Surface Plasmon Resonance Biosensor Technique*. Analytical Biochemistry, 1995. **229**(1): p. 119-124.

52. Boucher, C., et al., *Protein detection by Western blot via coiled–coil interactions*. Analytical Biochemistry, 2010. **399**(1): p. 138-140.

53. Vashist, S.K., et al., *One-step antibody immobilization-based rapid and highly-sensitive sandwich ELISA procedure for potential in vitro diagnostics*. Scientific Reports, 2014. **4**: p. 4407.

54. Zhang, H. and S. Wang, *Review on enzyme-linked immunosorbent assays for sulfonamide residues in edible animal products*. Journal of Immunological Methods, 2009. **350**(1–2): p. 1-13.

55. Gehring, A.G., et al., *Enzyme-linked immunomagnetic electrochemical detection of Salmonella typhimurium*. Journal of Immunological Methods, 1996. **195**(1): p. 15-25.

56. D Axelrod, a. T P Burghardt, and N.L. Thompson, *Total Internal Reflection Fluorescence*. Annual Review of Biophysics and Bioengineering, 1984. **13**(1): p. 247-268.

57. Li and L.J. Rothberg, *Label-Free Colorimetric Detection of Specific Sequences in Genomic DNA Amplified by the Polymerase Chain Reaction*. Journal of the American Chemical Society, 2004. **126**(35): p. 10958-10961.

58. Liu, X. and W. Tan, *A Fiber-Optic Evanescent Wave DNA Biosensor Based on Novel Molecular Beacons*. Analytical Chemistry, 1999. **71**(22): p. 5054-5059.

59. Sun, Y., et al., *Bioinspired optofluidic FRET lasers via DNA scaffolds*. Proceedings of the National Academy of Sciences, 2010. **107**(37): p. 16039-16042.

60. Cox, W.G. and V.L. Singer, *Fluorescent DNA hybridization probe preparation using amine modification and reactive dye coupling*. Biotechniques, 2004. **36**(1): p. 114-123.

61. Dante, S., et al., *All-optical phase modulation for integrated interferometric biosensors*. Optics Express, 2012. **20**(7): p. 7195-7205.

62. Janz, S., et al., *Photonic wire biosensor microarray chip and instrumentation with application to serotyping of Escherichia coliisolates*. Optics Express, 2013. **21**(4): p. 4623-4637.

63. Jágerská, J., et al., *Refractive index sensing with an air-slot photonic crystal nanocavity*. Optics Letters, 2010. **35**(15): p. 2523-2525.

64. Liedberg, B., C. Nylander, and I. Lunström, *Surface plasmon resonance for gas detection and biosensing*. Sensors and Actuators, 1983. **4**: p. 299-304.

65. Homola, J., S.S. Yee, and G. Gauglitz, *Surface plasmon resonance sensors: review*. Sensors and Actuators B: Chemical, 1999. **54**(1–2): p. 3-15.

66. Hoa, X.D., A.G. Kirk, and M. Tabrizian, *Towards integrated and sensitive surface plasmon resonance biosensors: A review of recent progress*. Biosensors and Bioelectronics, 2007. **23**(2): p. 151-160.

67. Matsubara, K., S. Kawata, and S. Minami, *Optical chemical sensor based on surface plasmon measurement*. Applied Optics, 1988. **27**(6): p. 1160-1163.

68. Liedberg, B., I. Lundström, and E. Stenberg, *Principles of biosensing with an extended coupling matrix and surface plasmon resonance*. Sensors and Actuators B: Chemical, 1993. **11**(1): p. 63-72.

69. Gupta, B.D. and R.K. Verma, *Surface Plasmon Resonance-Based Fiber Optic Sensors: Principle, Probe Designs, and Some Applications*. Journal of Sensors, 2009. **2009**: p. 12.

70. Yu, F., et al., *Surface Plasmon Enhanced Diffraction for Label-Free Biosensing*. Analytical Chemistry, 2004. **76**(13): p. 3530-3535.

71. Slavík, R. and J. Homola, *Ultrahigh resolution long range surface plasmon-based sensor*. Sensors and Actuators B: Chemical, 2007. **123**(1): p. 10-12.

72. Taylor, A.D., et al., *Comparison of E. coli O157:H7 preparation methods used for detection with surface plasmon resonance sensor*. Sensors and Actuators B: Chemical, 2005. **107**(1): p. 202-208.

73. Homola, J., *Present and future of surface plasmon resonance biosensors*. Analytical and Bioanalytical Chemistry, 2003. **377**(3): p. 528-539.

74. Hofmann, M., et al., *Asymmetric Mach–Zehnder interferometers without an interaction window in polymer foils for refractive index sensing*. Applied Optics, 2016. **55**(5): p. 1124-1131.

75. Misiakos, K., et al., *All-silicon monolithic Mach-Zehnder interferometer as a refractive index and bio-chemical sensor*. Optics Express, 2014. **22**(22): p. 26803-26813.

76. Melnik, E., et al., *Human IgG detection in serum on polymer based Mach-Zehnder interferometric biosensors*. Journal of Biophotonics, 2016. **9**(3): p. 218-223.

77. Khor, K.N. and M.M. Shahimin. *Design of integrated optical Mach-Zehnder interferometer biosensor for ideal surveillance rapid diagnostic test*. in *Biomedical Engineering and Sciences (IECBES), 2014 IEEE Conference on*. 2014.

78. Mukundan, H., et al., *Waveguide-Based Biosensors for Pathogen Detection*. Sensors, 2009. **9**(7): p. 5783.

79. Fan, Y., et al., *Optical waveguide sensor based on silica nanotube arrays for label-free biosensing*. Biosensors and Bioelectronics, 2015. **67**: p. 230-236.

80. Jin, Z., et al., *A stable and high resolution optical waveguide biosensor based on dense TiO2/Ag multilayer film*. Applied Surface Science, 2016. **377**: p. 207-212.

81. Lee, M. and P.M. Fauchet, *Two-dimensional silicon photonic crystal based biosensing platform for protein detection*. Optics Express, 2007. **15**(8): p. 4530-4535.

82. Frascella, F., et al., *A Fluorescent One-Dimensional Photonic Crystal for Label-Free Biosensing Based on Bloch Surface Waves*. Sensors, 2013. **13**(2): p. 2011.

83. Shafiee, H., et al., *Nanostructured Optical Photonic Crystal Biosensor for HIV Viral Load Measurement*. Scientific Reports, 2014. **4**: p. 4116.

84. Chakravarty, S., et al., *Multiplexed specific label-free detection of NCI-H358 lung cancer cell line lysates with silicon based photonic crystal microcavity biosensors*. Biosensors and Bioelectronics, 2013. **43**: p. 50-55.

85. Toccafondo, V., et al., *Single-strand DNA detection using a planar photonic-crystal-waveguide-based sensor*. Optics Letters, 2010. **35**(21): p. 3673-3675.

86. Zlatanovic, S., et al., *Photonic crystal microcavity sensor for ultracompact monitoring of reaction kinetics and protein concentration*. Sensors and Actuators B: Chemical, 2009. **141**(1): p. 13-19.

87. Zeder-Lutz, G., et al., *Thermodynamic Analysis of Antigen–Antibody Binding Using Biosensor Measurements at Different Temperatures*. Analytical Biochemistry, 1997. **246**(1): p. 123-132.

88. Wegner, G.J., et al., *Real-Time Surface Plasmon Resonance Imaging Measurements for the Multiplexed Determination of Protein Adsorption/Desorption Kinetics and Surface Enzymatic Reactions on Peptide Microarrays*. Analytical Chemistry, 2004. **76**(19): p. 5677-5684.

89. Tamada, K., et al., *SPR-based DNA Detection with Metal Nanoparticles*. Plasmonics, 2007. **2**(4): p. 185-191.

90. Chryssis, A.N., et al., *Detecting hybridization of DNA by highly sensitive evanescent field etched core fiber Bragg grating sensors*. IEEE Journal of Selected Topics in Quantum Electronics, 2005. **11**(4): p. 864-872.

91. Liang, W., et al., *Highly sensitive fiber Bragg grating refractive index sensors*. Applied Physics Letters, 2005. **86**(15): p. 151122.

92. Zhi, Y., et al., *Refractometric sensing with silicon quantum dots coupled to a microsphere*. Plasmonics, 2013. **8**(1): p. 71-78.

93. Sedlmeir, F., et al., *High-Q MgF 2 whispering gallery mode resonators for refractometric sensing in aqueous environment*. Optics Express, 2014. **22**(25): p. 30934-30942.

94. Kim, D.C. and R.C. Dunn, *Integrating Whispering Gallery Mode Refractive Index Sensing with Capillary Electrophoresis Separations Using Phase Sensitive Detection*. Analytical Chemistry, 2016. **88**(2): p. 1426-1433.

95. Lane, S., et al., *Protein biosensing with fluorescent microcapillaries*. Optics Express, 2015. **23**(3): p. 2577-2590.

96. Pasquardini, L., et al., *Whispering gallery mode aptasensors for detection of blood proteins*. Journal of biophotonics, 2013. **6**(2): p. 178-187.

97. Vollmer, F., et al., *Multiplexed DNA quantification by spectroscopic shift of two microsphere cavities*. Biophysical journal, 2003. **85**(3): p. 1974-1979.

98. Wu, F.C., et al., *Ratiometric Detection of Oligonucleotide Stoichiometry on Multifunctional Gold Nanoparticles by Whispering Gallery Mode Biosensing*. The Analyst, 2015. **140**(9): p. 2969-2972.

99. Dantham, V.R., et al., *Taking whispering gallery-mode single virus detection and sizing to the limit*. Applied Physics Letters, 2012. **101**(4): p. 043704.

100. Schmidt, H. and A.R. Hawkins, *Single-virus analysis through chip-based optical detection*. Bioanalysis, 2016. **8**(9): p. 867-870.

101. Baaske, M.D., M.R. Foreman, and F. Vollmer, *Single-molecule nucleic acid interactions monitored on a label-free microcavity biosensor platform*. Nature Nanotechnology, 2014. **9**(11): p. 933-939.

102. Armani, A.M., et al., *Label-Free, Single-Molecule Detection with Optical Microcavities*. Science, 2007. **317**(5839): p. 783-787.

103. He, L., et al., *Detecting single viruses and nanoparticles using whispering gallery microlasers*. Nat Nanotechnol, 2011. **6**(7): p. 428-32.

104. Himmelhaus, M. and A. François, *In-vitro sensing of biomechanical forces in live cells by a whispering gallery mode biosensor*. Biosensors and Bioelectronics, 2009. **25**(2): p. 418-427.

105. Schubert, M., et al., *Lasing within live cells containing intracellular optical microresonators for barcode-type cell tagging and tracking*. Nano Letters, 2015. **15**(8): p. 5647-5652.

106. Humar, M. and S.H. Yun, *Intracellular microlasers*. Nature Photonics, 2015. **9**: p. 572-576.

107. Klantsataya, E., et al., *Surface Plasmon Scattering in Exposed Core Optical Fiber for Enhanced Resolution Refractive Index Sensing*. Sensors, 2015. **15**(10): p. 25090.

108. Jorgenson, R.C. and S.S. Yee, *A fiber-optic chemical sensor based on surface plasmon resonance*. Sensors and Actuators B: Chemical, 1993. **12**(3): p. 213-220.

109. Piliarik, M., et al., *Surface plasmon resonance sensor based on a single-mode polarization-maintaining optical fiber*. Sensors and Actuators B: Chemical, 2003. **90**(1–3): p. 236-242.

110. Caucheteur, C., T. Guo, and J. Albert, *Review of plasmonic fiber optic biochemical sensors: improving the limit of detection*. Analytical and Bioanalytical Chemistry, 2015. **407**(14): p. 3883-3897.

111. Zhang, X., et al., *Coupled optofluidic ring laser for ultrahigh-sensitive sensing*. Optics Express, 2011. **19**(22): p. 22242-22247.

112. Beck, T., et al., *High-Q polymer resonators with spatially controlled photo-functionalization for biosensing applications*. Applied Physics Letters, 2013. **102**(12): p. 121108.

113. Li, H. and X. Fan, *Characterization of sensing capability of optofluidic ring resonator biosensors*. Applied Physics Letters, 2010. **97**(1): p. 011105.

114. Wu, F., et al., *Integrating a DNA Strand Displacement Reaction with a Whispering Gallery Mode Sensor for Label-Free Mercury (II) Ion Detection*. Sensors, 2016. **16**(8): p. 1197.

115. Özdemir, Ş.K., et al., *Highly sensitive detection of nanoparticles with a self-referenced and self-heterodyned whispering-gallery Raman microlaser*. Proceedings of the National Academy of Sciences, 2014. **111**(37): p. 3836-3844.

116. Zhu, J., et al., *On-chip single nanoparticle detection and sizing by mode splitting in an ultrahigh-Q microresonator*. Nature Photonics, 2010. **4**(1): p. 46-49.

117. Mie, G., *Beiträge zur Optik trüber Medien, speziell kolloidaler Metallösungen*. Annalen der Physik, 1908. **330**(3): p. 377-445.

118. Debye, P., *Der Lichtdruck auf Kugeln von beliebigem Material*. Annalen der Physik, 1909. **335**(11): p. 57-136.

119. Rayleigh, L., *CXII. The problem of the whispering gallery*. Philosophical Magazine Series 6, 1910. **20**(120): p. 1001-1004.

120. Spillane, S., T. Kippenberg, and K. Vahala, *Ultralow-threshold Raman laser using a spherical dielectric microcavity*. Nature, 2002. **415**(6872): p. 621-623.

121. Jones, B.D., et al., *Splitting and lasing of whispering gallery modes in quantum dot micropillars*. Optics Express, 2010. **18**(21): p. 22578-22592.

122. McCall, S.L., et al., *Whispering - gallery mode microdisk lasers*. Applied Physics Letters, 1992. **60**(3): p. 289-291.

123. Pan, Y.-L. and R.K. Chang, *Highly efficient prism coupling to whispering gallery modes of a square μ cavity*. Applied Physics Letters, 2003. **82**(4): p. 487-489.

124. Moon, H.-J., K. An, and J.-H. Lee, *Single spatial mode selection in a layered square microcavity laser*. Applied Physics Letters, 2003. **82**(18): p. 2963-2965.

125. Tang, M.-Y., et al., *Mode selection in square resonator microlasers for widely tunable single mode lasing*. Optics Express, 2015. **23**(21): p. 27739-27750.

126. Bohren, C.F. and D.R. Huffman, *Absorption and Scattering by a Sphere*, in *Absorption and Scattering of Light by Small Particles*. 2007, Wiley-VCH Verlag GmbH. p. 82-129.

127. Johnson, B.R., *Theory of morphology-dependent resonances- shape resonances and width formulas.pdf*. J. Opt. Soc. Am. B, 1993. **10**(2).

128. Teraoka, I. and S. Arnold, *Theory of resonance shifts in TE and TM whispering gallery modes by nonradial perturbations for sensing applications*. Journal of the Optical Society of America B, 2006. **23**(7): p. 1381-1389.

129. Riesen, N., et al., *Q-factor limits for far-field detection of whispering gallery modes in active microspheres*. Optics Express, 2015. **23**(22): p. 28896-28904.

130. Yu, H.-H., C.-H. Yi, and C.-M. Kim, *Mechanism of Q-spoiling in deformed optical microcavities*. Optics Express, 2015. **23**(9): p. 11054-11062.

131. Ilchenko, V.S., et al., *Whispering gallery mode diamond resonator*. Optics Letters, 2013. **38**(21): p. 4320-4323.

132. Gorodetsky, M.L., A.A. Savchenkov, and V.S. Ilchenko, *Ultimate Q of optical microsphere resonators*. Optics Letters, 1996. **21**(7): p. 453-455.

133. Boriskina, S.V. and A.I. Nosich, *Radiation and absorption losses of the whispering-gallery-mode dielectric resonators excited by a dielectric waveguide*. IEEE Transactions on Microwave Theory and Techniques, 1999. **47**(2): p. 224-231.

134. Uetake, S., R.S.D. Sihombing, and K. Hakuta, *Stimulated Raman scattering of a high-Q liquid-hydrogen droplet in the ultraviolet region*. Optics Letters, 2002. **27**(6): p. 421-423.

135. Tzeng, H.M., et al., *Laser-induced shape distortions of flowing droplets deduced from morphology-dependent resonances in fluorescence spectra*. Optics Letters, 1985. **10**(5): p. 209-211.

136. Carrier, J.-R., M. Boissinot, and C. Nì. Allen, *Dielectric resonating microspheres for biosensing: An optical approach to a biological problem*. American Journal of Physics, 2014. **82**(5): p. 510-520.

137. François, A., et al., *Polymer based whispering gallery mode laser for biosensing applications*. Applied Physics Letters, 2015. **106**(3): p. 031104.

138. Kushida, S., et al., *Conjugated Polymer Blend Microspheres for Efficient, Long-Range Light Energy Transfer*. ACS Nano, 2016. **10**(5): p. 5543-5549.

139. Petermann, A.B., et al., *All-polymer whispering gallery mode sensor system*. Optics Express, 2016. **24**(6): p. 6052-6062.

140. Reynolds, T., et al., *Dynamic Self-Referencing Approach to Whispering Gallery Mode Biosensing and Its Application to Measurement within Undiluted Serum*. Analytical Chemistry, 2016. **88**(7): p. 4036-4040.

141. Martín, L., et al., *Laser emission in Nd3+ doped barium–titanium–silicate microspheres under continuous and chopped wave pumping in a non-coupled pumping scheme*. Laser Physics, 2013. **23**(7): p. 075801.

142. Svitelskiy, O., et al., *Fiber coupling to BaTiO3 glass microspheres in an aqueous environment*. Optics Letters, 2011. **36**(15): p. 2862-2864.

143. Creedon, D.L., et al., *High Q-factor sapphire whispering gallery mode microwave resonator at single photon energies and millikelvin temperatures*. Applied Physics Letters, 2011. **98**(22): p. 222903.

144. Goryachev, M., et al., *High-Cooperativity Cavity QED with Magnons at Microwave Frequencies*. Physical Review Applied, 2014. **2**(5): p. 054002.

145. Yu, L. and V. Fernicola, *Spherical-sapphire-based whispering gallery mode resonator thermometer*. Review of Scientific Instruments, 2012. **83**(9): p. 094903.

146. Ashkin, A. and J.M. Dziedzic, *Observation of Resonances in the Radiation Pressure on Dielectric Spheres*. Physical Review Letters, 1977. **38**(23): p. 1351-1354.

147. He, L., Ş.K. Özdemir, and L. Yang, *Whispering gallery microcavity lasers*. Laser & Photonics Reviews, 2013. **7**(1): p. 60-82.

148. Chen, L.-J., et al., *Microfluidic fabrication of cholesteric liquid crystal core–shell structures toward magnetically transportable microlasers*. Lab on a Chip, 2016. **16**(7): p. 1206-1213.

149. Fan, X. and S.-H. Yun, *The potential of optofluidic biolasers*. Nat Meth, 2014. **11**(2): p. 141-147.

150. Jonas, A., et al., *In vitro and in vivo biolasing of fluorescent proteins suspended in liquid microdroplet cavities*. Lab on a Chip, 2014. **14**(16): p. 3093-3100.

151. Vollmer, F., et al., *Protein detection by optical shift of a resonant microcavity*. Applied Physics Letters, 2002. **80**(21): p. 4057-4059.

152. Dong, C.-H., et al., *Fabrication of high-Q polydimethylsiloxane optical microspheres for thermal sensing*. Applied Physics Letters, 2009. **94**(23): p. 231119.

153. Collot, L., et al., *Very High- Q Whispering-Gallery Mode Resonances Observed on Fused Silica Microspheres*. EPL (Europhysics Letters), 1993. **23**(5): p. 327.

154. Van Hoi, P., C.T.T. Ha, and H.Q. Hung, *Long-band emission of microsphere lasers based on erbium-doped sol-gel silica-alumina glasses*. Applied Physics Letters, 2005. **87**(16): p. 161110.

155. Ferreira, M.S., J.L. Santos, and O. Frazão, *Silica microspheres array strain sensor*. Optics Letters, 2014. **39**(20): p. 5937-5940.

156. Wilson, K.A., et al., *Whispering gallery mode biosensor quantification of fibronectin adsorption kinetics onto alkylsilane monolayers and interpretation of resultant cellular response*. Biomaterials, 2012. **33**(1): p. 225-236.

157. Braginsky, V.B., M.L. Gorodetsky, and V.S. Ilchenko, *Quality-factor and nonlinear properties of optical whispering-gallery modes*. Physics Letters A, 1989. **137**(7): p. 393-397.

158. Hanumegowda, N.M., et al., *Refractometric sensors based on microsphere resonators*. Applied Physics Letters, 2005. **87**(20): p. 201107.

159. Laine, J.P., B.E. Little, and H.A. Haus, *Etch-eroded fiber coupler for whispering-gallery-mode excitation in high-Q silica microspheres*. IEEE Photonics Technology Letters, 1999. **11**(11): p. 1429-1430.

160. Panitchob, Y., et al., *Whispering gallery mode spectra of channel waveguide coupled microspheres*. Optics Express, 2008. **16**(15): p. 11066-11076.

161. Gorodetsky, M.L. and V.S. Ilchenko, *High-Q optical whispering-gallery microresonators: precession approach for spherical mode analysis and emission patterns with prism couplers*. Optics Communications, 1994. **113**(1): p. 133-143.

162. Gorodetskii, M., et al., *High-Q Factor Optical Whispering-Gallery Mode Microresonators and Their Use in Precision Measurements*. Measurement Techniques, 2015. **12**(57): p. 1386-1395.

163. Yang, S., Y. Wang, and H. Sun, *Advances and Prospects for Whispering Gallery Mode Microcavities*. Advanced Optical Materials, 2015. **3**(9): p. 1136-1162.

164. Song, W., et al., *Entanglement dynamics for three nitrogen-vacancy centers coupled to a whispering-gallery-mode microcavity*. Optics Express, 2015. **23**(11): p. 13734-13751.

165. D'Aguanno, G. and C.R. Menyuk, *Nonlinear mode coupling in whispering-gallery-mode resonators*. Physical Review A, 2016. **93**(4): p. 043820.

166. Manolatou, C., et al., *Coupling of modes analysis of resonant channel add-drop filters*. IEEE Journal of Quantum Electronics, 1999. **35**(9): p. 1322-1331.

167. Tapalian, C., J.P. Laine, and P.A. Lane, *Thermo-optical switches using coated microsphere resonators*. MRS Proceedings, 2011. **708**.

168. Gohring, J.T., P.S. Dale, and X. Fan, *Detection of HER2 breast cancer biomarker using the opto-fluidic ring resonator biosensor*. Sensors and Actuators B: Chemical, 2010. **146**(1): p. 226-230.

169. Suter, J.D., et al., *Label-free quantitative DNA detection using the liquid core optical ring resonator*. Biosensors and Bioelectronics, 2008. **23**(7): p. 1003-1009.

170. François, A., Y. Zhi, and A. Meldrum, *Whispering Gallery Mode Devices for Sensing and Biosensing*. 1 ed. Photonic Materials for Sensing, Biosensing and Display Devices, ed. J.M. Serpe, Y. Kang, and M.Q. Zhang. Vol. 229. 2016, Cham: Springer International Publishing. 237-288.

171. Zhixiong, G., Q. Haiyong, and P. Stanley, *Near-field gap effects on small microcavity whispering-gallery mode resonators*. Journal of Physics D: Applied Physics, 2006. **39**(24): p. 5133.

172. Ballard, Z., M.D. Baaske, and F. Vollmer, *Stand-off biodetection with free-space coupled asymmetric microsphere cavities*. Sensors, 2015. **15**(4): p. 8968-8980.

173. Shao, L., et al., *Ultrahigh-Q, largely deformed microcavities coupled by a free-space laser beam*. Applied Physics Letters, 2013. **103**(12): p. 121102.

174. Zhu, J., et al., *Interfacing whispering-gallery microresonators and free space light with cavity enhanced Rayleigh scattering*. Scientific Reports, 2014. **4**: p. 6396.

175. Benisty, H., et al. *Confined photon systems*. in *Lecture Notes in Physics, Berlin Springer Verlag*. 1999.

176. Nuhiji, E. and P. Mulvaney, *Detection of unlabeled oligonucleotide targets using whispering gallery modes in single, fluorescent microspheres*. Small, 2007. **3**(8): p. 1408-1414.

177. Himmelhaus, M., S. Krishnamoorthy, and A. Francois, *Optical Sensors Based on Whispering Gallery Modes in Fluorescent Microbeads: Response to Specific Interactions*. Sensors, 2010. **10**(6): p. 6257.

178. Taly, V., et al., *Detecting biomarkers with microdroplet technology*. Trends in Molecular Medicine, 2012. **18**(7): p. 405-416.

179. Kryzhanovskaya, N.V., M.V. Maximov, and A.E. Zhukov, *Whispering-gallery mode microcavity quantum-dot lasers*. Quantum Electronics, 2014. **44**(3): p. 189.

180. Zhi, Y., J. Valenta, and A. Meldrum, *Structure of whispering gallery mode spectrum of microspheres coated with fluorescent silicon quantum dots*. JOSA B, 2013. **30**(11): p. 3079-3085.

181. Ghulinyan, M., et al., *Whispering-gallery modes and light emission from a Si-nanocrystal-based single microdisk resonator*. Optics Express, 2008. **16**(17): p. 13218-13224.

182. Huckabay, H.A. and R.C. Dunn, *Whispering gallery mode imaging for the multiplexed detection of biomarkers*. Sensors and Actuators B: Chemical, 2011. **160**(1): p. 1262-1267.

183. Wienhold, T., et al., *All-polymer photonic sensing platform based on whispering-gallery mode microgoblet lasers*. Lab on a Chip, 2015. **15**(18): p. 3800-3806.

184. Afshar V, S., et al., *Self-formed cavity quantum electrodynamics in coupled dipole cylindrical-waveguide systems*. Optics Express, 2014. **22**(9): p. 11301-11311.

185. Hernández, J. and I.M. Thompson, *Prostate-specific antigen: A review of the validation of the most commonly used cancer biomarker*. Cancer, 2004. **101**(5): p. 894-904.

186. Kozak, K.R., et al., *Characterization of serum biomarkers for detection of early stage ovarian cancer*. Proteomics, 2005. **5**(17): p. 4589-4596.

187. Francois, A. and M. Himmelhaus, *Whispering gallery mode biosensor operated in the stimulated emission regime*. Applied Physics Letters, 2009. **94**(3): p. 031101.

188. François, A., et al., *Enhancing the radiation efficiency of dye doped whispering gallery mode microresonators*. Optics Express, 2013. **21**(19): p. 22566-22577.

189. François, A., T. Reynolds, and T.M. Monro, *A fiber-tip label-free biological sensing platform: a practical approach toward in-vivo sensing*. Sensors, 2015. **15**(1): p. 1168-1181.

190. François, A., et al., *Combining whispering gallery mode lasers and microstructured optical fibers: limitations, applications and perspectives for in-vivo biosensing*. MRS Advances, 2016: p. 1-12.

191. François, A., Y. Zhi, and A. Meldrum, *Whispering Gallery Mode Devices for Sensing and Biosensing*, in *Photonic Materials for Sensing, Biosensing and Display Devices*. 2016, Springer. p. 237-288.

192. Armani, D.K., et al., *Ultra-high-Q toroid microcavity on a chip*. Nature, 2003. **421**(6926): p. 925-928.

193. Martin, L., et al., *High pressure tuning of whispering gallery mode resonances in a neodymium-doped glass microsphere*. JOSA B, 2013. **30**(12): p. 3254-3259.

194. Zamanian, A.H. and T. Ioppolo, *Effect of wall pressure and shear stress on embedded cylindrical microlasers*. Applied Optics, 2015. **54**(23): p. 7124-7130.

195. Manzo, M. and T. Ioppolo, *Untethered photonic sensor for wall pressure measurement*. Optics Letters, 2015. **40**(10): p. 2257-2260.

196. Pérez-Rodríguez, C., et al., *Temperature response of the whispering gallery mode resonances from the green upconversion emission of an Er 3+ –Yb 3+ co-doped microsphere*. Laser Physics Letters, 2015. **12**(4): p. 046003.

197. Labrador-Paez, L., et al., *Optical humidity sensor based on a liquid whispering-gallery mode resonator*. arXiv preprint arXiv:1602.03322, 2016.

198. Kumar, T.A., et al., *Detection of phase transitions from the study of whispering gallery mode resonance in liquid crystal droplets*. Applied Physics Letters, 2015. **106**(5): p. 051101.

199. Vollmer, F. and L. Yang, *Review Label-free detection with high-Q microcavities: a review of biosensing mechanisms for integrated devices*. Nanophotonics, 2012. **1**(3-4): p. 267-291.

200. Estrada, I.A., et al. *Multiplex detection of pathogen biomarkers in human blood, serum, and saliva using silicon photonic microring resonators*. in *Advances in Global Health through Sensing Technologies 2015*. 2015. Baltimore, Maryland, USA: International Society for Optics and Photonics.

201. Knittel, J., et al., *Interferometric detection of mode splitting for whispering gallery mode biosensors*. Applied Physics Letters, 2010. **97**(12): p. 123704.

202. White, I.M. and X. Fan, *On the performance quantification of resonant refractive index sensors*. Optics Express, 2008. **16**(2): p. 1020-1028.

203. Zeltner, R., et al., *Crystalline MgF2 whispering gallery mode resonators for enhanced bulk index sensitivity*. The European Physical Journal Special Topics, 2014. **223**(10): p. 1989-1994.

204. Reynolds, T., et al., *Optimization of whispering gallery resonator design for biosensing applications*. Optics Express, 2015. **23**(13): p. 17067-17076.

205. Berneschi, S., et al., *High Q silica microbubble resonators fabricated by arc discharge*. Optics Letters, 2011. **36**(17): p. 3521-3523.

206. Sumetsky, M., Y. Dulashko, and R.S. Windeler, *Optical microbubble resonator*. Optics Letters, 2010. **35**(7): p. 898-900.

207. Cohoon, G.A., K. Kieu, and R.A. Norwood, *Observation of two-photon fluorescence for Rhodamine 6G in microbubble resonators*. Optics Letters, 2014. **39**(11): p. 3098-3101.

208. Lee, W., et al., *A quasi-droplet optofluidic ring resonator laser using a micro-bubble*. Applied Physics Letters, 2011. **99**(9): p. 091102.

209. François, A., et al., *Lasing of whispering gallery modes in optofluidic microcapillaries*. Optics Express, 2016. **24**(12): p. 12466-12477.

210. Lane, S., et al., *Whispering gallery mode structure and refractometric sensitivity of fluorescent capillary-type sensors*. Sensors and Actuators B: Chemical, 2014. **190**: p. 752-759.

211. Teraoka, I. and S. Arnold, *Enhancing the sensitivity of a whispering-gallery mode microsphere sensor by a high-refractive-index surface layer*. Journal of the Optical Society of America B, 2006. **23**(7): p. 1434-1441.

212. Teraoka, I., S. Arnold, and F. Vollmer, *Perturbation approach to resonance shifts of whispering-gallery modes in a dielectric microsphere as a probe of a surrounding medium*. Journal of the Optical Society of America B, 2003. **20**(9): p. 1937-1946.

213. Baaske, M. and F. Vollmer, *Optical Resonator Biosensors: Molecular Diagnostic and Nanoparticle Detection on an Integrated Platform*. ChemPhysChem, 2012. **13**(2): p. 427-436.

214. Hu, Y.-W., et al., *Hybrid photonic–plasmonic mode for refractometer and nanoparticle trapping*. Optics Communications, 2013. **291**: p. 380-385.

215. Min, B., et al., *High-Q surface-plasmon-polariton whispering-gallery microcavity*. Nature, 2009. **457**(7228): p. 455-458.

216. Silverstone, J., et al., *Ultimate resolution for refractometric sensing with whispering gallery mode microcavities*. Optics Express, 2012. **20**(8): p. 8284-8295.

217. Cheema, M.I., et al., *Optimizing the Signal to Noise Ratio of Microcavity Sensors*. IEEE Photonics Technology Letters, 2014. **26**(20): p. 2023-2026.

218. Cheema, M.I., et al., *Simultaneous measurement of quality factor and wavelength shift by phase shift microcavity ring down spectroscopy*. Optics Express, 2012. **20**(8): p. 9090-9098.

219. Johnson, B.R., *Theory of morphology-dependent resonances: shape resonances and width formulas*. Journal of the Optical Society of America A, 1993. **10**(2): p. 343-352.

220. Lam, C.C., P.T. Leung, and K. Young, *Explicit asymptotic formulas for the positions, widths, and strengths of resonances in Mie scattering*. Journal of the Optical Society of America B, 1992. **9**(9): p. 1585-1592.

221. Datsyuk, V.V., *Some characteristics of resonant electromagnetic modes in a dielectric sphere*. Applied Physics B, 1992. **54**(2): p. 184-187.

222. Yang, Y., J. Ward, and S.N. Chormaic, *Quasi-droplet microbubbles for high resolution sensing applications*. Optics Express, 2014. **22**(6): p. 6881-6898.

223. Masamitsu, F., et al., *Characteristics of Whispering Gallery Modes in Single Dielectric Spheroid Excited by Gaussian Beam*. Japanese Journal of Applied Physics, 2005. **44**(7R): p. 4948.

224. Hall, J.M., et al., *Method for predicting whispering gallery mode spectra of spherical microresonators*. Optics Express, 2015. **23**(8): p. 9924-37.

225. Quan, H. and Z. Guo, *Simulation of whispering-gallery-mode resonance shifts for optical miniature biosensors*. Journal of Quantitative Spectroscopy and Radiative Transfer. **93**(1–3): p. 231-243.

226. Chew, H., M. Kerker, and P.J. McNulty, *Raman and fluorescent scattering by molecules embedded in concentric spheres**. Journal of the Optical Society of America, 1976. **66**(5): p. 440-444.

227. Chew, H., *Radiation and lifetimes of atoms inside dielectric particles*. Phys. Rev. A 1988. **38**: p. 3410.

228. Chew, H., *Transition rates of atoms near spherical surfaces*. J. Chem. Phys., 1987. **87**: p. 1355.

229. Gersten, J. and A. Nitzan, *Electromagnetic theory of enhanced Raman scattering by molecules adsorbed on rough surfaces*. The Journal of Chemical Physics, 1980. **73**(7): p. 3023-3037.

230. Schmidt, M.K., et al., *Dielectric antennas - a suitable platform for controlling magnetic dipolar emission*. Optics Express, 2012. **20**(13): p. 13636-13650.

231. Taflove, A. and S.C. Hagness, *Computational electrodynamics: the finite-difference time-domain method*. Norwood, 2nd Edition, MA: Artech House, l995, 1995.

232. Charlebois, M., et al., *Toward Automatic Label-Free Whispering Gallery Modes Biodetection with a Quantum Dot-Coated Microsphere Population*. Nanoscale Research Letters, 2010. **5**(3): p. 524.

233. van der Molen, K.L., et al., *Laser threshold of Mie resonances*. Optics Letters, 2006. **31**(10): p. 1432-1434.

234. Karow, M.M., et al., *On-chip light detection using monolithically integrated quantum dot micropillars*. Applied Physics Letters, 2016. **108**(8): p. 081110.

235. Li, Q., et al., *Ultralow-threshold laser in a Nd3+ doped silica microsphere*. Optics Communications, 2015. **356**: p. 368-372.

236. Li, M., et al., *Inversed Vernier effect based single-mode laser emission in coupled microdisks*. Scientific reports, 2015. **5**.

237. Yakunin, S., et al., *Low-threshold amplified spontaneous emission and lasing from colloidal nanocrystals of caesium lead halide perovskites*. Nat Commun, 2015. **6**: p. 8056.

238. Smotrova, E.I., et al., *Optical coupling of whispering-gallery modes of two identical microdisks and its effect on photonic molecule lasing*. IEEE Journal of Selected Topics in Quantum Electronics, 2006. **12**(1): p. 78-85.

239. Gmachl, C., et al., *High-Power Directional Emission from Microlasers with Chaotic Resonators*. Science, 1998. **280**(5369): p. 1556-1564.

240. Fujita, M. and T. Baba, *Proposal and finite-difference time-domain simulation of whispering gallery mode microgear cavity*. IEEE Journal of Quantum Electronics, 2001. **37**(10): p. 1253-1258.

241. Smotrova, E.I. and A.I. Nosich, *Mathematical study of the two-dimensional lasing problem for the whispering-gallery modes in a circular dielectric microcavity*. Optical and Quantum Electronics, 2004. **36**(1): p. 213-221.

242. Chang, S.-W., *Modeling of Micro and Nanolaser Cavities*. The Current Trends of Optics and Photonics, ed. C.-C. Lee. Vol. 129. 2015, Dordrecht: Springer Netherlands. 361-376.

243. Datsyuk, V.V., *Gain effects on microsphere resonant emission structures*. Journal of the Optical Society of America B, 2002. **19**(1): p. 142-147.

244. Sandoghdar, V., et al., *Very low threshold whispering-gallery-mode microsphere laser*. Physical Review A, 1996. **54**(3): p. 1777-1780.

245. Gargas, D.J., et al., *Whispering Gallery Mode Lasing from Zinc Oxide Hexagonal Nanodisks*. ACS Nano, 2010. **4**(6): p. 3270-3276.

246. Tang, T., et al., *Packaged optofluidic microbubble resonators for optical sensing*. Applied Optics, 2016. **55**(2): p. 395-399.

247. Ward, J.M., Y. Yang, and S.N. Chormaic, *Highly Sensitive Temperature Measurements With Liquid-Core Microbubble Resonators*. IEEE Photonics Technology Letters, 2013. **25**(23): p. 2350-2353.

248. Yang, Y., et al., *High-Q, ultrathin-walled microbubble resonator for aerostatic pressure sensing*. Optics Express, 2016. **24**(1): p. 294-299.

249. Zamora, V., et al., *Refractometric sensor based on whispering-gallery modes of thin capillarie*. Optics Express, 2007. **15**(19): p. 12011-12016.

250. Wang, J., et al., *Thermo-optic effects in on-chip lithium niobate microdisk resonators*. Optics Express, 2016. **24**(19): p. 21869-21879.

251. Kuo, P.S., J. Bravo-Abad, and G.S. Solomon, *Second-harmonic generation using -quasi-phasematching in a GaAs whispering-gallery-mode microcavity*. Nature Communications, 2014. **5**: p. 3109.

252. Knight, J., et al., *Phase-matched excitation of whispering-gallery-mode resonances by a fiber taper*. Optics Letters, 1997. **22**(15): p. 1129-1131.

253. Ilchenko, V.S., X.S. Yao, and L. Maleki, *Pigtailing the high-Q microsphere cavity:? a simple fiber coupler for optical whispering-gallery modes*. Optics Letters, 1999. **24**(11): p. 723-725.

254. Gorodetsky, M.L. and V.S. Ilchenko, *Optical microsphere resonators: optimal coupling to high-Q whispering-gallery modes*. Journal of the Optical Society of America B, 1999. **16**(1): p. 147-154.

255. Guo, Z., H. Quan, and S. Pau, *Numerical characterization of whispering-gallery mode optical microcavities*. Applied Optics, 2006. **45**(4): p. 611-618.

256. Dubreuil, N., et al., *Eroded monomode optical fiber for whispering-gallery mode excitation in fused-silica microspheres*. Optics Letters, 1995. **20**(8): p. 813-815.

257. Cai, M., O. Painter, and K.J. Vahala, *Observation of Critical Coupling in a Fiber Taper to a Silica-Microsphere Whispering-Gallery Mode System*. Physical Review Letters, 2000. **85**(1): p. 74-77.

258. Spillane, S.M., et al., *Ideality in a Fiber-Taper-Coupled Microresonator System for Application to Cavity Quantum Electrodynamics*. Physical Review Letters, 2003. **91**(4): p. 043902.

259. Vollmer, F. and S. Arnold, *Whispering-gallery-mode biosensing: label-free detection down to single molecules*. Nature Methods, 2008. **5**(7): p. 591-596.

260. Flatae, A.M., et al., *Optically controlled elastic microcavities*. Light Sci Appl, 2015. **4**: p. 282.

261. Nunzi Conti, G., S. Berneschi, and S. Soria, *Aptasensors Based on Whispering Gallery Mode Resonators*. Biosensors, 2016. **6**(3): p. 28.

262. Righini, G. and S. Soria, *Biosensing by WGM Microspherical Resonators*. Sensors, 2016. **16**(6): p. 905.

263. Ioppolo, T., et al., *Micro-optical force sensor concept based on whispering gallery mode resonators*. Applied Optics, 2008. **47**(16): p. 3009-3014.

264. Ding, Y., et al., *Ultralow-threshold neodymium-doped microsphere lasers on a silicon chip*. Optics Communications, 2016.

265. Ristić, D., et al., *Photoluminescence and lasing in whispering gallery mode glass microspherical resonators*. Journal of Luminescence, 2016. **170**: p. 755-760.

266. Kishi, T., et al., *Quasi-single mode laser output from a terrace structure added on a Nd3+-doped tellurite-glass microsphere prepared using localized laser heating*. Optics Express, 2015. **23**(16): p. 20629-20635.

267. Rafizadeh, D., et al., *Waveguide-coupled AlGaAs/GaAs microcavity ring and disk resonators with high finesse and 21.6-nm free spectral range*. Optics Letters, 1997. **22**(16): p. 1244-1246.

268. Chao, C.-Y. and L.J. Guo, *Biochemical sensors based on polymer microrings with sharp asymmetrical resonance*. Applied Physics Letters, 2003. **83**(8): p. 1527-1529.

269. White, I.M., et al., *Integrated multiplexed biosensors based on liquid core optical ring resonators and antiresonant reflecting optical waveguides*. Applied Physics Letters, 2006. **89**(19): p. 191106.

270. White, I.M., et al., *Versatile waveguide-coupled optofluidic devices based on liquid core optical ring resonators*. Applied Physics Letters, 2007. **91**(24): p. 241104.

271. Washburn, A.L., L.C. Gunn, and R.C. Bailey, *Label-Free Quantitation of a Cancer Biomarker in Complex Media Using Silicon Photonic Microring Resonators*. Analytical Chemistry, 2009. **81**(22): p. 9499-9506.

272. Scheler, O., et al., *Label-free, multiplexed detection of bacterial tmRNA using silicon photonic microring resonators*. Biosensors and Bioelectronics, 2012. **36**(1): p. 56-61.

273. Luchansky, M.S. and R.C. Bailey, *Silicon Photonic Microring Resonators for Quantitative Cytokine Detection and T-Cell Secretion Analysis*. Analytical Chemistry, 2010. **82**(5): p. 1975-1981.

274. Luchansky, M.S. and R.C. Bailey, *Rapid, Multiparameter Profiling of Cellular Secretion Using Silicon Photonic Microring Resonator Arrays*. Journal of the American Chemical Society, 2011. **133**(50): p. 20500-20506.

275. Washburn, A.L., et al., *Quantitative, Label-Free Detection of Five Protein Biomarkers Using Multiplexed Arrays of Silicon Photonic Microring Resonators*. Analytical Chemistry, 2010. **82**(1): p. 69-72.

276. Mazzei, A., et al., *Controlled Coupling of Counterpropagating Whispering-Gallery Modes by a Single Rayleigh Scatterer: A Classical Problem in a Quantum Optical Light*. Physical Review Letters, 2007. **99**(17): p. 173603.

277. Savchenkov, A.A., et al., *Tunable Optical Frequency Comb with a Crystalline Whispering Gallery Mode Resonator*. Physical Review Letters, 2008. **101**(9): p. 093902.

278. Savchenkov, A.A., et al., *High-order tunable filters based on a chain of coupled crystalline whispering gallery-mode resonators*. IEEE Photonics Technology Letters, 2005. **17**(1): p. 136-138.

279. Sprenger, B., H.G.L. Schwefel, and L.J. Wang, *Whispering-gallery-mode-resonator-stabilized narrow-linewidth fiber loop laser*. Optics Letters, 2009. **34**(21): p. 3370-3372.

280. Grudinin, I.S., A.B. Matsko, and L. Maleki, *Brillouin Lasing with a ${\mathrm{CaF}}_{2}$ Whispering Gallery Mode Resonator*. Physical Review Letters, 2009. **102**(4): p. 043902.

281. Greenspan, P., E.P. Mayer, and S.D. Fowler, *Nile red: a selective fluorescent stain for intracellular lipid droplets*. The Journal of Cell Biology, 1985. **100**(3): p. 965-973.

282. Ren, H.-C., et al., *High-Q microsphere biosensor - analysis for adsorption of rodlike bacteria*. Optics Express, 2007. **15**(25): p. 17410-17423.

283. Vareiro, M.M.L.M., et al., *Surface Plasmon Fluorescence Measurements of Human Chorionic Gonadotrophin: Role of Antibody Orientation in Obtaining Enhanced Sensitivity and Limit of Detection*. Analytical Chemistry, 2005. **77**(8): p. 2426-2431.

284. Chen, S., et al., *Controlling Antibody Orientation on Charged Self-Assembled Monolayers*. Langmuir, 2003. **19**(7): p. 2859-2864.

285. Tajima, N., M. Takai, and K. Ishihara, *Significance of Antibody Orientation Unraveled: Well-Oriented Antibodies Recorded High Binding Affinity*. Analytical Chemistry, 2011. **83**(6): p. 1969-1976.

286. Pujari, S.P., et al., *Covalent Surface Modification of Oxide Surfaces*. Angewandte Chemie International Edition, 2014. **53**(25): p. 6322-6356.

287. Qin, M., et al., *Two methods for glass surface modification and their application in protein immobilization*. Colloids and Surfaces B: Biointerfaces, 2007. **60**(2): p. 243-249.

288. Lee, K.S. and R.J. Ram, *Plastic-PDMS bonding for high pressure hydrolytically stable active microfluidics*. Lab on a Chip, 2009. **9**(11): p. 1618-1624.

289. Bohner, M., et al., *Synthesis and characterization of porous -tricalcium phosphate blocks*. Biomaterials, 2005. **26**(31): p. 6099-6105.

290. Zhu, H., et al., *Aptamer Based Microsphere Biosensor for Thrombin Detection*. Sensors, 2006. **6**(8): p. 785.

291. Berneschi, S., et al. *Localized biomolecules immobilization in optical microbubble resonators*. 2016.

292. Pastells, C., et al., *Two photon versus one photon fluorescence excitation in whispering gallery mode microresonators*. Journal of Luminescence, 2016. **170, Part 3**: p. 860-865.

293. Guider, R., et al., *Design and Optimization of SiON Ring Resonator-Based Biosensors for Aflatoxin M1 Detection*. Sensors, 2015. **15**(7): p. 17300.

294. Cras, J.J., et al., *Comparison of chemical cleaning methods of glass in preparation for silanization*. Biosensors and Bioelectronics, 1999. **14**(8–9): p. 683-688.

295. Fiorilli, S., et al., *Vapor-phase self-assembled monolayers of aminosilane on plasma-activated silicon substrates*. Journal of Colloid and Interface Science, 2008. **321**(1): p. 235-241.

296. Nguyen, L.V., et al., *Molecular beacons immobilized within suspended core optical fiber for specific DNA detection*. Optics Express, 2012. **20**(28): p. 29378-29385.

297. Warren-Smith, S.C., et al., *Fluorescence-Based Aluminum Ion Sensing Using a Surface-Functionalized Microstructured Optical Fiber*. Langmuir, 2011. **27**(9): p. 5680-5685.

298. Sciacca, B., et al., *Multiplexing of radiative-surface plasmon resonance for the detection of gastric cancer biomarkers in a single optical fiber*. Sensors and Actuators B: Chemical, 2013. **183**: p. 454-458.

299. Sciacca, B., et al., *Radiative-surface plasmon resonance for the detection of apolipoprotein E in medical diagnostics applications*. Nanomedicine: Nanotechnology, Biology and Medicine, 2013. **9**(4): p. 550-557.

300. Iqbal, M., et al., *Label-free biosensor arrays based on silicon ring resonators and high-speed optical scanning instrumentation*. IEEE Journal of Selected Topics in Quantum Electronics, 2010. **16**(3): p. 654-661.

301. Carlborg, C.F., et al., *A packaged optical slot-waveguide ring resonator sensor array for multiplex label-free assays in labs-on-chips*. Lab on a Chip, 2010. **10**(3): p. 281-290.

302. Zhu, H., et al., *Rapid and Label-Free Detection of Breast Cancer Biomarker CA15-3 in Clinical Human Serum Samples with Optofluidic Ring Resonator Sensors*. Analytical Chemistry, 2009. **81**(24): p. 9858-9865.

303. Danczyk, R., et al., *Comparison of antibody functionality using different immobilization methods*. Biotechnology and Bioengineering, 2003. **84**(2): p. 215-223.

304. Fowler, J.M., M.C. Stuart, and D.K.Y. Wong, *Self-Assembled Layer of Thiolated Protein G as an Immunosensor Scaffold*. Analytical Chemistry, 2007. **79**(1): p. 350-354.

305. Bog, U., et al., *Large-Scale Parallel Surface Functionalization of Goblet-type Whispering Gallery Mode Microcavity Arrays for Biosensing Applications*. Small, 2014. **10**(19): p. 3863-3868.

306. Berneschi, S., et al., *Fluorescence biosensing in selectively photo–activated microbubble resonators*. Sensors and Actuators B: Chemical.

307. Wijaya, E., et al., *Surface plasmon resonance-based biosensors: From the development of different SPR structures to novel surface functionalization strategies*. Current Opinion in Solid State and Materials Science, 2011. **15**(5): p. 208-224.

308. Masson, J.-F., et al., *Reduction of nonspecific protein binding on surface plasmon resonance biosensors*. Analytical and Bioanalytical Chemistry, 2006. **386**(7): p. 1951-1959.

309. Bolduc, O.R., J.N. Pelletier, and J.-F. Masson, *SPR Biosensing in Crude Serum Using Ultralow Fouling Binary Patterned Peptide SAM*. Analytical Chemistry, 2010. **82**(9): p. 3699-3706.

310. Ostuni, E., et al., *A Survey of Structure−Property Relationships of Surfaces that Resist the Adsorption of Protein*. Langmuir, 2001. **17**(18): p. 5605-5620.

311. Wang, F., et al., *PEG Functionalization of Whispering Gallery Mode Optical Microresonator Biosensors to Minimize Non-Specific Adsorption during Targeted, Label-Free Sensing*. Sensors, 2015. **15**(8): p. 18040-18060.

312. Qavi, A.J., et al., *Anti-DNA:RNA Antibodies and Silicon Photonic Microring Resonators: Increased Sensitivity for Multiplexed microRNA Detection*. Analytical Chemistry, 2011. **83**(15): p. 5949-5956.

313. Huckabay, H.A., S.M. Wildgen, and R.C. Dunn, *Label-free detection of ovarian cancer biomarkers using whispering gallery mode imaging*. Biosensors and Bioelectronics, 2013. **45**: p. 223-229.

314. Kim, D.C., K.P. Armendariz, and R.C. Dunn, *Integration of microsphere resonators with bioassay fluidics for whispering gallery mode imaging*. Analyst, 2013. **138**(11): p. 3189-3195.

Chapter 2

Review of Whispering Gallery Modes in Active Microresonators

2.1 Whispering Gallery Modes in Active Microresonators

P1. T. Reynolds, N. Riesen, A. Meldrum, X. Fan, J. M. M. Hall, T. M. Monro, and A. François, "Fluorescent and lasing whispering gallery mode microresonators: an emerging paradigm for sensing application", submitted to Laser & Photonics Review (2016)

2.1.1 Publication Overview

Active WGM microresonators have evolved significantly since the first observations of lasing WGMs from crystalline and liquid drop resonators, now including a diverse range of geometries with a novel variety of both inorganic and organic gain mediums. Notably, they have also opened up a whole range of new sensing opportunities with their ability to enable remote excitation and collection of the WGM spectrum. This has been most significantly taken advantage of for biosensing applications, enabling the possibility of conducting *in-vivo* measurements, including from within living cells. However, for all the success and promise they have shown, there is still significant work that must be completed to improve sensing performance, durability and reusability to produce commercially viable sensors.

In this review, recent work using active WGM microresonators is dissected, highlighting novel geometries from liquid droplets to polygons, capillaries/microfibers, toroids, goblets and disks through to solid and free-floating microspheres, gain mediums and applications including physical sensing (pressure, temperature, humidity) and biosensing (refractive index and intensity based) that have been documented so far. Further noting areas that still require investigating, such as forming a consensus on contribution of the components that influence the lasing threshold, as well as mapping out the future directions, potential combinations with other sensing technologies and prospects of active WGM sensors as a whole.

2.1.2 Statement of Contribution

Statement of Authorship

Title of Paper	Fluorescent and lasing whispering gallery mode microresonators: an emerging paradigm for sensing applications
Publication Status	☐ Published ☐ Accepted for Publication ☒ Submitted for Publication ☐ Unpublished and Unsubmitted w ork w ritten in manuscript style
Publication Details	T. Reynolds, N. Riesen, A. Meldrum, X. Fan, J. M. M. Hall, T. M. Monro, and A. Francois, "Fluorescent and lasing whispering gallery mode microresonators: an emerging paradigm for sensing applications," submitted to Laser & Photonics Review (October 2016)

Principal Author

Name of Principal Author (Candidate)	Tess Reynolds		
Contribution to the Paper	Primarily wrote the paper and acted as one of the corresponding authors, contributing to all sections of the review and overall development of the manuscript.		
Overall percentage (%)	70		
Certification:	This paper reports on original research I conducted during the period of my Higher Degree by Research candidature and is not subject to any obligations or contractual agreements with a third party that would constrain its inclusion in this thesis. I am the primary author of this paper.		
Signature		Date	11-11-16

Co-Author Contributions

By signing the Statement of Authorship, each author certifies that:

i. the candidate's stated contribution to the publication is accurate (as detailed above);

ii. permission is granted for the candidate in include the publication in the thesis; and

iii. the sum of all co-author contributions is equal to 100% less the candidate's stated contribution.

Name of Co-Author	Nicolas Riesen		
Contribution to the Paper	Contributed to the physical sensing applications section as well as assisting in the evaluation and editing of the entire manuscript.		
Signature		Date	16-11-16

Name of Co-Author	Al Meldrum		
Contribution to the Paper	Contributed to the resonators and future prospects section as well as assisting in the evaluation and editing of the entire manuscript.		
Signature		Date	15-11-16

Name of Co-Author	Xudong Fan		
Contribution to the Paper	Contributed to the resonator, gain medium, applications and future prospects section as well as assisting in the evaluation and editing of the final manuscript.		
Signature		Date	14-11-16

Name of Co-Author	Jonathan M. M. Hall		
Contribution to the Paper	Contributed to the theoretical section as well as assisting in the evaluation and editing of the final manuscript.		
Signature		Date	11-11-16

Name of Co-Author	Tanya M. Monro		
Contribution to the Paper	Supervised the project as well as assisted in the evaluation and editing of the manuscript.		
Signature		Date	14-11-16

Name of Co-Author	Alexandre Francois		
Contribution to the Paper	Supervised the development of the review and helped contribute to the overall manuscript editing and evaluation during the entire project, acting as one of the corresponding authors		
Signature		Date	15-11-16

Fluorescent and Lasing Whispering Gallery Mode Microresonators: An Emerging Paradigm for Sensing Applications

T. Reynolds,[1] N.Riesen,[1,3] A. Meldrum,[2] X. Fan,[4] J. M. M. Hall,[1] T. M. Monro,[1,3] and A. François[1,3]

[1]*The Institute for Photonics and Advanced Sensing (IPAS), University of Adelaide, Adelaide SA 5005, Australia*

[2]*Department of Physics, University of Alberta, Edmonton, AB, T6G2E1, Canada*

[3]*University of South Australia, Adelaide SA 5000, Australia*

[4]*Department of Biomedical Engineering, University of Michigan, Ann Arbor, MI 48109, USA*

Abstract: Whispering gallery modes (WGMs) have been exploited for a broad range of sensing applications. However, the vast majority of such WGM sensors consist of passive resonators, requiring complex interrogation systems to be employed, ultimately limiting their practicality.

Active resonators containing a gain medium, allowing remote excitation and interrogation of the WGM-modulated fluorescence spectra, have emerged as an alternative to passive resonators. Although research is still in its infancy, recent progress has reduced the performance gap between the two paradigms, fueled by the potential for new applications that could not previously be realized.

Here, recent developments in sensors based on active WGM microresonators are reviewed, beginning with a discussion of the theory of fluorescence-based and lasing WGMs, followed by a discussion of the variety of gain media, resonator architectures, and emerging sensing applications. We conclude with a discussion of the prospects and future directions for improving active WGM sensors.

1. Introduction

Whispering gallery modes (WGMs) are optical resonances arising from light being trapped due to total internal reflection at the boundary of a dielectric structure having at least one axis of symmetry. The light propagating along the inner surface of the resonator gives rise to constructive interference when returning in phase after each round trip. This creates resonance features, with spectral positions and linewidths that depend on the dielectric function and geometry of the resonator, as well as the surrounding environment.

Due to their extremely high Quality factor (Q-factor), defined as the ability to store energy, and their small mode volume[1, 2], WGM resonators have found applications spanning sensing [3-5] through to quantum electrodynamics (QED) [6-8] and non-linear optics [9-11]. The applications come with an equal

diversity of geometries including spheres [4], capillaries [12], bubbles [13], bottles [14], fibers [15], toroids [16], rings [17] and disks [18-33]. Materials used for such resonators can be amorphous [4, 19, 34, 35] or crystalline [36-41], and organic or inorganic [17, 22, 42, 43]. The vast majority of resonators studied are passive, requiring an evanescent-wave coupler to interrogate the WGMs. Commonly, these couplers take the form of a tapered optical fiber or a prism, with the taper waist diameter chosen to fulfill the required phase-matching conditions [44]. In the case of prism coupling the incidence angle is tuned to achieve the phase matching [45, 46]. In either case this allows efficient coupling to the WGMs. Passive resonators have shown tremendous performance, especially in terms of the Q-factor which in some cases can exceed 10^{11} [1], but also in terms of ultra-small mode volumes which is important for QED and non-linear applications. Note however that the requirement for external evanescent coupling configurations, may render any real life applications outside laboratory environments problematic.

In recent years several attempts to reap the performance benefits of passive resonators for real-world applications have emerged. Beyond the more obvious approaches of integrating resonators onto a sensing chip [43, 47, 48], Agarwal *et al.* [49] have integrated a passive silica microsphere at the end of an optical fiber stem with two conical taper couplers, into a monolithic device for dip sensing applications, while Shi *et al.* [50] have directly written, using femtosecond machining, a ring-resonator onto the core of a polished optical fiber. Other researchers have investigated approaches that allow for free-space coupling into passive WGM resonators. Ballard *et al.* [51] and Shao *et al.* [52] for instance used deformed microspheres and microtoroids, respectively, presenting "nodes" to couple into, while Zhu *et al.* [53] have used nanoparticles to induce scattering to the same effect. Moreover Zullo *et al.* [54] used a focused free-space edge-coupling scheme to achieve similar results. Using passive free space coupling strategies however comes at the cost of reduced performance.

Active resonators that contain a gain medium are particularly suited to remote excitation and collection of the WGM signal, thereby alleviating some of the practical limitations of typical passive resonators. The first reported active whispering gallery mode resonator was in 1961, barely a year after the first laser was demonstrated by Theodore Maiman. Samarium-doped CaF_2 microspheres were excited by a flashlamp [55], apparently surpassing their lasing threshold at a wavelength of 708.5 nm. In general, upon excitation of the gain medium the emitted fluorescence intensity is modulated at the resonance frequencies as a direct manifestation of the Purcell Effect (*i.e.* increasing the fluorescence intensity at the particular resonance wavelengths) [53, 56, 57].

Fluorescent-based approaches also facilitate the use of smaller resonators thereby in general allowing for greater refractive index sensitivity. Microspheres of 15 μm diameter or even smaller [42], and arrays of resonators can, for example, be interrogated simply by using a scanning microscope [43]. As

mentioned active resonators however have reduced Q-factors. The lower Q-factor observed in active resonators is due to several factors. The asphericity can play a significant role for the case of fluorescent microspheres, as shown by Riesen *et al*.,[58] who investigated the Q-factor of a dye-doped polymer microsphere measured in free space and through a fiber taper. The asphericity lifts the degeneracy of the resonances in different equatorial planes, so that when indiscriminate collection of these WGMs occurs in free space, the partially overlapping modes effectively result in broader linewidths hence reducing the Q-factor. Similarly, a reduction in the Q-factor of fluorescent cylindrical microcavities has also been observed [59, 60]. As a result, fluorescence-based resonators typically remain somewhat restricted to sensing applications and are unsuitable for non-linear optics and QED applications where high Q-factors and small mode volumes are critical.

For biosensing, single molecule detection has become well established using passive resonators with multiple demonstrations being reported [19, 29, 61-63]. However, since fluorescent resonators have considerably lower Q-factors, and hence higher detection limits, single molecule detection with fluorescent resonators remains challenging. Nonetheless, the free space excitation and collection platform enabled by fluorescent resonators allows for novel applications not possible using passive resonators. For example, free-floating resonators can be inserted into living cells for sensing [64], or for tagging and tracking purposes, using the specific spectral fingerprint of each individual WGM resonator [65, 66]. Even single cells can be turned into WGM resonators by injecting a mixture of fluorescent dye and high refractive index oil, providing the required gain medium to generate the WGMs and also the required light confinement owing to the refractive index contrast between the oil droplet and its surrounding environment [66]. Further, by combining fluorescent microspheres with flow cytometry, automated high-throughput sensing can be achieved using a robust data analysis algorithm to extract real-time information about the resonator's properties from its WGM spectrum [67], while fluorescent cholesteric liquid crystal core shell structures have also shown tremendous potential as magnetically transportable light sources for in-channel illumination applications [68]. In addition, fluorescent resonators can be turned into microscopic laser sources using a lasing gain medium and a suitable pump source, enabling slight enhancements in the Q-factors to be realized upon reaching the lasing threshold [22, 42, 43, 48, 68, 69] and also lowering the detection limit for sensing applications [22, 69].

While there are a large number of review articles in the literature on WGMs, focusing on different aspects such as theory and applications [70, 71], especially related to sensing [3, 5, 72-75], none of them have focused on fluorescent-based resonators and their prospects as sensors. In this review an overview of the recent work on fluorescent-based WGM resonators, which stands as a prolific research field with emerging sensing applications, is provided. First, the basic theory of fluorescent WGMs is discussed,

focusing on lasing behavior. Next, strategies for incorporating a gain medium, either organic or inorganic, into resonators and the resulting resonator properties are reviewed, followed by an overview of fluorescent resonator geometries and applications. Concluding remarks focus on future prospects and research opportunities.

2. Fluorescent Based and Lasing WGM Theory

Fluorescent resonators can be modeled analytically by extending classical Mie Scattering theory. For example, Beier *et al*. [76], developed a model to describe quantum dot (QD) coated microspheres, while Chew *et al*. [77, 78], described fluorescent microspheres by considering distributions of dipoles within a resonator. By developing analytical models such as these, key characteristics including the resonance positions, Q-factor, refractive index sensitivity ($S = \delta\lambda/\delta n$) and free-spectral range can be extracted and used for instance in optimizing sensing performance [79]. The main advantage of analytical models over computationally intensive numerical methods such as the Finite-Element Method (FEM) [80] or Finite-Difference Time-Domain (FDTD) [81], is the ability to scan a vast parameter space relatively efficiently [82]. Numerical techniques on the other hand do facilitate the investigation of a broader variety of resonator shapes [36], as well as providing access to intermediate values of the fields in the time-domain, which allows for the study of transient or emergent optical phenomena such as directional emission in deformed cavities [83-87]. Novel resonator design has also begun focusing on microbubbles, and single/multi-layered microspheres [88-91], with such resonators demonstrating improved refractive index sensitivity [80, 91] and also generating interest for non-linear optics [11, 92-94].

WGM microcavities have also been able to be operated as ultra-low-threshold microlasers in various configurations [22, 42, 43, 48, 68, 95-97]. Examples of the typical behavior of lasing WGMs in fluorescent resonators can be seen in Figure 2.1 (a) and (b), where the mode intensity increases rapidly above the lasing threshold. The Q-factor also increases upon lasing, typically by a factor of approximately 4 [22, 42].

Employing the lasing eigenvalue problem (LEP) formulation [98, 99], which introduces gain through an imaginary part of the refractive index, the lasing frequency and threshold can be determined numerically [100]. However, modeling how the resonator's Q-factor and effective mode volume (V_{eff}) influence the lasing threshold and how the modes behave above the lasing threshold remain largely unknown.

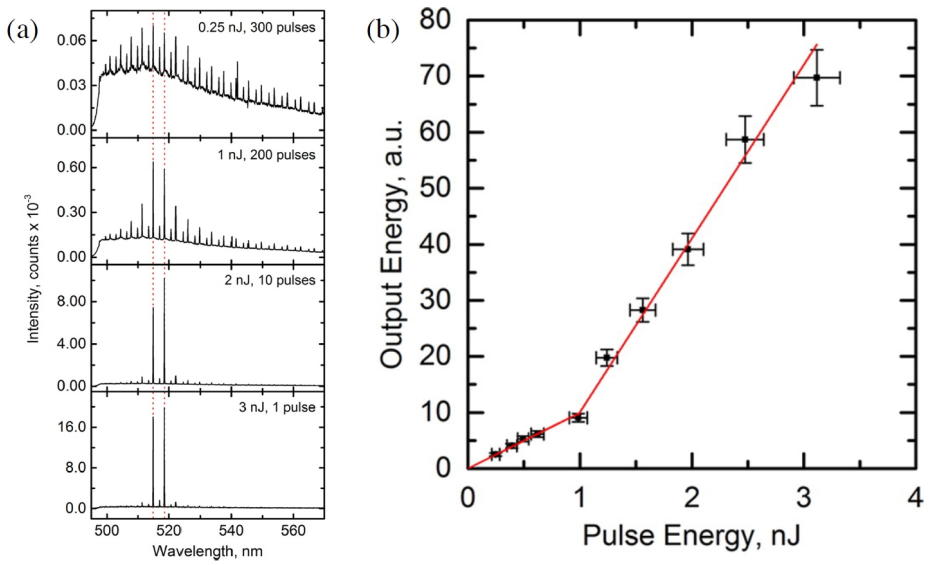

Figure 2.1. (a) WGM spectra exhibiting the typical transition between fluorescence and stimulated emission regimes and (b) Output energy of the fluorescent WGM signal as function of the pump power [65]. Reproduced (adapted) with permission from [65]. Copyright (2015), American Chemical Society.

Spillane *et al*. [101] have established a relation for the Raman lasing threshold of a fiber coupled microsphere where the lasing threshold ($I_{threshold}$) scales proportionally with the gain factor (A) and more importantly with V_{eff}/Q^2:

$$I_{threshold} = A\frac{V_{eff}}{Q^2}. \qquad (2.1)$$

The gain factor, A, is related to the Raman gain coefficient for a Raman laser [101], or the gain medium concentration and quantum yield in the case of a fluorescent dye [42]. As expected, the lasing threshold as described in Equation. 1, is inversely proportional to the Purcell enhancement factor, F, given by [56],

$$F = 3Q\frac{\left(\frac{\lambda_c}{n}\right)^3}{4\pi^2 V_{eff}} \sim \frac{Q}{V_{eff}}. \qquad (2.2)$$

In other words, a low lasing threshold is achieved if the Purcell factor is high.

However, in earlier work by Sandoghdar *et al*. [102], the lasing threshold of neodymium doped silica microspheres was found to have a linear dependency on Q^{-1}. More recently, Gargas *et al*. [103] established the same Q-factor dependency on the lasing threshold of a ZnO microdisk, further indicating that the behavior of lasing WGMs and especially the lasing threshold is not yet fully understood.

3. Gain Media

The most important feature of fluorescence-based resonators, besides the resonator geometry, is the gain medium, which provides the required fluorescence emission that is then modulated by the WGM resonances. In the following section the different types of gain media used are reviewed, including how they have been incorporated into or combined with WGM resonators. In most cases the approach used for incorporating the gain medium is independent of the resonator geometry itself. It is however strongly influenced by the nature of the gain medium and the resonator material.

3.1. Organic Gain Media

Fluorescent dyes are the most common gain media used for active microresonators, providing a broad range of emission bands stretching from the UV [104], to the visible and through to the near infrared [105, 106] as shown in Table 2.1.

A large body of literature exists on the chemistry of various organic dyes in polymer matrices [107], in which the dye chemistry (*i.e.*, solubility, reactivity, and so on) can be classified on the basis of the presence of azo (–N=N–) groups, quinone groups (anthraquinone dyes), or phthalocyanines. Organic fluorophores are commonly mixed with a polymer (*e.g.* PMMA, SU8, PDMS, Polystyrene), and then fabricated into rings, disks [31, 33, 108], solid or liquid microspheres [109], or drawn into solid fibers or capillaries [110, 111]. Alternatively, fluorescent dyes can be introduced into already-formed polymer microresonators. A common method, especially for polystyrene microspheres is to use a two-phase liquid system where the resonators are suspended in an aqueous solution while the fluorophore is dissolved in an organic dye that is not miscible with water [42]. Alternatively, resonators can simply be coated with fluorescent dye molecules using chemical moieties on both the dye and the resonator surface [112, 113].

Fluorescent dyes were pivotal in the development of lasing WGM microcavities with thresholds as low as a few tens of nJ/mm^2 [31, 114] to a few μJ/mm^2 [33]. It should be noted that the lasing threshold is strongly influenced by the fluorescent dye quantum yield, concentration and the resonator configuration (Q-factor and mode volume) [31]. Ultimately, the fluorescent dye concentration must be carefully controlled in order to minimize the lasing threshold [42]. Fluorescent dye-doped polymers tend to be plagued by instabilities associated with photochemical degradation under lasing conditions (commonly referred to as “photobleaching”) [115], eventually resulting in loss of optical gain. This is a notable limitation in the application of active biosensing devices. Fluorescent dyes are typically excited with pulsed lasers not only to reach the lasing threshold, but also in order to minimize deleterious photochemical effects (*i.e.*, dye-dye or dye-oxygen [116] interactions) and to reduce the formation of nonradiative triplet states [117].

Table 2.1. Examples of organic dye doped resonators.

Dye	Excitation/Emission Wavelength (nm)	Resonator Type
CY-3	480/540	Dye-doped SU8 microring [31]*
Coumarin 540	420/530	Dye-doped liquid droplet [235]*
Coumarin 6G	480/510	Dye-doped polystyrene microsphere [64, 166]
CY-3	480/540	Dye-doped SU8 microring [31]*
Yellow Venus protein	500/530	Liquid droplet [126]*
Rhodamine B	532/580-600	Dye-doped monolithic microdisk [108]* Dye-doped melamine-formaldehyde resin microsphere [38] Dye-doped solid and hollow PMMA fibers [110, 111]* Dye-doped liquid crystal droplet [236] Dye-doped SU8 photoresist [33]*
Rhodamine 6G	532/580-600	Liquid filled microcapillary [106]* Free floating liquid droplet [109], methanol droplet in PDMS matrix [237] Dye-doped SU8 microring [31]* Dye-coated rolled microtube [113]
Nile Red	532/580-600	Dye-doped polystyrene microsphere [42, 69, 209]* Dye-doped polymer coating on microcapillary [238]* Dye-doped oil droplets [66, 239]*
CY-5	570/760	Dye-doped SU8 microring [31]*
DCM	490/600-800	Micro hemisphere [240]
Rhodamine 640 perchlorate	620/700	Liquid droplet [158]*
Chlorophyll	430/680-730	Liquid filled microcapillary [127]*

* Lasing of the WGM(s) was observed.

Alternatively, conjugated polymers can be used which are naturally fluorescent and are known to lase [117]. They typically consist of alternating single and double bonded C atoms, producing an electronic structure with extensive orbital delocalization and semiconductor-like energy gap. Conjugated polymer devices can be especially sensitive to the surrounding environment in terms of changes in the lasing intensity or threshold, for example showing "amplified quenching" due to their relatively high carrier mobility. This property makes them sensitive turn-off sensors for nitro compounds [118]. Thus, conjugated polymers could be used for fabricating new and ultra-sensitive resonators for sensing vapors of toxic or dangerous substances, similar to how the lasing intensity of plasmonic cavities is quenched by nitroaromatics [119]. However, the synthesis of WGM-compatible structures from conjugated polymers is difficult [120] without blending with another polymer. Kushida *et al.* [121] were among the first to exploit blends of conjugated polymer, with one donor and one emitter, enabling Fluorescent Resonant Energy Transfer (FRET). A FRET approach could be highly beneficial for limiting photobleaching using adequate donor/acceptor pairs [122], paving the way to a WGM FRET laser [123, 124].

Fluorescent proteins have also been exploited as gain media for active resonators [125], Jonáš *et al.* [126] for instance demonstrated the potential of liquid microdroplet resonators, doped with suspended

fluorescent proteins, as optofluidic biolasers. They revealed that even a single fluorescent bacterium, producing this fluorescent protein, is sufficient for inducing lasing. Chen *et al*. [127] used the fluorescent properties of chlorophylls to develop the first optofluidic chlorophyll laser, laying the path for future biocompatible and biodegradable lasers.

3.2. Inorganic Gain Media

Inorganic gain media allow continuous wave laser excitation and are relatively impervious to photobleaching. They are chemically robust, stable and offer several accessible excitation wavelength windows, depending on their energy level structure, as shown in Table 2.2.

Table 2.2**:** Examples of inorganic material used as gain medium in microcavities.

Material	Excitation/Emission Wavelength (nm)	Resonator Type
ZnO	355/390	Hexagonal shaped sub-micron disk [103] *, Microwire [134, 241] * Microsphere [133, 242]
GaN/InGaN	350-500	Core-shell wire [243]
CdZnS/ZnS Q dots	440	Liquid filled capillary [244]*
PbI_2	400/~500	Hexagonal shaped crystal [36]*
$CsPbBr_3$	520-540	Rectangular cross sectioned nanowire [245]*
Er^{3+}	530-460	Upconversion emission doped microsphere [148], Upconversion lasing on microtoroid [150]*
Tm^{3+}	1064/450, 461, 784, 802, 816	Upconversion lasing on microtoroid [149]*
$CH_3NH_3PbBr_3$	400/560	Square shaped microrod [143, 246]*
CdSe/ZnS Q-dots	433/655	Single Q-dot coating inside thin wall capillary [128]*
$CsPbX_3$, X = Cl, Br, and I)	400/420-700	Square shaped crystal [142]*
Si Q-dots	770	Q-dot coated capillaries [131]
Nd^{3+}	780/1064	Doped barium titanium silicate microsphere [173]*, Doped silica microsphere [95]*, Glass microsphere [174]*, Doped tellurite microsphere [147]*
InAs/InGaAsGaAs/	532/1270	Microring [136]*
HgTe Q-dots	1250	Q-dot coated microsphere [138]*
Er^{3+}	1535	Doped microtoroid [247]*, Doped microspheres [145]*
Ge/SiGe Quantum well	1450-1650	Microdisk [244]
Tm^{3+}	1550-1610/2000	Microtoroid [97, 153]*
InAsSb/InAsPSb Quantum well	4000	Microdisk [32]

* Lasing of the WGM(s) was observed.

Owing to the commercial availability of Quantum Dots (QDs) [128], semiconductors have risen as a popular gain medium. Unlike organic fluorophores where the pump wavelength has to be in a specific region of the optical spectrum (*i.e*. the maximum absorption wavelength), the only requirement for exciting semiconductor materials is for the pump wavelength to be shorter than the band gap. Further, as varying the size of the QDs provides control over the fluorescence emissions, and as QDs can all be excited with a single pump source, multiplexed sensing is easily achievable [129]. The QDs can be

covalently attached [130], grown onto the resonator surface [131] or embedded within the resonator itself [132]. More recently, semiconductor oxides such as ZnO [133, 134] and TiO_2 [135] have been exploited for their light emitting properties. Alternatively, quantum well heterostructures can be used for the fabrication of disk or pillar resonators using state-of-the-art fabrication processes [32, 136, 137], allowing them to be in some cases electrically driven [137] instead of using light for excitation. Lasing using semiconductors has been demonstrated with both quantum well heterostructures [48] and QDs [136, 138]. However, non-radiative Auger recombination, exhibiting a recombination rate significantly higher than radiative transitions can drastically reduce the efficiency of such gain media for lasing applications [139, 140].

Perovskite is an emerging new type of gain medium, which refers to crystalline materials with a composition ABX_3, where A and B are two cations and X is an anion bonding to both A and B, such as $CsPbBr_3$. The chemical composition dictates the bandgap structure [141] (*i.e.* direct or indirect bandgap) as well as its emission wavelength [142]. Various perovskites have been used to fabricate micron-sized polygonal resonators (*i.e.* squares, pentagons, or hexagons) supporting WGMs. Lasing of perovskite resonators has also been demonstrated, however the lasing threshold ranges from the relatively high values of a few $\mu J/cm^2$ [143] to tens of $\mu J/cm^2$ [36] owing to the lower Q-factor exhibited by these polygonal resonators.

Rare-earth ions such as Er^{3+}, Nd^{3+} and Tm^{3+}, utilized for telecom fiber amplifiers and fiber lasers, have been used for microsphere fabrication by melting rare-earth doped fused silica fiber to realize microspheres with high Q-factors [144, 145]. Rare-earth ions can also be dissolved in different glass hosts, such as ZBLAN [146] or tellurites [147], unlocking different emission wavelength windows, especially in the mid-infrared where silica's absorption becomes an issue. Upconversion has also been exploited for rare-earth systems, enabling fluorescence emission [148, 149] and lasing [149, 150] at shorter wavelengths. The use of rare earth doped sol-gel coatings has also been investigated for coating fused silica microspheres [145, 151]. This method has also been applied to other resonator geometries such as toroids, taking advantage of their low mode volume and large Q-factor, for lasing applications [97, 150]. Many of the fundamental characteristics of WGM-based lasing have been carefully investigated using rare-earth doped microsphere systems [152], with CW lasing thresholds ranging from μW [95] to several mW [153].

4. Fluorescent Resonator Geometries

Microscale resonators have been fabricated from a diverse range of media spanning liquids to polymers, and glass to semiconductors with an equally large variety of geometries. Here we summarize some of the more commonly utilized fluorescence and lasing WGM resonator geometries and the materials from which they are fabricated.

4.1 Liquid Droplets

Microsphere liquid-drop resonators have resurfaced as candidates for microlasers [68, 154] and biosensors [126, 155], despite initial limitations preventing their widespread usage [156]. Liquid droplets form naturally smooth spherical surfaces due to surface tension, allowing high Q-factors to be realized (4.2×10^9 at 300 nm) [157]. Fluorescent dye-doped droplet-based resonators have found applications in microfluidics [158] (Figure 2.2 (a)), and can also readily be manipulated using optical tweezers [159]. Further, using a water-in-oil-in-water (W/O/W) double emulsion, depicted in Figure 2.2 (c), where magnetic nanoparticles were incorporated into the center, the droplets can be controlled using a magnet [68].

A key advantage of droplet resonators is their ability to be tuned. For example, nematic liquid crystal (LC) droplets [160] provide the means to tune the WGM resonances by using electric fields to manipulate the LC orientations [161], while Tang *et al*. demonstrated the tuning capability via manipulating the diameter of the droplets as they travel into a microfluidic chip and are slowly dissolved [158]. Similar behavior has been reported with self-assembled static dye-doped polystyrene microdroplets formed in a PDMS matrix [162]. Finally, free-floating liquid droplets, shown in Figure 2.2 (b), have the capability to change their shape under external stimulus, allowing for tuning of the resonance wavelengths [163].

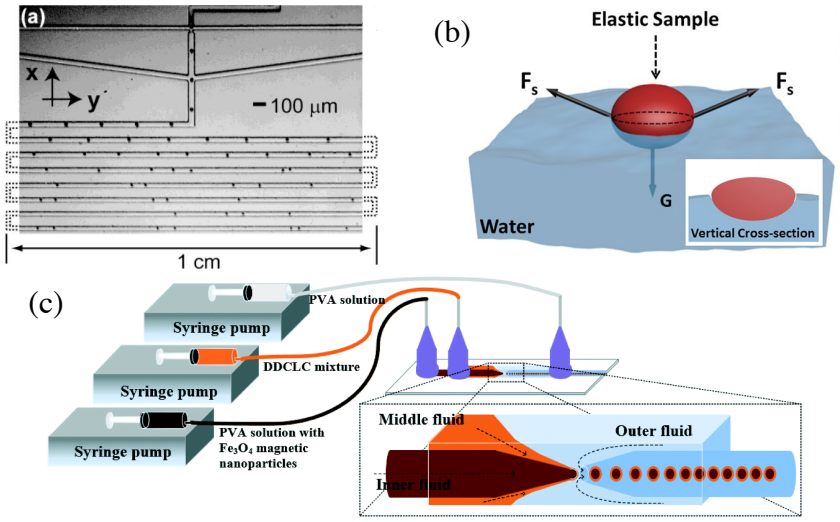

Figure 2.2. (a) Rhodamine 640 perchlorate doped free-floating benzyl alcohol micro droplets in sodium dodecyl sulfate in a microfluidic chip [158], (b) free floating Rhodamine 6G doped dichloromethane and epoxy resin micro droplet laser [163], (c) diagram of glass capillary microfluidic setup for producing W/O/W double-emulsion droplets [68]. (a) Reproduced with permission from [158]. Copyright (2011), Optical Society of America. (b) Reproduced with permission from [163]. Copyright (2016), Nature Publishing Group. (c) Reproduced with permission from [68]. Copyright (2016), Royal Society of Chemistry.

4.2 Solid Microspheres

Solid fluorescent microsphere resonators [67, 121, 164] are commonly fabricated from polymers due to their low cost, structural flexibility and ease of fabrication and integration of a gain medium [42, 121, 162, 165-167]. Beyond the straightforward approach of using a single microsphere resonator, either trapped with optical tweezers [168] or simply deposited onto various substrates [166], there has been interest in combining fluorescent microspherical resonators with capillaries [169], or microstructured optical fibers (MOF) [69, 170, 171], as shown in Figure 2.3 (a) and (b). This approach allows the fiber to be used to simultaneously excite and collect the fluorescent/lasing WGM signal. Further, the local environment of a MOF near a fluorescent microsphere enhances specific modes due to the Purcell Effect and also improves the lasing efficiency [172]. The combination of a MOF and a fluorescent microsphere can for instance be used for sensing applications, whereby the microsphere resides in one of the fiber's axial holes [69].

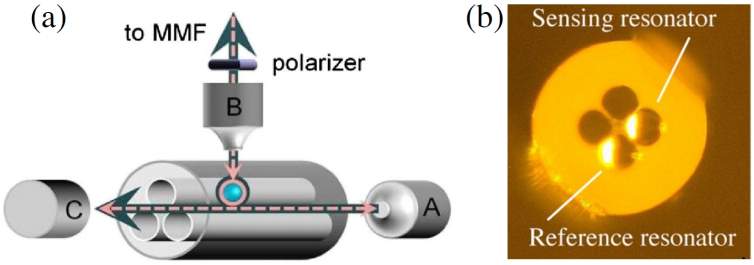

Figure 2.3. Dye-doped polymer microspheres (a) inside [170] and (b) on a tip [209] of a microstructured optical fiber. (a) Reproduced with permission from [170]. Copyright (2013), Optical Society of America. (b) Reproduced with permission from [209]. Copyright (2016), American Chemical Society.

Rare-earth doped microspheres are also commonly used although the vast majority of research undertaken with such resonators still employs a fiber taper for evanescent coupling. In comparison, the few free space experiments that have been reported have displayed lower performance [148, 173, 174], although some interesting opportunities have still been identified notably by Kishi *et al*. who introduce a "terrace" structure, which breaks the microsphere symmetry to achieve quasi-single mode output lasing [147].

4.3 Polygon Resonators

Polygons can also support WGMs, and have recently become an interesting addition to more traditional circularly-symmetric resonator geometries. They are often characterized by their number of facets (m), where $m = 2$ corresponds to a Fabry-Perot cavity and cavities with $m \geq 3$ can support quasi-WGMs [175]. The Q factor for non-absorptive cavities is given as,

$$Q = \frac{m\pi nD \sin\left(\frac{2\pi}{m}\right) R^{m/4} \upsilon_0}{2c(1-R^{m/2})} \qquad (2.3)$$

where n is the cavity index of refraction, R the is reflectivity of the polygon facet, D is the polygon diameter, c is the speed of light, and v_0 is the resonance position. By considering the normalized Q-factor, and holding the diameter of the resonator constant, it can be seen that the Q-factor tends to decrease as m increases, revealing why the vast majority of the facetted crystals supporting WGMs (see Figure 2.4), exhibit as few facets as possible [175]. Polygonal resonators are commonly grown using Chemical Vapor Deposition from perovskite, which has a fairly large refractive index (typically above 2 in the visible) [36], providing strong confinement of the WGMs [36, 79, 142]. The Q-factors of these resonators however remain somewhat limited to below ~10^3.

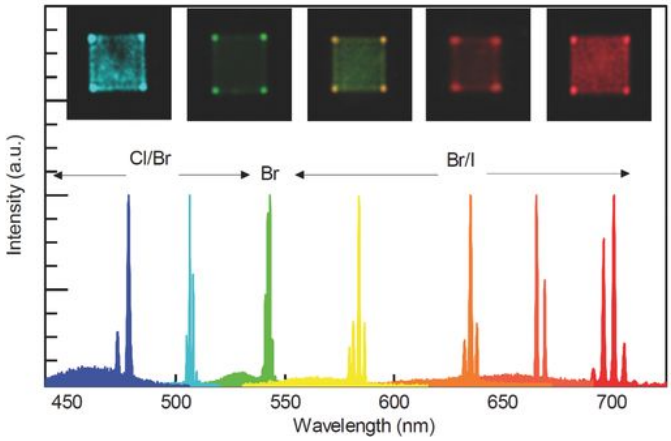

Figure 2.4. Cesium lead halide ($CsPbX_3$; X=Cl, Br, I) square nanocrystals exhibiting WGM lasing at different wavelengths [142]. Reproduced with permission from [142]. Copyright (2016), Wiley.

4.4 Toroid, Goblet, Microdisk and Ring Resonators

Microfabrication techniques have also been exploited for producing integrated microresonators, the most famous example being toroid resonators initially developed by Vahala *et al*. at Caltech [16]. These techniques have since been adapted by many other research groups. Earlier examples of microfabricated WGM resonators include microdisks [18, 176] and micro-rings [17, 177]. These particular resonant structures have the ability to confine light in ultra-small volumes [178], making them particularly suited to QED and lasing applications. Over the last few years, active variants of toroid or "goblet" resonators [43, 178, 179], disks [43, 178] and ring resonators (Figure 2.5) [31] have emerged.

Fluorescent goblet resonators can for instance be integrated into microfluidic chips and interrogated remotely using a scanning confocal microscope [43]. It is envisioned that the large-scale integration of lasing resonant microstructures such as microgoblets could be highly advantageous for multiplexed sensing, with each individual resonator functionalized for the detection of a specific analyte. Adding a

photo-responsive liquid on top of the goblet resonator, for example, could also enable fast tuning of the lasing output wavelength through the elastic deformation of the resonator [179].

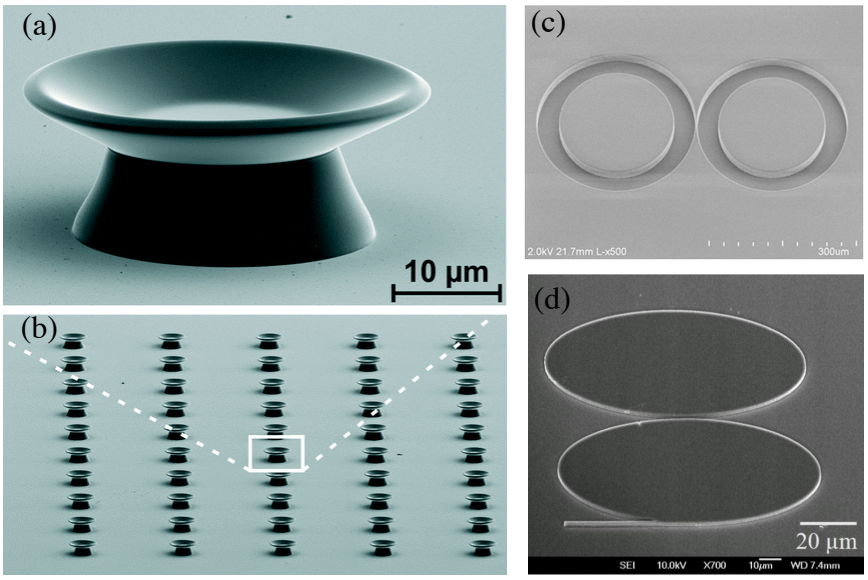

Figure 2.5. (a), (b) Fluorescent PMMA goblet resonators on a chip [43]. (c) Coupled ring resonators etched on fused silica and coated with a fluorescent dye-doped high refractive index polymer [31] and (d) coupled disk resonator with a protruding waveguide for directional emission [33]. (a), (b) Reproduced with permission from [43]. Copyright (2015), Royal Society of Chemistry. (c) Reproduced with permission from [31]. Copyright (2015), Nature Publishing Group. (d) Reproduced with permission from [33]. Copyright (2015), Elsevier.

Microfabrication techniques have also allowed for the design and fabrication of coupled resonators, which requires both resonators to have almost identical dimensions to ensure spectral overlap of the resonances [180]. Coupled disk and ring resonators have been used to exploit the Vernier effect [181] and have also allowed for the realization of single-mode WGM lasers [31, 33]. Microfabrication can also be used for the development of alternative resonator geometries with controlled deformations [33] or with directly connected waveguides for unidirectional emission [33, 182] for integrated photonics applications.

The creation of reusable [183] and reconfigurable [31] ring resonator lasers has recently been demonstrated by Chandrahalim *et al*., opening up the possibility of realizing photonic devices such as on-chip coherent light sources. The reusability of the resonators was demonstrated through depositing, removing and re-depositing both a dye-doped polymer liquid and solid, while wavelength reconfiguration was demonstrated using a similar process via interchanging the gain medium.

Finally, Sun *et al*. investigated the use of proteins for the fabrication of biocompatible disk resonators, using femtosecond machining [108]. By combining a protein matrix with fluorescent dyes, lasing behavior

of the resonator was demonstrated, paving the way for novel biocompatible materials to be used as laser sources.

4.5 Capillaries and Microfibers

Capillary-type structures with fluorescent channel coatings can also support fluorescent WGMs and have been used as refractometric sensors [22, 131, 184, 185] or biosensors [48]. For microcapillaries to function as active WGM-based sensors, the capillary must be coated with a fluorescent layer that: (a) has a high refractive index in order to support WGMs, and (b) has a thickness of less than ~1 μm so that the resonant field profile extends sufficiently far into the channel medium as shown in Figures 2.6 (a) & (b). Recently, the first capillary-based WGM laser sensor for refractometric sensing was developed using a dye-doped polymer [22], in theory yielding an order of magnitude improvement in the limit of detection, as compared to the same device operated below the lasing threshold.

Microfibers supporting WGMs such as R6G-doped PMMA [25, 111] or CdSe–ZnS core–shell QD-doped polyvinylpyrrolidone (PVP) nanowires [132], forming cylindrical structures whose width can be precisely controlled, are shown in Figures 2.6 (c), (d) & (e). Such structures can exhibit lasing WGMs with unusually high refractive index sensitivities of up to 300 nm/RIU [25]. Inkjet-printed fluorescent dye-doped epoxy resin, and PDMS fibers have also been shown to support WGM lasing with good sensitivity to external strain [111, 162, 163], generating interest due to their high flexibility and mechanical robustness. Fluorescent dye-doped-polymer-coated waveguides have similar benefits and are suitable candidates for future biosensing experiments [31].

Development in nanofabrication techniques [186] have enabled the realization of self-rolled nanotubes from bi-layers materials [187-190]. The bi-layer is strained and deposited atop of a sacrificial substrate, which is subsequently etched away, releasing the layer and allowing it to roll and form a nanotube [186]. Most commonly the bi-layer is SiO/SiO_2, enabling robust, transparent and biocompatible sensors to be fabricated [187, 188]. Moreover, hybrid polymer/oxide/polymer tubes have also been fabricated [189], and novel composite cavities made from dielectric and metal materials have also recently been proposed [190]. The diameter and wall thickness of these nanotubes can be controlled during the deposition process, and there is also the possibility of incorporating a thin organic active layer [187]. These structures have proven to be successful candidates for refractive index sensors, with sensitivities as high as 450 nm/RIU reported [188]. They have also been shown to allow for the detection of volatile organic compounds [187], could serve as humidity sensors [189], and also present great promise for lab-on-chip integration due to their compact size.

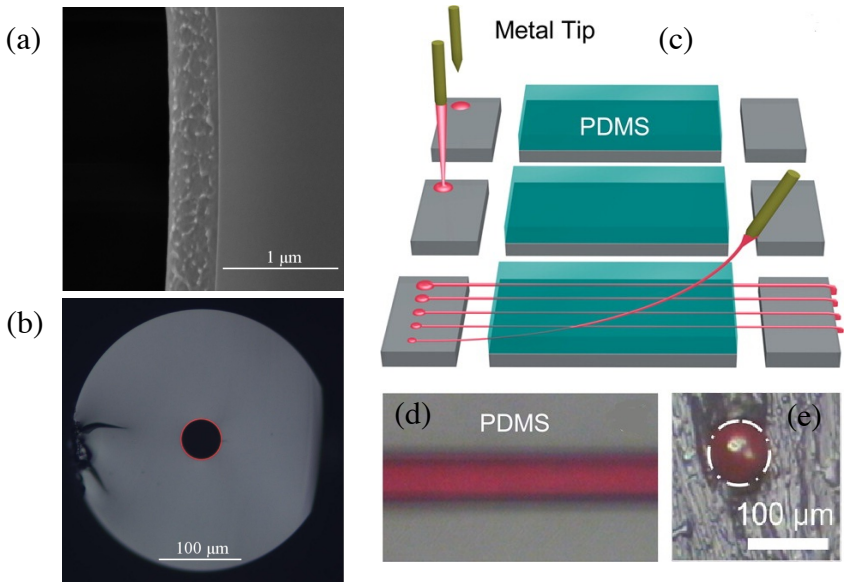

Figure 2.6. (a)(b) Microcapillaries with a dye-doped polymer coating [238] and (c)-(e) Dye-doped polymer fibers [111]. (a), (b) Reproduced with permission from [238]. Copyright (2013), Optical Society of America. (c), (d) and (e) Reproduced with permission from [111]. Copyright (2014), American Chemical Society.

5. Applications

WGMs are inherently suited to optical sensing due to the dependence of the spectral positions of the resonances on both the resonator geometry and the refractive index of the surrounding environment. This has been exploited for sensing pressure, temperature, humidity, electric fields, and also for biological sensing. While passive resonators are intrinsically limited to the tracking of resonance positions for the transduction, fluorescent and lasing WGM resonators can be used for transduction via the associated intensity changes of the modes.

5.1 Physical Sensors

5.1.1 Pressure/Deformation

Pressure/deformation sensing using active microresonators has been well documented. For instance, Himmelhaus *et al.,* incorporated fluorescent dye-doped microspheres into living cells, enabling the measurement of cell stress via the blue shift of the resonances of the microsphere [64]. This application enables biomechanical stress induced during endocytosis and phagocytosis to be analyzed, with applicability to a variety of cells. Martin *et al.,* investigated the effects of pressure on Nd^{3+} doped, barium titanium silicate microspheres, with an average sensitivity of 6.5×10^{-4} GPa^{-1}, which is higher than conventional ruby pressure sensors [191]. Pressure sensing has also been demonstrated with other resonator geometries, for example Chen *et al.*, used optically pumped dye-doped microfibers

encapsulated with PDMS elastomer. Strain-induced refractive index changes from either tensile or compressive forces incurred during bending allows for bidirectional tuning of the WGM resonances, enabling a new range of bend sensing applications [111]. Similarly, Zamanian *et al*., have demonstrated numerical simulations on the effect of shear stress and wall pressure on the resonances of multiple cylindrical microlasers encapsulated in a slab, allowing for simultaneous wall pressure and shear stress measurement [192]. Finally, Manzo *et al*., demonstrated the use of a rhodamine 6G doped dome-shaped polymer WGM microlaser with the incorporation of a membrane, for pressure sensing with a resolution as low as 9 Pa [193].

5.1.2 Temperature

Active whispering gallery microresonators have also found applications in temperature sensing. For example SBN Er^{3+}-Yb^{3+} co-doped glass microspheres were demonstrated for temperature sensing in the range of 290-380 K [148]. Excitation of the microspheres at a wavelength of 1 μm led to a broad upconversion emission in the green, which is modulated by the sphere resonances yielding a resonance shift resolution of 4.7 pm/K with a minimum temperature resolution of around 0.01 K [148]. Furthermore, microbottle lasers fabricated from Er:Yb glass molten onto silica capillaries were demonstrated by Ward *et al*. for the same purpose, with the Er:Yb doped outer glass pumped at a wavelength of 980 nm via a taper, while the WGMs were recorded at ~1535 nm. This structure allows for thermo-optic tuning of the microlaser modes by passing gas through the capillary, exploiting the cooling effect that shifts the WGMs to shorter wavelengths. A tuning of the lasing modes was demonstrated over 70 GHz. The setup can also be used to measure liquid flow rate, and a water flow rate sensitivity of 1 GHz/nL/s was demonstrated. Alternatively, the bottle resonators could be calibrated to allow for gas flow rate or indeed temperature measurements by monitoring the WGM shifts [194]. Although this particular example uses a fiber taper for pumping the gain medium and collecting the lasing WGM signal, one can clearly envision this particular application could be replicated using a free space approach. Phase transitions in dye-doped LC droplets, resulting in a change of the resonator Q-factor can also be exploited for temperature sensing, although they typically exhibit a very small dynamic range of a few degrees around the LC phase transition [161].

5.1.3 Humidity

Labrador-Paez *et al*., have demonstrated a liquid-state WGM resonator that allows for highly sensitive humidity sensing. The microdroplets used consist of glycerol doped with rhodamine 6G. Since glycerol is highly hygroscopic the refractive index and radius of the microdroplets change with humidity, resulting in shifts in the resonance wavelength positions. The sensors allow for a relatively high sensitivity of 10^{-3} per relative humidity percent (% RH^{-1}) [109].

5.2 Biosensing Applications

Since the first demonstration of the capabilities of WGM resonators for label-free biological sensing, measuring either the wavelength shift [4] or Q-factor spoiling [195] upon adsorption of biological molecules onto the resonator surface, significant effort has been invested into improving the sensitivity, selectivity, detection limit and response time of such sensors. While single molecule detection has been achieved with passive resonators providing a gateway for investigating fundamental processes in biology on the nanoscale, single molecule detection is of limited relevance for the vast majority of biosensing applications and especially for medical diagnostics, where biomarkers such as proteins are usually found in concentrations ranging from a few ng/mL [196] to hundreds of μg/mL [197].

5.2.1 Refractive Index Biosensing

Refractive index sensing is still the most common WGM sensing application, in which changes in the refractive index (δn) within the WGM evanescent field induce shifts (δλ) in the resonance wavelengths:

$$\frac{\delta n}{n} = \frac{\delta \lambda}{\lambda} . \qquad (2.4)$$

The wavelength shift induced by adsorption of molecules with excess polarizability (α_{ex}) and a surface density (σ_s) is given by [4],

$$\frac{\delta \lambda}{\lambda} = \frac{\alpha_{ex} \sigma_S}{\varepsilon_0 \left(n_1^2 - n_2^2 \right) R} , \qquad (2.5)$$

where ε_0 is the vacuum permittivity, R is the radius of the resonator, and n_1 and n_2 are the refractive indices of the resonator and the surrounding medium, respectively. The excess polarizability can be approximated from the Clausius-Mossotti equation, in which the polarizability is linearly proportional to the molecular weight. It follows that the sensitivity (S) is strongly dependent on the molecular weight of the molecule to be detected, as is the case for other refractive-index-based sensing techniques.

Here, the sensitivity S depends on the fraction of energy of the WGM contained within the sensing medium [199, 200]. Therefore, increasing the magnitude of the evanescent part of the field through controlling the resonator diameter or the refractive index contrast between the resonator and its surrounding environment, naturally affects the sensitivity [79]. Alternatively, depositing a thin layer of high refractive index material onto the resonator surface can shift the mode field profile in such a way as to enhance S [91]. Depositing a monolayer of QDs onto the surface of polystyrene microspheres has

also been shown to increase the sensitivity [201], but this also reduces the Q-factor. As the magnitude of the evanescent field increases, the Q-factor drops [79], which raises the detection limit [202]. Consequently, an appropriate tradeoff between the sensitivity and the Q-factor needs be made to optimize the sensing performance [79]. Lasing microresonators are highly beneficial in this context, providing a way to significantly increase the Q-factor [22, 42, 43, 48, 68, 96] without affecting S, and thus lowering the detection limit [22, 69]. Another way to improve S is to use coupled resonators, utilizing the Vernier effect in coupled microspheres [203] or microcapillaries, with the latter resulting in a sensitivity above 2510 nm/RIU [204]. One application of the Vernier effect in two polymer microfibers resulted in a twofold increase in the sensitivity compared with the individual resonators [25].

The vast majority of the literature relating to WGM resonators for biosensing applications focuses on characterizing the sensitivity of the proposed device. Table 2.3 provides a non-exhaustive overview canvasing the performance of both active and passive resonators from the literature in terms of the sensitivity, Q-factor and detection limit. Although the detection limit of passive sensing configurations may be lower than that of active ones, the practical advantages of active sensing configurations remains unmatched by passive resonators [42, 64-68, 126, 127, 137].

Beyond simply characterizing a bulk refractive index change, WGM resonators have also been used for detecting various biomolecules. Bioreceptors, including antibodies [205], aptamers [206], and DNA strands [207, 208] have been immobilized onto WGM resonator surfaces. As proof-of-concept demonstrations of active biosensors, the highly specific interaction of streptavidin and biotin/biotinylated proteins has been utilized on a number of devices including, dye-doped polystyrene microspheres [69, 209], dye-doped polymer coated microcapillaries [131], polymer microring resonators [210] and polymeric microgoblets [211]. This approach also forms the basis of more complicated surface functionalization approaches, such as the immobilization of biotinylated proteins or antigens. For example, one novel large-scale functionalization technique involves the deposition of fluorescently-labeled phospholipids and the incorporation of biotinylated ink in the procedure. This work demonstrated that microgoblets can be used as biolasers for the detection of anti-2,4-Dinitrophenol [212]. Other examples of biosensing include polystyrene microspheres embedded with CdSe/ZnS QDs for thrombin detection [76], dye-doped polymer coated microcapillaries for detecting Vitamin D Binding Protein [213], fluorescent microspheres for the detection of unlabeled oligonucleotide targets [208], and the multiplexed quantification of ovarian cancer markers [205]. In terms of reaching the same single-molecule detection capability of passive resonators, a self-referenced and self-heterodyned WGM Raman microlaser was recently demonstrated [214]. This set-up is restricted in its practical application compared with free space interrogated active resonators, due to the precise alignment, and laser frequency stability and locking requirements.

The capability of a sensor to distinguish or eliminate the effects of non-specific binding is critical for sensing within complex biological samples. Successful prevention of non-specific binding has been demonstrated in passive configurations using covalent surface functionalization strategies, notably using polyethylene glycol (PEG) [215], allowing Pasquardini *et al*. to detect thrombin (down to ~ 8 μM) in 10-fold diluted human serum samples [216]. Alternatively, a simpler approach using two active microspheres, with one acting as a floating reference measuring the non-specific binding component, and the second resonator measuring both the non-specific and specific signal has been used for measuring the neutravidin concentration in undiluted human serum [209].

Table 2.3: Examples of refractive index sensitivities for active and passive resonators.

Sensitivity (nm/RIU)	**Q-factor**	**Detection Limit (RIU)**	**Resonator Details (passive/active, dimension, refractive index)**
1.1 (TM) 0.73 (TE)	2.1×10^8 (TM) 1.7×10^8 (TE)	1.5×10^{-3}	Crystalline (birefringent) magnesium fluoride (MgF_2), 2.4 and 5.8 mm microdisks ($n_o = 1.375$, $n_e = 1.387$) [248]
0.5	6×10^7	1.0×10^{-6}	Silica microbubble resonators with diameters 340 μm (n = 1.45) [249]
3	2×10^3	2.6×10^{-2}	Dye-doped polymer coating (1 μm, n = 1.56) inside a 100 μm diameter fused silica capillary [22]*
6.5	3.0×10^4	6.2×10^{-4}	38 μm diameter barium-titanate microsphere (n = 2.43) excited with a tunable diode laser at 633 nm using a dove prism [35]
7.7	4.5×10^4	5.2×10^{-4}†	9 μm diameter Er doped tellurite microsphere (n = 2.03 at 633 nm) [34]
9.8	800 (Type I) 1500 (Type II)	7.2×10^{-3}	Si Q-dot coated silica capillary (Type I: Inner diameter 25 μm and outer diameter 360 μm, Type II: Inner diameter 100 μm and outer diameter 160 μm) [184]
10	1.5×10^3	4.0×10^{-4}†	Si Q-dot coated silica capillary (50 μm Inner diameter, 360 μm outer diameter) [131]
10	1×10^5	5×10^{-4}	Dye-doped 50 μm diameter PMMA microgoblet (n = 1.48) [43]*
20	1.2×10^6	1.0×10^{-6}	Silica (n = 1.45) liquid core ring resonator (100 μm outer diameter, 2-3 μm wall thickness) [250]
30	800	10^{-3}	Dye-doped polymer coating (1 μm, n = 1.56) inside a 50 μm diameter fused silica capillary [238]
33	1.3×10^7	8.7×10^{-6}	50 μm diameter PMMA microgoblet (n = 1.48) [211]
50	7×10^4	8×10^{-5}	10 μm diameter dye-doped polystyrene microsphere [42]*
50	2×10^4	2.6×10^{-5}	Dye-coated 38 μm diameter soda-lime microsphere emitting at 630 nm [221]
100	10^3 §	4×10^{-4}	CdSe/ZnS quantum dot embedded 10 μm diameter polystyrene microspheres (n = 1.59) emitting at 550 nm [76]
100	1700	1×10^{-4}	Si Q-dot coated 30 μm diameter silica (n = 1.45) microsphere [251]
300	8.2×10^3	-	Dye-doped 36 μm diameter PMMA microfiber (n = 1.48) emitting at 600 nm [25]
390	500	1×10^{-4}	Thin wall silica (n = 1.45) capillary (11 μm outer diameter, 0.8 μm wall thickness) [252]
570	1.2×10^5	2.8×10^{-7}	Thin wall silica (n = 1.45) capillary (70 μm outer diameter, 2-3 μm wall thickness) [253]
5930	2.5×10^3 §	2.7×10^{-5}	Coupled optofluidic ring laser (125 μm diameter, n = 1.52) [254]*

* Lasing of the WGM(s) was observed; † Calculated values of detection limit based on the refractive index sensitivity (S) and Q-factor, assuming a wavelength resolution of 4 pm achievable with a high resolution spectrometer; § Calculated values of the Q-factor from the WGM spectrum.

Another advantage of fluorescent or lasing WGM biosensors is their multiplexing capability; especially for medical diagnostics whereby monitoring multiple markers can facilitate better understanding of disease development and diagnosis [217, 218]. Vollmer *et al*.'s remarkable demonstration of multiplexed DNA sensing using passive microspheres, is nevertheless difficult to extend to larger numbers of resonators/biomarkers due to the stringent light coupling requirements [219]. Recently, Genalyte Inc. developed a passive multiplexed silicon photonic chip diagnostic platform using ring resonators with integrated waveguides, capable of detecting up to 32 biological analytes from a single sample [220]. Fluorescent resonators also provide the possibility of realizing highly multiplexed biosensors such as the fluorescent-labeled microspheres used by Huckabay *et al*. [221], or the fluorescent microgoblets developed by Wienhold *et al* [43].

5.2.2 Intensity Based Biosensing

Intensity based sensing provides a novel sensing modality, removing the need to continually monitor and track the precise position of resonances. In this case the sensitivity, limit of detection, and the dynamic range of the sensor can all be redefined in terms of intensity changes [198, 222]. Figure 2.7 shows a comparison between the operating principles of an intensity based and resonant-wavelength shift WGM sensing system. It is clear from Figure 2.7 that in an intensity based system the sensitivity becomes strongly dependent on the Q-factor of the resonator, as higher Q-factors result in sharper resonances allowing smaller variations in intensity to be measured. Intensity-based detection systems have also demonstrated higher sensitivities and lower detection limits compared with wavelength-shift sensing methods, albeit with significantly smaller dynamic ranges [210].

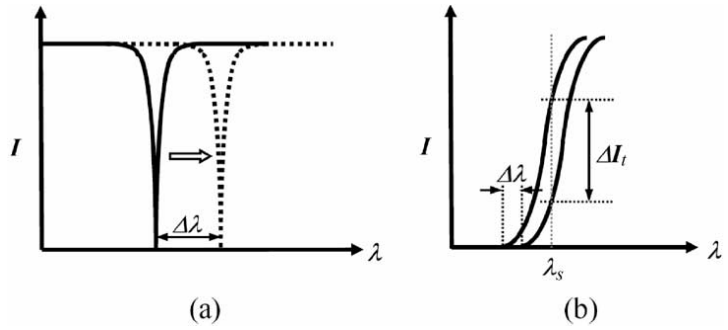

Figure 2.7. Two sensing schemes measuring (a) resonant-wavelength shift and (b) intensity variation. Reproduced with permission from [222]. Copyright (2006), Optical Society of America.

By incorporating biochemical/biological molecules directly into the gain medium and taking advantage of the sensitive nature of the lasing threshold on the resonator parameters, optofluidic biolasers have emerged as a highly effective platform for a range of biosensing applications [155]. Capillary-based

sensors, such as optofluidic ring-resonators or fluorescent-core microcapillaries, are particularly interesting with their ability to blend microfluidics and laser technology together, alleviating complexities involved with sample delivery. For example, Sun *et al*. incorporated DNA samples and probes into the gain medium, which is flown through the channel of an optofluidic ring-resonator, allowing sensitive and selective detection of two different DNA sequences [223].

Alternatively, recent work by Chen *et al*. demonstrated the ability to position the gain medium onto the surface of the resonator, producing an optofluidic laser with a single molecular layer of gain, opening up the possibility for surface-based detection, a feature that is not commonly observed in optofluidic lasing platforms [224].

6. Conclusion and Future Prospects

Despite many emerging sensing applications, the performance gap between passive and active resonators remains significant. Fluorescent-based resonators typically exhibit a lower Q-factor which can constrain the sensor detection limit, despite lasing of the WGMs of such resonators potentially allowing for a slight improvement of both the Q-factor and signal to noise ratio. Nevertheless, there are many avenues worth exploring that could enable the emergence of new hybrid sensing methodologies.

One envisioned approach combines fluorescent resonators with plasmonic effects. While plasmonic nanoparticles have been successfully used to reach single molecule detection [19, 225] and passive resonators have been coated with a metal layer to induce a WGM-like behavior of the plasmonic wave [226], the adaptation of the same methodologies to fluorescent resonator has not yet been investigated. Even more interesting is the prospect of using another plasmonic effect, namely Metal Enhanced Fluorescence (MEF), which is well suited for lasing microresonators. MEF is attributed to the stronger interactions occurring between a fluorophores' excited states and the induced surface plasmon resonances (SPR) in metal particles or films due to the increased electromagnetic field in the proximity of metal [227]. As a result, the radiative fluorescence lifetime could be drastically decreased, resulting in an enhancement of the fluorescence intensity. This phenomenon is obviously of particular interest for fluorescent/lasing-based microresonators, potentially driving down the lasing threshold. However, MEF also has very strict requirements. First, the SPR has to match the excitation wavelength of the gain medium. Most of the noble metals used for their plasmonic properties (Au, Ag) exhibit SPRs in the shorter-wavelength range of the visible spectrum, restricting the gain media that could be used. In addition, MEF requires the gain medium to be positioned a few nanometers above the metal supporting the SPR, in order to produce the maximum enhancement [227]. Therefore, only two options appear to be viable for fluorescent microresonators to benefit from MEF. First, one may coat or incorporate metallic

nanoparticles in fluorescent resonators, similar to what has been achieved with plasmonic epitope [19, 225], although one may question the impact this procedure will have on the Q-factor, since these nanoparticles are likely to behave as scattering centers. Second, depositing micron size resonators onto specifically engineered substrates that can support a long range SPR (LRSPR) [228] may further extend the penetration depth of the plasmonic field, and consequently increase the distance above the metallic coating at which the fluorescence is enhanced.

Enhanced Raman Scattering is another intriguing phenomenon, taking advantage of either the hot spots created by the propagating WGMs at the resonator surface to enhance the Raman effect without the use of metallic nanoparticles (cavity enhanced Raman scattering) [229, 230] or through the addition of nanoparticles inducing scattering at the microresonator surface [231]. Lasing microresonators are of particular interest for exploiting these effects, promising highly sensitive detection modalities. However, these effects require the resonator to exhibit very high Q-factors.

As discussed, simply using the WGM fluorescence intensity for sensing has been widely exploited, relying on the fluorescent/lasing gain medium emission that is varied upon interaction with the analyte to be detected. However, the Q-factor can be affected by binding events occurring at the resonator surface, with the first demonstration of this phenomenon being documented over 14 years ago by Nadeau *et al*. [195] More recently, Hu *et al*. theoretically investigated the resonance broadening induced by dielectric nanoparticles and revealed that a single particle can be detected without resorting to any sensitivity enhancement mechanism or active noise control technique [232]. The same mechanism was experimentally used by Shao *et al*. for the detection of a single virus particle [233]. This novel sensing mechanism holds great promise for lasing resonators, as any Q-factor spoiling should result in an increase of the lasing threshold. Although measuring the lasing threshold could be somehow impractical, one can resort to measuring only the intensity of the lasing modes, assuming that both the gain medium and pump source intensity are stable. This method would not only allow better performance to be achieved but also alleviate practical requirements related to the specialized and expensive equipment used for performing such measurements, potentially paving the way for viable commercial application of WGM-based sensing technologies.

Finally, fluorescent microresonators offer the potential for *in-vivo* sensing. After the first demonstration of intracellular sensing [64] and tagging [65, 66], the concept of free-floating resonators inside blood vessels no longer seems quite as unrealistic, especially with the emergence of flow cytometry [154]. However, for this vision to be realized one would have to use a gain medium in the NIR rather than in the visible spectrum [234], as the latter is strongly absorbed by tissue. Powerful spectral analysis methods for the

determination and characterization of binding events without prior knowledge of the resonance spectra would be required in such setups.

Acknowledgements T. M. Monro acknowledges the support of an Australian Research Council Georgina Sweet Laureate Fellowship. The authors acknowledge the support of the ARC Centre of Excellence in Nanoscale Biophotonics.

References

1. 1. M. Gorodetskii, Y. Demchenko, D. Zaitsev, V. Krutikov, Y. Zolotarevskii and V. Lyaskovskii, Meas. Tech. **12**, 1386-1395 (2015).
2. C. Zou, C. Dong, J. Cui, F. Sun, Y. Yang, X. Wu, Z. Han and G. Guo, Sci. Sin. Phys. Mech. Astron. **42**, 1155 (2012).
3. M. R. Foreman, J. D. Swaim and F. Vollmer, Adv. Opt. Photon. **7**, 168-240 (2015).
4. F. Vollmer, D. Braun, A. Libchaber, M. Khoshsima, I. Teraoka and S. Arnold, Appl. Phys. Lett. **80**, 4057-4059 (2002).
5. A. François, Y. Zhi and A. Meldrum, Photonic Materials for Sensing, Biosensing and Display Devices, Vol. 229 (Springer International Publishing, Cham, 2016), p. 237-288.
6. Z. K. Minev, K. Serniak, I. M. Pop, Z. Leghtas, K. Sliwa, M. Hatridge, L. Frunzio, R. J. Schoelkopf and M. H. Devoret, Phys. Rev. Applied **5**, 044021 (2016).
7. J. Volz, M. Scheucher, C. Junge and A. Rauschenbeutel, Nat. Photon. **8**, 965-970 (2014).
8. W. Song, W. Yang, Q. Chen, Q. Hou and M. Feng, Opt. Express **23**, 13734-13751 (2015).
9. G. D'Aguanno and C. R. Menyuk, Phys. Rev. A **93**, 043820 (2016).
10. I. Breunig, Laser Photon. Rev. **10**, 569-587 (2016).
11. N. Riesen, W. Q. Zhang and T. M. Monro, Opt. Express **24**, 8832-8847 (2016).
12. I. M. White, H. Oveys and X. Fan, Opt. Lett. **31**, 1319-1321 (2006).
13. M. Sumetsky, Y. Dulashko and R. S. Windeler, Opt. Lett. **35**, 1866-1868 (2010).
14. M. Sumetsky, Opt. Lett. **29**, 8-10 (2004).
15. L. Tong, R. R. Gattass, J. B. Ashcom, S. He, J. Lou, M. Shen, I. Maxwell and E. Mazur, Nature **426**, 816-819 (2003).
16. D. K. Armani, T. J. Kippenberg, S. M. Spillane and K. J. Vahala, Nature **421**, 925-928 (2003).
17. C.-Y. Chao and L. J. Guo, Appl. Phys. Lett. **83**, 1527-1529 (2003).
18. S. L. McCall, A. F. J. Levi, R. E. Slusher, S. J. Pearton and R. A. Logan, Appl. Phys. Lett. **60**, 289-291 (1992).
19. M. D. Baaske, M. R. Foreman and F. Vollmer, Nat. Nanotechnol. **9**, 933-939 (2014).

20. A. Chiasera, Y. Dumeige, P. Feron, M. Ferrari, Y. Jestin, G. Nunzi Conti, S. Pelli, S. Soria and G. C. Righini, Laser Photon. Rev. **4**, 457-482 (2010).
21. J. M. Ward, N. Dhasmana and S. N. Chormaic, Eur. Phys. J. Spec. Top. **223**, 1917-1935 (2014).
22. A. François, N. Riesen, K. Gardner, T. M. Monro and A. Meldrum, Opt. Express **24**, 12466-12477 (2016).
23. M. Sumetsky, R. S. Windeler, Y. Dulashko and X. Fan, Opt. Express **15**, 14376-14381 (2007).
24. W. Lee, Y. Sun, H. Li, K. Reddy, M. Sumetsky and X. Fan, Appl. Phys. Lett. **99**, 091102 (2011).
25. V. Duong Ta, R. Chen, L. Ma, Y. Jun Ying and H. Dong Sun, Laser Photon. Rev. **7**, 133-139 (2013).
26. Q. Yang, X. Jiang, X. Guo, Y. Chen and L. Tong, Appl. Phys. Lett. **94**, 101108 (2009).
27. X. Jiang, L. Tong, G. Vienne, X. Guo, A. Tsao, Q. Yang and D. Yang, Appl. Phys. Lett. **88**, 223501 (2006).
28. F. Xu, P. Horak and G. Brambilla, Opt. Express **15**, 7888-7893 (2007).
29. J. Zhu, S. K. Ozdemir, Y.-F. Xiao, L. Li, L. He, D.-R. Chen and L. Yang, Nat. Photon. **4**, 46-49 (2010).
30. J. Su, A. F. Goldberg and B. M. Stoltz, Light. Sci. Appl. **5**, e16001 (2016).
31. H. Chandrahalim and X. Fan, Sci. Rep. **5**, 18310 (2015).
32. R. Henriet, G. Lin, A. Coillet, M. Jacquot, L. Furfaro, L. Larger and Y. K. Chembo, Opt. Lett. **40**, 1567-1570 (2015).
33. S. K. Vanga and A. A. Bettiol, Nucl. Instr. Meth. Phys. Res. **348**, 209-212 (2015).
34. Y. Ruan, K. Boyd, H. Ji, A. François, H. Ebendorff-Heidepriem, J. Munch and T. M. Monro, Opt. Express **22**, 11995-12006 (2014).
35. S. M. Wildgen and R. C. Dunn, Biosensors **5**, 118-130 (2015).
36. X. Liu, S. T. Ha, Q. Zhang, M. de la Mata, C. Magen, J. Arbiol, T. C. Sum and Q. Xiong, ACS Nano. **9**, 687-695 (2015).
37. M. Förtsch, G. Schunk, J. U. Fürst, D. Strekalov, T. Gerrits, M. J. Stevens, F. Sedlmeir, H. G. Schwefel, S. W. Nam and G. Leuchs, Phys. Rev. A **91**, 023812 (2015).
38. J. Pfeifle, A. Coillet, R. Henriet, K. Saleh, P. Schindler, C. Weimann, W. Freude, I. V. Balakireva, L. Larger and C. Koos, Phys. Rev. Lett. **114**, 093902 (2015).
39. I. S. Grudinin, A. B. Matsko and L. Maleki, Opt. Express **15**, 3390-3395 (2007).
40. V. S. Ilchenko, A. A. Savchenkov, A. B. Matsko and L. Maleki, Phys. Rev. Lett. **92**, 043903 (2004).

41. I. S. Grudinin, A. B. Matsko, A. A. Savchenkov, D. Strekalov, V. S. Ilchenko and L. Maleki, Opt. Commun. **265**, 33-38 (2006).
42. A. François, N. Riesen, H. Ji, S. Afshar V and T. M. Monro, Appl. Phys. Lett. **106**, 031104 (2015).
43. T. Wienhold, S. Kraemmer, S. F. Wondimu, T. Siegle, U. Bog, U. Weinzierl, S. Schmidt, H. Becker, H. Kalt, T. Mappes, S. Koeber and C. Koos, Lab Chip **15**, 3800-3806 (2015).
44. J. Knight, G. Cheung, F. Jacques and T. Birks, Opt. Lett. **22**, 1129-1131 (1997).
45. Y.-L. Pan and R. K. Chang, Appl. Phys. Lett. **82**, 487-489 (2003).
46. V. B. Braginsky, M. L. Gorodetsky and V. S. Ilchenko, Phys. Lett. A **137**, 393-397 (1989).
47. K. A. Knapper, K. D. Heylman, E. H. Horak and R. H. Goldsmith, Adv. Mater. **28**, 2945-50 (2016).
48. M. M. Karow, P. Munnelly, T. Heindel, M. Kamp, S. Höfling, C. Schneider and S. Reitzenstein, Appl. Phys. Lett. **108**, 081110 (2016).
49. M. Agarwal and I. Teraoka, Anal. Chem. **87**, 10600-10604 (2015).
50. L. Shi, T. Zhu, D. Huang, M. Liu, M. Deng and W. Huang, Opt. Lett. **40**, 3770-3 (2015).
51. Z. Ballard, M. D. Baaske and F. Vollmer, Sensors **15**, 8968-8980 (2015).
52. L. Shao, L. Wang, W. Xiong, X.-F. Jiang, Q.-F. Yang and Y.-F. Xiao, Appl. Phys. Lett. **103**, 121102 (2013).
53. J. Zhu, S. Özdemir, H. Yilmaz, B. Peng, M. Dong, M. Tomes, T. Carmon and L. Yang, Sci. Rep. **4**, 6396 (2014).
54. R. Zullo, A. Giorgini, S. Avino, P. Malara, P. De Natale and G. Gagliardi, Proc. SPIE **9727**, 972713-972713 (2016).
55. C. G. B. Garrett, W. Kaiser and W. L. Bond, Phys. Rev. **124**, 1807-1809 (1961).
56. H. Benisty, C. Weisbuch, J.-M. Gérard, R. Houdré and J. Rarity, in: Lecture Notes in Physics, Berlin Springer Verlag, 1999.
57. T. Baba and D. Sano, IEEE J. Sel. Top. Quantum Electron. **9**, 1340-1346 (2003).
58. N. Riesen, T. Reynolds, A. François, M. R. Henderson and T. M. Monro, Opt. Express **23**, 28896-28904 (2015).
59. S. Afshar V, M. R. Henderson, A. D. Greentree, B. C. Gibson and T. M. Monro, Opt. Express **22**, 11301-11311 (2014).
60. M. Sumetsky, Opt. Express **13**, 6354-6375 (2005).
61. V. R. Dantham, S. Holler, C. Barbre, D. Keng, V. Kolchenko and S. Arnold, Nano Lett. **13**, 3347-3351 (2013).
62. S. I. Shopova, R. Rajmangal, S. Holler and S. Arnold, Appl. Phys. Lett. **98**, 243104 (2011).

63. M. Baaske and F. Vollmer, ChemPhysChem **13**, 427-436 (2012).
64. M. Himmelhaus and A. François, Biosens. Bioelectron. **25**, 418-427 (2009).
65. M. Schubert, A. Steude, P. Liehm, N. M. Kronenberg, M. Karl, E. C. Campbell, S. J. Powis and M. C. Gather, Nano Lett. **15**, 5647-5652 (2015).
66. M. Humar and S. H. Yun, Nat. Photon. **9**, 572-576 (2015).
67. J.-R. Carrier, M. Boissinot and C. Nì. Allen, Am. J. Phys. **82**, 510-520 (2014).
68. L.-J. Chen, L.-L. Gong, Y.-L. Lin, X.-Y. Jin, H.-Y. Li, S.-S. Li, K.-J. Che, Z.-P. Cai and C. J. Yang, Lab Chip **16**, 1206-1213 (2016).
69. A. François, T. Reynolds and T. M. Monro, Sensors **15**, 1168-1181 (2015).
70. A. N. Oraevsky, Quant. Electron. **32**, 377-400 (2002).
71. K. J. Vahala, Nature **424**, 839-846 (2003).
72. S. Arnold, S. Holler and X. Fan, Nano-Structures for Optics and Photonics, Vol. (Springer, 2015), p. 309-322.
73. J. H. Wade and R. C. Bailey, Annu. Rev. Anal. Chem. **9**, 1-25 (2016).
74. F. Vollmer and S. Arnold, Nat. Meth. **5**, 591-596 (2008).
75. Y. Sun and X. Fan, Anal. Bioanal. Chem. **399**, 205-211 (2011).
76. H. T. Beier, G. L. Coté and K. E. Meissner, Ann. Biomed. Eng. **37**, 1974-1983 (2009).
77. H. Chew, Phys. Rev. A **38**, 3410 (1988).
78. H. Chew, J. Chem. Phys. **87**, 1355 (1987).
79. T. Reynolds, M. Henderson, A. François, N. Riesen, J. Hall, S. Afshar, S. Nicholls and T. Monro, Opt. Express **23**, 17067-17076 (2015).
80. Y. Yang, J. Ward and S. N. Chormaic, Opt. Express **22**, 6881-6898 (2014).
81. J. M. Hall, V. S. Afshar, M. R. Henderson, A. François, T. Reynolds, N. Riesen and T. M. Monro, Opt. Express **23**, 9924-37 (2015).
82. T. C. Preston and J. P. Reid, J. Opt. Soc. Am. A. Opt. Image. Sci. Vis. **32**, 2210-7 (2015).
83. N. L. Aung, L. Ge, O. Malik, H. E. Türeci and C. F. Gmachl, Appl. Phys. Lett. **107**, 151106 (2015).
84. X.-P. Zhan, J.-F. Ku, Y.-X. Xu, X.-L. Zhang, J. Zhao, W. Fang, H.-L. Xu and H.-B. Sun, IEEE Photon. Technol. Lett. **27**, 311-314 (2015).
85. Q. J. Wang, C. Yan, N. Yu, J. Unterhinninghofen, J. Wiersig, C. Pflügl, L. Diehl, T. Edamura, M. Yamanishi, H. Kan and F. Capasso, Proc. Natl. Acad. Sci. U.S.A. **107**, 22407-22412 (2010).
86. J. U. Nöckel, A. D. Stone and R. K. Chang, Opt. Lett. **19**, 1693-1695 (1994).

87. C. Gmachl, F. Capasso, E. E. Narimanov, J. U. Nöckel, A. D. Stone, J. Faist, D. L. Sivco and A. Y. Cho, Science **280**, 1556-1564 (1998).
88. H. Chew, M. Kerker and P. J. McNulty, J. Opt. Soc. Am. **66**, 440-444 (1976).
89. W. Liang, Y. Xu, Y. Huang, A. Yariv, J. G. Fleming and S.-Y. Lin, Opt. Express **12**, 657-669 (2004).
90. W. Yang, Appl. Opt. **42**, 1710-1720 (2003).
91. I. Teraoka and S. Arnold, J. Opt. Soc. Am. B **23**, 1434-1441 (2006).
92. S. K. Biswas and S. Kumar, Opt. Express **23**, 26738-26753 (2015).
93. Q. Lu, S. Liu, X. Wu, L. Liu and L. Xu, Opt. Lett. **41**, 1736-1739 (2016).
94. M. Li, X. Wu, L. Liu and L. Xu, Opt. Express **21**, 16908-16913 (2013).
95. Y. Ding, H. Fan, X. Zhang, X. Jiang and M. Xiao, Opt. Commun. (2016).
96. S. Yakunin, L. Protesescu, F. Krieg, M. I. Bodnarchuk, G. Nedelcu, M. Humer, G. De Luca, M. Fiebig, W. Heiss and M. V. Kovalenko, Nat. Commun. **6**, 8056 (2015).
97. H. Fan, X. Jiang, Y. Ding and M. Xiao, Sci. China Phys. Mech. **58**, 1-5 (2015).
98. E. I. Smotrova and A. I. Nosich, Opt. Quant. Electron. **36**, 213-221 (2004).
99. S.-W. Chang, The Current Trends of Optics and Photonics, Vol. 129 (Springer Netherlands, Dordrecht, 2015), p. 361-376.
100. Y. Huang and Y. Y. Lu, J. Mod. Opt. **61**, 390-396 (2014).
101. S. Spillane, T. Kippenberg and K. Vahala, Nature **415**, 621-623 (2002).
102. V. Sandoghdar, F. Treussart, J. Hare, V. Lefèvre-Seguin, J. M. Raimond and S. Haroche, Phys. Rev. A **54**, 1777-1780 (1996).
103. D. J. Gargas, M. C. Moore, A. Ni, S.-W. Chang, Z. Zhang, S.-L. Chuang and P. Yang, ACS Nano. **4**, 3270-3276 (2010).
104. M. Gupta, D. K. Maity, S. K. Nayak and A. K. Ray, J. Photochem. Photobiol. A **300**, 15-21 (2015).
105. O. Redy-Keisar, K. Huth, U. Vogel, B. Lepenies, P. H. Seeberger, R. Haag and D. Shabat, Org. Biomol. Chem. **13**, 4727-4732 (2015).
106. G. Niu, W. Liu, J. Wu, B. Zhou, J. Chen, H. Zhang, J. Ge, Y. Wang, H. Xu and P. Wang, J. Org. Chem. **80**, 3170-3175 (2015).
107. W. H. Organization, IARC Monograph on the Evaluation of Carcinogenic Risk to Humans **99**, 55-67 (2010).
108. Y.-L. Sun, Z.-S. Hou, S.-M. Sun, B.-Y. Zheng, J.-F. Ku, W.-F. Dong, Q.-D. Chen and H.-B. Sun, Sci. Rep. **5**, 12852 (2015).

109. L. Labrador-Paez, K. Soler-Carracedo, M. Hernandez-Rodriguez, I. R. Martin, T. Carmon and L. L. Martin, arXiv preprint arXiv:1602.03322 (2016).

110. C. Linslal, M. Kailasnath, S. Mathew, T. Nideep, P. Radhakrishnan, V. Nampoori and C. Vallabhan, Opt. Lett. **41**, 551-554 (2016).

111. R. Chen, V. D. Ta and H. Sun, ACS Photonics **1**, 11-16 (2014).

112. Y. S. L. V. Narayana, D. Venkatakrishnarao, A. Biswas, M. A. Mohiddon, N. Viswanathan and R. Chandrasekar, ACS Appl. Mater. Interfaces **8**, 952-958 (2016).

113. X. Lin, Y. Fang, L. Zhu, J. Zhang, G. Huang, J. Wang and Y. Mei, Adv. Opt. Mater. **4**, 936-942 (2016).

114. S. Lacey, I. M. White, Y. Sun, S. I. Shopova, J. M. Cupps, P. Zhang and X. Fan, Opt. Express **15**, 15523-15530 (2007).

115. V. Marx, Nat. Meth. **12**, 187-190 (2015).

116. L. Song, E. J. Hennik, I. T. Young and H. J. Tanke, Biophys. J. **68**, 2588-2600 (1995).

117. A. J. Kuehne and M. C. Gather, Chem. Rev. (2016).

118. S. Rochat and T. M. Swager, ACS Appl. Mater. Interfaces **5**, 4488-502 (2013).

119. R. M. Ma, S. Ota, Y. Li, S. Yang and X. Zhang, Nat. Nanotechnol. **9**, 600-4 (2014).

120. K. Tabata, D. Braam, S. Kushida, L. Tong, J. Kuwabara, T. Kanbara, A. Beckel, A. Lorke and Y. Yamamoto, Sci. Rep. **4**, 5902 (2014).

121. S. Kushida, D. Braam, T. D. Dao, H. Saito, K. Shibasaki, S. Ishii, T. Nagao, A. Saeki, J. Kuwabara, T. Kanbara, M. Kijima, A. Lorke and Y. Yamamoto, ACS Nano. **10**, 5543-5549 (2016).

122. A. J. Lam, F. St-Pierre, Y. Gong, J. D. Marshall, P. J. Cranfill, M. A. Baird, M. R. McKeown, J. Wiedenmann, M. W. Davidson, M. J. Schnitzer, R. Y. Tsien and M. Z. Lin, Nat. Meth. **9**, 1005-1012 (2012).

123. L. Cerdan, E. Enciso, V. Martin, J. Banuelos, I. Lopez-Arbeloa, A. Costela and I. Garcia-Moreno, Nat. Photon. **6**, 621-626 (2012).

124. M. Berggren, A. Dodabalapur, R. E. Slusher and Z. Bao, Nature **389**, 466-469 (1997).

125. M. C. Gather and S. H. Yun, Nat. Photon. **5**, 406-410 (2011).

126. A. Jonas, M. Aas, Y. Karadag, S. Manioglu, S. Anand, D. McGloin, H. Bayraktar and A. Kiraz, Lab Chip **14**, 3093-3100 (2014).

127. Y.-C. Chen, Q. Chen and X. Fan, Lab Chip **16**, 2228-2235 (2016).

128. A. Kiraz, Q. Chen and X. Fan, ACS Photonics **2**, 707-713 (2015).

129. C.-S. Wu, M. K. Khaing Oo and X. Fan, ACS Nano. **4**, 5897-5904 (2010).

130. Y. Zhi, J. Valenta and A. Meldrum, J. Opt. Soc. Am. B **30**, 3079-3085 (2013).

131. S. Lane, P. West, A. François and A. Meldrum, Opt. Express **23**, 2577-2590 (2015).

132. X. Yang and B. Li, ACS Macro Lett. **3**, 1266-1270 (2014).

133. R. S. Moirangthem and A. Erbe, Appl. Phys. Lett. **103**, 051108 (2013).

134. C. Czekalla, C. Sturm, R. Schmidt-Grund, B. Cao, M. Lorenz and M. Grundmann, Appl. Phys. Lett. **92**, 241102 (2008).

135. A. Paunoiu, R. S. Moirangthem and A. Erbe, Phys. Status Solidi RRL **9**, 241-244 (2015).

136. M. V. Maximov, N. V. Kryzhanovskaya, A. M. Nadtochiy, E. I. Moiseev, I. I. Shostak, A. A. Bogdanov, Z. F. Sadrieva, A. E. Zhukov, A. A. Lipovskii and D. V. Karpov, Nanoscale Res. Lett. **9**, 1-7 (2014).

137. E. Stock, F. Albert, C. Hopfmann, M. Lermer, C. Schneider, S. Höfling, A. Forchel, M. Kamp and S. Reitzenstein, Adv. Mater. **25**, 707-710 (2013).

138. S. Shopova, G. Farca, A. Rosenberger, W. Wickramanayake and N. Kotov, Appl. Phys. Lett. **85**, 6101-6103 (2004).

139. W. K. Bae, Y.-S. Park, J. Lim, D. Lee, L. A. Padilha, H. McDaniel, I. Robel, C. Lee, J. M. Pietryga and V. I. Klimov, Nat. Commun. **4**, 2661 (2013).

140. V. I. Klimov, A. A. Mikhailovsky, D. W. McBranch, C. A. Leatherdale and M. G. Bawendi, Science **287**, 1011-1013 (2000).

141. C. Motta, F. El-Mellouhi, S. Kais, N. Tabet, F. Alharbi and S. Sanvito, Nat. Commun. **6**, 7026 (2015).

142. Q. Zhang, R. Su, X. Liu, J. Xing, T. C. Sum and Q. Xiong, Adv. Funct. Mater. **26**, 6238-6245 (2016).

143. K. Wang, S. Sun, C. Zhang, W. Sun, Z. Gu, S. Xiao and Q. Song, arXiv preprint arXiv:1606.07542 (2016).

144. L. Collot, V. Lefevre-Seguin, M. Brune, J. Raimond and S. Haroche, EPL **23**, 327 (1993).

145. D. Ristić, S. Berneschi, M. Camerini, D. Farnesi, S. Pelli, C. Trono, A. Chiappini, A. Chiasera, M. Ferrari and A. Lukowiak, JOL **170**, 755-760 (2016).

146. Y. Deng, R. K. Jain and M. Hossein-Zadeh, Opt. Lett. **39**, 4458-4461 (2014).

147. T. Kishi, T. Kumagai, S. Shibuya, F. Prudenzano, T. Yano and S. Shibata, Opt. Express **23**, 20629-20635 (2015).

148. C. Pérez-Rodríguez, L. Labrador-Páez, I. R. Martín and S. Ríos, Laser. Phys. Lett. **12**, 046003 (2015).

149. S. Mehrabani and A. M. Armani, Opt. Lett. **38**, 4346-4349 (2013).

150. T. Lu, L. Yang, R. V. A. van Loon, A. Polman and K. J. Vahala, Opt. Lett. **34**, 482-484 (2009).

151. Q. Li, Y. Huang, Y. Lin, J. Wu, J. Huang and T. Wu, Opt. Commun. **356**, 368-372 (2015).

152. V. Lefevre-Seguin, Opt. Mater. **11**, 153-165 (1999).

153. A. Pal, S. Y. Chen, R. Sen, T. Sun and K. Grattan, Laser. Phys. Lett. **10**, 085101 (2013).

154. R. Lessard, O. Rousseau-Cyr, M. Charlebois, C. Riviere, O. Mermut and C. N. Allen, SPIE LASE **8600**, 86001Q-86001Q-8 (2013).

155. X. Fan and S.-H. Yun, Nat. Meth. **11**, 141-147 (2014).

156. A. Ashkin and J. M. Dziedzic, Phys. Rev. Lett. **38**, 1351-1354 (1977).

157. S. Uetake, R. S. D. Sihombing and K. Hakuta, Opt. Lett. **27**, 421-423 (2002).

158. S. K. Y. Tang, R. Derda, Q. Quan, M. Lončar and G. M. Whitesides, Opt. Express **19**, 2204-2215 (2011).

159. S. Anand, M. Eryürek, Y. Karadag, A. Erten, A. Serpengüzel, A. Jonáš and A. Kiraz, J. Opt. Soc. Am. B **33**, 1349-1354 (2016).

160. I. Muševič, Liq. Cryst. Rev. **4**, 1-34 (2016).

161. T. A. Kumar, M. A. Mohiddon, N. Dutta, N. K. Viswanathan and S. Dhara, Appl. Phys. Lett. **106**, 051101 (2015).

162. V. D. Ta, R. Chen and H. D. Sun, Sci. Rep. **3**, 1362 (2013).

163. S. Yang, Y. Wang, R. Chen, T. He, H. V. Demir and H. Sun, Sci. Rep. **6**, 27200 (2016).

164. A. B. Petermann, A. Varkentin, B. Roth, U. Morgner and M. Meinhardt-Wollweber, Opt. Express **24**, 6052-6062 (2016).

165. C. Wei, M. Gao, F. Hu, J. Yao and Y. S. Zhao, Adv. Opt. Mater. 1009-1014 (2016).

166. M. Himmelhaus, Optik & Photonik **11**, 43-47 (2016).

167. S. Kushida, D. Braam, C. Pan, T. D. Dao, K. Tabata, K. Sugiyasu, M. Takeuchi, S. Ishii, T. Nagao, A. Lorke and Y. Yamamoto, Macromolecules **48**, 3928-3933 (2015).

168. P. G. Schiro and A. S. Kwok, Opt. Express **12**, 2857-2863 (2004).

169. H. Li, S. Hao, L. Qiang, J. Li and Y. Zhang, Appl. Phys. Lett. **102**, 231908 (2013).

170. Kosma, G. Zito, K. Schuster and S. Pissadakis, Opt. Lett. **38**, 1301-1303 (2013).

171. Y. Liu, M. Luo, Z. Wang, Z. Li, W.-Y. Zhou, J. Guo, W. Huang and X. Liu, J. Lightwave Technol. **PP**, (2016).

172. A. François, K. J. Rowland, V. S. Afshar, M. R. Henderson and T. M. Monro, Opt. Express **21**, 22566-22577 (2013).

173. L. Martín, D. Navarro-Urrios, F. Ferrarese-Lupi, C. Pérez-Rodríguez, I. Martín, J. Montserrat, C. Domínguez, B. Garrido and N. Capuj, Laser Phys. **23**, 075801 (2013).

174. T. Kumagai, T. Kishi and T. Yano, J. Appl. Phys. **117**, 113104 (2015).

175. A. K. Bhowmik, Appl. Opt. **39**, 3071-3075 (2000).

176. B. Gayral, J. M. Gérard, A. Lemaître, C. Dupuis, L. Manin and J. L. Pelouard, Appl. Phys. Lett. **75**, 1908-1910 (1999).

177. A. L. Washburn, L. C. Gunn and R. C. Bailey, Anal. Chem. **81**, 9499-9506 (2009).

178. M. Ghulinyan, A. Pitanti, G. Pucker and L. Pavesi, Opt. Express **17**, 9434-9441 (2009).

179. A. M. Flatae, M. Burresi, H. Zeng, S. Nocentini, S. Wiegele, C. Parmeggiani, H. Kalt and D. Wiersma, Light. Sci. Appl. **4**, 282 (2015).

180. V. N. Astratov, Photonic Microresonator Research and Applications, Vol. 156 (Springer, 2010), p. 423-457.

181. M. Li, N. Zhang, K. Wang, J. Li, S. Xiao and Q. Song, Sci. Rep. **5**, (2015).

182. L. X. Zou, Y. Z. Huang, X. M. Lv, X. W. Ma, J. L. Xiao, Y. De Yang and Y. Du, Electron. Lett. **51**, 1442-1443 (2015).

183. H. Chandrahalim, S. C. Rand and X. Fan, Sci. Rep. **6**, 32668 (2016).

184. C. P. K. Manchee, V. Zamora, J. W. Silverstone, J. G. C. Veinot and A. Meldrum, Opt. Express **19**, 21540-21551 (2011).

185. S. Lane, J. Chan, T. Thiessen and A. Meldrum, Sens. Actuator B-Chem. **190**, 752-759 (2014).

186. O. G. Schmidt and K. Eberl, Nature **410**, 168-168 (2001).

187. C. Vervacke, C. C. Bof Bufon, D. J. Thurmer and O. G. Schmidt, RSC Adv. **4**, 9723-9729 (2014).

188. G. Huang, V. A. Bolaños Quiñones, F. Ding, S. Kiravittaya, Y. Mei and O. G. Schmidt, ACS Nano. **4**, 3123-3130 (2010).

189. J. Zhang, J. Zhong, Y. F. Fang, J. Wang, G. S. Huang, X. G. Cui and Y. F. Mei, Nanoscale **6**, 13646-13650 (2014).

190. S. Tang, Y. Fang, Z. Liu, L. Zhou and Y. Mei, Lab Chip **16**, 182-187 (2016).

191. L. Martin, S. León-Luis, C. Pérez-Rodríguez, I. Martín, U. Rodríguez-Mendoza and V. Lavín, J. Opt. Soc. Am. B **30**, 3254-3259 (2013).

192. A. H. Zamanian and T. Ioppolo, Appl. Opt. **54**, 7124-7130 (2015).

193. M. Manzo and T. Ioppolo, Opt. Lett. **40**, 2257-2260 (2015).

194. J. M. Ward, Y. Yang and S. N. Chormaic, arXiv preprint arXiv:1601.05493 (2016).

195. J. L. Nadeau, V. S. Iltchenko, D. Kossakovski, G. H. Bearman and L. Maleki, Proc. SPIE **4629**, 172-180 (2002).

196. J. Hernández and I. M. Thompson, Cancer **101**, 894-904 (2004).

197. K. R. Kozak, F. Su, J. P. Whitelegge, K. Faull, S. Reddy and R. Farias-Eisner, Proteomics **5**, 4589-4596 (2005).

198. X. Zhou, L. Zhang and W. Pang, Opt. Express **24**, 18197-18208 (2016).

199. S. Arnold, M. Khoshsima, I. Teraoka, S. Holler and F. Vollmer, Opt. Lett. **28**, 272-274 (2003).

200. H. Zhu, I. M. White, J. D. Suter, P. S. Dale and X. Fan, Opt. Express **15**, 9139-9146 (2007).

201. H. T. Beier, G. L. Coté and K. E. Meissner, J. Opt. Soc. Am. B **27**, 536-543 (2010).

202. I. M. White and X. Fan, Opt. Express **16**, 1020-1028 (2008).

203. S. V. Boriskina, J. Opt. Soc. Am. B **23**, 1565-1573 (2006).

204. L. Ren, X. Wu, M. Li, X. Zhang, L. Liu and L. Xu, Opt. Lett. **37**, 3873-3875 (2012).

205. H. A. Huckabay, S. M. Wildgen and R. C. Dunn, Biosens. Bioelectron. **45**, 223-229 (2013).

206. G. Nunzi Conti, S. Berneschi and S. Soria, Biosensors **6**, 28 (2016).

207. F. Vollmer and L. Yang, Nanophotonics **1**, 267-291 (2012).

208. E. Nuhiji and P. Mulvaney, Small **3**, 1408-1414 (2007).

209. T. Reynolds, A. François, N. Riesen, M. E. Turvey, S. J. Nicholls, P. Hoffmann and T. M. Monro, Anal. Chem. **88**, 4036-4040 (2016).

210. C.-Y. Chao, W. Fung and L. J. Guo, IEEE J. Sel. Top. Quantum Electron. **12**, 134-142 (2006).

211. T. Beck, M. Mai, T. Grossmann, T. Wienhold, M. Hauser, T. Mappes and H. Kalt, Appl. Phys. Lett. **102**, 121108 (2013).

212. U. Bog, F. Brinkmann, H. Kalt, C. Koos, T. Mappes, M. Hirtz, H. Fuchs and S. Köber, Small **10**, 3863-3868 (2014).

213. J. Chan, T. Thiessen, S. Lane, P. West, K. Gardner, A. François and A. Meldrum, IEEE Sens. J. **15**, 3467-3474 (2015).

214. Ş. K. Özdemir, J. Zhu, X. Yang, B. Peng, H. Yilmaz, L. He, F. Monifi, S. H. Huang, G. L. Long and L. Yang, Proc. Natl. Acad. Sci. U.S.A. **111**, 3836-3844 (2014).

215. F. Wang, M. Anderson, M. T. Bernards and H. K. Hunt, Sensors **15**, 18040-18060 (2015).

216. L. Pasquardini, S. Berneschi, A. Barucci, F. Cosi, R. Dallapiccola, M. Insinna, L. Lunelli, G. N. Conti, C. Pederzolli and S. Salvadori, J. Biophotonics. **6**, 178-187 (2013).

217. S. Spindel and K. E. Sapsford, Sensors **14**, 22313-22341 (2014).

218. J. M. Humphries, M. A. Penno, F. Weiland, M. Klingler-Hoffmann, A. Zuber, A. Boussioutas, M. Ernst and P. Hoffmann, Biochim. Biophys. Acta **1844**, 1051-1058 (2014).

219. F. Vollmer, S. Arnold, D. Braun, I. Teraoka and A. Libchaber, Biophys. J. **85**, 1974-1979 (2003).

220. I. A. Estrada, R. W. Burlingame, A. P. Wang, K. Chawla, T. Grove, J. Wang, S. O. Southern, M. Iqbal, L. C. Gunn and M. A. Gleeson, in: Advances in Global Health through Sensing Technologies 2015, Baltimore, Maryland, USA, 2015.

221. H. A. Huckabay and R. C. Dunn, Sens. Actuator B-Chem. **160**, 1262-1267 (2011).

222. C.-Y. Chao and L. J. Guo, J. Lightwave Technol. **24**, 1395-1402 (2006).

223. Y. Sun and X. Fan, Angew. Chem. Int. Ed. **51**, 1236-1239 (2012).

224. Q. Chen, M. Ritt, S. Sivaramakrishnan, Y. Sun and X. Fan, Lab Chip **14**, 4590-4595 (2014).

225. F. Wu, Y. Wu, Z. Niu and F. Vollmer, Sensors **16**, 1197 (2016).

226. B. Min, E. Ostby, V. Sorger, E. Ulin-Avila, L. Yang, X. Zhang and K. Vahala, Nature **457**, 455-458 (2009).

227. C. D. Geddes, Metal-enhanced fluorescence, Vol. (John Wiley & Sons, 2010), p.

228. C.-J. Huang, J. Dostalek, A. Sessitsch and W. Knoll, Anal. Chem. **83**, 674-677 (2011).

229. L. K. Ausman and G. C. Schatz, J. Chem. Phys **129**, 054704 (2008).

230. I. M. White, H. Oveys and X. Fan, Spectroscopy **21**, 36-42 (2006).

231. R.-S. Liu, W.-L. Jin, X.-C. Yu, Y.-C. Liu and Y.-F. Xiao, Phys. Rev. A **91**, 043836 (2015).

232. Y. Hu, L. Shao, S. Arnold, Y.-C. Liu, C.-Y. Ma and Y.-F. Xiao, Phys. Rev. A **90**, 043847 (2014).

233. L. Shao, X. F. Jiang, X. C. Yu, B. B. Li, W. R. Clements, F. Vollmer, W. Wang, Y. F. Xiao and Q. Gong, Adv. Mater. **25**, 5616-5620 (2013).

234. Y.-C. Chen, Q. Chen and X. Fan, Optica **3**, 809-815 (2016).

235. S. Yang, Y. Wang, Y. Gao, T. He, R. Chen, H. V. Demir and H. Sun, Appl. Phys. Lett. **107**, 221103 (2015).

236. M. Iqbal, R. W. Burlingame, R. Romero, A. Wang, T. Grove and M. A. Gleeson, Label-Free Biosensor Methods in Drug Discovery, Vol. (Spring New York 2015), p. 133-153.

237. M. Saito, H. Shimatani and H. Naruhashi, Opt. Express **16**, 11915-11919 (2008).

238. K. J. Rowland, A. François, P. Hoffmann and T. M. Monro, Opt. Express **21**, 11492-11505 (2013).

239. M. Humar, M. C. Gather and S.-H. Yun, Opt. Express **23**, 27865-27879 (2015).

240. D. Venkatakrishnarao and R. Chandrasekar, Adv. Opt. Mater. **4**, 112-119 (2016).

241. J. Li, Y. Lin, J. Lu, C. Xu, Y. Wang, Z. Shi and J. Dai, ACS Nano. **9**, 6794-6800 (2015).

242. K. Okazaki, T. Shimogaki, K. Fusazaki, M. Higashihata, D. Nakamura, N. Koshizaki and T. Okada, Appl. Phys. Lett. **101**, 211105 (2012).

243. S.-H. Gong, S.-M. Ko, M.-H. Jang and Y.-H. Cho, Nano Lett. **15**, 4517-4524 (2015).

244. Y. Wang, K. S. Leck, V. D. Ta, R. Chen, V. Nalla, Y. Gao, T. He, H. V. Demir and H. Sun, Adv. Mater. **27**, 169-175 (2015).

245. S. W. Eaton, M. Lai, N. A. Gibson, A. B. Wong, L. Dou, J. Ma, L.-W. Wang, S. R. Leone and P. Yang, Proc. Natl. Acad. Sci. U.S.A. **113**, 1993-1998 (2016).

246. Q. Liao, K. Hu, H. Zhang, X. Wang, J. Yao and H. Fu, Adv. Mater. **27**, 3405-3410 (2015).

247. X.-F. Liu, F. Lei, M. Gao, X. Yang, C. Wang, Ş. K. Özdemir, L. Yang and G.-L. Long, Opt. Express **24**, 9550-9560 (2016).

248. F. Sedlmeir, R. Zeltner, G. Leuchs and H. G. Schwefel, Opt. Express **22**, 30934-30942 (2014).

249. S. Berneschi, D. Farnesi, F. Cosi, G. N. Conti, S. Pelli, G. Righini and S. Soria, Opt. Lett. **36**, 3521-3523 (2011).

250. H. Zhu, I. M. White, J. D. Suter, M. Zourob and X. Fan, Anal. Chem. **79**, 930-937 (2007).

251. Y. Zhi, C. Manchee, J. Silverstone, Z. Zhang and A. Meldrum, Plasmonics **8**, 71-78 (2013).

252. V. Zamora, A. DÝez, M. V. AndrÚs and B. Gimeno, Opt. Express **15**, 12011-12016 (2007).

253. H. Li and X. Fan, Appl. Phys. Lett. **97**, 011105 (2010).

254. X. Zhang, L. Ren, X. Wu, H. Li, L. Liu and L. Xu, Opt. Express **19**, 22242-22247 (2011).

Chapter 3

Optimizing Resonator Design

3.1 Optimizing Resonator Design for Fluorescence Based Whispering Gallery Mode Biosensing

P2. T. Reynolds, M. R. Henderson, A. François, J. M. M. Hall, N. Riesen, S. Afshar V., S. J. Nicholls and T. M. Monro, "Optimization of whispering gallery resonator design for biosensing applications," Optics Express, 23 (13), 17067-17076, 2015.

3.1.1 Publication Overview

The selection of the ideal resonator for conducting WGM biosensing requires considerations of many aspects such as the biocompatibility, availability, cost, fabrication requirements and importantly the resonators sensing performance. As discussed previously, two of the key metrics for assessing sensing performance are the Q-factor and refractive index sensitivity, both of which can be directly obtained from the WGM spectrum. Ideally, the resonator of choice should have a high Q-factor, for increased resolution, as well as high refractive index sensitivity, to allow smaller changes in refractive index to be observed. However, a compromise must be made between these two connected parameters. Accordingly, to allow the comparisons of the sensing performance between two resonators to take place, a simple figure of merit is defined as the product of these two parameters. Therefore, through developing an analytical model that is capable of generating the fluorescence modulated WGM spectrum of any spherical resonator (R, n_1) residing in any medium (n_2), over a given wavelength range, and extracting the Q-factor and refractive index sensitivity, large sets of resonators can easily and efficiently be compared and assessed to find the optimal combination of resonator parameters (R, n_1) for maximized sensing performance. It should be noted that further considerations of intrinsic noise sources pertaining to individual experiments can be included as necessary, however, this work focuses on developing an initial design tool purely for the resonator selection.

As an example of how this model can be implemented, a set of resonators (diameters of 2-20 um and refractive indices ranging from 1.45-2.0, residing in water, over the wavelength range 600-615 nm) is examined, calculating the refractive index sensitivity, Q-factor and figure of merit. This particular set of resonators is selected to cover commonly used materials for active resonators (i.e. polystyrene, PMMA) along with commonly utilized organic dyes such as Coumarin derivatives and Nile Red, which have previously been implemented as gain mediums for active WGM biosensing. By taking into consideration experimental constraints, such as the resolution of a spectrometer used to observe the WGM spectrum, the ideal combinations of resonator diameter and refractive index can be identified.

3.1.2 Statement of Contribution

Statement of Authorship

Title of Paper	Optimization of whispering gallery resonator design for biosensing applications
Publication Status	☒ Published ☐ Accepted for Publication ☐ Submitted for Publication ☐ Unpublished and Unsubmitted w ork w ritten in manuscript style
Publication Details	T. Reynolds, M. R. Henderson, A. Francois, J. M. M. Hall, N. Riesen, S. Afshar V., and T. M. Monro, "Optimization of whispering gallery resonators design for biosensing applications," Opt. Express, 23 (13), 17067-17076, 2015.

Principal Author

Name of Principal Author (Candidate)	Tess Reynolds		
Contribution to the Paper	Developed and implemented the analytical model capable of generating the WGM fluorescence spectrum of a microspherical resonator of any size and refractive index, primarily wrote the paper and acted as corresponding author.		
Overall percentage (%)	70		
Certification:	This paper reports on original research I conducted during the period of my Higher Degree by Research candidature and is not subject to any obligations or contractual agreements with a third party that would constrain its inclusion in this thesis. I am the primary author of this paper.		
Signature		Date	11-11-16

Co-Author Contributions

By signing the Statement of Authorship, each author certifies that:

i. the candidate's stated contribution to the publication is accurate (as detailed above);

ii. permission is granted for the candidate in include the publication in the thesis; and

iii. the sum of all co-author contributions is equal to 100% less the candidate's stated contribution.

Name of Co-Author	Matthew R. Henderson		
Contribution to the Paper	Assisted with the formalization of the analytical model, along with contributions to manuscript editing and evaluation.		
Signature		Date	16-11-16

Name of Co-Author	Alexandre Francois		
Contribution to the Paper	Supervised the development of the work and helped with the manuscript editing and evaluation.		
Signature		Date	14-11-16

Name of Co-Author	Jonathan M. M. Hall		
Contribution to the Paper	Assisted with the formalization of the analytical model, along with contributions to manuscript editing and evaluation.		
Signature		Date	11-11-16

Name of Co-Author	Nicolas Riesen		
Contribution to the Paper	Helped to evaluate and edit the manuscript. Assisted in the writing of the discussion and interpretation of results.		
Signature		Date	16-11-16

Name of Co-Author	Shahraam Afshar V.		
Contribution to the Paper	Assisted with the formalization of the analytical model, along with contributions to manuscript editing and evaluation.		
Signature		Date	16-11-16

Name of Co-Author	Stephen J. Nicholls		
Contribution to the Paper	Helped to evaluate and edit the manuscript.		
Signature		Date	16-11-16

Name of Co-Author	Tanya M. Monro		
Contribution to the Paper	Supervised the project and contributed to manuscript editing and evaluation.		
Signature		Date	14-11-16

Optimization of whispering gallery resonator design for biosensing applications

T. Reynolds,[1,*] M. R. Henderson,[1] A. François,[1] N. Riesen,[1] J. M. M. Hall,[1] S. V. Afshar,[1,3] S. J. Nicholls,[2] and T. M. Monro[1,3]

[1]*The Institute for Photonics and Advanced Sensing (IPAS), and ARC Centre of Excellence for Nanoscale BioPhotonics (CNBP), University of Adelaide, Adelaide SA 5005, Australia*
[2]*South Australian Health & Medical Research Institute (SAHMRI), Adelaide SA 5000, Australia*
[3]*University of South Australia, Adelaide SA 5000, Australia*
** tess.reynolds@adelaide.edu.au*

Abstract: Whispering gallery modes (WGMs) within microsphere cavities enable highly sensitive label-free detection of changes in the surrounding refractive index. This detection modality is of particular interest for biosensing applications. However, the majority of biosensing work utilizing WGMs to date has been conducted with resonators made from either silica or polystyrene, while other materials remain largely uninvestigated. By considering characteristics such as the quality factor and sensitivity of the resonator, the optimal WGM sensor design can be identified for various applications. This work explores the choice of resonator refractive index and size to provide design guidelines for undertaking refractive index biosensing using WGMs.

OCIS codes: (070.5753) Resonators; (140.3945) Microcavities; (230.0230) Optical devices; (280.1415) Biological sensing and sensors.

References and links

1. F. Vollmer and S. Arnold, "Whispering-gallery-mode biosensing: label-free detection down to single molecules," Nat. Methods **5**(7), 591–596 (2008).
2. P. Zijlstra, K. L. van der Molen, and A. P. Mosk, "Spatial refractive index sensor using whispering gallery modes in an optically trapped microsphere," Appl. Phys. Lett. **90**(16), 161101 (2007).
3. A. François, T. Reynolds, and T. M. Monro, "A fiber-tip label-free biological sensing platform: a practical approach toward *in-vivo* sensing," Sensors (Basel) **15**(1), 1168–1181 (2015).
4. S. Pang, R. E. Beckham, and K. E. Meissner, "Quantum dot-embedded microspheres for remote refractive index sensing," Appl. Phys. Lett. **92**(22), 221108 (2008).
5. S. Arnold, M. Khoshsima, I. Teraoka, S. Holler, and F. Vollmer, "Shift of whispering-gallery modes in microspheres by protein adsorption," Opt. Lett. **28**(4), 272–274 (2003).
6. M. D. Baaske, M. R. Foreman, and F. Vollmer, "Single-molecule nucleic acid interactions monitored on a label-free microcavity biosensor platform," Nat. Nanotechnol. **9**(11), 933–939 (2014).
7. M. I. Cheema, S. Mehrabani, A. A. Hayat, Y. A. Peter, A. M. Armani, and A. G. Kirk, "Simultaneous measurement of quality factor and wavelength shift by phase shift microcavity ring down spectroscopy," Opt. Express **20**(8), 9090–9098 (2012).
8. D. W. Vernooy, V. S. Ilchenko, H. Mabuchi, E. W. Streed, and H. J. Kimble, "High-Q measurements of fused-silica microspheres in the near infrared," Opt. Lett. **23**(4), 247–249 (1998).
9. J. R. Schwesyg, T. Beckmann, A. S. Zimmermann, K. Buse, and D. Haertle, "Fabrication and characterization of whispering-gallery-mode resonators made of polymers," Opt. Express **17**(4), 2573–2578 (2009).
10. F. Vollmer and L. Yang, "Label-free detection with high-Q microcavities: a review of biosensing mechanisms for integrated devices," Nanophotonics **1**(3-4), 267–291 (2012).
11. Y. Ruan, K. Boyd, H. Ji, A. François, H. Ebendorff-Heidepriem, J. Munch, and T. M. Monro, "Tellurite microspheres for nanoparticle sensing and novel light sources," Opt. Express **22**(10), 11995–12006 (2014).
12. R. S. Moirangthem and A. Erbe, "Interfacial refractive index sensing using visible-excited intrinsic zinc oxide photoluminescence coupled to whispering gallery modes," Appl. Phys. Lett. **103**(5), 051108 (2013).
13. A. Paunoiu, R. S. Moirangthem, and A. Erbe, "Whispering gallery modes in intrinsic TiO_2 microspheres coupling to the defect-related photoluminescence after visible excitation," Phys. Status Solidi RRL **9**(4), 241–244 (2015).
14. N. M. Hanumegowda, C. J. Stica, B. C. Patel, I. White, and X. D. Fan, "Refractometric sensors based on microsphere resonators," Appl. Phys. Lett. **87**(20), 201107 (2005).

#242247 Received 2 Jun 2015; accepted 10 Jun 2015; published 19 Jun 2015

15. A. Ksendzov and Y. Lin, "Integrated optics ring-resonator sensors for protein detection," Opt. Lett. **30**(24), 3344–3346 (2005).
16. M. L. Gorodetsky and V. S. Ilchenko, "Optical microsphere resonators: optimal coupling to high-Q whispering gallery modes," J. Opt. Soc. Am. B **16**(1), 147–154 (1999).
17. Z. Ballard, M. D. Baaske, and F. Vollmer, "Stand-off biodetection with free-space coupled asymmetric microsphere cavities," Sensors (Basel) **15**(4), 8968–8980 (2015).
18. M. R. Foreman, W. L. Jin, and F. Vollmer, "Optimizing detection limits in whispering gallery mode biosensing," Opt. Express **22**(5), 5491–5511 (2014).
19. M. L. Gorodetsky, A. D. Pryamikov, and V. S. Ilchenko, "Rayleigh scattering in high-Q microspheres," J. Opt. Soc. Am. B **17**(6), 1051–1057 (2000).
20. M. L. Gorodetsky, A. A. Savchenkov, and V. S. Ilchenko, "Ultimate Q of optical microsphere resonators," Opt. Lett. **21**(7), 453–455 (1996).
21. Z. Guo, H. Quan, and S. Pau, "Near-field gap effects on small microcavity whispering gallery mode resonators," J. Phys. D Appl. Phys. **39**(24), 5133–5136 (2006).
22. M. Himmelhaus and A. François, "In-vitro sensing of biomechanical forces in live cells by a whispering gallery mode biosensor," Biosens. Bioelectron. **25**(2), 418–427 (2009).
23. I. M. White and X. Fan, "On the performance quantification of resonant refractive index sensors," Opt. Express **16**(2), 1020–1028 (2008).
24. J. Hu, X. Sun, A. Agarwal, and L. C. Kimerling, "Design guidelines for optical resonator biochemical sensors," J. Opt. Soc. Am. B **26**(5), 1032–1041 (2009).
25. M. I. Cheema, C. Shi, A. M. Armani, and A. G. Kirk, "Optimizing the signal to noise ratio of microcavity sensors," IEEE Photon. Technol. Lett. **26**(20), 2023–2026 (2014).
26. H. Chew, "Transition rates of atoms near spherical surfaces," J. Chem. Phys. **87**(2), 1355–1360 (1987).
27. H. Chew, "Radiation and lifetimes of atoms inside dielectric particles," Phys. Rev. A **38**(7), 3410–3416 (1988).
28. C. F. Bohren and D. R. Huffman, *Absorption and Scattering by a Sphere* (Wiley-VCH Verlag GmbH, 2007).
29. R. Lessard, O. Rousseau-Cyr, M. Charlebois, C. Riviere, O. Mermut, and C. N. Allen, "Flow cytometer system for single-shot biosensing based on whispering gallery modes in fluorescent microspheres," Proc. SPIE **8600**, 86001 (2013).
30. J. M. M. Hall, V. Shahraam Afshar, M. R. Henderson, A. François, T. Reynolds, N. Riesen, and T. M. Monro, "Method for predicting whispering gallery mode spectra of spherical microresonators," Opt. Express **23**(8), 9924–9937 (2015).
31. V. S. Ilchenko, A. M. Bennett, P. Santini, A. A. Savchenkov, A. B. Matsko, and L. Maleki, "Whispering gallery mode diamond resonator," Opt. Lett. **38**(21), 4320–4323 (2013).
32. A. François, N. Riesen, H. Ji, S. Afshar V, and T. M. Monro, "Polymer based whispering gallery mode laser for biosensing applications," Appl. Phys. Lett. **106**(3), 031104 (2015).
33. M. Himmelhaus, S. Krishnamoorthy, and A. François, "Optical sensors based on whispering gallery modes in fluorescent microbeads: response to specific interactions," Sensors (Basel) **10**(6), 6257–6274 (2010).
34. J. Lutti, W. Langbein, and P. Borri, "High Q optical resonances of polystyrene microspheres in water controlled by optical tweezers," Appl. Phys. Lett. **91**(14), 141116 (2007).
35. J. Zhang, L. Xue, and Y. Han, "Fabrication gradient surfaces by changing polystyrene microsphere topography," Langmuir **21**(1), 5–8 (2005).
36. G. E. Yakubov, O. I. Vinogradova, and H. J. Butt, "A study of the linear tension effect on the polystyrene microsphere wettability with water," Colloid J. **63**(4), 518–525 (2001).
37. L. Xiang, C. Zhuang-Qi, S. Qi-Shun, and Y. Yan-Fang, "Study on the thermo-optic properties of DR1/PMMA composite," Chin. Phys. **15**(10), 2439–2444 (2006).
38. S. N. Kasarova, N. G. Sultanova, and I. D. Nikolov, "Temperature dependence of refractive characteristics of optical plastics," J. Phys. Conf. Ser. **253**, 012028 (2010).
39. R. Bischler, M. Olszyna, M. Himmelhaus, and L. Dähne, "Development of a fully automated in-vivo diagnostic system based on low-Q whispering gallery modes in fluorescent microparticles," Eur. Phys. J. Spec. Top. **223**(10), 2041–2055 (2014).
40. J. R. Schwesyg, T. Beckmann, A. S. Zimmermann, K. Buse, and D. Haertle, "Fabrication and characterization of whispering-gallery-mode resonators made of polymers," Opt. Express **17**(4), 2573–2578 (2009).
41. M. Humar, M. Ravnik, S. Pajk, and I. Muševič, "Electronically tunable liquid crystal optical microresonators," Nat. Photonics **3**(10), 595–600 (2009).
42. K. Sasagawa, Z.- Yonezawa, R. Iwai, J. Ohta, and M. Nunoshita, "S-band Tm 3+-doped tellurite glass microsphere laser via a cascade process," Appl. Phys. Lett. **85**(19), 4325 (2004).
43. A. François, K. J. Rowland, S. V. Afshar, M. R. Henderson, and T. M. Monro, "Enhancing the radiation efficiency of dye doped whispering gallery mode microresonators," Opt. Express **21**(19), 22566–22577 (2013).

1. Introduction

The use of whispering gallery modes (WGMs) within microsphere resonators for detecting changes in the surrounding refractive index has been extensively studied and exploited for use in biological sensing [1–6]. The phenomenon of WGMs in microspheres arises from light

#242247 Received 2 Jun 2015; accepted 10 Jun 2015; published 19 Jun 2015

being trapped inside the resonator circumference due to total internal reflection. The circulating light has an evanescent field that extends beyond the resonator into the surrounding medium, enabling changes in the surrounding refractive index to be monitored via the shifts in the resonance wavelengths. The addition of surface functionalization to the microsphere allows interaction with specific analytes as they bind to the surface, enabling highly sensitive and selective, label-free detection of molecules to be made [5, 6] down to the single molecule level [6]. The amount of time the light remains circulating within the resonator determines the quality (Q) factor. The Q-factor can be expressed equivalently in terms of a variety of quantities including the cavity ring down time [7], the ratio between resonance wavelength and linewidth, the energy stored in the resonator as well as the loss mechanisms of the resonator (i.e. surface scattering, material absorption and radiation losses) [8]. As the Q-factor increases, the resonance linewidth decreases, enabling smaller wavelength shifts to be measured [5]. Such improvements in the resolution are of particular importance for biosensing applications.

The majority of biosensing work previously conducted utilizing WGMs in microspheres has involved the use of silica [1, 5, 6] or polystyrene [3, 4, 9], with other materials remaining largely uninvestigated [10], apart from a few examples of high refractive index glass [11], ZnO [12] or TiO_2 [13] microspheres. Silica microspheres are usually produced via melting of the tip of an optical fiber [5, 6] and typically range from 50 to 100 μm in diameter [14]. As the microsphere remains attached to the fiber during this fabrication process, it can be secured in position, allowing light from a tunable laser to be coupled evanescently to the microsphere using a phase matched fiber taper [14], waveguide [15] or prism [16]. Free space coupling to microspheres has also recently been demonstrated for the case of asymmetric resonators [17]. Optimization of the sensing performance of silica microspheres has previously been conducted by examining the detection limits [18], as well as increasing the Q-factor by reducing the material absorption and scattering contributions [19]. Q-factors as high as 8×10^9 have been demonstrated using evanescent coupling, closing in on the ultimate Q-factor, as dictated by material attenuation, of 9×10^9 at 633 nm [20].

Despite the extremely high Q-factors that have been recorded using evanescent coupling, the alignment requirements in such systems, impose practical limitations on the use of the sensors. For example, any change in the position of a fiber taper with respect to a microresonator will induce changes in the positions of the resonance peaks due to a change in effective refractive index [21], which may be indistinguishable from changes in refractive index of the surrounding medium or binding events. Furthermore, the fiber taper used for coupling light into the resonator may become contaminated during the sensing experiment, resulting in reduced throughput [17]. In contrast, fluorescence based sensing, such as that involving dye-doped microspheres, alleviates some of the practical constraints by enabling remote interrogation of the WGM modulated fluorescence of the microsphere. However, the significantly lower Q-factors reported for such systems restrict the achievable sensing performance. The finite resolution of the detection system, often a spectrometer for fluorescence-based methods, may also limit the performance.

In order to capitalize on the practical benefits shown by small fluorescent microspheres such as remote excitation and detection [3], which can be used for e.g. interrogating complex phenomenon within living cells [22], different resonator materials and sizes need to be investigated to help bridge the performance gaps between passive (fiber taper or prism coupled) and active (free space coupled fluorescent) microspheres. This could for instance allow for the detection of smaller biomolecules and within lower concentrations even when using active microspheres, matching the performance achieved with fiber taper coupled passive microspheres [1, 6, 7]. The problem of determining the optimal WGM sensor design has been approached previously by considering a variety of different parameters. These include, but are not limited to, the detection limit [23], introducing a new parameter of time normalized sensitivity to allow comparison of sensors in the white-noise-limited regime [24],

#242247 Received 2 Jun 2015; accepted 10 Jun 2015; published 19 Jun 2015

and optimizing the signal to noise ratio [25]. Our method of investigating a large range of different resonator refractive indices and sizes is to utilize an analytical model [26, 27], simulating the WGM spectrum as a way towards characterizing the sensing performance by extracting parameters such as the resonator's sensitivity and Q-factor directly from WGM spectra. The model allows for any sphere (refractive index n_1 and radius R) to be assessed and compared with any other sphere.

The aim of the current research is to consider a subset of resonators and demonstrate how the model can be applied to provide guidelines for designing WGM based refractive index sensing fluorescent microspheres.

2. Theoretical considerations

The WGM spectrum of a dielectric microsphere of radius R and refractive index n_1 can be predicted by extending classical Mie Scattering theory, as illustrated by Chew [26, 27]. Consider an arbitrary distribution of dipoles within a spherical dielectric resonator, of radius R and refractive index n_1, within a medium of refractive index n_2. The resulting total average power radiated from the sphere is given by the sum of the radial and tangential oscillations, as defined in [27]:

$$P = 2H\sum_{n=1}^{\infty}\frac{2n+1}{3}\left(\frac{J_n}{|D_n|^2}+\frac{GK_n}{|D_n^{'}|^2}\right) \tag{1}$$

where,

$$H=\frac{9\varepsilon_1}{4\rho_1^5}\sqrt{\frac{\varepsilon_1\varepsilon_2\mu_1}{\mu_2}},\quad G=\frac{\mu_1\mu_2}{\varepsilon_1\varepsilon_2}$$

$$K_n=\left(\frac{\rho_1^3}{2}\right)\left[j_n^2(\rho_1)-j_{n+1}(\rho_1)j_{n-1}(\rho_1)\right],\ J_n=K_{n-1}-n\rho_1 j_n^2(\rho_1)$$

$$D_n=\varepsilon_1 j_n(\rho_1)\left[\rho_2 h_n^{(1)}(\rho_2)\right]^{'}-\varepsilon_2 h_n^{(1)}(\rho_2)\left[\rho_1 j_n(\rho_1)\right]^{'},\ D_n^{'}=D_n(\varepsilon_{1,2}\to\mu_{1,2})$$

$$\rho_{1,2}=k_{1,2}R$$

where H and G are normalization factors, $D_n^{'}$ and D_n are the electric and magnetic multiple terms (equivalent to the Mie Scattering coefficients), j_n is the n^{th} order spherical Bessel function of the first kind, $h_n^{(1)}$ is the n^{th} order spherical Hankel function of the first kind, $\varepsilon_{1,2}$ and $\mu_{1,2}$ are the permittivity and permeability of the sphere and surrounding medium, respectively, and $\rho_{1,2}$ is the size parameter [27].

The Chew formulation for modeling WGM spectra has previously been shown to be consistent with classical Mie scattering with agreement of the resonance positions [28]. It has also previously been implemented in flow cytometer systems for the efficient identification of the (R, n_1) values of microsphere populations [29]. Recently, we have confirmed that this formulation agrees with other analytical models and also that it is consistent with computational simulations based on the Finite-Difference Time-Domain (FDTD) method [30]. We note here that the FDTD method provides the opportunity to investigate other resonator geometries, as well as provide insight extending beyond the spectral information, including transient phenomena. In contrast, the Chew model is significantly less computationally expensive to run, and hence allows for more efficient scanning over large parameter spaces.

By generating the WGM spectrum of a resonator of any combination of radius and material, it is possible to characterize sensing performance through the calculation of key parameters such as the Q-factor (or components thereof) and refractive index sensitivity. The

#242247 Received 2 Jun 2015; accepted 10 Jun 2015; published 19 Jun 2015

overall cavity Q-factor is intrinsically tied to the losses of the resonator and so can be expressed in terms of the individual loss mechanisms involved,

$$\frac{1}{Q} = \frac{1}{Q_m} + \frac{1}{Q_s} + \frac{1}{Q_c} \tag{2}$$

where Q_m is due to material loss, Q_s is due to scattering from surface roughness and Q_c is the geometric (tunneling loss) contribution derived from the Chew model. For a given resonance wavelength λ and linewidth Δλ, Q_c can be calculated directly from the simulated WGM spectrum as,

$$Q_c = \frac{\lambda}{\Delta\lambda} \tag{3}$$

Both λ and Δλ are determined by Gaussian fitting routines that have been written to analyze the WGM spectra. The Chew model enables calculation of only a single contribution to the total Q-factor, and therefore to create a more realistic model to compare with experimental data, all Q-factor components need to be considered. The limiting factor on Q is often material absorption or surface scattering. The limit of the Q-factor due to material losses can be determined by considering the absorption of light by both the resonator and the surrounding medium using an absorption decay constant α_m, as,

$$Q_m = \frac{2\pi n_1}{\lambda \alpha_m} \tag{4}$$

The absorption decay constant is dependent on how tightly the light is confined within the resonator, the wavelength range, and the environment of the measurement.

Scattering contributions can be calculated by modeling the surface roughness as a changing dielectric constant and it has been used to determine upper limits on the Q-factors of small silica spheres [19]. One expression for the limit of the Q-factor due to surface scattering is,

$$Q_s \approx \frac{3\lambda^3 R}{8 n_1 \pi^2 B^2 \sigma^2} \tag{5}$$

where B is the correlation length and σ is the variance of the surface roughness [31].

The refractive index sensitivity is calculated by considering the shift in a resonance wavelength position due to a change in the surrounding refractive index, $S = \Delta\lambda/\Delta n$. By simulating the WGM spectrum, and not just determining the resonance positions, other features such as the change in Q_c can also be tracked, as is demonstrated in Fig. 1(a).

3. Results and discussion

To demonstrate how this model can be used, simulations of microspheres with diameters ranging from R = 1 – 10 μm and refractive indices ranging from n_1 = 1.45 – 2.0 residing in water (n_2 = 1.3325) were carried out using the analytical model described above, with spectral information over the range of 600-615 nm being generated for every (R, n_1) pair. This parameter set was chosen as the refractive index range allows comparison with previous experimental work based on polystyrene microspheres [3, 4, 22, 32, 33], and the wavelength range selected is a common region for organic dyes such as Nile Red [3, 32] or Coumarin derivatives that have previously been utilized for WGM biosensing [22, 33].

Over the entire parameter space considered, each spectrum produced represents the total average power radiating from the resonator which has been normalized to the power of the dipole sources within the medium [27], indicating that to observe the modulation of the

#242247 Received 2 Jun 2015; accepted 10 Jun 2015; published 19 Jun 2015

WGMs on top of the fluorescence background and for it to be above any background noise from the experiment, the peak height must exceed unity. This defines the boundary (black line), as observed in Fig. 2, below which no peaks would be observed experimentally.

For every resonator (R, n_1) within the parameter space, to decrease computation time, an initial WGM spectrum (3750 points) is generated over the wavelength range considered, allowing the approximate positions and intensities of the resonance peaks to be identified. To isolate peaks that would be observable experimentally, a threshold on the spectrum is then introduced, with peaks having a height less than unity not being considered. The selected peaks are then regenerated at a higher resolution to accurately determine their position and linewidth. During the regeneration process, care needs to be taken to ensure only one peak is regenerated at a time. If more than one peak resides within the same wavelength window then the calculation of both Q_c and S will either be incorrect or the single peak fitting formulation will fail. Every eligible peak in the spectrum is considered, with the maximum values of S and Q_c being recorded.

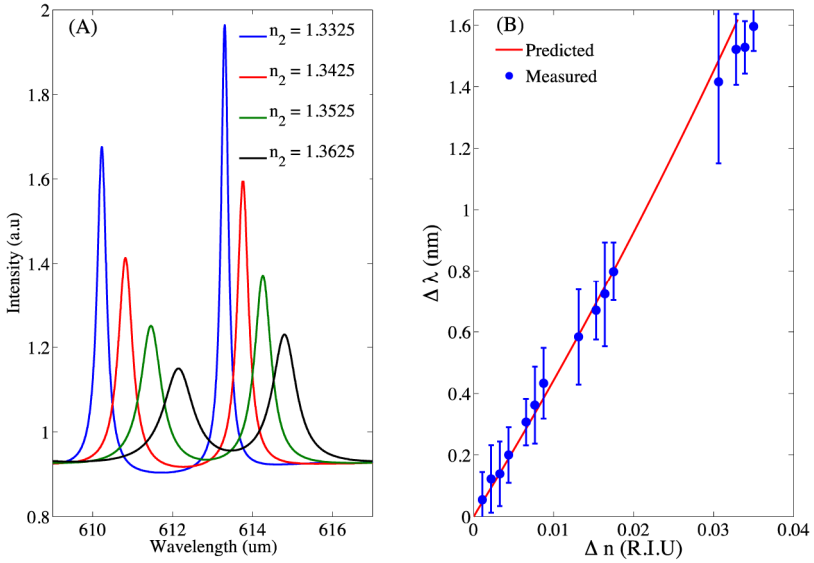

Fig. 1. (a) A demonstration of how the position of the resonance peaks changes for a 5 μm radius polystyrene sphere (n_1 = 1.59) initially in water (n_2 = 1.3325) for incremental increases in the surrounding refractive index n_2 up to 0.01 R.I.U. (b) Comparison of the predicted sensitivity from the analytical Chew model (red line) with the measured sensitivity for a R~5 μm polystyrene sphere in water.

The first feature considered is the refractive index sensitivity. Initially, all the spheres considered reside in water (n_2 = 1.3325). In order to calculate S, new spectra are generated after increasing the value of n_2 (step size Δn = 0.0005 R.I.U.) until the surrounding refractive index has increased by 0.01 R.I.U., monitoring the shift in the position of the resonance peak at each step. An example of this process is shown in Fig. 1(a). The predicted sensitivity for a polystyrene sphere in water with R ~5 μm is compared with measured sensitivities, and the result is shown in Fig. 1(b). Excellent agreement is seen between the model and experimental data, therefore validating the numerical model. As expected, the shift in the position of the resonance peaks $\Delta\lambda$ displays a linear response to changes in n_2 over the range of Δn considered, even as Δn extends to values that are higher than those typically observed experimentally for refractive index sensing. The sensitivity of a resonator is related to how tightly the light is confined inside the circumference of the sphere with poor confinement leading to greater sensitivity as more light extends out of the resonator enhancing the interaction with the surrounding environment.

#242247 Received 2 Jun 2015; accepted 10 Jun 2015; published 19 Jun 2015

This approach of calculating the sensitivity can be extended to cover the entire parameter space. Figure 2 shows a contour plot of the refractive index sensitivity as functions of radius and refractive index of the resonator. This sensitivity map shows that, for a given sphere radius R, the sensitivity decreases with increasing sphere refractive index, as the increasing index contrast results in the light becoming more tightly confined within the resonator. The region corresponding to the highest sensitivity is located just above the boundary of unit peak height (i.e. black line), and it shows that the higher the refractive index, the smaller the sphere can be whilst maintaining the same sensitivity.

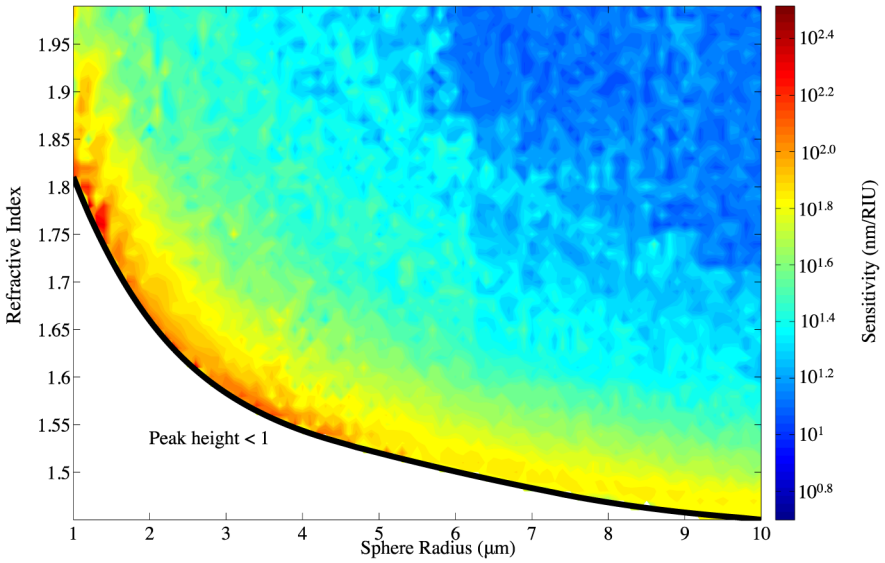

Fig. 2. Contour plot of the sensitivity in nm/R.I.U., calculated using the analytical Chew model for spherical resonators over the parameter space ranging from R = 1 – 10 μm and microsphere refractive index n_1 = 1.45 – 2.0 within the wavelength range of 600 – 615 nm.

The Q-factor was also evaluated over the same parameter space as is shown in Fig. 3. Initially, the Q-factor contribution Q_c as derived from the Chew model was determined. Afterwards, other loss mechanisms (e.g. material absorption and surface scattering) can be incorporated as required, but these are strongly dependent on the material properties, nature of the gain medium (organic dye vs quantum dots) and fabrication processes used to produce the microspheres. This implies that Q_c represents an upper limit, for the ideal situation of a perfect sphere with only tunneling losses. In calculating Q_c, every peak within each resonator (R, n_1) spectrum was assessed, and the peak corresponding to the highest Q-factor was recorded as Q_c, noting that this peak is not necessarily the same peak as that of greatest sensitivity. Since we are considering fluorescent microspheres, the maximum Q-factor which can be resolved with the spectrometer (2400 mm^{-1} grating ~4 pm resolution, 2048 pixels CCD camera) results in the 1.5×10^5 cut-off shown in Fig. 3. Beyond this value of Q-factor, the spectrometer cannot resolve any improvement in WGM linewidth, limiting the benefit of having ultra-high Q resonators in this context.

#242247 Received 2 Jun 2015; accepted 10 Jun 2015; published 19 Jun 2015

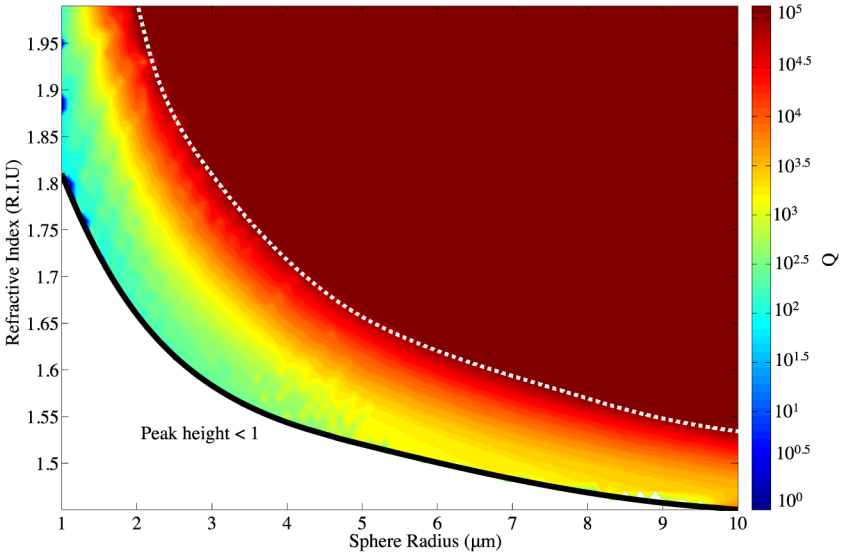

Fig. 3. The quality factor, Q_c, derived using the analytical Chew model for spherical resonators, including the limit placed on the observable Q of fluorescence based microsphere WGMs due to the finite resolution of the spectrometer used (4 pm), over the parameter space ranging from R = 1 – 10 μm and microsphere refractive index range of n_1 = 1.45 – 2.0, and within the wavelength range of 600-615 nm. The white dotted-line highlights the resolution limit of the spectrometer beyond which any increase in the Q factor cannot be resolved experimentally.

As mentioned, for each specific case the individual loss mechanisms due to surface scattering, material absorption and geometric imperfections can be incorporated providing a more accurate calculation of the total cavity Q-factor. For the present example, focusing on polystyrene microspheres, the loss due to surface scattering was first considered. Q_s was calculated based on the typical surface roughness of polystyrene of 10 nm or greater [34–36]. This results in Q-factor values much larger than that of Q_c, (e.g. for R = 5 μm, n_1 = 1.59, Q_c ~4.4×10^3, Q_s ~5×10^7) indicating that its contribution to Q through Eq. (2) is insignificant. It is only when the roughness is increased up towards 50 nm, which is unlikely for polystyrene, that Q_s starts to become a limiting factor on the overall Q-factor. For the material losses, it has previously been shown that the intrinsic absorption of polystyrene can be estimated by the typical losses of polymer fibers, corresponding to an absorption coefficient of 0.23 m^{-1} [34], resulting in Q_m ~7.2×10^7. This is once again orders of magnitude larger, indicating that it too is not the limiting factor on the Q-factor and suggests that another contribution has to be considered.

One possible explanation arises from the fact that the Chew model is based on the assumption that the resonator is perfectly spherical, which in reality is not the case. It is well established that fractional changes in a sphere's radius induces a shift in the resonances. As an example, a ± 5 nm radius deviation for a R = 5 μm polystyrene microsphere results in up to a 0.61 nm wavelength shift. Therefore, we hypothesize that the intrinsic asphericity of a microsphere, falling within the same radius deviation might be the predominant mechanism in lowering the Q-factor of free-floating fluorescent microspheres. For fluorescent microspheres the WGM spectrum originates from all excited equatorial planes. While no discrepancy would be observable for a perfect microsphere, a slightly aspherical one, which can be thought of as having multiple equatorial planes of different effective radius, would exhibit a superposition of perturbed resonances, effectively resulting in the broadening of each individual peak and hence a reduction in the measured Q-factor.

#242247 Received 2 Jun 2015; accepted 10 Jun 2015; published 19 Jun 2015

For biological sensing, to achieve the best sensing performance, both high refractive index sensitivity and high Q-factors are required, with the latter dictating the smallest resolvable wavelength shift. However, it appears that the Q-factor and the sensitivity are influenced in very different ways by both the resonator's refractive index and size. Therefore, optimizing the sensing performance requires finding a compromise between these two parameters. Incorporating noise sources, such as, thermal noise, spectral noise and amplitude noise which can be caused either by the optical setup used to interrogate the resonator (e.g. pump power fluctuations, resolution limit of the detector) or by the material constituting the resonator (e.g. thermo optic effect), as shown by White et al. [23], allows for further refinement of the model to be made, but these are specific to individual scenarios. While resonator performance is indeed independent of noise sources specific to individual experimental setups, further consideration of the material properties of the resonator could assist in the sensor design. As an example to highlight this, it is possible to find two materials such as a polymer and a glass (e.g. PMMA and NBK7), which have the same refractive index yet very different thermo optic constants (-1.20×10^{-4} K^{-1} [37] and 1.6×10^{-5} K^{-1} respectively [38]). Nevertheless, as an initial design tool, it is reasonable to compare the sensing performance of the microresonators considered here by using a Figure of Merit (FOM) defined as the product of Q and *S*, without noise considerations, which fall outside the present scope,

$$FOM = QS \tag{6}$$

On the FOM map shown in Fig. 4, a white dotted-line is shown which corresponds to the maximum FOM (~6.0×10^6) achievable for fluorescent microspheres where the maximum resolution of the spectrometer (4 pm with a 2400 mm^{-1} grating and 2400 pixels CCD camera) used to record the WGM spectra will eventually restrict the performance of this sensing approach.

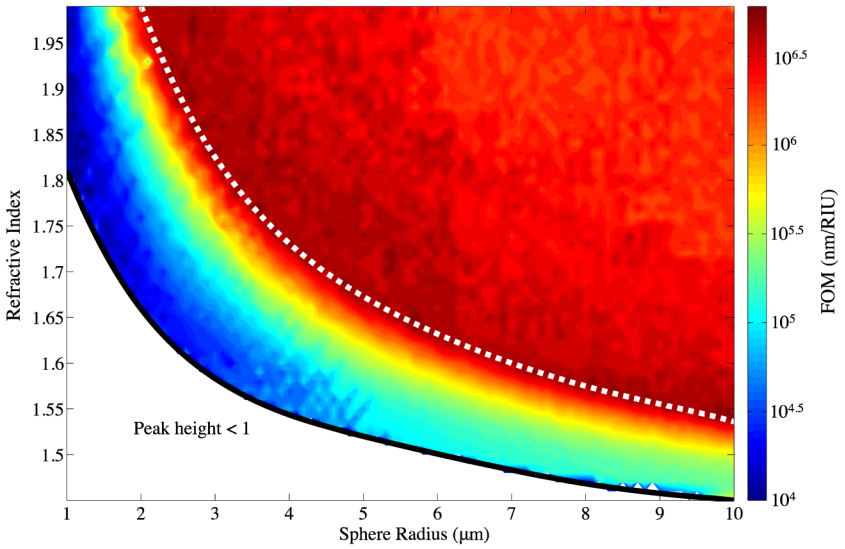

Fig. 4. Figure of Merit (FOM [nm/R.I.U.]) mapped over the parameter space R = 1 – 10 μm and microsphere refractive index n_1 = 1.45 – 2.0 within the wavelength range 600-615 nm. The white dotted line represents the maximum value as limited by the spectrometer resolution of 4 pm for fluorescent microspheres.

In order to obtain a high FOM for fluorescent microspheres in water (the typical situation for biosensing applications), spheres with smaller radius and larger refractive indices are required. This could be realized by using materials such as polymers (polystyrene [3, 4, 22, 32, 33], melamine [39], PMMA [40], PDMS [41]), higher refractive index glasses doped with

#242247 Received 2 Jun 2015; accepted 10 Jun 2015; published 19 Jun 2015

Erbium [11] or Thulium [42] or other oxides like ZnO [12] or TiOx [13]. The parameter space used in this paper is representative of our previous experiments using dye-doped polystyrene spheres [3, 32], and the results can be used to infer how the performance is likely to compare with other materials. For example, according to the model, a $R = 5$ μm melamine ($n_1 = 1.68$) sphere will provide a significantly larger FOM (5.05×10^6) compared with a $R = 5$ μm polystyrene ($n_1 = 1.59$) sphere (2.23×10^5). The FOM map also allows for other resonator material and size combinations to be assessed for specific applications. However the performance is still significantly lower compared to passive microspheres for which the Q-factor is not limited by the resolution of a spectrometer. For instance silica microspheres of $R = 55$ μm with a FOM = 1.5×10^8 corresponding to a $Q \sim 5 \times 10^6$ and $S = 30$ nm/R.I.U. have been demonstrated experimentally [14]. This highlights the need for alternative detection modalities for fluorescent microspheres with improved spectral resolution.

While experimentally the Q-factors of fluorescent microspheres are significantly lower than the theoretical values presented here, and as a consequence the FOM is lower than predicted by the model, several improvements are possible. These include operating the active microspheres within their stimulated emission regimes [32] or investigating alternative coupling strategies [43], which result in increased Q-factors.

4. Conclusion

This work represents the first application of the analytical model developed by Chew [26,27] to fluorescence based WGM refractive index biosensors, that allows the sensing performance of any microsphere of refractive index n_1 and radius R to be predicted using simulated WGM spectra. The model demonstrates excellent agreement with measured refractive index sensitivity values, whilst providing an upper limit on the achievable resonator Q-factor. By combining the S and Q_c parameters, a Figure of Merit can be given for sensing performance, where additional information specific to the sensing task can be incorporated as required. An example of how this model can be implemented was given, focusing on fluorescence based WGM microspheres. By providing a relatively simple method for generating WGM spectra for any resonator size and material over any given wavelength range, this model serves as an initial step in the resonator selection process for WGM biosensing by predicting the sensitivity and Q-factor for any number of resonators in a range of different situations.

Acknowledgments

The authors acknowledge the support of T.M.M's ARC Georgina Sweet Laureate Fellowship, and the ARC Centre for Nanoscale BioPhotonics. This research was also supported by a grant from the National Breast Cancer Foundation Australia.

#242247 Received 2 Jun 2015; accepted 10 Jun 2015; published 19 Jun 2015

Chapter 4

Q-Factor Limits of Fluorescent Microspheres

4.1 Q-Factor Limits for Far-Field Detection of Whispering Gallery Modes in Active Microspheres

P3. N. Riesen, T. Reynolds, A. François, M. R. Henderson and T. M. Monro, "Q-Factor limits for far-field detection of whispering gallery modes in active microspheres", Optics Express, 23 (22), 28896-28904, 2015.

4.1.1 Publication Overview

One of the observations to come out of the theoretical work completed in Chapter 3 was that the limiting factor on the Q-factor of active microspherical resonators was not material absorption or due to scattering from surface roughness, but possibly arising due to imperfections in the resonator. More specifically, the analytical model employed is derived on the assumption of a perfectly spherical resonator; however, in reality this is never the case, especially for free-floating polymer-based resonators that are commonly utilized for active resonator sensing. For free-space excited resonators, the WGM spectrum has contributions from all the excited equatorial planes. In the case of a perfectly spherical microsphere no discrepancy from the analytical model would be observed, as each plane is exactly the same. However, for a slightly aspherical resonator, consisting of multiple different equatorial planes (corresponding to different effective radii), the resulting WGM spectrum will be a super position of the all excited planes, resulting in a broadening of each of the resonance peaks. Similarly, elliptical aspherical perturbations that lift the degeneracy between polar modes, can also lead to broadening of the resonance peaks.

In order to investigate this thoroughly, experimental, theoretical and imaging techniques are implemented. Firstly, the Q-factors of dye doped polystyrene microspheres are compared using far field and fiber taper collections, highlighting the advantages of utilizing the highly mode-selective fiber taper in both free-space and taper excitation scenarios. Next, a Q-factor component for an active microsphere due to the inherent asphericity is derived theoretically using both a multi-plane and elliptical model, with both models producing very similar results. Finally, the dye-doped microspheres are imaged using a scanning-electron microscope (SEM) to attempt to quantify the asphericity of the resonators, with an upper limit on the size of the asphericity being identified.

4.1.2 Statement of Contribution

Statement of Authorship

Title of Paper	Q-Factor limits for far-field detection of whispering gallery modes in active microspheres
Publication Status	☒ Published ☐ Accepted for Publication ☐ Submitted for Publication ☐ Unpublished and Unsubmitted w ork w ritten in manuscript style
Publication Details	N. Riesen, T. Reynolds, A. Francois, M. R. Henderson, and T. M. Monro, "Q-Factor limits for far-field detection of whispering gallery modes in active microspheres," Opt. Express, 23 (22), 28896-28904, 2015.

Principal Author

Name of Principal Author (Candidate)	Nicolas Riesen
Contribution to the Paper	Performed the experimental work investigating how the measurement strategy influences the Q-factor of fluorescent microspheres. Developed and implemented both the simple and elliptical model to complete a comparative analysis with the analytical model. Primarily wrote the paper and acted as corresponding author.
Signature	Date: 16-11-16

Co-Author Contributions

By signing the Statement of Authorship, each author certifies that:

i. the candidate's stated contribution to the publication is accurate (as detailed above);

ii. permission is granted for the candidate in include the publication in the thesis; and

Name of Co-Author	Tess Reynolds
Contribution to the Paper	Conducted the modelling work using the analytical model developed to investigate the Q-factor spoiling as a result of collecting from multiple planes, performed and analysed the scanning electron microscope (SEM) image of the polystyrene microspheres for determining an upper limit on the asphericity of the microsphere. Contributed to the editing and evaluation of the manuscript. Overall percentage: 15%

Certification:	This paper reports on original research I conducted during the period of my Higher Degree by Research candidature and is not subject to any obligations or contractual agreements with a third party that would constrain its inclusion in this thesis. I am the primary author of this paper.		
Signature		Date	11-11-16

Name of Co-Author	Alexandre Francois		
Contribution to the Paper	Supervised the project and contributed to manuscript editing and evaluation.		
Signature		Date	15-11-16

Name of Co-Author	M. R. Henderson		
Contribution to the Paper	Contributed to the implementation of the modelling work using the analytical model developed, assisted in performing and analysing the scanning electron microscope (SEM) image of the polystyrene microspheres for determining an upper limit on the asphericity of the microsphere. Contributed to the editing and evaluation of the manuscript.		
Signature		Date	16-11-16

Name of Co-Author	Tanya M. Monro		
Contribution to the Paper	Supervised the project and contributed to manuscript editing and evaluation.		
Signature		Date	14-11-16

Q-factor limits for far-field detection of whispering gallery modes in active microspheres

Nicolas Riesen,[1,*] Tess Reynolds,[1] Alexandre François,[1,2] Matthew R. Henderson,[1] and Tanya M. Monro[1,2]

[1]*The Institute for Photonics and Advanced Sensing (IPAS) and ARC Centre for Nanoscale BioPhotonics (CNBP), School of Physical Sciences, The University of Adelaide, Adelaide, SA 5005, Australia*
[2]*University of South Australia, Adelaide, SA 5001, Australia*
[*]*nicolas.riesen@adelaide.edu.au*

Abstract: This paper investigates the Q-factor limits imposed on the far-field detection of the whispering gallery modes of active microspherical resonators. It is shown that the Q-factor measured for a given active microsphere in the far-field using a microscope is significantly lower than that measured using evanescent field collection through a taper. The discrepancy is attributed to the inevitable small asphericity of microspheres that results in mode-splitting which becomes unresolvable in the far-field. Analytic expressions quantifying the Q-factor limits due to small levels of asphericity are subsequently derived.

OCIS codes: (140.3945) Microcavities; (230.5750) Resonators; (260.2510) Fluorescence.

References and links

1. M. L. Gorodetsky, A. A. Savchenkov, and V. S. Ilchenko, "Ultimate Q of optical microsphere resonators," Opt. Lett. **21**(7), 453–455 (1996).
2. T. J. Kippenberg, *Nonlinear optics in ultra-high-Q whispering-gallery optical microcavities* (CIT, 2004).
3. K. J. Vahala, "Optical microcavities," Nature **424**(6950), 839–846 (2003).
4. A. François, N. Riesen, H. Ji, S. Afshar V., and T. M. Monro, "Polymer based whispering gallery mode laser for biosensing applications," Appl. Phys. Lett. **106**(3), 031104 (2015).
5. F. Vollmer and S. Arnold, "Whispering-gallery-mode biosensing: label-free detection down to single molecules," Nat. Methods **5**(7), 591–596 (2008).
6. M. Himmelhaus and A. François, "In-vitro sensing of biomechanical forces in live cells by a whispering gallery mode biosensor," Biosens. Bioelectron. **25**(2), 418–427 (2009).
7. M. A. Gouveia, P. D. Avila, T. H. R. Marques, M. C. Torres, and C. M. B. Cordeiro, "Morphology dependent polymeric capillary optical resonator hydrostatic pressure sensor," Opt. Express **23**(8), 10643–10652 (2015).
8. B. E. Little, J.-P. Laine, and H. A. Haus, "Analytic theory of coupling from tapered fibers and half-blocks into microsphere resonators," J. Lightwave Technol. **17**(4), 704–715 (1999).
9. Y. Zhi, J. Valenta, and A. Meldrum, "Structure of whispering gallery mode spectrum of microspheres coated with fluorescent silicon quantum dots," J. Opt. Soc. Am. B **30**(11), 3079–3085 (2013).
10. H. T. Beier, G. L. Coté, and K. E. Meissner, "Modeling whispering gallery modes in quantum dot embedded polystyrene microspheres," J. Opt. Soc. Am. B **27**(3), 536–543 (2010).
11. Z. Ballard, M. D. Baaske, and F. Vollmer, "Stand-off biodetection with free-space coupled asymmetric microsphere cavities," Sensors (Basel) **15**(4), 8968–8980 (2015).
12. H.-H. Yu, C.-H. Yi, and C.-M. Kim, "Mechanism of Q-spoiling in deformed optical microcavities," Opt. Express **23**(9), 11054–11062 (2015).
13. H. M. Lai, P. T. Leung, K. Young, P. W. Barber, and S. C. Hill, "Time-independent perturbation for leaking electromagnetic modes in open systems with application to resonances in microdroplets," Phys. Rev. A **41**(9), 5187–5198 (1990).
14. G. Kurizki, A. Kofman, A. Kozhekin, and G. Harel, "Control of atomic state decay in cavities and microspheres," New J. Phys. **2**, 28 (2000).
15. K. Srinivasan, O. Painter, A. Stintz, and S. Krishna, "Single quantum dot spectroscopy using a fiber taper waveguide near-field optic," Appl. Phys. Lett. **91**(9), 091102 (2007).
16. B. Redding, E. Marchena, T. Creazzo, S. Shi, and D. W. Prather, "Comparison of raised-microdisk whispering-gallery-mode characterization techniques," Opt. Lett. **35**(7), 998–1000 (2010).
17. N. Riesen, S. Afshar V., A. François, and T. M. Monro, "Material candidates for optical frequency comb generation in microspheres," Opt. Express **23**(11), 14784–14795 (2015).
18. J. Zhang, L. Xue, and Y. Han, "Fabrication gradient surfaces by changing polystyrene microsphere topography," Langmuir **21**(1), 5–8 (2005).
19. H. Chew, "Radiation and lifetimes of atoms inside dielectric particles," Phys. Rev. A **38**(7), 3410–3416 (1988).

#246072 Received 29 Jul 2015; revised 15 Oct 2015; accepted 15 Oct 2015; published 27 Oct 2015

20. T. Reynolds, M. R. Henderson, A. François, N. Riesen, J. M. M. Hall, S. Afshar V., S. J. Nicholls, and T. M. Monro, "Optimization of whispering gallery resonator design for biosensing applications," Opt. Express **23**(13), 17067–17076 (2015).
21. M. J. Humphrey, E. Dale, A. Rosenberger, and D. Bandy, "Calculation of optimal fiber radius and whispering-gallery mode spectra for a fiber-coupled microsphere," Opt. Commun. **271**(1), 124–131 (2007).

1. Introduction

Whispering gallery modes (WGMs), otherwise referred to as morphology dependent resonances, are optical modes propagating in resonators having at least one axis of revolution such as capillaries, disks or toroids, spheres and shells [1–4]. Light that is trapped by total internal reflection circulates inside the cavity close to the surface, and when returning in phase gives rise to resonance features. In recent years there has been growing interest in WGMs in part because the spectral positions of the resonances are strongly dependent on the refractive index contrast between the resonator and its surrounding environment, and this phenomenon has been exploited for refractive index sensing applications such as label-free biosensing [5]. Furthermore, the position of the resonances is also dependent on the geometry of the resonator, and this aspect has been used to measure e.g. resonator deformation induced by mechanical stress in various contexts [6,7].

Several approaches have been used to excite and collect WGMs in microresonators such as microspheres, the most common being through a tapered optical fiber, phase-matched with the propagating WGMs in the resonator [2,5,8]. Recently, there has been emerging interest in the use of active microresonators, i.e. resonators that contain a gain medium, enabling either fluorescence [9,10] or lasing of the WGMs [4]. Active microresonators permit the use of free-space excitation and collection of the WGMs, alleviating some of the practical issues related to the use of tapered fibers. The practical issues include fluctuation of the taper position with respect to the resonator which can result in increased spectral noise in the WGM signal, or the inevitable degradation of the transmission of the fiber taper from the fouling of the surface during e.g. biological sensing experiments [11]. Nevertheless, in most cases the WGMs excited and collected with a tapered fiber show extremely high Quality factors (Q-factors) ($\sim 10^5$ to 10^9) [1,5], defined as the ratio between the wavelength position of the mode and its linewidth ($\lambda/\Delta\lambda$). In contrast, the vast majority of work in the literature involving far-field WGM collection from fluorescent microspheres reports Q-factors several orders of magnitude lower (500 to $\sim 10^4$) [4,9,10]. In this paper we demonstrate that a contributing factor to the difference is the increased role of geometric eccentricity on the spoiling of the Q-factor for far-field detection. This is in addition to the role of spectral broadening and fluorescence emitter linewidth in decreasing the Q-factor for active resonators [9].

In a recent paper by Yu *et al*. [12], a numerical demonstration was given of the spoiling of the Q-factor in disks resulting from small deformations. In this paper, we consider the case of spherical resonators, and it is shown that for active microspheres the spoiling of the Q-factor due to geometric eccentricity involves a different mechanism. We demonstrate that the collection scheme of the WGMs (tapered fibers vs far-field) from a given active microsphere plays a significant role in determining the measured Q-factor. This is a consequence of WGMs having spectral positions that are highly dependent on the resonator's morphology as stated above, and the fact that a microsphere is never perfect, always having a certain degree of asphericity. The asphericity essentially lifts the degeneracy between modes of different polar number resulting in 'mode-splitting,' in which the modes have unique resonance frequencies [6,13,14]. The split in modes is unique to different planes, all of which are excited in the case of an active microsphere. The difference between taper and far-field collection is that the highly mode-selective nature of the taper allows for the collection of a much smaller subset of polar modes, that are confined to a single equatorial plane [8]. In the case of far-field collection a near-continuum of split-modes from multiple planes are sampled indiscriminately. This results in linewidth broadening and hence a reduction in the effective Q-factor.

#246072 Received 29 Jul 2015; revised 15 Oct 2015; accepted 15 Oct 2015; published 27 Oct 2015

2. Experimental results

These hypotheses are investigated in this paper by comparing taper and far-field sampling of the WGMs of active microspheres excited in both cases by free-space illumination. The reduction in Q-factor of active microspheres in the far-field due to asphericity is also modelled numerically, and a novel Q-factor component is derived to take into account the spoiling of the cavity Q-factor.

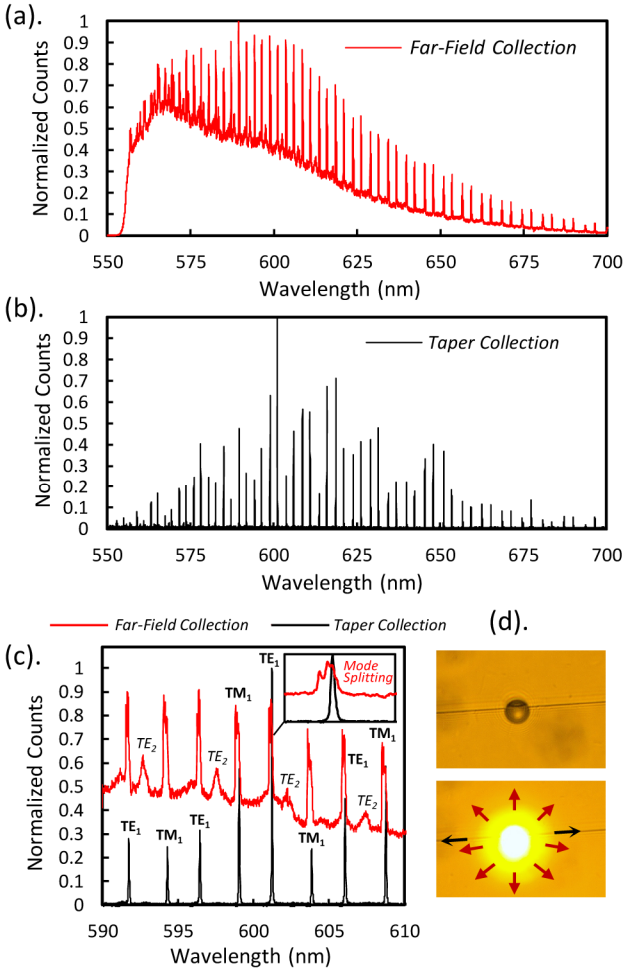

Fig. 1. (a)-(b) Whispering gallery mode spectra sampled in the far-field (red) and via the taper (black) of the same dye-doped polystyrene microsphere excited with free-space illumination. The measurements were taken simultaneously at the same pump power. (c) A closer look at the whispering gallery mode spectra of the polystyrene microsphere, and signs of mode-splitting for far-field collection (inset). (d) Microscope images showing the taper and attached microsphere under free-space excitation.

In order to reach an unambiguous conclusion, we used an experimental setup [15, 16] where the WGM signal from a single active microsphere can be acquired simultaneously from both a phase-matched tapered optical fiber and in the far-field, ensuring identical settings for the comparison. To achieve that goal, a drop of dye-doped polystyrene microsphere solution was placed onto a microscope glass slide positioned onto an inverted microscope (IX 71, Olympus, Japan) set up in a confocal arrangement, allowing for the simultaneous excitation and far-field collection of the fluorescent microspheres. A packaged 1 micron diameter fiber taper was fixed to a separate 3-axis stage, allowing for the fiber taper to

#246072 Received 29 Jul 2015; revised 15 Oct 2015; accepted 15 Oct 2015; published 27 Oct 2015

be maneuvered independently above the glass slide and within the microsphere solution droplet. This allowed for the taper to be positioned in contact with single microspheres. The microspheres were prepared from non-fluorescent commercial polystyrene spheres in aqueous solution (Ø ~15 μm; n = 1.59; Polysciences Inc., USA) by doping them with a fluorescent dye (Nile Red, λ_{abs} ~532 nm, λ_{em} ~590 nm, Sigma Aldrich) using a method described elsewhere [4]. The free-space excitation of the microspheres was achieved through the inverted microscope with a × 20 objective, using a λ ~532 nm CW laser as the pump source. The pump power at the focal point of the microscope objective was 3.0 mW with a spot size comparable with the microsphere's diameter (Ø~15 μm). For far-field collection, the emission was collected back through the same × 20 objective and coupled into a 200 μm patch fiber. For both WGM collection strategies (i.e. far-field vs tapered fiber), the WGM spectra were resolved with a spectrometer (iHR550, Horiba, Japan) equipped with a 2400 mm^{-1} grating and a cooled CCD (Synapse 2048 pixels, Horiba, Japan).

Figures 1(a) and 1(b) show the WGM spectrum of a single free-space illuminated microsphere collected in the far-field through the microscope and through the attached fiber taper, respectively. Microscope images of the microsphere and attached taper are given in Fig. 1(d). In both cases, the WGMs are clearly distinguishable, although the fluorescence background in the far-field spectrum of Fig. 1(a), is absent in the fiber taper collection spectrum of Fig. 1(b) as would be expected due to the negligible off-resonant coupling. The smaller, broad peaks visible in the far-field spectrum were identified as higher-order modes which do not couple efficiently with the taper. The highly mode-selective nature of tapers means that such discrepancies in far-field and tapered fiber transmission spectra are to be expected. A closer view of both spectra centered at 600 nm is provided in Fig. 1(c), highlighting the difference in linewidth and therefore Q-factor measured for the same microsphere excited at the same pump power, but collected in two different ways. This result demonstrates the significant dependence of the measured Q-factor on the collection mechanism used. In the case of far-field collection the Q-factor is ~2600, whereas for taper-collection for the same microsphere at the same time and under the same excitation conditions yields a Q-factor of ~12,600. This approximately five-fold increase in Q-factor was consistent amongst many microspheres tested. Note that the presence of the taper appeared to have negligible influence on the far-field Q-factor, with no change observed upon attachment. Furthermore the measured Q-factors were steady suggesting minimal spectral noise due to motion of the sphere or taper.

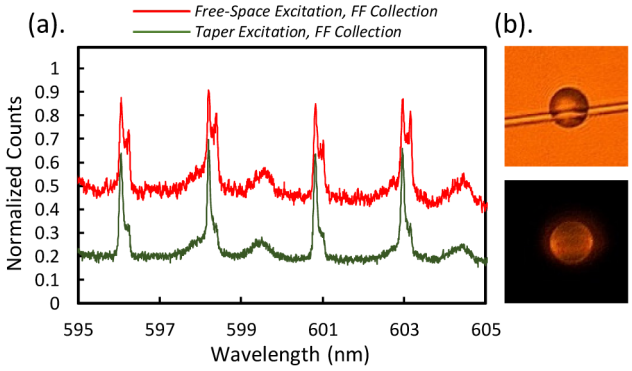

Fig. 2. (a) Whispering gallery mode spectra sampled in the far-field of the same dye-doped polystyrene microsphere excited with either the taper (green) or with free-space illumination (red). (b) Microscope images showing taper excitation of the microsphere with the pump wavelength removed using a dichroic filter.

Given the clear difference in Q-factor for the two different collection schemes (i.e. taper vs far-field) we also investigated the influence of the excitation mechanism. This involved comparing the far-field collected spectrum of an active microsphere for free-space (red curve)

#246072 Received 29 Jul 2015; revised 15 Oct 2015; accepted 15 Oct 2015; published 27 Oct 2015

and taper excitation (green curve) as shown in Fig. 2. In this case the Q-factor is improved by only a factor two when using the taper.

As seen in Fig. 2(b) the WGMs of the active microsphere excited with the taper are more spatially confined than is observed for free-space excitation (see Fig. 1(d)). However since the fluorescent dye emits in all directions the WGM confinement to a single plane is weak. The Q-factor improvement using taper excitation is less significant than when using taper collection (i.e. Figure 1), due to both the near indiscriminate emission of the dye into various WGMs/planes of the sphere, regardless of the excitation technique, and the indiscriminate sampling occurring for far-field collection. This results in a larger number of near-degenerate modes being sampled than for taper collection, which overlap to contribute to linewidth broadening. Compared with free-space excitation, the mode-splitting is more clearly evident here due to the smaller subset of modes/planes excited when using taper excitation. The dual-peak resonances in Fig. 2 are indicative of an ellipticity in the resonator [13]. Note also that the higher-order modes are present in both spectra due to the indiscriminate nature of far-field sampling.

3. Theoretical analysis

In the following section we propose and model a Q-factor component for an active microsphere due to a given degree of asphericity, assumed to be small, for free-space WGM excitation and collection. This Q-factor component (denoted here by Q_{FF}) contributes to the overall cavity Quality factor through the usual expression, $Q^{-1} = \sum 1/Q_i$, where Q_i are the individual components accounting for radiative losses from the curved microsphere surface (Q_{geo}) [17], scattering losses due to surface in-homogeneities (Q_s), material losses (Q_{mat}) [1,17], and as mentioned, the asphericity of the microsphere (Q_{FF}).

In the case of the polystyrene microspheres, $Q_s \sim 10^6$ assuming a surface roughness with correlation length and variance of 25 nm [18]. In the extreme case of a correlation length and variance of 50 nm, the Q-factor due to scattering reduces to $Q_s \sim 6 \times 10^4$, which is still significantly higher than the measured Q-factor. The Q-factor due to material losses [1] is $Q_{mat} \sim 10^7$, assuming an attenuation coefficient of $\alpha_m = 0.3$ dB/m. The Q-factor due to tunneling or radiation losses determined using the Chew model is $Q_{geo} \sim 2 \times 10^5$ [19]. In our experiments the resolution of the spectrometer was 4 pm, equivalent to a maximum Q-factor that can be resolved at 600 nm of $Q_{spect} \sim 5 \times 10^4$. The measured Q-factor ($Q \sim 10^3$) for far-field collection is however consistently far lower than any of these Q-factor components even with conservative estimates. As mentioned, the discrepancy can in part be attributed to the slight asphericity of the resonator.

Two different approaches were adopted for modeling the Q-factor spoiling due to the asphericity (Q_{FF}). The first involved modelling the excitation of many sphere planes with slightly varying radii, and the second involved modelling polar mode-splitting of a single plane due to an elliptical distortion of the sphere (as described in [13]).

3.1 Multiple-plane model

The spoiling of Q-factor by the free-space excitation and collection of resonances from multiple sphere planes of slightly different radii was modeled by calculating the wavelength shift of the most sensitive resonances of a perfect sphere, i.e. the first-order fundamental ($m = l$) modes, as the radius ρ, is varied over a range $\Delta\rho$. Since multiple planes are excited indiscriminately in an active microsphere, the result is the sampling of almost a continuum of slightly perturbed resonances, which superimpose to broaden the initial resonances, hence resulting in the dramatic reduction in the Q-factor. The corresponding Q-factor component (Q_{FF}) can be approximated by $\lambda/\Delta\lambda$, where λ is the wavelength of a given fundamental mode, and $\Delta\lambda$ is the range of resonance wavelength perturbations across all sampled WGM planes. For very small perturbations, the value $\Delta\lambda$ can be determined simply from the range of effective radii over all sampled planes, $\Delta\rho$. Here effective radius is simply the radius of a perfect sphere with circumference equal to the boundary of a given irregular plane. If there is

#246072 Received 29 Jul 2015; revised 15 Oct 2015; accepted 15 Oct 2015; published 27 Oct 2015

a continuum of radii within the range $\Delta\rho$ for all the excited/sampled planes, the modes overlap and broaden the initial linewidth resulting in a reduction of the effective Q-factor.

Assuming that $l \sim 2\pi\rho n/\lambda$ which is an appropriate estimate for e.g. the fundamental modes in the limit of $l >> 1$, an approximation of Q_{FF} for an active microsphere is,

$$Q_{FF} = \frac{\omega}{\Delta\omega} \approx \frac{\rho}{\Delta\rho} \tag{1}$$

This expression is given by the black line in Fig. 3(b) for ρ = 7.5 μm. This far-field Q-factor component (Q_{FF}) is not dependent to first-order on the specific wavelength or refractive index contrast, whereas it is proportional to the size of the microsphere. For a given level of asphericity $\Delta\rho$, the value of Q_{FF} decreases with smaller sphere size, as might be expected. Note however that the influence of Q_{FF} on the overall Q-factor is likely to be less significant for very small microspheres ($\rho \sim\lambda$) or small refractive index contrast Δn, due to the inherently low Q_{geo} to begin with.

At this point it should be noted that since far-field detection relies on radiative tunneling losses (or surface scattering) the collection mechanism tends to become inefficient for large ρ, such that the resonances might no longer be detected [16]. This is one of the reasons why tapered fiber collection is prefered for large microspheres. Far-field collection can only be used in the regime where radiative bending losses are greater or comparable to the internal loss mechanisms of the resonator or when scattering losses are high [16], and the models presented in this paper are limited in practice to this regime.

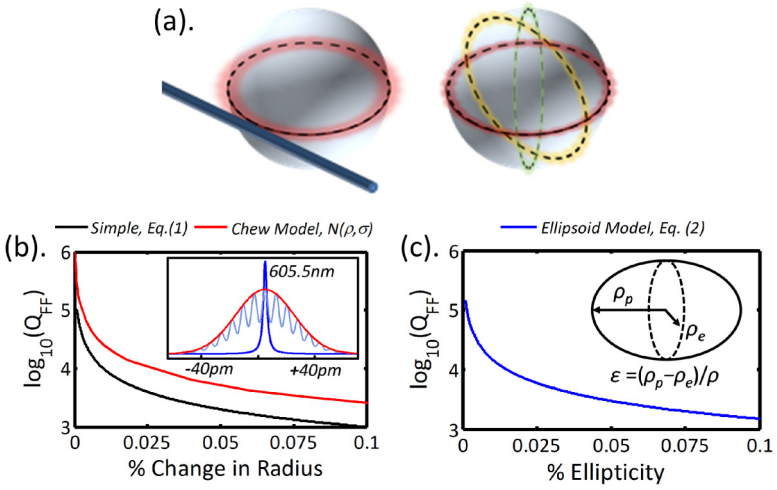

Fig. 3. (a) Depiction of the fiber taper and far-field collection of the WGM signal of the microsphere. Quantification of the spoiling of the Q-factor of an active microsphere when using far-field excitation and collection by (b) modelling the wavelength shift over a range of radii $\Delta\rho$ of a perfect microsphere or (c) the wavelength shift associated with mode-splitting for given levels of ellipticity ε. The inset of (b) shows the Q-factor spoiling occurring for a Gaussian distribution of radii with mean 7.5 μm and standard deviation σ = 0.5 nm modelled using the Chew model [19, 20]. Here the dark blue curve is the fundamental mode for a perfect sphere, whereas the light blue peaks are the non-degenerate fundamental ($m = l$) modes for an aspherical resonator, which overlap to yield linewidth broadening as suggested by the red Gaussian fit.

The Q-factor spoiling was also calculated numerically using the same approach as before, but this time using the Chew model [19, 20]. WGM spectra of perfect spheres were generated for a range of radii $\Delta\rho$ and then summed, with the spectrum generated for each radius weighted with respect to the radii distribution used. Here a normal distribution was used (compared with a uniform distribution assumed for Eq. (1)) such that the range $\Delta\rho$ corresponds to radii within 3 standard deviations of the mean, i.e. with mean ρ and standard

#246072 Received 29 Jul 2015; revised 15 Oct 2015; accepted 15 Oct 2015; published 27 Oct 2015

deviation $\sigma = \Delta\rho/6$. The Q_{FF} component based on $\lambda/\Delta\lambda$ was calculated from the summed spectrum by fitting a Gaussian distribution. An example calculation is shown in the inset of Fig. 3(b) for $\sigma = 0.5$ nm. The resulting Q-factors are shown by the red line in Fig. 3(b). The discrepancy with Eq. (1) arises due to the assumption of a normal distribution here which naturally yields higher Q-factor estimates for a given value of $\Delta\rho$.

We infer from Eq. (1) that if the variation in radius exceeds 190 picometres ($>2.5 \times 10^{-3}$%) for the polystyrene microspheres, the asphericity is likely to become the limiting factor on the Q-factor. For the experimental results the Q-factor measured (Q_{FF} ~2600) would suggest a 0.05% variation in radius equivalent to a plausible deviation of 3 nm across all equatorial planes.

3.2 Ellipsoid model

The second approach for modelling the Q-factor degradation for far-field collection due to asphericity involves considering an ellipsoidal perturbation. Ellipticity of a microsphere lifts the degeneracy between the polar modes as described in [13], which can then effectively broaden the initial resonance peak. To determine the associated Q-factor component, we first consider the quantum numbers commonly assigned to the modes of a microsphere for a given equatorial plane. These are the radial q, angular l, polar m (where $|m| \leq l$), and polarization mode numbers p [8]. The radial and angular mode numbers determine the number of nodes in the radial and azimuthal directions, respectively, and the number of lobes in the polar direction is determined by $l-m+1$. The fundamental modes ($m = l$) usually dominate, and correspond to propagation closest to the equator of the sphere [8]. In a perfect microsphere the subspace of modes of given q, l and p but with different values of m is $2l + 1$ fold degenerate. In practice the degeneracy is always lifted to some extent due to the asphericity of the microsphere resulting in a range of m-dependent frequencies. The asphericity essentially removes the degeneracy in path-length of modes with different polar order, m. Only a select number of these m-dependent modes of appropriate spatial confinement couple efficiently with an attached taper [8, 21]. In fact, using coupled mode theory it can be shown that the power coupled between a taper and the microsphere is proportional to $\exp(-\Delta\beta^2)$, where $\Delta\beta = \beta_f - m/\rho$ is the phase mismatch between taper and microsphere modes and β_f is the fiber modal propagation constant [8]. The exponential dependence implies that the taper-to-sphere coupling is highly mode-selective, as is well established, allowing for coupling with only a small subset of the m-dependent modes. The WGMs of lower polar order m also have wider polar distribution of the fields such that the spatial overlap with the taper modes is much lower. This can dominate over the phase mismatch since the propagation constants do not vary dramatically for different polar orders [8, 21]. The high mode-selectivity of the taper means that the mode-splitting is usually resolvable and evidenced by just a few different peaks in the sampled spectrum, with minimal linewidth broadening occurring [2, 13, 14]. For far-field collection there is almost no discrimination between different m-dependent modes (or different sphere planes). A large number of modes are therefore sampled, which partially overlap, resulting in linewidth broadening of the initial peak.

The expressions for mode-splitting in an ellipsoid of axially symmetric shape distortion are given by [13]. Assuming $l >> 1$, the relative shift in angular frequency due to an elliptical deformation (as defined in Eq. (1.2) of [13] with L = 2, M = 0) for polar mode m is [13],

$$\frac{\Delta\omega}{\omega} = \frac{\varepsilon}{6}\left(\frac{3m^2}{l^2} - 1\right) \tag{2}$$

where $\varepsilon = (\rho_p - \rho_e)/\rho$ is the ellipticity, and ρ_p and ρ_e are the polar and equatorial radii, respectively. We assume here that the ellipticity is sufficiently small such that the modes partially overlap. If we take the final peak width to be the total range of individual polar mode shifts, by calculating the difference between the two extremes $m = 0$ and $m = l$, we find a width of $\Delta\omega = 2\varepsilon\omega/3$, yielding a Q_{FF} of $3/2\varepsilon$. Figure 3(c) shows the slightly higher estimate in

#246072 Received 29 Jul 2015; revised 15 Oct 2015; accepted 15 Oct 2015; published 27 Oct 2015

Q-factor predicted by this model. For the Q-factor of 2600 measured for the polystyrene microspheres, this model would suggest a microsphere ellipticity of $\varepsilon \sim 5.8 \times 10^{-4}$ (i.e. $|\rho_p - \rho_e| = 4$ nm).

To determine whether the low levels of asphericity predicted by the two models are plausible, scanning electron microscopy (SEM) was used to image a number of the polystyrene microspheres. Samples were coated with a 5 nm platinum coating and imaged with a Quanta 450 SEM at a resolution of 4096 × 3775 pixels at × 5000 magnification. Images were then processed by adjusting the brightness/contrast, followed by the use of a threshold to obtain a two colour image of the sphere as shown in Fig. 4(b). An ellipse was then fit to each two colour sphere image using the Matlab image processing function "regionprops".

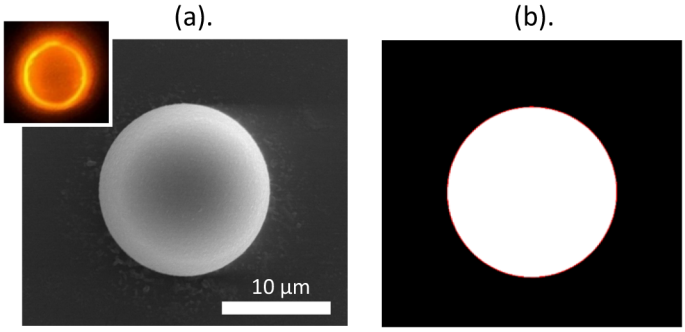

Fig. 4. (a) Low resolution scanning electron microscope (SEM) image of a 15 µm polystyrene microsphere. Inset shows the same sphere when excited by the taper (b) Corresponding two color threshold image with an ellipse fit shown (red line).

Over the seven samples measured, the difference in major and minor ellipse axes was 11 ± 4 pixels (corresponding to 80 ± 30 nm) with ellipse orientation of 2 ± 7°. Such a regular axis difference, with orientation consistently near 0°, is indicative of a systematic unequal aspect ratio of the imaging system (i.e. image stretching/contracting) rather than an actual ellipticity of the spheres. After compensating for this unequal aspect ratio, the ellipse fit was repeated for the spheres, yielding an average ellipticity of 4 pixels or 30 nm with random orientation. This level of ellipticity is at the detection limit of the measurement system and therefore represents an upper limit. It corresponds to a relative distortion of about 0.2% for the 15 µm spheres.

These SEM images demonstrate that the few nanometer asphericity suggested by the Q-factor spoiling in the far-field is plausible. The very low levels of asphericity are however very difficult to measure accurately, given the relatively large resonators considered. Indeed Q-factor degradation could be used as an indirect method of measuring such minute geometric asphericities. The SEM images also do not allow one to differentiate between the two models described. Note however that the two models merely represent two different ways of describing a small geometric perturbation, and yield nearly identical results.

4. Conclusions

This paper has investigated the Q-factor limits for active microspheres in the far-field due to slight asphericity. It has been shown that even minute geometric eccentricity of the order of tens of nanometers or less can significantly spoil the Q-factor for far-field collection. In this paper a Q-factor spoiling of more than a factor 5 is shown for 15 µm polystyrene microspheres due to a several nanometer eccentricity. Given these findings it is likely that the low Q-factors of active microspheres measured in far-field experiments could be mistaken for higher contributions from either scattering or material absorption. The technique of comparing both the far-field and evanescently coupled WGM signal from an active

#246072 Received 29 Jul 2015; revised 15 Oct 2015; accepted 15 Oct 2015; published 27 Oct 2015

microsphere could be exploited for various applications including strain sensing in which very small cavity deformations could be measured [6].

Acknowledgments

The authors acknowledge the support of an Australian Research Council Georgina Sweet Laureate Fellowship awarded to T. M. Monro, FL130100044. We also acknowledge Adelaide Microscopy for the use of SEM facilities. M. R. Henderson was supported by a grant from the National Breast Cancer Foundation Australia, NC-13-05.

#246072 Received 29 Jul 2015; revised 15 Oct 2015; accepted 15 Oct 2015; published 27 Oct 2015

Chapter 5

Fibre Tip Sensing

5.1 A Fibre-Tip Label Free Biological Sensing Platform: A Practical Approach Toward *in-vivo* Sensing

P4. François, T. Reynolds, and T.M. Monro, "A fibre-tip, label free biological sensing platform: A practical approach to *in-vivo* sensing," *Sensors* 15 (1)**,** 1168-1181, 2015.

5.1.1 Publication Overview

As highlighted in Chapter 4, the Q-factor of dye-doped polystyrene microspheres can be improved using a phase-matched fiber taper for the collection of the WGM modulated fluorescence spectrum. However, as previously detailed, implementing such a coupling scheme severely limits the practical applicability of the sensor. An alternative approach, which still results in an increase of the Q-factor by breaking the symmetry of the resonator, is to place the resonator in one of the holes at the tip of a MOF. Not only does the fibre provide the excitation and collection method for the WGMs, but also provides a robust and easy to manipulate dip sensing architecture that circumvents the need for complex microfluidic integration as well as having the potential to be used *in-vivo* if it were to be combined with a catheter.

The potential of this sensor, based on combining dye-doped polystyrene microspheres with a MOF, to conduct real-time biosensing can be examined utilizing the well-known specific interaction model based on Biotin/neutravidin within pure solutions. A key element in determining a sensors performance, asides from the Q-factor and refractive index sensitivity, is the surface functionalization. Therefore, before moving to monitor a specific interaction, the physiosorption process of depositing of layers of alternating charges of polyelectrolytes was examined closely to identify the number of layers required ensure complete coverage and hence maximize the available amine sites for the immobilization of the Biotin. Next, the specific interaction was monitored in varying concentrations when the resonator was operated both below and above its lasing threshold. This revealed that the increase in Q-factor, due to operating the resonator above its lasing threshold, provided an increase in resolution and hence allowed lower concentrations of Neutravidin to be observed.

5.1.2 Statement of Contribution

Statement of Authorship

Title of Paper	A fibre-tip, label-free biological sensing platform: A practical approach to *in-vivo* sensing
Publication Status	☒ Published ☐ Accepted for Publication ☐ Submitted for Publication ☐ Unpublished and Unsubmitted w ork w ritten in manuscript style
Publication Details	A. Francois, T. Reynolds, and T. M. Monro, "A fibre-tip, label-free biological sensing platform: A practical approach to *in-vivo* sensing," Sensors, 15 (1), 1168-1181, 2015.

Principal Author

Name of Principal Author (Candidate)	Alexandre Francois		
Contribution to the Paper	Proposed the work, designed, supervised and performed the experiment and acted as corresponding author.		
Signature		Date	15-11-16

Co-Author Contributions

By signing the Statement of Authorship, each author certifies that:

i. the candidate's stated contribution to the publication is accurate (as detailed above);

ii. permission is granted for the candidate in include the publication in the thesis; and

Name of Co-Author	Tess Reynolds		
Contribution to the Paper	Contributed to data analysis and writing and editing of the manuscript. Overall percentage: 30%		
Certification:	This paper reports on original research I conducted during the period of my Higher Degree by Research candidature and is not subject to any obligations or contractual agreements with a third party that would constrain its inclusion in this thesis. I am the primary author of this paper.		
Signature		Date	11-11-16

Name of Co-Author	Tanya M. Monro		
Contribution to the Paper	Supervised the project and contributed to manuscript editing and evaluation.		
Signature		Date	14-11-16

Sensors **2015**, *15*, 1168-1181; doi:10.3390/s150101168

OPEN ACCESS

sensors

ISSN 1424-8220

www.mdpi.com/journal/sensors

Article

A Fiber-Tip Label-Free Biological Sensing Platform: A Practical Approach toward *In-Vivo* Sensing

Alexandre François [1,*], Tess Reynolds [1] and Tanya M. Monro [1,2]

[1] The Institute for Photonics and Advanced Sensing (IPAS) and ARC Centre of Excellence for Nanoscale Biophotonics (CNBP), the University of Adelaide, Adelaide SA 5005, Australia; E-Mails: tess.reynolds@adelaide.edu.au (T.R.); tanya.monro@adelaide.edu.au (T.M.M.)

[2] University of South Australia, Adelaide SA 5000, Australia

[*] Author to whom correspondence should be addressed; E-Mail: alexandre.francois@adelaide.edu.au; Tel.: +61-8-8313-2328; Fax: +61-8-8313-4380.

Academic Editor: W. Rudolf Seitz

Received: 2 October 2014 / Accepted: 31 December 2014 / Published: 9 January 2015

Abstract: The platform presented here was devised to address the unmet need for real time label-free *in vivo* sensing by bringing together a refractive index transduction mechanism based on Whispering Gallery Modes (WGM) in dye doped microspheres and Microstructured Optical Fibers. In addition to providing remote excitation and collection of the WGM signal, the fiber provides significant practical advantages such as an easy manipulation of the microresonator and the use of this sensor in a dip sensing architecture, alleviating the need for a complex microfluidic interface. Here, we present the first demonstration of the use of this approach for biological sensing and evaluate its limitation in a sensing configuration deprived of liquid flow which is most likely to occur in an *in vivo* setting. We also demonstrate the ability of this sensing platform to be operated above its lasing threshold, enabling enhanced device performance.

Keywords: fiber optics sensors; biological sensors; microcavities; laser resonators

1. Introduction

Over the last decade, whispering gallery modes (WGMs) have found applications in label-free optical biosensing, enabling operation down to the single molecule level [1,2] and also miniature laser

sources [3–5], waveguides [6], filters [7] and mechanical [8,9] and temperature [10,11] sensors. Generally, WGMs can be described as light being trapped within a resonator by total internal reflection, circulating along the inner surface and returning in phase after a single or multiple round trips to satisfy the resonance conditions [12]. Multiple resonator geometries have been reported in the literature, ranging from rings/toroids [13] and spheres [14] to cylinders and capillaries [15,16]. The spectral position of the resonances is dictated not only by the resonator geometry (diameter, sphericity) and optical properties but also by the refractive index of the environment surrounding the resonator [12], making this phenomenon particularly interesting for label-free biosensing applications.

A key parameter of such resonators is the quality factor (Q) which effectively describes how many round trips a photon can undergo within the resonator before being lost by absorption or scattering. WGMs can exhibit extremely low losses; when the refractive index contrast at the resonator boundaries is high, the radius of curvature of the resonator exceeds several wavelengths and the intrinsic scattering and surface roughness is small [15], the Q factor can reach several millions, as demonstrated for silica spheres and toroids [13,17]. While such high Q factor resonators can exhibit outstanding sensing performance, their utilization remains restricted in practice. For high Q factor resonators, light must typically be coupled into the resonator through the evanescent field of carefully aligned fiber taper [12,14] or a prism [18]. These approaches are limited by the requirement to maintain a precise gap between the resonator and the tapered fiber or prism to stabilize the position of the resonance [19], realistically rendering these platforms unfit for non-laboratory applications such as point of care or *in vivo* diagnostics.

Our approach is to combine WGMs as transduction mechanism using an active spherical resonator integrated onto the tip a suspended core Microstructured Optical Fiber (MOF) to create a label-free biosensing platform with the potential application for *in vivo* biosensing. A single dye doped microsphere is located onto one of the holes at the tip of a suspended core fiber as shown in Figure 1B,C. This simple approach takes advantage of the Purcell effect to amplify the emission of light from a gain medium at the resonance frequencies when located within the resonator [20]. Positioning the fluorescent microsphere onto the suspended core microstructured optical fiber tip as seen in the Figure 1A provides a pathway for both the remote excitation and collection of the WGM modulated fluorescence emission seen in the Figure 2A,B, alleviating the need for a cumbersome positioning/coupling scheme [21] as described above. While the use of a high refractive index polymer such as polystyrene (polystyrene = 1.59) as the sphere material enables us to use smaller resonators with higher refractive index sensitivity compared to larger silica spheres, this choice impact the resonator's Q factor, since polymer microspheres have relatively low Q factors [22]. It is important to note that since the analysis of the WGM signal is performed using a standard monochromator to resolve both the spectral position and linewidth of the resonance features, the resolution is ultimately limited by the detection system, which is typically around 4 pm using a 2400 L/mm grating.

In-vivo biological sensing is an emerging field with much promise for revolutionary medical diagnostic applications and fundamental breakthrough in biology by enabling measurements to be performed where it has not been possible so far [23]. In this context, optical fiber probes are particularly suited for minimally invasive procedure where the tip of the fiber is rendered active toward the detection of a specific biochemical compound [24,25]. While it is now possible to detect a wide

range of biomolecules, ranging from metabolite ions and chemicals [23] such as glucose [25] to enzymes [23,24], the specific detection and quantification of proteins remains an unmet challenge.

Here we evaluate the performance of our fiber tip WGM sensing platform [16,21] for biosensing applications using biotinylated microsphere to specifically capture neutravidin as a first demonstration of the biosensing capabilities of this platform. To mimic the conditions that such a sensor is likely to encounter in an *in vivo* sensing situation, we have deliberately chosen to perform the detection in static conditions and evaluate the detection limit as function of the surrounding neutravidin concentration to assess its suitability for such application. We also investigate how to improve the detection limit by inducing lasing of the WGM to increase the sensor resolution and eventually detection limit.

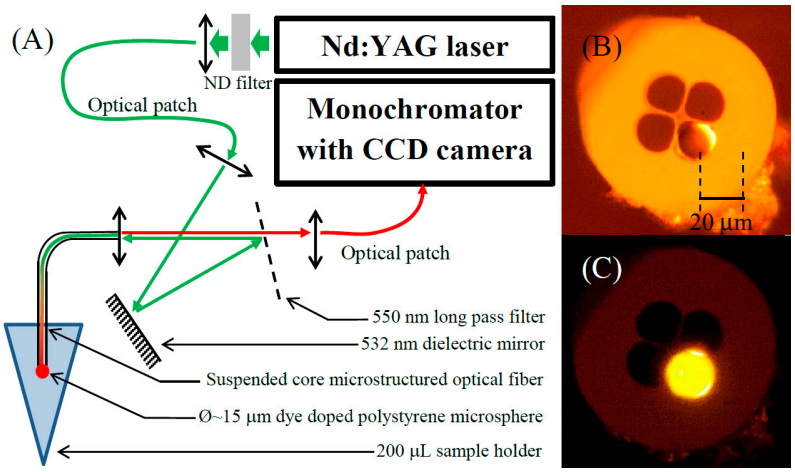

Figure 1. (**A**) schematic of the optical setup; (**B**,**C**) bright field and fluorescence images of a 20 µm diameter dye doped polystyrene microsphere positioned onto the tip of a suspended core silica fiber respectively ($Ø_{core}$ = 4 µm, $Ø_{hole}$ = 17 µm).

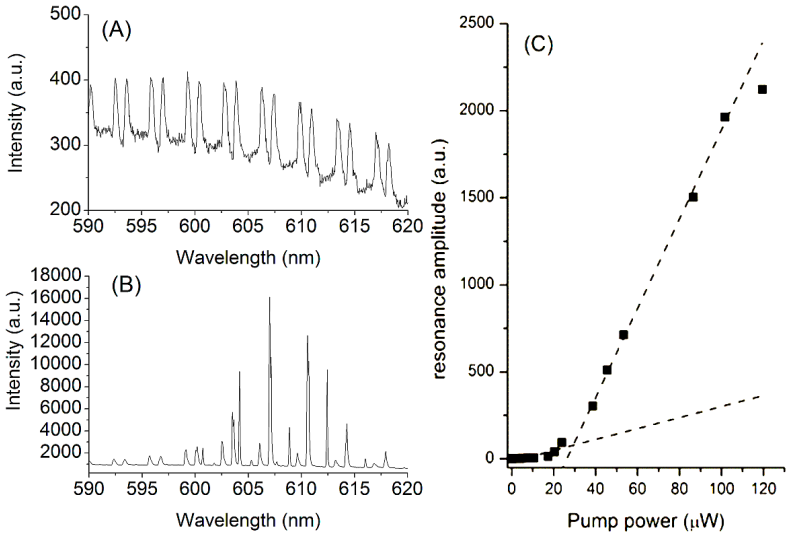

Figure 2. (**A**,**B**) WGM spectra below and above the lasing threshold respectively; (**C**) resonance amplitude as function of the pump power.

2. Experimental Section

2.1. Chemicals

Polystyrene (PS) microspheres (Ø~20 μm, nPS = 1.59) were purchased from Polysciences, Inc., (Warrington, PA, USA). Nile red fluorescent dye, xylene, poly(allylamine hydrochloride) (PAH), MW ~15,000 Da and poly(sodium 4 styrenesulfonate) (PSS), MW ~70,000 Da were received from Sigma-Aldrich (Sydney, Australia) , glycerol, >99%, was obtained from Chem-Supply (Gillman, Australia), all chemicals were used as received. N-hydroxysuccinimide (NHS), 1-Ethyl-3-[3-dimethylaminopropyl], carbodiimide hydrochloride (EDC), and ethanolamine hydrochloride (EA), 1 M, were obtained from VWR International (Murarrie, Australia) as a part of the Biacore amine coupling kit. Phosphate buffered saline (PBS) was received in the form of tablets from Sigma-Aldrich (Sydney, Australia) and dissolved in deionized (DI) water yielding a pH of 7.4. Biotin D and neutravidin were received from Sigma Aldrich (Sydney, Australia) and diluted to the relevant concentration in PBS.

2.2. Microspheres Preparation

Polystyrene microspheres with a nominal diameter of 20 μm (ΔØ = 0.8 μm, n = 1.59) were doped with a fluorescent laser dye (Nile Red, λ_{abs} = 532 nm, λ_{em} = 590 nm) using a liquid two phase system [16,21]. Among the different techniques reported in the literature to either introduce a gain medium within a polymer microsphere [26] or simply coat its surface with either quantum dots or organic dye molecules [27,28], this approach enables high dye content to be loaded within the polymer sphere which is critical for reaching the lasing threshold of the WGMs. The fluorescent dye was first dissolved into xylene until the solubility limit was reached. The resulting solution was poured on top of an aqueous solution of diluted microspheres and left on a magnetic stirrer plate until the xylene had completely evaporated. As xylene and water are immiscible and the fluorescent laser dye used hydrophobic, when the xylene evaporates, the fluorescent dye is transferred into the microspheres that come into contact with the dye solution. After the doping procedure, the microsphere solution was heated above the boiling temperature of the xylene for 1 h to remove any trace of solvent from the microspheres. The microspheres were then washed by centrifugation, the supernatant removed and the lost volume replaced by Millipore water.

2.3. Surface Functionalization

Immobilization of relevant proteins onto the microspheres surface was done through the use of polyelectrolyte (PE). Positively and negatively charged PE solutions, polyallylamine hydrochloride (PAH) and polystyrene sulfonate (PSS) respectively were prepared by dissolving 2 mg/mL of either PAH or PSS into a 1 M NaCl buffer. The deposition of the polyelectrolyte onto the microspheres was performed using the layer by layer technique described elsewhere [28,29]. Five layers (PAH/PSS/PAH/PSS/PAH) were deposited onto the spheres. Covalent binding of biotin-D onto the primary amine of the PAH coated sphere was performed in solution using 1-ethyl-3-(3-dimethylaminopropyl) carbodiimide (EDC) and N-hydroxysuccinimide (NHS) as coupling reagents. A

1 mg/mL biotin-D solution in PBS buffer (200 µL) was mixed with both a 1M EDC solution (100 µL) and 1 M NHS (100 µL) and then left incubating with the dye doped sphere solution (~2.5% volume, 100 µL) for two h. After the immobilization of the biotin-D onto the sphere surface, the microspheres were washed by centrifugation, the supernatant removed and the lost volume replaced by PBS. The passivation of the non-specific binding sites was achieved by incubating the functionalized spheres in a 2.5% casein solution for 24 h. After the passivation step, the sphere were again washed by centrifugation and redispersed in PBS buffer before being stored at 4 °C.

2.4. Optical Setup

The optical setup used to operate the sensor is depicted in the Figure 1A. A doubled frequency YAG laser (λ = 532 nm, ~9 ns pulse duration, 10 Hz repetition rate) was used for the excitation of the active microspheres. The beam emerging from the laser was first spatially filtered using a single mode fiber ($Ø_{core}$ = 8 µm) before being coupled into a silica suspended core Microstructured Optical Fiber (MOF; $Ø_{core}$ = 4 µm, $Ø_{hole}$ = 17 µm). A λ = 550 nm long pass filter was used at almost normal incidence, behaving as a dichroic mirror. This simple optical setup allowed the WGM modulated emission originated from the dye doped resonator, to be recaptured by the MOF, and launch it into a monochromator (600, 1200 and 2400 L/mm grating) equipped with a cooled CCD (2048 pixels) to record the WGM signal, while the sensor head, hence resonator onto the fiber tip, was dipped into a 200 µL sample holder.

2.5. Microsphere Attachment onto the MOF Tip

An inverted microscope equipped with a second three axis translation stage was used to position the microsphere onto the MOF tip. A drop of the microsphere solution was deposited onto a glass cover slip and inspected using the inverted microscope while the freshly cleaved MOF end was attached to the second translation stage with the fiber's tip pointing toward the drop of microsphere solution. A microsphere was selected from the many within the drop by qualitatively analyzing its emission spectrum via the confocal excitation and collection provided by the inverted microscope. Once located, the microsphere was brought into contact with the tip of a 80 cm long MOF which was aligned using the independent microscope stage. The microsphere and the MOF tip are both hydrophobic. Thus, once they come into contact, the microsphere tends to adhere to one of the holes of the MOF as shown in both Figure 1B,C. Once the microsphere is attached onto the fiber tip, it remains in this position, allowing easy manipulation of the sensor.

3. Results and Discussion

3.1. Characterization of the Lasing Behavior of the Dye Doped Resonator

To determine the lasing threshold of the processed dye doped polystyrene microspheres, the excitation power was systematically varied from 5 µW to 100 µW and the corresponding WGM spectra were recorded. The excitation power was calculated assuming a 50% coupling efficiency between the single mode fiber delivering the 532 nm double YAG and the suspended core fiber. This coupling efficiency was measured under the same conditions with a 532 nm CW laser following the

same optical pathway. Then, the mode exhibiting the highest lasing intensity was selected and fitted with a Gaussian function. Figure 2A,B shows typical WGM spectra below and above the lasing threshold from the same microsphere while Figure 2C displays the resulting dependence of the peak intensity on the excitation power. On Figure 2A,B the periodic repetition of the first order mode with different mode number and polarization can be seen as previously reported in the literature [4,8,21,22,26].

These figures show that only the modes located around 620 nm are lasing despite the fact the maximum emission of the dye used to dope the resonator is near 590 nm. This phenomenon can be explained by the higher absorption losses of the polystyrene at lower wavelengths [30], which reduces the gain at shorter wavelengths. The evolution of the peak intensity shows clearly two linear regimes with lower slope below and higher slope above threshold, respectively. Therefore, the lasing threshold could be determined by linear fitting of the two linear regions of spontaneous and stimulated emission as indicated by the dash lines in the Figure 2C and subsequent calculation of their intersection. This approach yields a lasing threshold for this resonator of 28 μW, in excellent agreement with previous reported values for a toroidal micro laser [31] and polystyrene microspheres [4,32], both with comparable Q factor. While the non lasing spheres typically exhibit a Q factor, ($Q = \lambda_{resonance}/\Delta\lambda_{resonance}$), around $3 \times 10^3 \pm 0.8 \times 10^3$, the lasing modes are significantly narrower as it can be seen in the Figure 2B, yielding a Q factor above $1.5 \times 10^4 \pm 0.5 \times 10^4$. As the Q factor is defined as the ratio of the stored energy into the resonator to the energy lost per cycle [33], a higher gain into the resonator, especially upon lasing will increase the stored energy while the lost energy per cycle which is an inherent property of the resonator remains constant, resulting in an increased Q factor. This increase of the Q factor is highly beneficial for sensing purposes as it increase the resolution of the sensor, enabling the detection of smaller changes in the resonance wavelength position [34].

3.2. Analysis of the Sensing Performance of the Dye Doped Resonator

To characterize the sensing performance of spheres in a situation that mimics an *in vivo* setting, we have deliberately chosen to simply dip the sensor head, meaning the microresonator attached to the fiber tip, into small Eppendorf tubes without providing any agitation of the solution under study. We do this to reflect the liquid flow that is most likely to occur while performing a measurement *in vivo* instead of using microfluidic flow cells. We sought also to identify the number of PE layers required to achieve a complete surface coverage of the sphere by monitoring the successive deposition of PE layers in real time for non-functionalized spheres. Once a suitable lasing resonator was identified and positioned onto the fiber tip, the sensor head was dipped into a 200 μL Eppendorf tube filled with Millipore water. A reference spectra of the sphere above its lasing threshold was acquired with the highest resolution grating available, yielding a resolution of 4 pm. The sensor head was then removed from the Millipore water and dipped into a second Eppendorf tube filled with PAH. Again another spectra was acquired under the same experimental conditions. After leaving the sensor head immersed in PAH solution for 30 min, it was removed and dipped into Millipore water for rinsing for 10 min before acquiring another spectra. As the concentration of the PE solutions used are very high (2 mg/mL), the coating efficiency/kinetic is thought not to be diffusion limited. This procedure was repeated for the deposition of each PE layer, up to five layers in total, with three different sensors. From each WGM

spectra, the spectral position of the resonance features were identify by fitting the resonance peaks with a Gaussian function.

The wavelength shift for three different spheres as function of the number of PE layers deposited is shown in Figure 3A. The error bars on Figure 3A are given as the fitting error of the resonance peaks. Figure 3B shows the results of the calculation of the deposited thickness achieved after each PE layer while the error bars on the determination of the layer thickness have been calculated as the standard deviation between the three different equivalent experiments and represent the accuracy in terms of reproducibility rather than the resolution of the sensor itself.

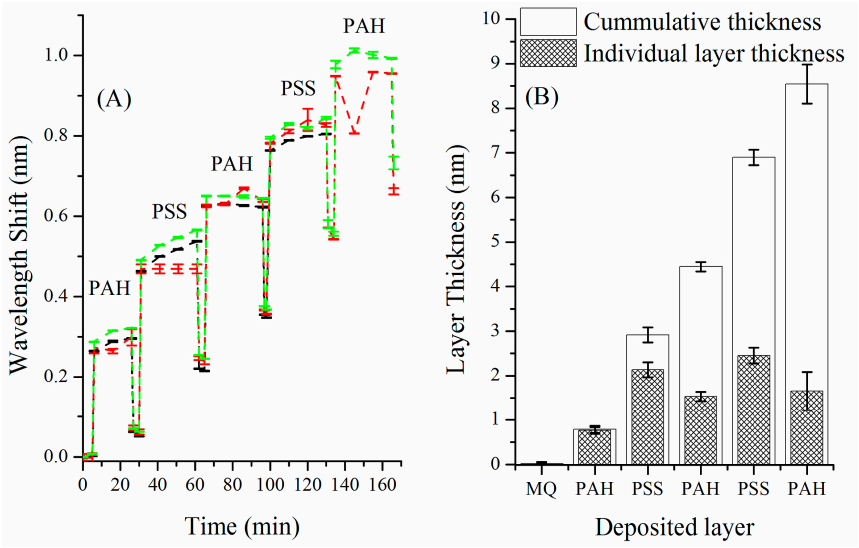

Figure 3. (**A**) Wavelength shift of the WGM of a Ø = 20 µm polystyrene dye doped microsphere for increasing number of deposited polyelectrolyte layers; (**B**) Cumulative and individual layer thickness calculated after the deposition of each polyelectrolyte layer.

From the wavelength shift, the increase of radius of the sphere can be calculated using Equation (1), where $\Delta\lambda$ is the wavelength shift, λ the initial resonance position, ΔR the effective increase in radius, R the initial resonator radius, e the thickness of the deposited layer, n_L and n_s the refractive index of the deposited layer, typically 1.5 for both PAH and PSS in solution [35], and the resonator respectively:

$$\frac{\Delta\lambda}{\lambda} = \frac{\Delta R}{R} = \frac{n_L e}{n_S R} \quad (1)$$

The initial radius can be calculated from the peak spacing of two successive modes with the same polarization using Equations (2) and (3):

$$R = \frac{\lambda_{m+1} \times m}{2\pi n_S} \quad (2)$$

$$m = \frac{\lambda_{m+1}}{\lambda_m - \lambda_{m+1}} + 1 \quad (3)$$

where m is the mode number, λ_{m+1} and λ_m the wavelength of two successive first order modes with the same polarization.

It becomes clear from the Figure 3B that the first layer (PAH) is significantly thinner than subsequent PAH layers. This indicates that the first layer doesn't fully cover the resonator which is not surprising and has been previously reported in the literature [28,29]. Nevertheless, the thickness of the first bi-layer (PAH/PSS) is about 3 nm, the second about 6.8 nm, which is good agreement with reported thicknesses of PAH/PSS bi layer deposited under the same conditions [36]. Therefore, we assumed for the subsequent surface functionalization steps that five PE layers would be sufficient to ensure good surface coverage and consequently maximize the density of free amine available for subsequent immobilization of biomolecules.

3.3. Demonstration of the Detection of a Specific Interaction

A similar experimental procedure was used to measure the specific binding kinetics of neutravidin onto the biotinylated surface of the resonator and determine what would be the detection limit in an *in vivo* sensing scenario. We choose to use biotin/neutravidin as a specific interaction model because it has been well characterized with other sensing platforms and therefore provides a useful benchmark test. Also it forms the basis of a surface functionalization process we recently used to produce an antibody coating with a specific orientation to increase the corresponding antigen capture efficiency [37].

From the estimate of the increase of radius from the previous section, one can calculate the quantity of adsorbed molecules as follows. The mass per unit surface of the adsorbed molecule is a convenient parameter that does not depend on the geometry of the sensor considered and therefore enables a direct comparison between different techniques and different sensor geometries. The mass per unit surface, *d*, can be calculated using the following equations [2]:

$$d = \frac{M}{N_A \sigma_p^{-1}} \tag{4}$$

$$\sigma_p^{-1} = \frac{n_S}{n_L} \frac{\alpha_{ex}}{\varepsilon_0 (n_S^2 - n_m^2)} \frac{1}{\delta R} \tag{5}$$

here, M is the molecular weight, N_A is the Avogadro number, σ_p^{-1} the projected area of the adsorbed molecule, α_{ex} its excess polarizability, and n_m the refractive index of the medium surrounding the microsphere (n_m = 1.33 for PBS buffer). In a first approximation, the polarizability, α, of the adsorbed molecule which can be calculated by means of the Clausius-Mossotti equation was used instead of the excess polarizability:

$$\alpha = \frac{\varepsilon_r - 1}{\varepsilon_r + 2} \frac{3M\varepsilon_0}{N_A \rho_m} \tag{6}$$

here, ε_r is the dielectric function of the considered molecule ($\varepsilon_r = n^2$ where n = 1.5 for most proteins [38], N_A is the Avogadro number and ρ_m the mass density (ρ_m = 1.37 g·cm^{-3} for most proteins [38]).

3.3.1. Binding Kinetics below the Lasing Threshold

As a first test, we replace the pulsed YAG laser pump source with a CW 532 nm solid state laser (2 mW pump power) and triggered the excitation with the acquisition (0.1 s) of the WGM signal performed once per minute to reduce the photobleaching of the organic dye. The objective behind this first set of measurements was to benchmark the binding kinetics when the sensor is operated below its lasing threshold. Figure 4A shows the binding kinetics for the neutravidin (M = 55,000 kDa) with concentrations ranging from 1600 nM (88 µg/mL) down to 4 nM (0.22 µg/mL). As observed in the Figure 4A, the highest concentration (1600 nM) can be easily detected and a saturation of the radius increase occurs within the first minute. We found that the surface density achieved at the steady state with the 1600 nM concentration is about 177 ± 45 ng/cm^2. This value, within the error, is about half of the density of a full neutravidin monolayer as reported in literature with surface plasmon sensors (445 ng/cm^2) [37].

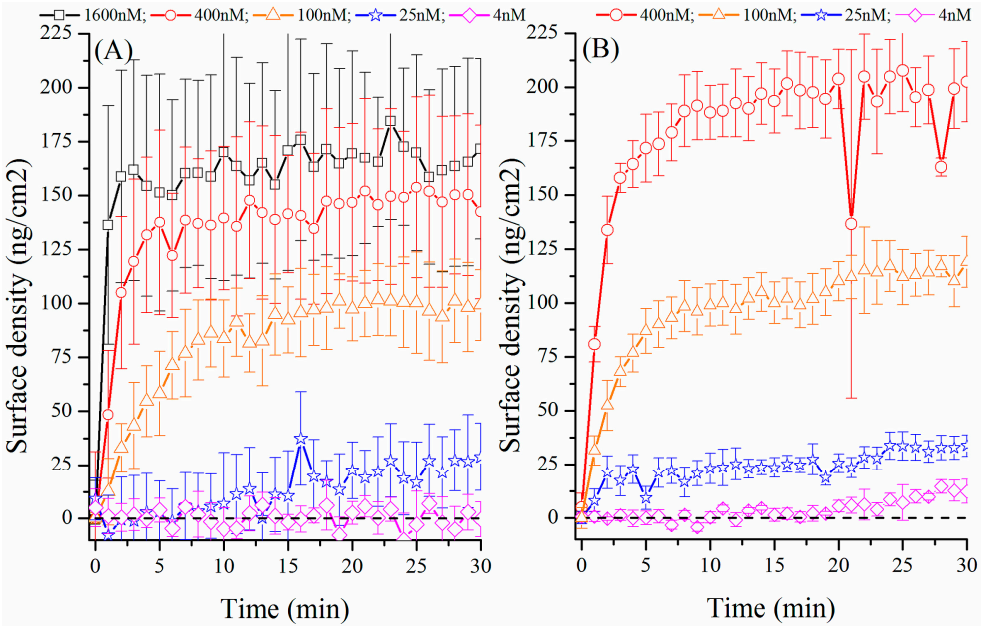

Figure 4. Binding kinetic for neutravidin on a Ø = 20 µm biotin functionalized sphere with sphere operated (**A**) below and (**B**) above the lasing threshold.

An explanation can be found from the observation that approximately one half of the resonator protrudes from the hole on the suspended fiber tip. Given that low concentrations are used during this experiment and that the sample is not subjected to agitation, we infer that the neutravidin did not penetrate into the hole of suspended core fiber, leaving a significant portion of the resonator surface unexposed to the analyte. For the 400 nM concentration, it takes about 5 min to reach the saturation level with a saturation value about half that obtained with the 1600 nM concentration while for the 100 nM concentration, equilibrium is reached after 15 min with an even lower saturation level. Reducing further the concentration a similar trend is found, although the equilibrium regime is then barely reached after 30 min. For the lowest concentration used, 4 nM, no noticeable change of the resonance position was observed beyond the noise level, indicating that this concentration is beyond

the detection limit of the sensor. The error bars have been calculated as the standard deviation from the three sets of experimental data acquired for each concentration.

3.3.2. Binding Kinetic above the Lasing Threshold

We repeated the same binding kinetics measurements using the frequency doubled YAG laser as a pump source to operate the spheres above their lasing threshold in an attempt to increase the Q factor and thus improve the detection limit of the sensor defined as the ration between the sensor's resolution and resolution (DL = R/S) [34].

The binding kinetics presented in Figure 4B, obtained with lasing resonators, follow a similar trend as the binding kinetics obtained while exciting the resonators below their lasing threshold. Saturation of the sensor surface upon exposure to the 400 nM neutravidin solution is observed after few minutes while the other concentrations never yielded saturation within the 30 min time frame. However a slight wavelength shift of the WGM, and therefore binding of the neutravidin onto the sensor surface can be observed with the 4 nM concentration, which is not the case with the spheres operated below their lasing threshold. To confirm the specificity of the interaction, the results observed with the lowest neutravidin concentration were repeated using the microspheres without the biotin coating but passivated against non-specific binding with casein following the protocol previously described. In this case, no binding was observed confirming that casein can efficiently block non-specific binding from neutravidin and that for the lowest concentration, the observed wavelength shift is only due to the specific binding of neutravidin onto the biotinylated spheres. This is not surprising considering an effective increase of the Q factor induced by the lasing behavior and the resulting increase of limit of detection. In fact, it can be clearly seen by comparing Figure 4A,B that the error on the measurement which has been determined as the deviation from the mean value from the three sets of independent measurements performed is much lower when the microsphere is excited above its lasing threshold which allows to discriminate the increase of wavelength shift or surface density as presented in both Figure 4A,B from the noise. Despite the absence of flow, which certainly limits the sensor's performance, a limit of detection of 4 nM neutravidin solution is achieved. In term of surface density of bound protein, this is equivalent to 1.3×10^{15} molecules/m^{-2} or 120 pg/mm^2 in an environment deprived of liquid flow. This is approximately 50 times lower than the fiber based WGM sensor reported by Boleininger *et al.* (LOD = 7×10^{16} molecules/m^{-2}) [39] or half of the detection limit claimed by Chao *et al.* (LOD = 250 pg/mm^{-2}) [40].

4. Conclusions

In this paper, we have demonstrated the ability of a single dye-doped polymer microsphere to be turned into a microlaser at the tip of a suspended core optical fiber which in turns enables enhanced sensor resolution in individual measurements and can also to be used to detect a specific analyte, neutravidin in this case, down to a concentration of 4 nM (0.20 μg/mL) in an experimental setting deprived of liquid flow, mimicking the conditions anticipated for *in vivo* sensing applications. This result raises the question of the suitability of such sensing platform for the detection of proteins using an antibody/antigen assay, especially when the molecule to be detected is in small concentration. Therefore, at its present stage of development this technology is best suited to the detection of protein

that are present in relatively high concentrations such as for example ApoE or clusterin which are stress marker indicators with normal regulation range of 20 to 50 µg/mL [37,41]. To expand the application range of this platform a smaller resonator could offer improved refractive index sensitivity. In this paper, we have used Ø ~ 20 µm polystyrene microspheres which typically have a refractive index sensitivity of 25 nm/RIU. Reducing the diameter of the resonator to 10 µm should results in a two-fold increase of the refractive index sensitivity [21] although lasing with such microsphere has not been demonstrated yet. A more efficient approach would be to use coupled microspheres to take advantage of the Vernier effect to increase the sensitivity such as proposed by Boriskina [42] or recently demonstrated by Ren *et al.* [43] in coupled capillaries with refractive index sensitivity above 2510 nm/RIU. Beyond the current limitation of this platform, we demonstrate that this simple and robust sensing architecture can be used as a dip sensor, and we envision that it can be used to perform immunoassays in areas that that are present difficult to access with existing sensors.

Acknowledgments

T.M. Monro acknowledges the support of an ARC Georgina Sweet Laureate Fellowship and the ARC Centre of Excellence in Nanoscale BioPhotonics (CNBP). This work was performed in part at the Optofab node of the Australian National Fabrication Facility utilizing Commonwealth and SA State Government funding. Authors thank Roman Kosteski, Erik Schartner, Peter Henry and Alastair Dowler for help with the silica fiber fabrication.

Author Contributions

A.F. proposed the work, designed and supervised the experiment; A.F. performed the experiment and T.R. contributed to the data analysis; all authors wrote and commented on the paper; T.M.M. supervised the entire project.

Conflicts of Interest

The authors declare no conflict of interest.

References

1. Vollmer, F.; Arnold, S.; Keng, D. Single virus detection from the reactive shift of a whispering-gallery mode. *Proc. Natl. Acad. Sci. USA* **2008**, *105*, 20701–20704.
2. Arnold, S.; Khoshsima, M.; Teraoka, I.; Holler, S.; Vollmer, F. Shift of whispering-gallery modes in microspheres by protein adsorption. *Opt. Lett.* **2003**, *28*, 272–274.
3. Spillane, S.M.; Kippenberg, T.J.; Vahala, K.J. Ultralow-threshold Raman laser using a spherical dielectric microcavity. *Nature* **2002**, *415*, 621–623.
4. François, A.; Himmelhaus, M. Whispering gallery mode biosensor operated in the stimulated emission regime. *Appl. Phys. Lett.* **2009**, *94*, 031101.
5. Lahoz, F.; Oton, C.J.; López, D.; Marrero-Alonso, J.; Boto, A.; Diaz, M. Whispering gallery mode laser based on antitumor drug–dye complex gain medium. *Opt. Lett.* **2012**, *37*, 4756–4758.

6. Astratov, V.N.; Franchak, J.P.; Ashili, S.P. Optical coupling and transport phenomena in chains of spherical dielectric microresonators with size disorder. *Appl. Phys. Lett.* **2004**, *85*, 5508–5510.
7. Blue, R.; Li, L.; Flockhart, G.M.H.; Uttamchandani, D. MEMS-actuated wavelength drop filter based on microsphere whispering gallery modes. *J. Micromech. Microeng.* **2011**, *21*, 115020.
8. Himmelhaus, M.; François, A. *In-vitro* sensing of biomechanical forces in live cells by a whispering gallery mode biosensor. *Biosens. Bioelectron.* **2009**, *2*, 418–427.
9. Nguyen, N.Q.; Gupta, N.; Ioppolo, T.; Ötügen, M.V. Whispering gallery mode-based micro-optical sensors for structural health monitoring of composite material. *J. Mater. Sci.* **2009**, *44*, 1560–1571.
10. Weng, W.; Anstie, J.D.; Stace, T.M.; Campbell, G.; Baynes, F.N.; Luiten A.N. Nano-Kelvin Thermometry and Temperature Control: Beyond the Thermal Noise Limit. *Phys. Rev. Lett.* **2014**, *112*, 160801, doi:10.1103/PhysRevLett.112.160801.
11. Özel, B.; Nett, R.; Weigel, T.; Schweiger, G.; Ostendorf, A. Temperature sensing by using whispering gallery modes with hollow core fibers. *Meas. Sci. Technol.* **2010**, *21*, 094015.
12. Oraevsky, A.N. Whispering-gallery waves. *Quantum Electron.* **2002**, *32*, 377–400.
13. Armani, A.M.; Kulkarni, R.P.; Fraser, S.E.; Flagan, R.C.; Vahala, K.J. Label-free, single-molecule detection with optical microcavities. *Science* **2007**, *317*, 783–787.
14. Vollmer, F.; Yang, L. Review Label-free detection with high-Q microcavities: A review of biosensing mechanisms for integrated devices. *Nanophotonics* **2012**, *1*, 267–291.
15. Bianucci, P.; Rodríguez, J.R.; Clements, C.; Hessel, C.M.; Veinot, J.G.C.; Meldrum, A. Whispering gallery modes in silicon nanocrystal coated microcavities. *Phys. Status Solidi A* **2009**, *206*, 973–975.
16. Rowland, K.J.; François, A.; Hoffmann, P.; Monro, T.M. Fluorescent polymer coated capillaries as optofluidic refractometric sensors. *Opt. Express* **2013**, *21*, 11492–11505.
17. Matsko, A.B.; Savchenkov, A.A.; Yu, N.; Maleki, L. Whispering-gallery-mode resonators as frequency references I. Fundamental limitations. *J. Opt. Soc. Am. B* **2007**, *24*, 1324–1335.
18. Mazzei, A.; Götzinger, S.; Menezes, L.S.; Sandoghdar, V.; Benson, O. Optimization of prism coupling to high-Q modes in a microsphere resonator using a near-field probe. *Opt. Commun.* **2005**, *250*, 428–433.
19. Guo, Z.; Quan, H.; Pau, S. Near-field gap effects on small microcavity whispering-gallery mode resonators. *J. Phys. D Appl. Phys.* **2006**, *39*, 5133–5136.
20. Purcell, E.M. Spontaneous emission probabilities at radio frequencies. *Phys. Rev.* **1946**. 69, 681.
21. François, A.; Rowland, K.J.; Monro, T.M. Highly efficient excitation and detection of whispering gallery modes in a dye-doped microsphere using a microstructured optical fiber. *Appl. Phys. Lett.* **2011**, *99*, 141111.
22. Himmelhaus, M.; Krishnamoorthy, S.; François, A. Optical sensors based on whispering gallery modes in fluorescent microbeads: Response to specific interactions. *Sensors* **2010**, *10*, 6257–6274.
23. Eckert, M.A.; Vu, P.Q.; Zhang, K.; Kang, D.; Ali, M.M.; Xu, C.; Zhao, W. Novel Molecular and Nanosensors for In Vivo Sensing. *Theranostics* **2013**, *3*, 583–584.
24. Hjelme, D.R.; Aune, O.; Falch, B.; Østling, D.; Ellingsen, R. Fiber-Optic Biosensor Technology for Rapid, Accurate and Specific Detection of Enzymes. In Proceeding of the Optical Sensors Conference, Barcelona, Spain, 27–31 July 2014.

25. Liao, K.C.; Chang, S.C.; Chiu, C.Y.; Chou, Y.H. Acute Response *In Vivo* of a Fiber-Optic Sensor for Continuous Glucose Monitoring from Canine Studies on Point Accuracy. *Sensors* **2010**, *10*, 7789–7802.
26. Beier, H.T.; Coté, G.L.; Meissner, K.E. Modeling whispering gallery modes in quantum dot embedded polystyrene microspheres. *J. Opt. Soc. Am. B* **2010**, *27*, 536–543.
27. Gómez, D.E.; Pastoriza-Santos, I.; Mulvaney, P. Tunable whispering gallery mode emission from quantum-dot-doped microspheres. *Small* **2005**, *1*, 238–241.
28. Schneider, G.; Decher, G.; Nerambourg, N.; Praho, R.; Werts, M.H.V.; Blanchard-Desce, M. Distance-dependent fluorescence quenching on gold nanoparticles unsheathed with layer-by-layer assembled polyelectrolytes. *Nano Lett.* **2006**, *6*, 530–536.
29. Decher, G. Fuzzy Nanoassemblies: Toward Layered Polymeric Multicomposites. *Science* **1997**, *277*, 1232–1237.
30. Zhang, J.; Liu, J.; Wang, S.; Zhan, P.; Wang, Z.; Ming, N. Facile methods to coat polystyrene and silica colloids with metal. *Adv. Funct. Mater.* **2004**, *14*, 1089–1096.
31. Yang, L.; Armani, D.K.; Vahala, K.J. Fiber-coupled erbium microlasers on a chip. *Appl. Phys. Lett.* **2003**, *83*, 825–826.
32. François, A.; Rowland, K.J.; Afshar, S.V.; Henderson, M.R.; Monro, T.M. Enhancing the radiation efficiency of dye doped whispering gallery mode microresonators. *Opt. Express* **2013**, *21*, 22566–22577.
33. Quan, H.; Guo, Z. Simulation of whispering-gallery-mode resonance shifts for optical miniature biosensors. *J. Quant. Spectrosc. Radiat. Transf.* **2005**, *93*, 231–243.
34. White, I.M.; Fan, X. On the performance quantification of resonant refractive index sensors. *Opt. Express* **2008**, *16*, 1020–1028.
35. Tronin, A.; Lvov, Y.; Nicolini, C. Ellipsometry and X-ray reflectometry characterization of self-assembly process of polystyrenesulfonate and polyallylamine. *Colloid Polym. Sci.* **1994**, *272*, 1317–1321.
36. Lösche, M.; Schmitt, J.; Decher, G.; Bouwman, W.G.; Kjaer, K. Detailed structure of solecularly thin polyelectrolyte multilayer films on solid substrates as revealed by neutron reflectometry. *Macromolecules* **1998**, *31*, 8893–8906.
37. Sciacca, B.; François, A.; Klinger-Hoffmann, M.; Brazzatti, J.; Penno, M.; Hoffmann, P.; Monro, T.M. Radiative-surface plasmon resonance for the detection of apolipoprotein E in medical diagnostics applications. *Nanomedicine* **2013**, *9*, 550–557.
38. Schweiger, G.; Horn, M. Effect of changes in size and index of refraction on the resonance wavelength of microspheres. *J. Opt. Soc. Am. B* **2006**, *23*, 212–217.
39. Boleininger, A.; Lake, T.; Hami, S.; Vallance, C. Whispering gallery modes in standard optical fibres for fibre profiling measurements and sensing of unlabelled chemical species. *Sensors* **2010**, *10*, 1765–1781.
40. Chao, C.Y.; Fung, W.; Guo, L.J. Polymer microring resonators for biochemical sensing applications. *IEEE J. Sel. Top. Quantum Electron.* **2006**, *12*, 134–142.
41. Sciacca, B.; François, A.; Hoffmann, P.; Monro, T.M. Multiplexing of radiative-surface plasmon resonance for the detection of gastric cancer biomarkers in a single optical fiber. *Sens. Actuators B Chem.* **2013**, *183*, 454–458.

42. Boriskina, S.V. Spectrally engineered photonic molecules as optical sensors with enhanced sensitivity: A proposal and numerical analysis. *J. Opt. Soc. Am. B* **2006**, *23*, 1565–1573.
43. Ren, L.; Wu, X.; Li, M.; Zhang, X.; Liu, L.; Xu, L. Ultrasensitive label-free coupled optofluidic ring laser sensor. *Opt. Lett.* **2012**, *37*, 3873–3875.

Chapter 6

Biosensing Application: Self-referenced Fiber Tip Sensing

6.1 Dynamic Self-Referencing Approach to Whispering Gallery Mode Biosensing and its Application to Measurement Within Diluted Serum

P5. T. Reynolds, A. François, N. Riesen, M. E. Turvey, S. J. Nicholls, P. Hoffmann and T. M. Monro, "Dynamic self-referencing approach to whispering gallery mode biosensing and its application to measurement within undiluted serum" Analytical Chemistry, 88 (7), 4036-4040, 2016.

6.1.1 Publication Overview

Being able to perform measurements in complex solutions such as human serum, saliva and whole blood represents a key step towards developing a sensor that is suited towards applications beyond only operating in controlled research environments. More specifically, the sensor must provide a way to eliminate or significantly reduce the effects of non-specific binding (NSB). One way to overcome the effects of NSB is to introduce a second resonator to act as a dynamic reference, allowing for both NSB and environment changes, such as fluctuations in temperature, to be compensated for. The sensing platform introduced in Chapter 5 lends itself to be self-referenced by simply adding a second, almost identical, resonator to the tip of the fibre in a neighboring hole. Both resonators can be excited simultaneously, without coupling with each other, producing clearly distinguishable spectra due to the slight, on the order of nanometers, differences in their radii and will be exposed to identical environmental conditions due to their positioning on the fibre tip. By taking advantage of surface functionalization techniques to prepare one sphere to monitor a specific interaction, while simply using a blocking agent on the other, the relative movement between the two sets of resonances can be used to eliminate unwanted interactions.

Here, the potential for this sensing platform to be used in complex solutions is successfully demonstrated using the well-known specific interaction of Biotin/neutravidin, whereby undiluted human serum samples (with the immunoglobulin removed) are spiked with known concentrations of neutravidin and the responses are compared with measurements made in pure solutions. This platform further lends itself to future multiplexed sensing applications by simply introducing more resonators onto the fibre tip, all functionalized to monitor different interactions.

6.1.2 Statement of Contribution

Statement of Authorship

Title of Paper	Dynamic self-referencing approach to whispering gallery mode biosensing and its applications to measurement within undiluted serum
Publication Status	[X] Published [ ] Accepted for Publication [ ] Submitted for Publication [ ] Unpublished and Unsubmitted w ork w ritten in manuscript style
Publication Details	T. Reynolds, A. Francois, N. Riesen, M. E. Turvey, S. J. Nicholls, P. Hoffmann, and T. M. Monro, "Dynamic self-referencing approach to whispering gallery mode biosensing and its applications to measurement within undiluted serum," Analytical Chemistry, 88 (7), 4036-4040, 2016.

Principal Author

Name of Principal Author (Candidate)	Tess Reynolds		
Contribution to the Paper	Performed the experiments, conducted the data analysis, was involved with the design and fabrication of the fibre, primarily wrote the paper and acted as corresponding author.		
Overall percentage (%)	70		
Certification:	This paper reports on original research I conducted during the period of my Higher Degree by Research candidature and is not subject to any obligations or contractual agreements with a third party that would constrain its inclusion in this thesis. I am the primary author of this paper.		
Signature		Date	11-11-16

Co-Author Contributions

By signing the Statement of Authorship, each author certifies that:

i. the candidate's stated contribution to the publication is accurate (as detailed above);

ii. permission is granted for the candidate in include the publication in the thesis; and

iii. the sum of all co-author contributions is equal to 100% less the candidate's stated contribution.

Name of Co-Author	Alexandre Francois		
Contribution to the Paper	Supervised the experiments and contributed to the editing and evaluation of the manuscript		
Signature		Date	14-11-16

Name of Co-Author	Nicolas Riesen		
Contribution to the Paper	Contributed to the editing and evaluation of the manuscript. Fabricated the fiber tapers and assisted in writing the discussion of the paper.		
Signature		Date	16-11-16

Name of Co-Author	Michelle E. Turvey		
Contribution to the Paper	Provided the A/G conjugated sepharose beads for removing the immunoglobulin form the serum samples and helped edit and evaluate the manuscript.		
Signature		Date	14-11-16

Name of Co-Author	S. J. Nicholls		
Contribution to the Paper	Contributed to the editing and evaluation of the manuscript.		
Signature		Date	16-11-16

Name of	
Contribut	
Signature	

Name of Co-Author:	**Peter Hoffmann**
Contribution to the Paper:	Advised and provided the A/G conjugated sepharose beads for removing the immunoglobulin from the serum samples and helped edit [illegible] uscript.
Signatu	Date: 14-11-16

Name of	
Contribut	
Signature	

Name of Co-Author:	**Tanya M. Monro**
Contribution to the Paper:	Supervised the project and contributed to manuscript editing and evaluation.
Signature:	Date: 14-11-16

analytical chemistry

Article

pubs.acs.org/ac

Dynamic Self-Referencing Approach to Whispering Gallery Mode Biosensing and Its Application to Measurement within Undiluted Serum

Tess Reynolds,*[,†] Alexandre François,[†,‡] Nicolas Riesen,[†] Michelle E. Turvey,[§] Stephen J. Nicholls,[∥] Peter Hoffmann,[†,§] and Tanya M. Monro[†,‡]

[†]The Institute for Photonics and Advanced Sensing (IPAS) and [§]Adelaide Proteomics Centre, University of Adelaide, Adelaide SA 5005, Australia

[‡]University of South Australia, Adelaide SA 5000, Australia

[∥]South Australian Health and Medical Research Institute (SAHMRI), University of Adelaide, Adelaide SA 5000, Australia

ABSTRACT: Biosensing within complex biological samples requires a sensor that can compensate for fluctuations in the signal due to changing environmental conditions and nonspecific binding events. To achieve this, we developed a novel self-referenced biosensor consisting of two almost identically sized dye-doped polystyrene microspheres placed on adjacent holes at the tip of a microstructured optical fiber (MOF). Here self-referenced biosensing is demonstrated with the detection of Neutravidin in undiluted, immunoglobulin-deprived human serum samples. The MOF allows remote excitation and collection of the whispering gallery modes (WGMs) of the microspheres while also providing a robust and easy to manipulate dip-sensing platform. By taking advantage of surface functionalization techniques, one microsphere acts as a dynamic reference, compensating for nonspecific binding events and changes in the environment (such as refractive index and temperature), while the other microsphere is functionalized to detect a specific interaction. The almost identical size allows the two spheres to have virtually identical refractive index sensitivity and surface area, while still having discernible WGM spectra. This ensures their responses to nonspecific binding and environmental changes are almost identical, whereby any specific changes, such as binding events, can be monitored via the relative movement between the two sets of WGM peaks.

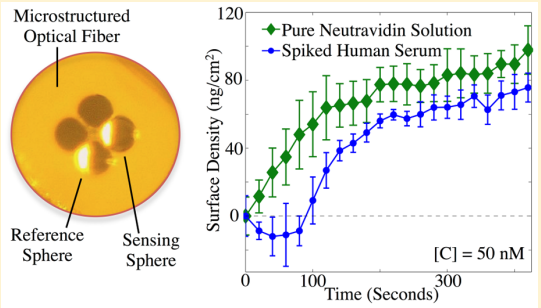

The phenomenon of whispering gallery modes (WGMs) within microresonators as a label-free sensing modality has emerged as a powerful contender for biosensing and medical diagnostic applications.[1,2] It has enabled unprecedented detection limits down to single molecules,[3] and has given way to new in vivo sensing opportunities.[1,4,5] The spectral positions of the WGMs are determined by both the properties of the resonator (e.g., diameter, shape, refractive index) as well as the surrounding medium. The latter feature allows changes in the environment to be monitored via shifts in the spectral positions of the resonances. Surface functionalization of the resonator can also be utilized allowing specific interactions with desired target analytes such as proteins,[6,7] bacteria,[8] and DNA[9,10] to be monitored within pure samples in controlled laboratory conditions.

However, the ability of a sensor, and in particular a label-free biosensor, to distinguish or eliminate unwanted fluctuations in the signal due to variations in, for example, temperature, surrounding refractive index, or nonspecific binding (NSB) is critical in real clinical samples. While it is usually possible to control the environmental conditions, such as temperature, reducing the effect of unwanted binding events in clinical samples is far more challenging. Different methods to overcome this critical issue have been proposed, all based on surface chemistry approaches, using, for example, NHS esters,[11] CM dextran,[12] or polyethylene glycol (PEG).[13,14] Integrating PEGs with silica microsphere resonators has, for example, allowed thrombin (~8 μM) to be detected in 10-fold diluted human serum inside a flow cell.[7] However, this method requires serum to be diluted, which adds an additional processing step and reduces the concentration of the analyte by the same factor, increasing the demands on the performance of the sensor. For some applications, such as the early diagnosis of myocardial infarctions in cardiology, for example, where the analyte concentration is already very small,[15−17] this technique might not be suitable and alternative approaches have to be found. One such approach is to design a self-referencing sensor that allows both environmental changes and NSB events to be compensated, as is presented here.

A relatively straightforward approach of developing a self-referencing sensor is to introduce a second resonator that serves

Received: January 27, 2016
Accepted: February 26, 2016
Published: March 8, 2016

DOI: 10.1021/acs.analchem.6b00365
Anal. Chem. 2016, 88, 4036−4040

as a dynamic reference, similar to multiplexed sensing techniques.[18] Multiplexing of WGM sensors has previously been proposed conceptually[18] and demonstrated in a range of resonator geometries and configurations including passive microspheres,[9] microdisks,[19] and liquid core ring resonators[20] and fluorescent microspheres.[21,22] Fluorescent or active resonators are particularly interesting in this context, as they allow remote excitation of the resonator, thereby alleviating some of the practical limitations of passive resonator configurations.[9,23−25] Active resonators do display lower Q-factors[26] in comparison with passive resonators,[27,28] however, techniques exist that can improve the Q-factor, such as operating the resonator within the stimulated emission regime[29] or breaking the symmetry of the resonator by placing it onto the tip of a microstructured optical fiber (MOF).[30] This second technique has the additional advantage of creating a robust and easy to use dip-sensing architecture.[1]

In this study we demonstrate a self-referenced WGM biosensing platform for the specific detection and quantification of biomolecules in undiluted human serum. Our self-referenced sensing platform is an extension of our previously reported dip sensing active WGM platform using a 4-hole silica MOF which allows for the remote excitation and collection of the WGM signal from a dye-doped polystyrene microsphere placed in one of the holes at the tip of the fiber.[1] A second, almost identical microsphere (reference resonator), but differing in its surface chemistry from the sensing microsphere, is placed in an adjacent hole acting as a dynamic reference, Figure 1A. The reference

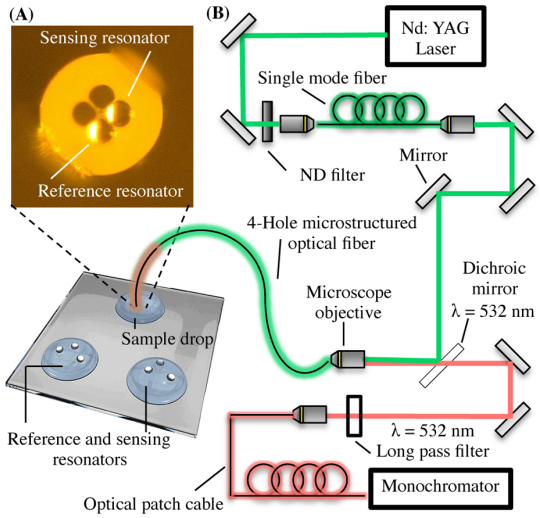

Figure 1. (A) Bright-field microscope image of two 15 μm diameter dye-doped polystyrene microspheres positioned onto the tip of a 4-hole microstructured optical fiber (MOF). (B) Schematic of the optical setup.

resonator compensates for nonspecific binding as well as environmental changes, acting as a dynamic reference, while the first sphere (sensing resonator) is functionalized for detecting a specific analyte. Due to the highly sensitive nature of the resonance wavelength positions to the resonator's effective radius, differences of only nanometers allows the spectrum of each individual sphere to be clearly distinguished. The nearly identical size of the resonators also guarantees that the two spheres have virtually identical refractive index sensitivity and surface area, so their response to any environmental changes or NSB is almost identical, while the proximity of the spheres on the MOF's tip allows them to simultaneously experience the same local environment. Furthermore, utilizing a single gain medium for both spheres ensures that the sensing performance (sensitivity and resolution) of both resonators remain comparable, allowing the use of the relative displacement between the two sets of peaks for tracking specific binding events.

To evaluate the performance of our self-referenced fiber tip sensing platform we used a well-known specific interaction model based on biotin-Neutravidin. The Neutravidin detection limit in buffer solution (PBS) was first characterized and then repeated in Neutravidin spiked undiluted, immunoglobulin-deprived human serum samples. Following from our previous work,[1] the measurements were performed in static conditions, by simply dipping the MOF tip with attached microsphere resonators into the different liquid samples, as shown in Figure 1B. In both sets of measurements, the nonspecific binding signal was monitored using the reference resonator, while the total contribution of specific and nonspecific interactions was measured using the sensing resonator. The relative movement between the two sets of resonances was then monitored.

EXPERIMENTAL SETUP, MATERIALS, AND METHOD

The polystyrene microspheres (nominal diameter of 15.00 ± 1.43 μm from Polyscience Inc.) were doped with the fluorescent dye Nile Red (λ_{ex} = 532 nm, λ_{em} = 590 nm)[31] using a liquid two-phase system.[32] Following this process, the microspheres were annealed and rinsed thoroughly to remove any trace of the organic solvent (xylene) used during the doping process, eliminating any potential drift of the resonance positions over time. The surface functionalization begins with the deposition of a series of positively and negatively charged polyelectrolyte layers, polyallylamine hydrochloride (PAH) and polystyrene sulfonate (PSS),[33] to form three layers (PAH/PSS/PAH).[1] The microspheres were then separated into two batches, sensing and reference resonators, with only the sensing resonator batch being biotinylated for monitoring the specific interaction with Neutravidin. For the sensing resonators, the primary amine of the PAH layer was used to covalently immobilize biotin-D using a solution of 1-ethyl-3-(3-dimethylamionpropyl) carbodimide (EDC) and *N*-hydroxysuccinimide (NHS) as coupling reagents. As a final process, both the reference and the sensing resonators were incubated in 2.5% casein solution for 24 h to cover nonspecific binding sites.

A schematic of the optical setup is shown in Figure 1B, where a frequency-doubled YAG laser (λ = 532 nm, ~800 ps pulse duration, 10 kHz repetition rate) was used for the excitation of the active microspheres beyond their lasing thresholds, enabling higher Q-factors, as previously shown.[32] The light from the YAG was spatially filtered using a tapered single mode fiber (SMF28 $Ø_{core}$ = 4 μm) before being coupled into the 4-hole silica MOF ($Ø_{core}$ = 7 μm, $Ø_{hole}$ ~ 15 μm) shown in Figure 1A. The WGM emission from the microspheres is then recaptured by the MOF and directed back through a dichroic mirror into a monochromator equipped with a cooled CCD (2048 pixels) where the WGM spectrum is recorded.

To attach a microsphere to the tip of the MOF a drop of water containing the microspheres was placed on top of a glass coverslip and positioned on an inverted microscope. A three-axis translational stage was used to hold and align the tip of the MOF as it was carefully lowered down into the drop of microspheres.

DOI: 10.1021/acs.analchem.6b00365
Anal. Chem. 2016, 88, 4036−4040

After recording the emission spectra of free floating microspheres from both the sensing and reference resonator batches, using free-space excitation and collection, one microsphere was selected from each droplet and brought into contact with the fiber tip. Due to the hydrophobic nature of both the MOF tip and the microspheres, the microspheres can easily be positioned in individual holes of the MOF, as seen in Figure 1A. It is important to note that once attached to the MOF tip, the microspheres stay in place and can be easily manipulated and dipped into other liquid droplets.

DATA ANALYSIS

All the binding kinetics presented here are presented in terms of the change in surface density of adsorbed molecules onto the surface of the resonator (d, ng/cm^2). This value can be estimated from the wavelength shift $\Delta\lambda$, through the effective radius increase ΔR using the following equations,[34] where λ is the initial resonance wavelength, R is the initial resonator radius which can be calculated from the spacing of successive modes with the same polarization using eqs 2 and 3, e is the thickness of the deposited layer, and n_L and n_s are the refractive indices of the layer and sphere, respectively. By fitting Gaussian functions to the resonance peaks, the spectral position of an initial resonance wavelength λ, and subsequent positions of the peak over time can be determined.

$$\frac{\Delta\lambda}{\lambda} = \frac{\Delta R}{R} = \frac{n_L e}{n_s R} \tag{1}$$

$$R = \frac{\lambda_{m+1} m}{2\pi n_s} \tag{2}$$

$$m = \frac{\lambda_{m+1}}{\lambda_m - \lambda_{m+1}} + 1 \tag{3}$$

where m is the azimuthal mode number and λ_{m+1} and λ_m are the wavelengths of two successive modes with the same polarization.

$$d = \frac{M}{N_A \sigma_p^{-1}} \tag{4}$$

$$\sigma_p^{-1} = \frac{n_s}{n_m} \frac{\alpha_{ex}}{\varepsilon_0 (n_s^2 - n_m^2)} \frac{1}{\Delta R} \tag{5}$$

$$\alpha_{ex} = \frac{\varepsilon_r - 1}{\varepsilon_r + 2} \frac{3M\varepsilon_0}{N_A \rho_m} \tag{6}$$

Here, M is the molecular weight, N_A is Avogadro's number, σ_p is the projected area of the adsorbed molecule, α_{ex} is the excess polarizability, which to a first approximation can be calculated using the Clausius-Mossotti formula (eq 6), ε_0 is the free-space permittivity, ε_r is the dielectric function of the molecule considered, ρ is the mass density (ρ = 1.37 g/cm^3 for most proteins[35]) and n_m and n_s are the refractive indices of the surrounding environment and microsphere, respectively. Calculating the surface density allows comparison with other techniques and sensing geometries as it removes the dependence on the geometry as well as the refractive index sensitivity of the sensor being considered.

RESULTS AND DISCUSSION

Figure 2A and B show the typical WGM spectra of the two-microsphere system above and below the lasing threshold, respectively. Below the lasing threshold the resonances of the two spheres cannot be distinguished. However, operating the spheres above their lasing thresholds not only allows the spectrum of each individual sphere to be clearly identified, but also improves the resolution, enabling lower detection limits to be reached.[1] The resonance spectra typically do not overlap, when operated in the stimulated emission regime as even a minute deviation in diameter between the two microspheres results in a discrepancy between the resonances. In this configuration, the spheres can either be tracked individually by following an individual peak or alternatively, by performing a convolution on the two resonator comb-like WGM spectrum as both spheres respond to the same environment, Figure 2C.

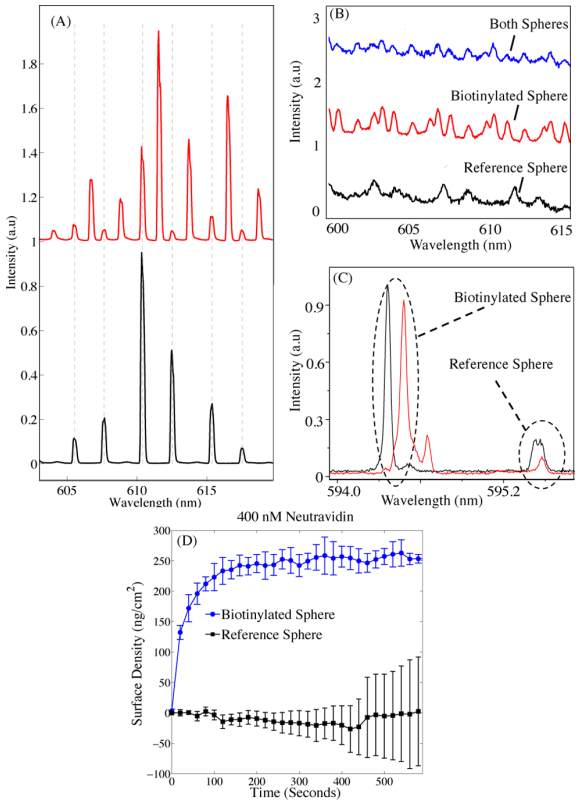

Figure 2. (A) Whispering gallery mode spectrum of the reference sphere alone (black trace) and both the biotinylated and reference spheres (red trace) attached to the tip of the microstructured optical fiber (MOF), operating above the lasing threshold. Both spheres are 15 μm in diameter. (B) Whispering gallery mode spectrum of the reference (black), biotinylated (red), and both the reference and biotin spheres, when attached to the tip of the microstructured optical fiber below the lasing threshold. (C) Comparison of the whispering gallery mode spectra of both the reference and biotinylated microspheres attached to the tip of the MOF when initially in water (black trace) and after dipping into Neutravidin solution for 8 min (red trace). (D) Binding kinetic of Neutravidin onto the biotinylated sphere (blue trace) and reference sphere (black trace).

Once both spheres were attached, spectra were taken at 20 s intervals as the fiber was moved into the Neutravidin solution. Figure 2D shows the response of both microspheres when placed in 400 nM Neutravidin solution. From the responses of the two spheres it is clear that binding is occurring on the biotinylated sphere, with equilibrium being reached after approximately 200 s, while the reference sphere spectrum remains relatively stable

DOI: 10.1021/acs.analchem.6b00365
Anal. Chem. 2016, 88, 4036−4040

throughout the measurement with deviations toward the end of the measurement. This result is consistent with our previous demonstrations of fiber tip[1] and fluorescent microcapillary[36] sensing. We also note that the presence of the reference sphere does not have any effect on the biotinylated sphere's performance. As such, the process is repeated for decreasing Neutravidin concentrations, with 3 measurements made for each concentration. Each individual measurement was completed with a new set of spheres. No deviation was observed for the reference spheres during the Neutravidin measurements, and for simplicity only the binding kinetic of the biotinilated sphere is shown for each of the concentrations in Figure 3, where the error bars have been calculated from the standard deviation of all three trials completed for each concentration.

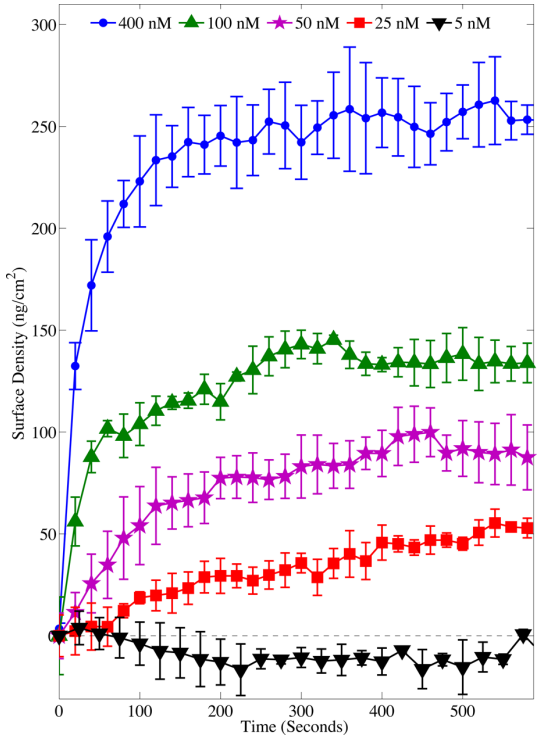

Figure 3. Binding kinetic of Neutravidin on a 15 μm biotinylated microsphere of five different concentrations 5−400 nM.

After completing these initial trials in PBS, the same experimental procedure was used to investigate the sensor's response in human serum samples. Drops of each of the sphere populations were once again placed on top of a glass coverslip, with a single sphere from each subsequently being attached to the fiber tip, along with 30 μL drops of 1:20 (v/v) and 1:40 (v/v) diluted human serum without Neutravidin added. The response of the individual spheres in the sensor is displayed in Figure 4. Examining Figure 4, it is clear that significant adsorption is occurring in both sphere populations, however there is a reduction in the adsorption of the biotinylated sphere as the dilution of the sample increases, Figure 4A, while the reference sphere's response remains almost unchanged, Figure 4B. Without any added Neutravidin in the diluted serum sample, these results indicate that there is another molecule present in the serum that is interacting and binding to the biotinylated sphere

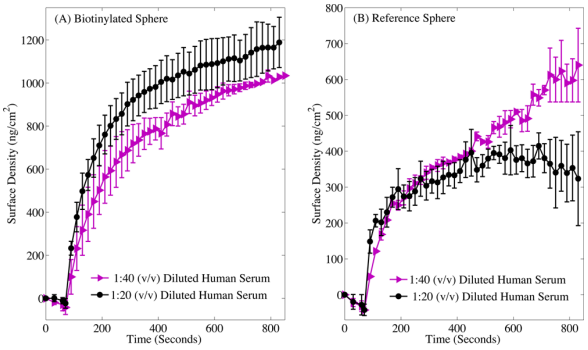

Figure 4. Binding kinetic of a sensing resonator (A) and reference resonator (B) attached to the tip of a fiber dipped into two human serum samples of different dilution.

surface. It has been reported that immunoglobulin can interact with biotin, resulting in false positive results for similar biotinylated-based immunoassays.[37]

Therefore, to avoid such false positive results while using biotin-Neutravidin as a specific interaction model, the immunoglobulin was removed from our serum samples by brief incubation and pull-down with protein A/G-conjugated sepharose beads. Four pull-downs with protein A/G beads were required to ensure that the false positive signal on the biotinylated microsphere was reduced to zero using undiluted serum while significant adsorption on the reference microsphere due to the nonspecific binding of the large protein content of the serum was still present.

Tests were repeated with pure human serum, with the immunoglobulin removed, avoiding the unwanted binding between the immunoglobulin and the sensing resonator, but spiked with a known Neutravidin concentration. The results for the lowest concentration tested are shown in Figure 5.

For all the tests performed, the reference resonator exhibited a similar behavior characterized by a sharp wavelength shift, or increase of the surface density, due to the large NSB component introduced by the serum, despite the use of casein as a blocking reagent. This highlights the fact that blocking solutions such as caseine, bovine serum albumin, and alike are inherently inefficient at preventing NSB in complex biological samples. The biotinylated microspheres, however, showed a steady increase in the surface density beyond the initial WGM wavelength shift due to the high refractive index of the serum, which characterizes the Langmuir adsorption of the Neutravidin onto the biotinylated resonator surface, down to 25 nM Neutravidin concentration. Once the contribution from the NSB is subtracted from the biotinylated microsphere response a perfect correlation between the Neutravidin binding kinetic in PBS and undiluted serum was reached as shown in the Figure 5D,E. For the lowest concentration tested (5 nM), no unambiguous positive detection of Neutravidin can be observed whether in PBS or undiluted serum.

In conclusion, this simple approach of using two almost identical microspheres, differing by their surface functionalization, for self-referencing purposes has shown that specific detection and quantification in undiluted serum samples can be realized. The reference microsphere allows for the compensation of the nonspecific binding, enabling the quantification of the binding of the analyte onto the sensing resonator surface in

DOI: 10.1021/acs.analchem.6b00365
Anal. Chem. 2016, 88, 4036−4040

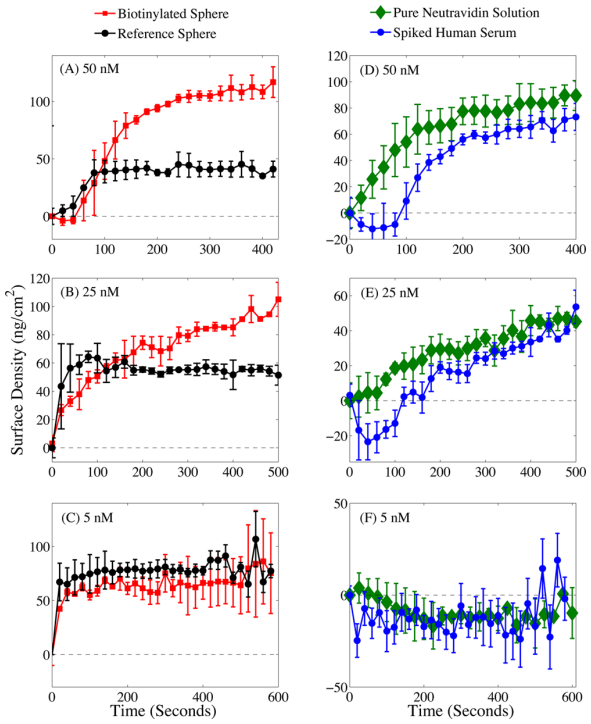

Figure 5. Individual sphere responses of the biotinylated (red trace) and reference (black trace) spheres when dipped into human serum samples spiked with (A) 50, (B) 25, and (C) 5 nM concentrations of Neutravidin. (D–F) Comparison of the corrected binding kinetic of the sensor in the spiked human serum samples (blue trace) with binding kinetic in the pure Neutravidin solution (green trace).

complex biological samples to be correlated with what happens with the same target analyte in buffer solution.

While for the sake of the specific interaction model used for this demonstration, the immunoglobulin had to be removed, one can appreciate that this approach can still be used for the detection of other more relevant biomolecules in serum, without having to process the serum by removing the immunoglobulin once antibodies are used to target a specific biomolecule instead of biotin. Furthermore, one can also expand this concept to multiplexed detection of different biomolecules simultaneously, taking advantage of the multiple holes on the MOF to accommodate microspheres targeting different biomolecules.

AUTHOR INFORMATION

Corresponding Author

*E-mail: tess.reynolds@adelaide.edu.au. Fax: +61-8-8313-4380.

Notes

The authors declare no competing financial interest.

ACKNOWLEDGMENTS

The authors acknowledge the support of T.M.M.'s ARC Georgina Sweet Laureate Fellowship. This work was performed in part at the Optofab node of the Australian National Fabrication Facility utilizing Commonwealth and SA State Government funding. Authors thank Roman Kostecki, Erik Schartner, Peter Henry, and Alastair Dowler for help with the silica microstructured fiber fabrication.

REFERENCES

(1) François, A.; Reynolds, T.; Monro, T. M. *Sensors* **2015**, *15*, 1168–1181.
(2) Agarwal, M.; Teraola, I. *Anal. Chem.* **2015**, *87*, 10600–10604.
(3) Baaske, M. D.; Foreman, M. R.; Vollmer, F. *Nat. Nanotechnol.* **2014**, *9*, 933–939.
(4) Humar, M.; Yun, S. H. *Nat. Photonics* **2015**, *9*, 572–576.
(5) Schubert, M.; Steude, A.; Liehm, P.; Kronenberg, N. M.; Karl, M.; Campbell, E. C.; Powis, S. J.; Gather, M. C. *Nano Lett.* **2015**, *15*, 5647–5652.
(6) Ballard, Z.; Baaske, M. D.; Vollmer, F. *Sensors* **2015**, *15*, 8968–8990.
(7) Pasquardini, L.; Berneschi, S.; Barucci, A.; Cosi, F.; Dallapiccola, R.; Insinna, M.; Lunelli, L.; Conti, G. N.; Pederzolli, C.; Salvadori, S.; Soria, S. *J. Biophotonics* **2013**, *6*, 178–187.
(8) Anderson, M. E.; O'Brien, E. C.; Grayek, E. N.; Hermansen, J. K.; Hunt, H. K. *Biosensors* **2015**, *5*, 562–576.
(9) Vollmer, F.; Arnold, S.; Braun, D.; Teraoka, I.; Libchaber, A. *Biophys. J.* **2003**, *85*, 1974–1979.
(10) Fan, X. D.; Sutter, J. D.; White, I. M.; Zhu, H. Y.; Shi, H. D.; Caldwell, C. W. *Biosens. Bioelectron.* **2008**, *23*, 1003–1009.
(11) Masson, J. F.; Battaglia, T. M.; Cramer, J.; Beaudoin, S.; Sierks, M.; Booksh, K. S. *Anal. Bioanal. Chem.* **2006**, *386*, 1951–1959.
(12) Bolduc, O. R.; Pelletier, J. N.; Masson, J. F. *Anal. Chem.* **2010**, *82*, 3699–3706.
(13) Ostuni, E.; Chapman, R. G.; Holmin, R. E.; Takayama, E.; Whitesides, G. M. *Langmuir* **2001**, *17*, 5605–5620.
(14) Wang, F.; Anderson, M.; Bernards, M. T.; Hunt, H. K. *Sensors* **2015**, *15*, 18040–18060.
(15) Konstantinides, S.; Geibel, A.; Olschewski, M.; Kasper, W.; Hruska, N.; Jäckle, S.; Binder, L. *Circulation* **2002**, *106*, 1263–1268.
(16) Maisel, A. *Circulation* **2002**, *105*, 2328–2331.
(17) Ridker, P. M. *Circulation* **2001**, *103*, 1813–1818.
(18) Boriskina, S. V.; Dal Negro, L. *Opt. Lett.* **2010**, *35*, 2496–2498.
(19) Qavi, A. J.; Kindt, J. T.; Gleeson, M. A.; Bailey, R. C. *Anal. Chem.* **2011**, *83*, 5949–5956.
(20) White, I. M.; Oveys, H.; Fan, X.; Smith, T. L.; Zhang, J. *Appl. Phys. Lett.* **2006**, *89*, 191106.
(21) Huckabay, H. A.; Wildgen, S. M.; Dunn, R. C. *Biosens. Bioelectron.* **2013**, *45*, 223–229.
(22) Kim, D. C.; Armendariz, K. P.; Dunn, R. C. *Analyst* **2013**, *138*, 3189–3195.
(23) Ksendov, A.; Lin, Y. *Opt. Lett.* **2005**, *30*, 3344–3346.
(24) Gorodetsky, M. L.; Illchenko, V. S. *J. Opt. Soc. Am. B* **1999**, *16*, 147–154.
(25) Guo, Z.; Quan, H.; Pau, S. *J. Phys. D: Appl. Phys.* **2006**, *39*, 5133–5136.
(26) Riesen, N.; Reynolds, T.; François, A.; Henderson, M. R.; Monro, T. M. *Opt. Express* **2015**, *23*, 28896–28904.
(27) Vernooy, D. W.; Ilchenko, V. S.; Mabuchi, H.; Steed, E. W.; Kimble, H. J. *Opt. Lett.* **1998**, *23*, 247–249.
(28) Gorodetsky, M. L.; Savchenkov, A. A.; Ilchenko, V. S. *Opt. Lett.* **1996**, *21*, 453–455.
(29) François, A.; Himmelhaus, M. *Appl. Phys. Lett.* **2009**, *94*, 031101.
(30) François, A.; Rowland, K. J.; Afshar, S. V.; Henderson, M. R.; Monro, T. M. *Opt. Express* **2013**, *21*, 22566–22577.
(31) Greenspan, P.; Mayer, E. P.; Fowler, S. D. *J. Cell Biol.* **1985**, *100*, 965–973.
(32) François, A.; Riesen, N.; Ji, H.; Afshar, V. S.; Monro, T. M. *Appl. Phys. Lett.* **2015**, *106*, 031104.
(33) Decher, G. *Science* **1997**, *277*, 1232–1237.
(34) Arnold, S.; Khoshsima, M.; Teraoka, I.; Holler, S.; Vollmer, F. *Opt. Lett.* **2003**, *28*, 272–274.
(35) Schweiger, G.; Horn, M. *J. Opt. Soc. Am. B* **2006**, *23*, 212–217.
(36) Lane, S.; West, P.; François, A.; Meldrum, A. *Opt. Express* **2015**, *23*, 2577–2590.
(37) Chen, T.; Hedman, L.; Mattila, P. S.; Jartti, L.; Jartii, T.; Ruuskanen, O.; Soderlund-Venermo, M.; Hedman, K. *PLoS One* **2012**, *7*, 43276.

DOI: 10.1021/acs.analchem.6b00365
Anal. Chem. 2016, 88, 4036–4040

Chapter 7

Conclusion and Future Work

This thesis advances the development of a fiber tip fluorescence-based whispering gallery mode biosensing platform. Initially, through modeling the WGM spectrum from fluorescent microspheres, the refractive index sensitivity and Q-factor as functions of both the microsphere resonator diameter and refractive index was mapped. Polystyrene was chosen as the resonator material due to its commercial availability, low cost and ease in which a gain medium can be introduced into the resonator and therefore, using the model developed, the specific diameter that provides the optimal tradeoff between Q-factor and refractive index sensitivity to optimize the detection limit of the resonator could be identified. Next, the limiting factor on the Q-factor of fluorescent microspheres was investigated further, and it was identified as being due to the inherent asphericity that is present in the resonator geometry. Therefore, moving away from far-field collection methods in which this effect on the Q-factor is more noticeable and taking advantage of the novel structure of suspended core MOFs that facilitates remote excitation and collection of the WGM modulated fluorescence signal, a novel and robust dip sensing architecture that alleviates the need for complex microfluidics and coupling could be realized.

Additionally, by utilizing surface functionalization techniques, bioreceptors can be immobilized on the resonator's surface, allowing specific interactions to be monitored demonstrating the platforms ability to be used for protein detection as well as noting its potential for *in-vivo* sensing through the ability to combine the fiber with a catheter. Further, enhancement to the sensing performance can be achieved by operating the resonator above its lasing threshold, where the increase in the Q-factor allows an increase in the resolution, reducing the uncertainty of the resonance wavelength and thus results in lowering the detection limit. Finally, by adding multiple microspheres to the tip of the fiber, a self-referenced sensing strategy was demonstrated whereby one of the microspheres is functionalized to detect a specific biomolecule while the second is functionalized to only measure the changes in the surrounding environment and monitor non-specific binding. Therefore, any shift in the WGM resonance wavelength associated with non-specific binding in complex samples, such as undiluted human serum samples, can be compensated for. The self-references sensing strategy lays the foundation for future multiplexed sensing, specifically to realize the detection of multiple proteins within a clinical sample, something that has never been achieved using WGM resonators before.

In Chapter 3 the analytical model originally for describing active WGM microspherical resonators developed by Chew (Section 1.1.2, MATLAB code in Appendix B) was applied for the first time to the problem of utilizing fluorescence based WGM resonators for conducting refractive index biosensing, specifically through assessing and comparing sensing performance of active microspherical resonators

using simulated WGM spectra. To demonstrate the viability of the model to predict sensing performance, the model was initially used to compare experimentally measured values for the refractive index sensitivity, demonstrating excellent agreement. Secondly, a figure of merit encompassing not only the refractive index sensitivity, but also the Q-factor of the resonator was defined, providing a way to easily assess and compare the sensing performance of any number of resonators. Finally, an example of how the model can be used to select a suitable resonator for undertaking refractive index biosensing was provided, selecting the resonators to be used in the subsequent Chapters. Although in this work the only other additional information considered was the resolution limit of the spectrometer capping the possible Q-factor values reached, the model easily allows for the inclusion of other specific information pertaining to the individual sensing tasks as required.

In Chapter 4 the Q-factor limits of fluorescent microspheres, and the influence of the coupling strategy (i.e. far-field or fiber taper), was investigated and attributed to the slight inherent asphericity present in the geometry of the resonator. It was shown, through theoretical modeling, imaging and experimental techniques, that significant Q-factor spoiling when using far-field collection occurs for asphericity as small as tens of nanometers or less. Specifically, for polystyrene based resonators with diameter of 15 um for example, a factor 5 decrease in the Q-factor in the far field due to a maximum eccentricity of only several nanometers was observed. As a result of this work it is proposed that a new contribution to the overall Q-factor should be included when considering active resonators in the far field that takes into account the effect of asphericity, instead of simply attributing it to scattering or material absorption.

In Chapter 5 the first biosensing demonstration of the platform formed by combining a MOF with a single dye-doped polystyrene fluorescent microsphere to detect proteins in pure solutions, including the lowering of the detection limit by inducing lasing in the microsphere was outlined. Initially, the lasing behavior of the dye-doped polystyrene microspheres was examined, including identifying the lasing threshold and comparison of the Q-factor above and below the lasing threshold, showing good agreement with previous experimental work. Next, the sensing performance of the resonators was investigated, including characterizing the initial surface functionalization steps to enable the subsequent immobilization of biomolecules to the resonators surface. Finally, the first demonstration of the detection of specific biological interaction using this platform was demonstrated involving the well-documented biotin/neutravidin specific interaction. The binding kinetics of the interaction above and below the lasing threshold were investigated, revealing a decrease in the detection limit when operating above the lasing threshold due to the increase in Q and hence higher resolution. Although this work did highlight some limitations in the performance of the platform, namely being more suited to detection

proteins in higher concentrations, it still demonstrated the simple and robust sensing architecture and how it can be used as a dip sensor, providing the potential for future measurements to be made in areas that are presently difficult to access with existing sensing architectures.

In Chapter 6 the sensing platform was extended by introducing a second, almost identical resonator to the tip of the MOF for self-referencing purposes, allowing the specific detection and quantification of proteins in undiluted human serum samples to be realized. The role of the second microsphere was to act as a dynamic reference, allowing any wavelength shift induced by nonspecific binging of other analytes present in the human serum samples to be compensated for. By simply taking advantage of surface functionalization techniques to create the reference and sensing microspheres, this approach still maintained all the previous advantages of the robust and easy to manipulate dip sensor architecture discussed in Chapter 5. As a result, it was shown that neutravidin concentrations as low as 25 nM could be detected, paving the way for future work expanding on the concept of the multiplexed detection of multiple biomarkers simultaneously. Importantly, this technique of self-referencing the sensor is independent of the sample (i.e. serum, whole blood, saliva) unlike other surface functionalization based approaches, opening up a wider range of possible applications of this sensing platform.

As outlined above, this thesis has demonstrated the ability of a fluorescent-based WGM fibre tip sensor to be used for biosensing applications, culminating in conducting measurements in undiluted human serum samples. For the platform to mature enough to be used in clinical settings and provide insightful diagnostic information there are several optimizations to the design and performance, as well as fundamental understanding that needs to be achieved. For example, in terms of final application of the platform as a diagnostic device, there is a growing need to be able to detect multiple biomarkers simultaneously, including monitoring relative concentrations of a combination of markers. The platform presented here provides the perfect base for future multiplexed sensing applications by using the remaining holes on the MOF to accommodate additional microspheres. Each of the additional microspheres could be functionalized for the detection of a different biomarker, allowing simultaneous monitoring to occur.

In terms of performance of the sensor, increasing the refractive index sensitivity is a key area of interest. For example, the possibility of developing hybrid sensing platforms for improving refractive index sensitivity have began to immerge, notably by increasing the local evanescent field through plasmonic effects. Alternatively, the Vernier effect between coupled resonators has provided a way to improve the refractive index sensitivity, without compromising the Q-factor and has been implemented for a variety of resonator geometries. However, in the platform's current configuration it is not possible

for the resonators to be coupled. Further, despite the potential to explore an alternative fiber design that could allow coupling between the resonators to occur on the fiber tip, the feasibility of this approach is questionable.

In its current form, the sensor is cost prohibitive to be used outside research environments with components such as a laboratory grade spectrometer and a specialized in-house fabricated fiber. One way to help lower the cost is to remove the need for the spectrometer. This could be achieved by utilizing the sensitive nature of the lasing threshold on variations in refractive index, whereby only a simple, and significantly cheaper, photodiode would be required for measurements. However, in order for this to be successfully implemented both theoretical and experimental work needs to be undertaken. As highlighted previously, from a theoretical point of view, understanding the behavior of the lasing threshold along with how it depends on resonator parameters such as Q-factor and mode volume remains incomplete. Being able to establish a concrete relationship between the lasing threshold and these parameters could open up the possibility of lasing within increasingly smaller resonators, with inherently greater refractive index sensitivities, for example. Experimentally, it is paramount that a stable gain medium (i.e. not susceptible to photobleaching) can be identified along with a stable laser source in order to provide reliable and reproducible performance.

Appendix A

MATLAB Code for Generating the Whispering Gallery Mode Spectra of Active Microspherical Resonators

Active Microsphere WGM Spectrum Simulator

```
%*********************************************************************
%Produces the WGM spectrum of microspherical resonator with a random
distribution of dipoles based on the Chew model for a given radius,
sphere refractive index, surrounding refractive index, over the
wavelength range x1-x2 in nm.

% Variables:
% a = Sphere radius in micron
% m0 = Sphere Refractive Index
% m1 = Surrounding Refractive Index
% x1 = start of wavelength range in nanometers
% x2 = end of wavelength range in nanometers

%This program with plot the WGM spectrum over the wavelength range x1
to x2. The resolution can modified by changing the spacing of lam1.

%Tess Reynolds and Matthew Henderson
%(2015)
%University of Adelaide, Australia.
%*********************************************************************

function data = TheChewSpec(a, m0, m1, x1, x2)

%clear

%Display the sphere radius and reractive index
disp(a)
disp(m0)

%Set the wavelength resolution
lam1 = linspace(x1, x2, 10000);
```

```
%Variables
lam = lam1./1000;                       %Wavelength
k1 = 2*pi*m0./lam;                      %Wavenumber - Sphere
k2 = 2*pi*m1./lam;                      %Wavenumber - Surrounding
p1 = a.*k1;                             %Size parameter - Sphere
p2 = a.*k2;                             %Size parameter - Surrounding
u1 = 1;                                 %u of Sphere
e1 = m0.^2;                             %e of Sphere
u2 = 1;                                 %u of Surrounding Medium
e2 = m1^2;                              %e of Surrounding Medium
sph = sqrt(pi./(2.*p1));                %Factor for spherical Bessel
sph2 = sqrt(pi./(2.*p2));               %Factor for spherical Bessel

%Initialize the array:
y2 = 0.*lam;

%Set up the other parameters: G & H%
G = (u1*u2)./(e1.*e2);
H = (9.*e1)./(4*p1.^5).*((u1.*e1.*e2)/u2).^0.5;

%Determine the max number of terms that need to be summed for the
series to converge
lim = p1(1)+4*p1(1)^(1/3)+2;
LI = round(lim);
N = m0/m1;
LI = abs(LI);
LI = round(LI);

%Begin the sum for total averaged rates:
for n = 1:LI
    if n == 1
        besseljnp05 = sph.*besselj(n+0.5,p1);
        besseljnm05 = sph.*besselj(n-0.5,p1);
        besselhnp05p2 = sph2.*besselh(n+0.5,p2);
        besselhnm05p2 = sph2.*besselh(n-0.5, p2);
    else
```

```
    %If we are past the first n, then just use the previous value for
    %n+0.5 as the new value for n-0.5 before we recalculate n+0.5.
    %E.g. we have n=2.  In the last iteration, n=1 and we calculated
    %n+0.5=1.5.  Now for n=2, n-0.5 = 1.5, so just use the old n+0.5
    %for this, as it is the same number.
        besseljnm05 = besseljnp05;
        besseljnp05 = sph.*besselj(n+0.5,p1);
        besselhnm05p2 = besselhnp05p2;
        besselhnp05p2 = sph2.*besselh(n+0.5,p2);
    end

    besseljnp15 = (2*(n+0.5)./p1).*besseljnp05 - besseljnm05;
    besseljnm15 = (2*(n-0.5)./p1).*besseljnm05 - besseljnp05;

    K = ((p1.^3)/2).*((besseljnp05).^2-besseljnp15.*besseljnm05);
    K1 = ((p1.^3)/2).*((besseljnm05).^2-besseljnp05.*besseljnm15);
    J = K1-n.*p1.*((besseljnp05).^2);

    dJ = p1.*besseljnm05-n.*besseljnp05;
    dH = p2.*besselhnm05p2-n.*besselhnp05p2;

    DnTm = e1.*besseljnp05.*dH-e2.*besselhnp05p2.*dJ;
    DnTe = u1.*besseljnp05.*dH-u2.*besselhnp05p2.*dJ;

    y1 = (J./(abs(DnTm).^2)+(G.*K)./(abs(DnTe).^2))*(2*n+1)/3;
    y2 = y1+y2;

end
y11 = y2.*2.*H;
%Plot the final spectrum

plot(lam*1000, abs(y11))
xlabel('Wavelength (nm)');
ylabel('Intensity (a.u)');

end
```

Appendix B

Fiber Fabrication

Four-hole Microstructured Optical Fiber

Ideally, an optical fibre specifically for use in WGM biosensing applications should have a tailored number, size and arrangement of holes for the specific application, a large core, and be made from a robust and easily manipulated material. Previous work has shown a possible enhancement of up to 30% in the Q-factor when the diameter of the microsphere resonator being used matched the diameter of the hole in the MOF. Therefore, as microspheres with nominal diameter of 15 μm and 20 μm were to be utilized, the fibre was designed to have holes within this size range. Further, the number and arrangement of holes was also considered, with a 4-hole design being selected to allow for more than one microsphere to be attached to the tip of the fiber at any one time, without interfering or coupling between any of the other microspheres. A core of between 5-7 μm was proposed to ensure efficiently coupling for both exciting and collecting the modulated fluorescence spectrum from the microsphere, and F300 silica glass (n = 1.45) was chosen as the material.

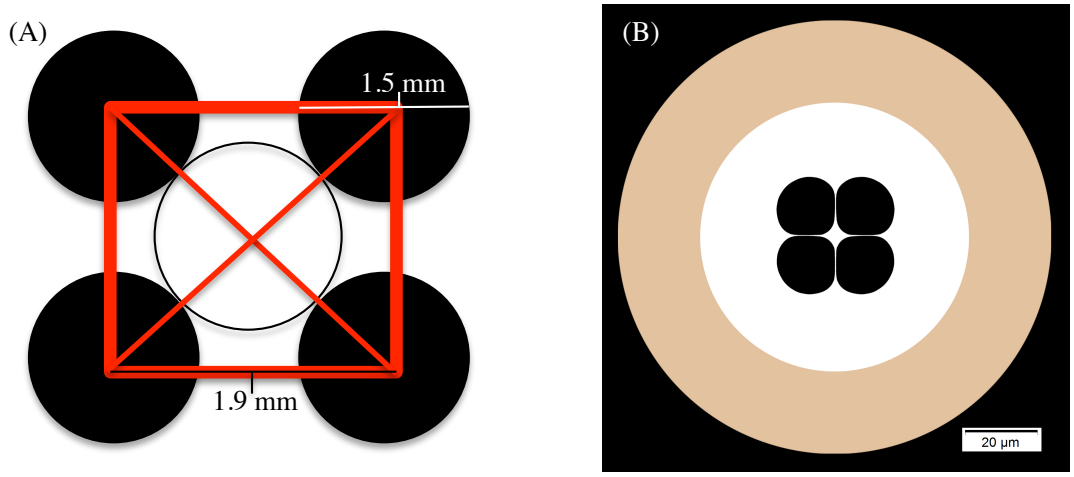

Fig. B.1 Schematics of (A) the preform drilling pattern (B) of the final 4-hole fiber design.

The final 4-hole fiber was made using a three-step process, beginning with drilling the preform, canning and then drawing the fiber. The preform was drilled in a 20 mm F300 Silica rod, approximately 100 mm in length, with 4 x 1.5 mm holes, placed in a square with spacing of 1.9 mm as depicted in Fig B.1. The canning process reduced the size of the preform to approximately 1.5 mm outer diameter, and then the cane was used to draw the final fibre with a diameter of 120 μm. The draw target parameters are summaries in Table B.1. A bright field image of the final fiber is shown in figure B.2 and a loss measurement in figure B.3. Approximately 2 km of fibre was drawn.

Fibre Drawing Target Parameters	
Temperature	2020 °C
Pressure	20 mbar
Feed	0.5 mm/min
Outer Diameter	120 µm

Table B.1 Summary of fibre drawing target parameters

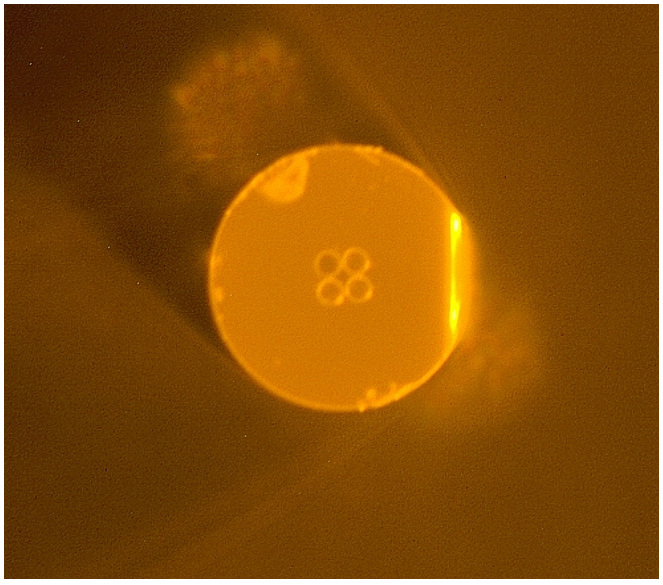

Fig. B.2 Bright field microscope image of two of the fabricated 4-hole MOF

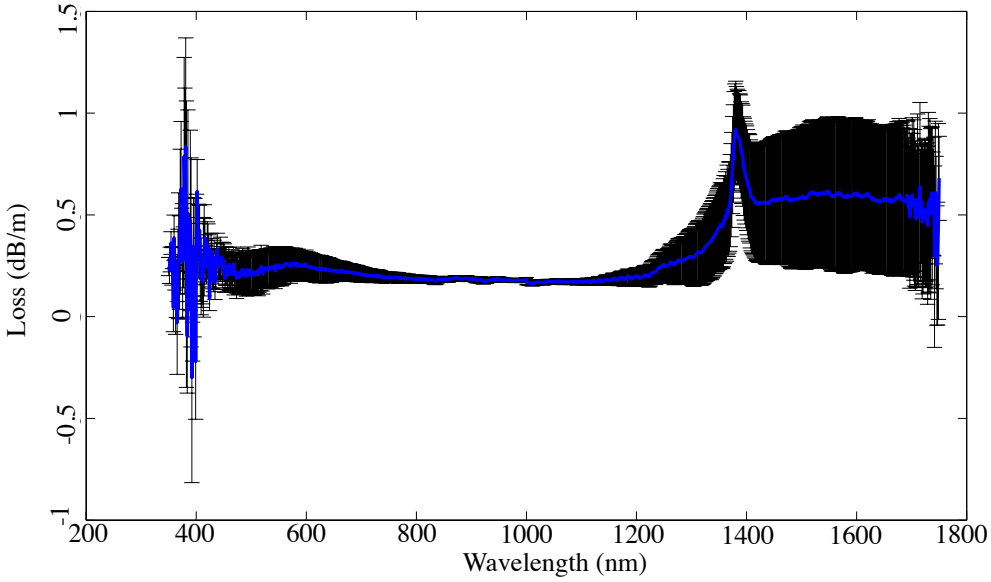

Fig. B. 3. Fibre lose measurement of the fabricated 4-hole MOF

Appendix C

The Theory of Active Multi-Layer Microsphere Resonators

C.1 Statement of Contribution

Statement of Authorship

Title of Paper	A unified theory of multilayer microspheres with single dipole or active layer sources
Publication Status	☐ Published ☒ Accepted for Publication ☐ Submitted for Publication ☐ Unpublished and Unsubmitted work written in manuscript style
Publication Details	J. M. M. Hall, T. Reynolds, M. R. Henderson, N. Riesen, T. M. Monro, and S. Afshar V., "A unified theory of multilayer microspheres with single dipole or active layer sources," Accepted for Publication in Optics Express, January 2017.

Principal Author

Name of Principal Author (Candidate)	Jonathan M. M. Hall		
Contribution to the Paper	Primarily wrote the paper and acted as corresponding author as well as assisting with the mathematical formulation of the analytical models throughout the project, along with assisting to write the MATLAB codes, primarily focusing on the single dipole case.		
Signature		Date	11-11-16

Co-Author Contributions

By signing the Statement of Authorship, each author certifies that:

i. the candidate's stated contribution to the publication is accurate (as detailed above);

ii. permission is granted for the candidate in include the publication in the thesis; and

Name of Co-Author	Tess Reynolds		
Contribution to the Paper	Assisted with the mathematical formulation of the analytical models throughout the project, along with assisting to writing the MATLAB codes, focusing on the dipole layer case, while also helping to evaluate and edit the manuscript. Overall percentage: 20%.		
Certification:	This paper reports on original research I conducted during the period of my Higher Degree by Research candidature and is not subject to any obligations or contractual agreements with a third party that would constrain its inclusion in this thesis. I am the primary author of this paper.		
Signature		Date	11-11-16

Name of Co-Author	Matthew R. Henderson		
Contribution to the Paper	Assisted with the mathematical formulation of the foundations of the analytical models derived as well as primarily writing the first iterations of the MATLAB codes.		
Signature		Date	16-11-16

Name of Co-Author	Nicolas Riesen		
Contribution to the Paper	Assisted with the mathematical formulation of the final forms of the analytical models derived along with helping to evaluate and edit the manuscript.		
Signature		Date	16-11-16

Name of Co-Author	Tanya M. Monro		
Contribution to the Paper	Supervised the entire project and contributed to the editing and evaluation of the manuscript.		
Signature		Date	16-11-16

Name of Co-Author	Shahraam Afshar V.		
Contribution to the Paper	Assisted with the mathematical formulation of the analytical models throughout the project, along with supervising the entire project and contributed to the editing and evaluation of the manuscript.		
Signature		Date	16-11-16

A unified theory of whispering gallery multilayer microspheres with single dipole or active layer sources

Jonathan M. M. Hall,[1,*] **Tess Reynolds,**[1] **Matthew R. Henderson,**[1] **Nicolas Riesen,**[1,2] **Tanya M. Monro**[1,2] **and Shahraam Afshar V.**[1,2]

[1]*Institute for Photonics & Advanced Sensing and ARC Centre for Nanoscale BioPhotonics, School of Physical Sciences, The University of Adelaide, Adelaide, SA 5005, Australia*

[2]*The University of South Australia, Adelaide, SA 5000, Australia*

[*]*jonathan.hall@adelaide.edu.au*

Abstract: The development of a fast and reliable whispering gallery mode (WGM) simulator capable of generating spectra that are comparable with experiment is an important step forward for designing microresonators. We present a new model for generating WGM spectra for multilayer microspheres, which allows for an arbitrary number of concentric dielectric layers, and any number of embedded dipole sources or uniform distributions of dipole sources to be modeled. The mode excitation methods model embedded nanoparticles, or fluorescent dye coatings, from which normalized power spectra with accurate representation of the mode coupling efficiencies can be derived. In each case, the emitted power is expressed conveniently as a function of wavelength, with minimal computational load. The model makes use of the transfer-matrix approach, incorporating improvements to its stability, resulting in a reliable, general set of formulae for calculating whispering gallery mode spectra. In the specific cases of the dielectric microsphere and the single-layer coated microsphere, our model simplifies to confirmed formulae in the literature.

OCIS codes: (140.3945) Microcavities; (230.0230) Optical devices; (230.5750) Resonators.

References and links

1. H. Chew, P. J. McNulty, and M. Kerker, "Model for Raman and fluorescent scattering by molecules embedded in small particles," Phys. Rev. A **13**, 396–404 (1976).
2. A. Moroz, "A recursive transfer-matrix solution for a dipole radiating inside and outside a stratified sphere," Annals of Physics **315**, 352–418 (2005).
3. F. Vollmer, D. Braun, A. Libchaber, M. Khoshsima, I. Teraoka, and S. Arnold, "Protein detection by optical shift of a resonant microcavity," Appl. Phys. Lett. **80**, 4057–4059 (2002).
4. S. Arnold, M. Khoshsima, I. Teraoka, S. Holler, and F. Vollmer, "Shift of whispering-gallery modes in microspheres by protein adsorption," Opt. Lett. **28**, 272–274 (2003).
5. H. Quan and Z. Guo, "Simulation of whispering-gallery-mode resonance shifts for optical miniature biosensors," J. Quant. Spectrosc. Radiat. Transfer **93**, 231–243 (2005).
6. Z. Guo, H. Quan, and S. Pau, "Near-field gap effects on small microcavity whispering-gallery mode resonators," J. Phys. D: Appl. Phys. **39**, 5133 (2006).
7. K. Imakita, H. Shibata, M. Fujii, and S. Hayashi, "Numerical analysis on the feasibility of a multi-layered dielectric sphere as a three-dimensional photonic crystal," Opt. Express **21**, 10651–10658 (2013).
8. R. Chance, A. Prock, and R. Silbey, "Molecular fluorescence and energy transfer near interfaces," Adv. Chem. Phys. **37**, 65 (1978).
9. H. Chew, "Radiation and lifetimes of atoms inside dielectric particles," Phys. Rev. A **38**, 3410–3416 (1988).

10. K. Kolmakov, V. N. Belov, J. Bierwagen, C. Ringemann, V. Muller, C. Eggeling, and S. W. Hell, "Red-emitting rhodamine dyes for fluorescence microscopy and nanoscopy," Chem. Eur. J. **16**, 158–166 (2010).
11. M. Li, X. Wu, L. Liu, and L. Xu, "Kerr parametric oscillations and frequency comb generation from dispersion compensated silica micro-bubble resonators," Opt. Express **21**, 16908–16913 (2013).
12. D. Farnesi, A. Barucci, G. C. Righini, G. N. Conti, and S. Soria, "Generation of hyper-parametric oscillations in silica microbubbles," Opt. Lett. **40**, 4508–4511 (2015).
13. N. Riesen, S. Afshar V., A. François, and T. M. Monro, "Material candidates for optical frequency comb generation in microspheres," Opt. Express **23**, 14784–14795 (2015).
14. G. Kozyreff, J. Dominguez-Juarez, and J. Martorell, "Nonlinear optics in spheres: from second harmonic scattering to quasi-phase matched generation in whispering gallery modes," Laser Photon. Rev. **5**, 737–749 (2011).
15. D. Farnesi, A. Barucci, G. C. Righini, S. Berneschi, S. Soria, and G. Nunzi Conti, "Optical frequency conversion in silica-whispering-gallery-mode microspherical resonators," Phys. Rev. Lett. **112**, 093901 (2014).
16. W. Liang, A. A. Savchenkov, Z. Xie, J. F. McMillan, J. Burkhart, V. S. Ilchenko, C. W. Wong, A. B. Matsko, and L. Maleki, "Miniature multioctave light source based on a monolithic microcavity," Optica **2**, 40–47 (2015).
17. Z. Ruan and S. Fan, "Superscattering of light from subwavelength nanostructures," Phys. Rev. Lett. **105**, 013901 (2010).
18. Y. He, H. Deng, X. Jiao, S. He, J. Gao, and X. Yang, "Infrared perfect absorber based on nanowire metamaterial cavities," Opt. Lett. **38**, 1179–1181 (2013).
19. C. Qu and E. C. Kinzel, "Polycrystalline metasurface perfect absorbers fabricated using microsphere photolithography," Opt. Lett. **41**, 3399–3402 (2016).
20. H. Chew, "Transition rates of atoms near spherical surfaces," J. Chem. Phys. **87**, 1355–1360 (1987).
21. Y. Xu, W. Liang, A. Yariv, J. G. Fleming, and S.-Y. Lin, "High-quality-factor bragg onion resonators with omnidirectional reflector cladding," Opt. Lett. **28**, 2144–2146 (2003).
22. Y. Xu, W. Liang, A. Yariv, J. G. Fleming, and S.-Y. Lin, "Modal analysis of bragg onion resonators," Opt. Lett. **29**, 424–426 (2004).
23. W. Liang, Y. Xu, Y. Huang, A. Yariv, J. Fleming, and S.-Y. Lin, "Mie scattering analysis of spherical Bragg "onion" resonators," Opt. Express **12**, 657–669 (2004).
24. I. Teraoka and S. Arnold, "Enhancing the sensitivity of a whispering-gallery mode microsphere sensor by a high-refractive-index surface layer," J. Opt. Soc. Am. B **23**, 1434–1441 (2006).
25. I. Teraoka and S. Arnold, "Theory of resonance shifts in TE and TM whispering gallery modes by nonradial perturbations for sensing applications," J. Opt. Soc. Am. B **23**, 1381–1389 (2006).
26. I. Teraoka and S. Arnold, "Whispering-gallery modes in a microsphere coated with a high-refractive index layer: polarization-dependent sensitivity enhancement of the resonance-shift sensor and TE-TM resonance matching," J. Opt. Soc. Am. B **24**, 653–659 (2007).
27. C. F. Bohren and D. R. Huffman, *Absorption and Scattering by a Sphere* (Wiley-VCH Verlag GmbH, 2007), pp. 82–129.
28. J. J. Kaufman, G. Tao, S. Shabahang, E.-H. Banaei, D. S. Deng, X. Liang, S. G. Johnson, Y. Fink, and A. F. Abouraddy, "Structured spheres generated by an in-fibre fluid instability," Nature **487**, 463–467 (2012).
29. G. Tao, J. J. Kaufman, S. Shabahang, R. Rezvani Naraghi, S. V. Sukhov, J. D. Joannopoulos, Y. Fink, A. Dogariu, and A. F. Abouraddy, "Digital design of multimaterial photonic particles," Proc. Nat. Acad. Sci. USA **113**, 6839–6844 (2016).
30. V. N. Astratov, J. P. Franchak, and S. P. Ashili, "Optical coupling and transport phenomena in chains of spherical dielectric microresonators with size disorder," Appl. Phys. Lett. **85**, 5508–5510 (2004).
31. D. K. Armani, T. J. Kippenberg, S. M. Spillane, and K. J. Vahala, "Ultra-high-Q toroid microcavity on a chip," Nature **421**, 925–928 (2003).
32. D. Xiao-Wei, L. Shao-Hua, F. Su-Chun, X. Ou, and J. Shui-Sheng, "All-fibre micro-ring resonator based on tapered microfibre," Chin. Phys. B **17**, 1029 (2008).
33. F. Monifi, S. Odemir, J. Friedlein, and L. Yang, "Encapsulation of a fiber taper coupled microtoroid resonator in a polymer matrix," IEEE Photon. Technol. Lett. **25**, 1458–1461 (2013).
34. N. Riesen, T. Reynolds, A. François, M. R. Henderson, and T. M. Monro, "Q-factor limits for far-field detection of whispering gallery modes in active microspheres," Opt. Express **23**, 28896–28904 (2015).
35. M. L. Gorodetsky and V. S. Ilchenko, "Optical microsphere resonators: optimal coupling to high-Q whispering-gallery modes," J. Opt. Soc. Am. B **16**, 147–154 (1999).
36. E. Nuhiji, F. G. Amar, H. Wang, N. Byrne, T.-L. Nguyen, and T. Lin, "Whispering gallery mode emission generated in tunable quantum dot doped glycerol/water and ionic liquid/water microdroplets formed on a superhydrophobic coating," J. Mater. Chem. **21**, 10823–10828 (2011).
37. J. Geng, R. W. Ziolkowski, R. Jin, and X. Liang, "Numerical study of the near-field and far-field properties of active open cylindrical coated nanoparticle antennas," IEEE Photon. J. **3**, 1093–1110 (2011).
38. N. V. Kryzhanovskaya, M. V. Maximov, and A. E. Zhukov, "Whispering-gallery mode microcavity quantum-dot lasers," IEEE J. Quant. Electron. **44**, 189–200 (2014).
39. A. François, T. Reynolds, and T. M. Monro, "A fiber-tip label-free biological sensing platform: A practical approach toward in-vivo sensing," Sensors **15**, 1168–1181 (2015).

40. T. C. Preston and J. P. Reid, "Determining the size and refractive index of microspheres using the mode assignments from Mie resonances," J. Opt. Soc. Am. A **32**, 2210–2217 (2015).
41. Y. Yang, J. Ward, and S. N. Chormaic, "Quasi-droplet microbubbles for high resolution sensing applications," Opt. Express **22**, 6881–6898 (2014).
42. J. M. M. Hall, S. Afshar V., M. R. Henderson, A. François, T. Reynolds, N. Riesen, and T. M. Monro, "Method for predicting whispering gallery mode spectra of spherical microresonators," Opt. Express **23**, 9924–9937 (2015).
43. T. Reynolds, M. R. Henderson, A. François, N. Riesen, J. M. M. Hall, S. Afshar V., S. J. Nicholls, and T. M. Monro, "Optimization of whispering gallery resonator design for biosensing applications," Opt. Express **23**, 17067–17076 (2015).
44. J. M. M. Hall, S. Afshar V., M. R. Henderson, A. François, T. Reynolds, N. Riesen, and T. M. Monro, "Determining the geometric parameters of microbubble resonators from their spectra," J. Opt. Soc. Am. B (2016).
45. H. Chew, M. Kerker, and P. J. McNulty, "Raman and fluorescent scattering by molecules embedded in concentric spheres," J. Opt. Soc. Am. **66**, 440–444 (1976).
46. W. Yang, "Improved recursive algorithm for light scattering by a multilayered sphere," Appl. Opt. **42**, 1710–1720 (2003).
47. A. François, K. J. Rowland, S. Afshar V., M. R. Henderson, and T. M. Monro, "Enhancing the radiation efficiency of dye doped whispering gallery mode microresonators," Opt. Express **21**, 22566–22577 (2013).
48. A. François, K. J. Rowland, and T. M. Monro, "Highly efficient excitation and detection of whispering gallery modes in a dye-doped microsphere using a microstructured optical fiber," Appl. Phys. Lett. **99**, 141111 (2011).
49. J. Blatt and V. Weisskopf, *Theoretical Nuclear Physics*, Dover Books on Physics Series (Dover Publications, 1991).
50. R. G. Barrera, G. A. Estevez, and J. Giraldo, "Vector spherical harmonics and their application to magnetostatics," Eur. J. Phys. **6**, 287 (1985).
51. J. Jackson, *Classical electrodynamics* (Wiley, 1975).
52. I. H. Malitson, "Interspecimen comparison of the refractive index of fused silica," J. Opt. Soc. Am. **55**, 1205–1209 (1965).
53. S. N. Kasarova, N. G. Sultanova, C. D. Ivanov, and I. D. Nikolov, "Analysis of the dispersion of optical plastic materials," Opt. Mater. **29**, 1481–1490 (2007).
54. A. Edmonds, *Angular Momentum in Quantum Mechanics*, Investigations in Physics Series (Princeton University, 1996).

1. Introduction

Due to their guidance of optical whispering gallery mode (WGM) resonances, dielectric microspheres have attracted a lot of interest in different fields of research, such as remote atmospheric sensing [1, 2], biosensing technologies [3–5], photonic band-gap devices [6, 7], fluorescence spectroscopy [8–10], nonlinear optics [11–16], superscattering [17], and metamaterial perfect absorbers [18, 19]. The extensive literature on these applications, together with the numerous theoretical works on light scattering from microspheres [1, 2, 9, 20–26] based on Mie scattering [27], clearly demonstrate a continually growing interest in this field of research. Technological advances have led to new possibilities for using microspheres with several dielectric layers, coatings of active materials, or doped with fluorescence nanoparticles [28, 29]. The excitation of WGM resonances of microspheres can also occur in numerous ways, such as via phase-matched optical waveguides [6, 30] or fiber tapers [31–34], prism coupling [35], fluorescence emission of incorporated nanoparticles [36–38], or active material coatings [39]. As a result, there is now a necessity to have more advanced models, as well as efficient numerical simulation tools, for describing these resonators and their excitation schemes accurately.

Simulation techniques are required for the interpretation of measured whispering gallery mode (WGM) spectra obtained from optical resonators. They may be used to identify the polarizations of the modes in a given WGM spectrum [40], and provide insight into how they can be used for sensing applications [25, 41–43]. Furthermore, the ability to calculate the underlying geometric parameters of a given resonator based solely on its spectrum [44] by scanning over a wide parameter space makes the development of a fast, reliable and general model for resonators of high importance.

The derivation of a model that contains multiple layers of concentric spheres has, until now, not been treated comprehensively. The development of a WGM spectrum model by

Chew [20, 45] considered spherical dielectric particles with embedded dipole sources, with the motivation being the modeling of Raman and fluorescence scattering. The Chew model was then extended to include a uniform distribution of dipole sources placed on the surface of a sphere [9]. A multilayer variant to the Chew model exists, but contains no derivation of the power spectrum [45]. Meanwhile, a generalization of Mie scattering theory, developed for spherical concentric 'onion' resonators, is constrained to external ray excitation [21–23], and does not provide emitted power spectra with which to compare to WGM resonances.

Analytic models typically make use of the transfer-matrix approach [2], which is faster and more convenient to construct mathematically than the multilayer Chew model. However, this approach suffers from numerical instabilities for certain parameter values [46], and needs to be treated carefully. More recent work on single-layer coated microspheres clearly separates the spectrum into TE and TM modes, and calculates the resonance positions [24, 26]. However, the correct identification of the TE and TM modes is not always achieved [2], and the work presented here clarifies these conventions. The key result of the present work is the derivation of a model for multilayer microsphere resonators, which may include dipole sources in any layer, or an active layer of sources. The model is able to generate the wavelength positions of the TE and TM modes, and calculate the emitted power spectrum, from a formalism that is general for any excitation strategy, unlike previous works [2].

The format of the article is as follows. In Section 2, the mathematics of the problem is summarized, and the conventions used in the literature are harmonized. In solving the boundary value problem of a multilayer microsphere using the transfer-matrix approach, the resonance positions are calculated. The formulae for the normalized power as a function of wavelength are then derived for two main cases. The first case is mode excitation via a single dipole placed on the surface with any desired orientation, analogous to embedded nanoparticles. The second case is a uniform distribution of dipoles of random orientation, extending the work by Chew [9], which is analogous to a fluorescent dye coating as commonly used in biosensing applications [47,48]. The distribution of dipoles can occur in any layer of the multilayer resonator. In Section 3, the formulae are shown to apply to specific cases, highlighting the differences between multilayer, single-layer and uncoated microsphere spectra. We showcase the results for active layer coated microspheres, and demonstrate the novelty of the unified multilayer model. A discussion of the implementation of the transfer-matrix algorithm is also included, demonstrating improvements made to the mean execution time. Tests showing that the model converges to the specific cases as the layer thickness becomes vanishingly small are given in the Appendix.

2. Theory

In this section, we state the basic equations required to find the wavelength positions of the resonances, and the radiation power spectrum of a multilayer microsphere, with either dipole sources or active layers for the excitation method.

2.1. Geometry

We consider a microsphere with an arbitrary number of concentric layers, N. The refractive index distribution and thicknesses are illustrated in Fig. 1. It is assumed that each layer includes a dipole emitter located at position $\mathbf{r}'_j$, where j is the layer number and the prime symbol is specifically used for the position of the *sources*. We use the radial coordinate $\mathbf{r}$ when representing fields at an arbitrary point in space, and r_j to specify unambiguously the radius of the boundary between the j^{th} and $j+1^{\text{th}}$ region. The outermost region is $N+1$, extended to infinity, and the innermost region is 1, hence the radius of the inner region is r_1 and r_N is the boundary of region N.

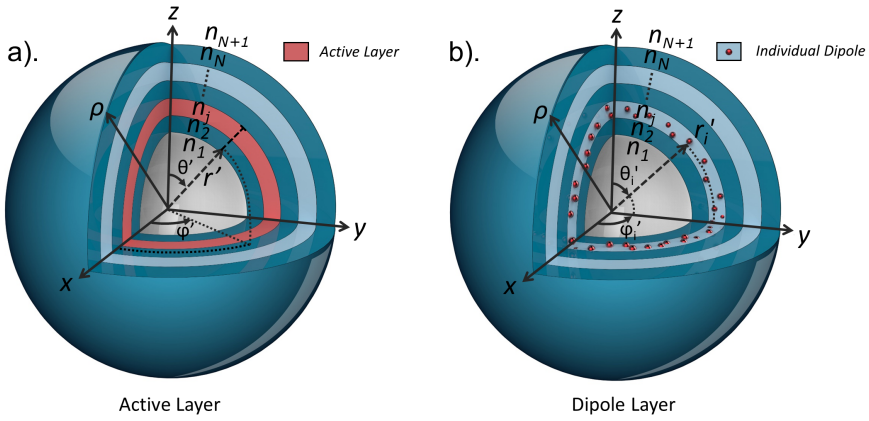

Fig. 1. The geometry of a spherical resonator with N layers. (a) A single layer contains a uniform distribution of dipoles, to represent an active layer. (b) One or more individual dipoles can be placed in a given layer, to represent one or more embedded nanoparticles.

2.2. *Conventions*

Considering the spherical symmetry of the problem, we use Vector Spherical Harmonics (VSH). Different conventions exist for the definition of VSH in the literature, e.g. atomic physics and electrodynamics (see [27] and [49]). We modify the definition given by Barrera [50],

$$\mathbf{Y}_{lm} = Y_{lm}(\theta,\phi)\hat{\mathbf{r}}, \quad \mathbf{\Psi}_{lm} = \left(\frac{1}{\mathrm{i}\sqrt{l(l+1)}}\right) r\nabla Y_{lm}(\theta,\phi), \quad \mathbf{\Phi}_{lm}(\theta,\phi) = \left(\frac{1}{\mathrm{i}\sqrt{l(l+1)}}\right)\mathbf{r}\times\nabla Y_{lm}(\theta,\phi), \tag{1}$$

where $Y_{lm}(\theta,\phi)$ are standard Scalar Spherical Harmonics [51], and l and m are the azimuthal quantum numbers. The vector functions $\mathbf{Y}_{lm}(\theta,\phi)$, $\mathbf{\Psi}_{lm}(\theta,\phi)$, and $\mathbf{\Phi}_{lm}(\theta,\phi)$ are orthonormal, and form a complete set (See Eqs. (68) and (69)), i.e. any vector field in spherical coordinates can be expanded based on these functions,

$$\mathbf{E}(r,\theta,\phi) = \sum_{l=0}^{\infty}\sum_{m=-l}^{m=l}\left[E^{r}_{lm}(r)\mathbf{Y}_{lm}(\theta,\phi) + E^{(1)}_{lm}(r)\mathbf{\Psi}_{lm}(\theta,\phi) + E^{(2)}_{lm}(r)\mathbf{\Phi}_{lm}(\theta,\phi)\right], \tag{2}$$

where the coefficients $E^{r}_{lm}, E^{(1)}_{lm}$ and $E^{(2)}_{lm}$ can be found by using orthogonality relations (see Appendix A). Note that $\mathbf{Y}_{lm}$ is in the radial direction and $\mathbf{\Psi}_{lm}$ and $\mathbf{\Phi}_{lm}$ are in the transverse plane perpendicular to $\hat{\mathbf{r}}$, and hence $E^{(1)}_{lm}$ and $E^{(2)}_{lm}$ represent the coefficients of the transverse field.

2.3. *Transfer Matrix Method*

We solve Maxwell's Equations in the SI system,

$$\mathbf{E} = \frac{\mathrm{i}c}{\omega\varepsilon}(\nabla\times\mathbf{H}), \quad \mathbf{H} = \frac{\mathrm{i}c}{\omega\varepsilon}(\nabla\times\mathbf{E}), \tag{3}$$

taking into account the boundary conditions of the problem. In general, the total electric and magnetic field in each region j can be written as the sum of the fields due to the dipole in the

layer, denoted $\mathbf{E}_{jd}, \mathbf{H}_{jd}$, and those associated with the reflection and transmission from other layers, denoted $\mathbf{E}_j, \mathbf{H}_j$. Hence $\mathbf{E}_j^{\text{total}} = \mathbf{E}_j + \mathbf{E}_{jd}$ and $\mathbf{H}_j^{\text{total}} = \mathbf{H}_j + \mathbf{H}_{jd}$. The fields $(\mathbf{E}_j, \mathbf{H}_j)$ can be written as [45]:

$$\begin{aligned}\mathbf{E}_j = &\sum_{l,m} \left(\frac{\mathrm{i}c}{n_j^2\omega}\right) A_j \nabla \times [j_l(k_j r)\mathbf{\Phi}_{lm}(\theta,\phi)] + \left(\frac{\mathrm{i}c}{n_j^2\omega}\right) B_j \nabla \times [h_l^{(1)}(k_j r)\mathbf{\Phi}_{lm}(\theta,\phi)] \\ &+ C_j j_l(k_j r)\mathbf{\Phi}_{lm}(\theta,\phi) + D_j h_l^{(1)}(k_j r)\mathbf{\Phi}_{lm}(\theta,\phi), \qquad (4)\\ \mathbf{H}_j = &\sum_{l,m} -\left(\frac{\mathrm{i}c}{\mu_j\omega}\right) C_j \nabla \times [j_l(k_j r)\mathbf{\Phi}_{lm}(\theta,\phi)] - \left(\frac{\mathrm{i}c}{\mu_j\omega}\right) D_j \nabla \times [h_l^{(1)}(k_j r)\mathbf{\Phi}_{lm}(\theta,\phi)] \\ &+ (\frac{1}{\mu_j}) A_j j_l(k_j r)\mathbf{\Phi}_{lm}(\theta,\phi) + (\frac{1}{\mu_j}) B_j h_l^{(1)}(k_j r)\mathbf{\Phi}_{lm}(\theta,\phi). \qquad (5)\end{aligned}$$

Here, A_j, B_j, C_j and D_j are coefficients that are determined through the boundary conditions. Note that A_j and B_j describe the transverse component of $\mathbf{H}_j$ and thus the TM modes, whereas C_j and D_j describe the TE modes, as defined by Jackson [51]. Also the choice of Bessel functions $j_l(k_j r)$ and $h_l^{(1)}(k_j r)$ ensures that appropriate functions of r can be constructed for any layer, including the innermost and outermost regions. Using the properties of the orthonormal functions $\mathbf{Y}_{lm}$, $\mathbf{\Psi}_{lm}$, and $\mathbf{\Phi}_{lm}$ (Eqs. (68) through (70)), we rewrite Eqs. (4) and (5) as

$$\begin{aligned}\mathbf{E}_j = &\sum_{l,m} \Bigg[-\left(\frac{\mathrm{i}c}{n_j^2\omega}\right) \frac{\sqrt{l(l+1)}}{\mathrm{i}} [A_j \frac{1}{r} j_l(k_j r) + B_j \frac{1}{r} h_l^{(1)}(k_j r)] \mathbf{Y}_{lm}(\theta,\phi) \\ &- \left(\frac{\mathrm{i}c}{n_j^2\omega}\right) \left\{ A_j \frac{1}{r}\frac{\mathrm{d}}{\mathrm{d}r}[r j_l(k_j r)] + B_j \frac{1}{r}\frac{\mathrm{d}}{\mathrm{d}r}[r h_l^{(1)}(k_j r)] \right\} \mathbf{\Psi}_{lm}(\theta,\phi) \\ &+ \left\{ C_j j_l(k_j r) + D_j h_l^{(1)}(k_j r) \right\} \mathbf{\Phi}_{lm}(\theta,\phi) \Bigg], \qquad (6)\\ \mathbf{H}_j = &\sum_{l,m} \Bigg[\left(\frac{\mathrm{i}c}{\mu_j\omega}\right) \frac{\sqrt{l(l+1)}}{\mathrm{i}} [C_j \frac{1}{r} j_l(k_j r) + D_j \frac{1}{r} h_l^{(1)}(k_j r)] \mathbf{Y}_{lm}(\theta,\phi) \\ &+ \left(\frac{\mathrm{i}c}{\mu_j\omega}\right) \left\{ C_j \frac{1}{r}\frac{\mathrm{d}}{\mathrm{d}r}[r j_l(k_j r)] + D_j \frac{1}{r}\frac{\mathrm{d}}{\mathrm{d}r}[r h_l^{(1)}(k_j r)] \right\} \mathbf{\Psi}_{lm}(\theta,\phi) \\ &+ (\frac{1}{\mu_j}) \left\{ A_j j_l(k_j r) + B_j h_l^{(1)}(k_j r) \right\} \mathbf{\Phi}_{lm}(\theta,\phi) \Bigg]. \qquad (7)\end{aligned}$$

This explicitly shows that the electric and magnetic fields $(\mathbf{E}_j, \mathbf{H}_j)$ in the layer j are written in terms of the orthonormal function set $\mathbf{Y}_{lm}(\theta,\phi)$, $\mathbf{\Psi}_{lm}(\theta,\phi)$, and $\mathbf{\Phi}_{lm}(\theta,\phi)$, in a form consistent with Eq. (2). The boundary conditions at the interfaces of the layers imply that transverse components of the fields are continuous, while there is a discontinuity in the normal components of the fields. We focus on transverse components of the fields, indicated by superscript (1) and (2) in Eq. (2), in layer j. We write them in a matrix form using Eqs. (6) and (7)

$$\mathbf{EH}_j = M_j(r)\mathbf{A}_j, \qquad (8)$$

where the block diagonal matrix $M_j(r) = \begin{pmatrix} M_j^{TM} & 0 \\ 0 & M_j^{TE} \end{pmatrix}$ and the vectors $\mathbf{EH}_j$ and $\mathbf{A}_j$ are defined as

$$M_j(r) = \frac{1}{k_j r} \begin{pmatrix} -\left(\frac{\mathrm{i}}{n_j}\right)\psi_l'(k_j r) & -\left(\frac{\mathrm{i}}{n_j}\right)\chi_l'(k_j r) & 0 & 0 \\ (\frac{1}{\mu_j})\psi_l(k_j r) & (\frac{1}{\mu_j})\chi_l(k_j r) & 0 & 0 \\ 0 & 0 & \psi_l(k_j r) & \chi_l(k_j r) \\ 0 & 0 & \left(\frac{\mathrm{i}n_j}{\mu_j}\right)\psi_l'(k_j r) & \left(\frac{\mathrm{i}n_j}{\mu_j}\right)\chi_l'(k_j r) \end{pmatrix}, \quad (9)$$

$$\mathbf{EH}_j(r) = \begin{pmatrix} E_j^{(1)}(r) \\ H_j^{(2)}(r) \\ E_j^{(2)}(r) \\ H_j^{(1)}(r) \end{pmatrix}, \quad \mathbf{A}_j = \begin{pmatrix} A_j \\ B_j \\ C_j \\ D_j \end{pmatrix}. \quad (10)$$

In arriving at Eq. (9) we have used $c/n_j\omega = 1/k_j$, Riccati-Bessel and Riccati-Hankel functions, $\psi_l(k_j r) = k_j r j_l(k_j r)$ and $\chi_l(k_j r) = k_j r h_l^{(1)}(k_j r)$, and their derivatives with respect to their arguments, $\psi_l^{'}(k_j r)$ and $\chi_l^{'}(k_j r)$. Note that the determinant of 2×2 blocks, M_j^{TM} and M_j^{TE}, are given by

$$\det(M_j^{TM}(r)) = \frac{\mathrm{i}}{\mu_j n_j k_j^2 r^2} W_{k_j r}[\psi_l(k_j r), \chi_l(k_j r)] = -\frac{1}{\mu_j n_j k_j^2 r^2}, \quad (11)$$

$$\det(M_j^{TE}(r)) = \frac{1}{k_j^2 r^2}\left(\frac{\mathrm{i}n_j}{\mu_j}\right) W_{k_j r_j}[\psi_l(k_j r), \chi_l(k_j r)] = -\frac{n_j}{\mu_j k_j^2 r^2}, \quad (12)$$

where the Wronskian is defined as

$$W_x[f(ax), g(ax)] \equiv f(ax)g'(ax) - f'(ax)g(ax), \quad \text{for the derivative with respect to } x. \quad (13)$$

Using Eq. (19) in [2], it can be shown that $W_{k_j r}[\psi_l(k_j r), \chi_l(k_j r)] = \mathrm{i}$. We write the fields $\mathbf{E}_{jd}(r), \mathbf{H}_{jd}(r)$ due to a dipole located in the layer j and at position $\mathbf{r}_j'$ in a similar way as Eq. (8), and hence we modify the field equations in [20] to write

$$\mathbf{EH}_{jd}(r) = \theta(r_j' - r) M_j(r)\mathbf{a}_{jL} + \theta(r - r_j') M_j(r)\mathbf{a}_{jH}. \quad (14)$$

Here, $\theta(r)$ is a step function [$\theta(r) = 0$ for $r < 0$ and $\theta(r) = 1$ for $r \geq 0$] that ensures the correct Bessel function $j_l(k_j r)$ or $h_l^{(1)}(k_j r)$ is selected to evaluate the fields at point r either when $r < r_j'$ (shown by subscript L in $\mathbf{a}_{jL}$) or $r > r_j'$ (shown by subscript H in $\mathbf{a}_{jH}$), respectively. The vectors $\mathbf{EH}_{jd}$, $\mathbf{a}_{jL}$ and $\mathbf{a}_{jH}$ are given by

$$\mathbf{EH}_{jd} = \begin{pmatrix} E_{jd}^{(1)} \\ H_{jd}^{(2)} \\ E_{jd}^{(2)} \\ H_{jd}^{(1)} \end{pmatrix}, \mathbf{a}_{jL} = \begin{pmatrix} a_{jEL} \\ 0 \\ a_{jML} \\ 0 \end{pmatrix}, \mathbf{a}_{jH} = \begin{pmatrix} 0 \\ a_{jEH} \\ 0 \\ a_{jMH} \end{pmatrix}, \quad (15)$$

where the coefficients a_{jEL}, a_{jML}, a_{jEH} and a_{jML} take the form [20]:

$$a_{jEL}(r'_j) = 4\pi k_j^2 \sqrt{\frac{\mu_j}{\varepsilon_j}} \mathbf{P}.\nabla'_j \times [h_l^{(1)}(k_j r'_j) \mathbf{\Phi}^*_{lm}(\theta'_j, \phi'_j)],\ a_{jML}(r'_j) = 4\pi \mathrm{i} k_j^3 \frac{1}{\varepsilon_j} h_l^{(1)}(k_j r'_j) \mathbf{P}.\mathbf{\Phi}^*_{lm}(\theta'_j, \phi'_j), \tag{16}$$

$$a_{jEH}(r'_j) = 4\pi k_j^2 \sqrt{\frac{\mu_j}{\varepsilon_j}} \mathbf{P}.\nabla'_j \times [j_l(k_j r'_j) \mathbf{\Phi}^*_{lm}(\theta'_j, \phi'_j)],\ a_{jMH}(r'_j) = 4\pi \mathrm{i} k_j^3 \frac{1}{\varepsilon_j} j_l(k_j r'_j) \mathbf{P}.\mathbf{\Phi}^*_{lm}(\theta'_j, \phi'_j). \tag{17}$$

The dipole coefficients a_{jEL} and a_{jEH} contribute to the TM modes, whereas a_{jML} and a_{jMH} contribute to the TE modes [27, 51], which has caused confusion in the literature [2]. Here, we use the subscripts E and M of the dipole coefficients to indicate their origin in the electric and magnetic multipole expansions, respectively. The ∇'_j symbol indicates derivatives with respect to the position $\mathbf{r}'_j$, and $\mathbf{P}$ is the dipole moment vector. Establishing field components in the layer j, we can construct the total field as the sum of fields in Eqs. (8) and (14), i.e.,

$$\mathbf{EH}_j^{\mathrm{T}}(r) = M_j(r)\mathbf{A}_j + \theta(r'_j - r) M_j(r)\mathbf{a}_{jL} + \theta(r - r'_j) M_j(r)\mathbf{a}_{jH}, \tag{18}$$

where superscript T indicates total fields in layer j. The continuity of the transverse components of the electric and magnetic fields at the interface of regions j and $j+1$ leads to

$$\mathbf{EH}_j^{\mathrm{T}}(r_j, \theta, \phi) = \mathbf{EH}_{j+1}^{\mathrm{T}}(r_j, \theta, \phi), \tag{19}$$

$$M_j(r_j)[\mathbf{A}_j + \mathbf{a}_{jH}] = M_{j+1}(r_j)[\mathbf{A}_{j+1} + \mathbf{a}_{j+1L}], \tag{20}$$

$$\mathbf{A}_{j+1} = M_{j+1}^{-1}(r_j) M_j(r_j)\mathbf{A}_j + M_{j+1}^{-1}(r_j) M_j(r_j)\mathbf{a}_{jH} - \mathbf{a}_{j+1L}. \tag{21}$$

Equation (20) can be used recursively to connect the coefficients in the outermost region, $N+1$, to the innermost region, 1, leading to

$$\mathbf{A}_{N+1} = T(N+1, 1)\mathbf{A}_1 + \mathbf{D}, \tag{22}$$

where matrix $T(N+1, j)$ is defined by

$$T(N+1, j) = M_{N+1}^{-1}(r_N) M_N(r_N) M_N^{-1}(r_{N-1}) M_{N-1}(r_{N-1}) M_{N-1}^{-1}(r_{N-2}) M_{N-2}(r_{N-2}) \ldots$$
$$M_{j+2}^{-1}(r_{j+1}) M_{j+1}(r_{j+1}) M_{j+1}^{-1}(r_j) M_j(r_j), \text{ for } 1 \le j < N+1, \tag{23}$$

$$T(N+1, j) = I_{4\times 4}, \text{ for } j = N+1. \tag{24}$$

Note that $T(N+1, j)$ is always composed of repetitive blocks of matrices in the form of $M_{j+1}^{-1}(r_j) M_j(r_j)$. Explicitly writing this matrix, it can be found that

$$M_{j+1}^{-1}(r_j) M_j(r_j) = \frac{\mathrm{i}}{n_{j+1}\mu_j} \frac{k_{j+1}}{k_j} G(j+1, j) = \frac{\mathrm{i}}{n_{j+1}\mu_j} \frac{k_{j+1}}{k_j} \begin{pmatrix} G_{11} & G_{12} & 0 & 0 \\ G_{21} & G_{22} & 0 & 0 \\ 0 & 0 & G_{33} & G_{34} \\ 0 & 0 & G_{43} & G_{44} \end{pmatrix}_{(j+1,j)}. \tag{25}$$

The sub-matrices $G^{TM} = \begin{pmatrix} G_{11} & G_{12} \\ G_{21} & G_{22} \end{pmatrix}$ and $G^{TE} = \begin{pmatrix} G_{33} & G_{34} \\ G_{43} & G_{44} \end{pmatrix}$ take the form

$$\begin{pmatrix} G_L \psi'_l(k_j r_j)\chi_l(k_{j+1} r_j) - G_R \psi_l(k_j r_j)\chi'_l(k_{j+1} r_j) & G_L \chi'_l(k_j r_j)\chi_l(k_{j+1} r_j) - G_R \chi_l(k_j r_j)\chi'_l(k_{j+1} r_j) \\ G_L \psi'_l(k_{j+1} r_j)\psi_l(k_j r_j) - G_R \psi_l(k_{j+1} r_j)\psi'_l(k_j r_j) & G_L \psi'_l(k_{j+1} r_j)\chi_l(k_j r_j) - G_R \psi_l(k_{j+1} r_j)\chi'_l(k_j r_j) \end{pmatrix} \tag{26}$$

for $G_L = \mu_j n_{j+1}^2/n_j$ and $G_R = \mu_{j+1} n_{j+1}$ in the case of G^{TM}, and $G_L = \mu_{j+1} n_j$ and $G_R = \mu_j n_{j+1}$ in the case of G^{TE}.

The constant vector $\mathbf{D}$ is given by

$$\mathbf{D} = \sum_{j=1}^{N+1} T(N+1,j)(1-\delta_{j,N+1})\mathbf{a}_{jH} - T(N+1,j)(1-\delta_{j,1})\mathbf{a}_{jL}. \tag{27}$$

The sum in Eq. (27) is effectively over the regions that contain dipoles, since terms associated with regions with no dipoles are zero. Equation (22) can be inverted to obtain $\mathbf{A}_1$ in terms of $\mathbf{A}_{N+1}$ as follows,

$$\mathbf{A}_1 = T^{-1}(N+1,1)\mathbf{A}_{N+1} + T^{-1}(N+1,1)\mathbf{D}. \tag{28}$$

Note that the constant vector $\mathbf{D}$, contains information about the structure through the scattering matrix T, and information about the dipole sources, through $\mathbf{a}_{jH}$ and $\mathbf{a}_{jL}$. However, matrices $T(N+1,1)$ and $T^{-1}(N+1,1)$ are independent of any source, and depend *only* on the parameters of the structure. Thus, they represent the scattering matrix of the entire structure. To avoid confusion between the elements of matrices $T(N+1,1)$ and $T(N+1,j)$, from now on, we use $T \equiv T(N+1,1)$ and $T^j \equiv T(N+1,j)$ for $j \neq 1$. The matrices of the form $T(N+1,j)$ are block diagonal matrices, since they have been built based on block diagonal matrices M. We define matrix $S \equiv \begin{pmatrix} S^{TM} & 0 \\ 0 & S^{TE} \end{pmatrix} = T^{-1}(N+1,1) = T^{-1}$ and hence

$$S = \begin{pmatrix} T_{11} & T_{12} & 0 & 0 \\ T_{21} & T_{22} & 0 & 0 \\ 0 & 0 & T_{33} & T_{34} \\ 0 & 0 & T_{43} & T_{44} \end{pmatrix}^{-1} = \begin{pmatrix} S_{11} & S_{12} & 0 & 0 \\ S_{21} & S_{22} & 0 & 0 \\ 0 & 0 & S_{33} & S_{34} \\ 0 & 0 & S_{43} & S_{44} \end{pmatrix}. \tag{29}$$

In the innermost region, the coefficients of Hankel functions in Eq. (4) and (5) are zero, and hence the vector $\mathbf{A}_1$ has the form $\mathbf{A}_1 = (A_1, 0, C_1, 0)$. Using this, Eq. (28) can be solved to find $\mathbf{A}_{N+1}$ in terms of A_1 and C_1 as

$$A_{N+1} = D_1 + \frac{S_{22}}{(-S_{21}S_{12} + S_{11}S_{22})} A_1, \tag{30}$$

$$B_{N+1} = D_2 - \frac{S_{21}}{(-S_{21}S_{12} + S_{11}S_{22})} A_1, \tag{31}$$

$$C_{N+1} = D_3 - \frac{S_{44}}{(S_{43}S_{34} - S_{33}S_{44})} C_1, \tag{32}$$

$$D_{N+1} = D_4 + \frac{S_{43}}{(S_{43}S_{34} - S_{33}S_{44})} C_1. \tag{33}$$

The coefficients $\mathbf{A}_{N+1} = (A_{N+1}, B_{N+1}, C_{N+1}, D_{N+1})^{\mathrm{T}}$ determine the fields in the region $N+1$, i.e., the outermost region, and hence are the scattering coefficients of the whole system of the microsphere and its sources. These coefficient are the same as a_n and b_n coefficients of Mie scattering, and represent different magnetic and electric dipole moments (B_{N+1} corresponds to a_n, and D_{N+1} corresponds to b_n).

Equations (31) through (32) are general, and can be used for a range of scenarios:

1. If there are no sources (i.e. no dipoles in the structure and no incident wave) then $\mathbf{D} = 0$, and from the above equations one can find the ratios B_{N+1}/A_{N+1} and D_{N+1}/C_{N+1}, which determine all the far field scattering coefficients. From these ratios one can find the TM and TE resonances of the structure, respectively (see Sections 8.1 and 8.2).

2. If there are dipole sources in the structure, then, without loss of generality, we can choose $A_{N+1} = C_{N+1} = 0$, solve for A_1 and C_1 from Eqs. (30) and (32) and then find B_{N+1} and D_{N+1} from Eqs. (31) and (33), respectively. This is due to the fact that the total emitted power must be the same in both the near and far fields.

3. If there is only an incident field, then $\mathbf{D} = 0$, and A_{N+1} and C_{N+1} are known from the incident wave expansion, and in turn A_1 and C_1 are known, which means that B_{N+1} and D_{N+1} are also known.

2.4. Structure Resonances

We consider the case where there are no sources- neither plane waves nor dipoles. Thus $\mathbf{D} = 0$ in Eqs. (31) through (32) and we can find

$$B_{N+1} = -\frac{S_{21}}{S_{22}} A_{N+1}, \tag{34}$$

$$D_{N+1} = -\frac{S_{43}}{S_{44}} C_{N+1}. \tag{35}$$

In the electric field of Eq.(4), B_{N+1} is the coefficient of the $h_l^{(1)}(kr)$ term and A_{N+1} is the coefficient of the $j_l(kr)$ term in the outermost region $N+1$. Hence the ratio of B_{N+1}/A_{N+1} should approach infinity near a resonance with a transverse magnetic component only. Similarly, in the magnetic field of Eq. (5), D_{N+1} is the coefficient of the $h_l^{(1)}(kr)$ term and C_{N+1} is the coefficient of the $j_l(kr)$ term, in the outer layer $N+1$. In this case, the ratio of D_{N+1}/C_{N+1} should approach infinity near a resonance with a transverse electric component only. As a result, both S_{21}/S_{22} and $S_{43}/S_{44} \to \infty$, which means the TM and TE resonances of the structure can be found by setting

$$T_{11} = 0 \text{ for TM resonances}, \tag{36}$$

$$T_{33} = 0 \text{ for TE resonances}. \tag{37}$$

These equations are in general multivalued, and for a given azimuthal quantum number l, the solutions to Eqs. 36 and 37 form the fundamental radial modes and their harmonics. The numerical code associated with this paper[1] uses the optical and geometrical properties of any structure, to find the T matrix, and numerically solves Eqs. (36) and (37) for any given wavelengths range.

2.5. Scattered power in the outer region

We are interested in calculating the total radiated power of the system. Thus, we need to calculate the fields as $r \to \infty$. In the outermost region $N+1$ and for $r \gg r'_j$, the total transverse parts of the fields in Eq. (18) are given by

$$\mathbf{EH}^{\mathrm{T}}_{N+1}(r) = M_{N+1}(r)\mathbf{A}_{N+1} + \theta(r - r'_{N+1}) M_{N+1}(r)\mathbf{a}_{N+1H}(r'_{N+1}). \tag{38}$$

In the limit of $r \to \infty$, this equation leads to the following forms for the scattered fields,

[1] http://www.photonicsimulation.net

$$\mathbf{E}_{sc} = -\sum_{l,m}\left(\frac{\mathrm{i}}{n_{N+1}}\right)\frac{1}{k_{N+1}r}\chi_l^{'}(k_{N+1}r)\mathbf{\Psi}_{lm}(\theta,\phi)[B_{N+1}+a_{N+1EH}(r'_{N+1})]$$
$$+\sum_{l,m}\mathbf{\Phi}_{lm}(\theta,\phi)\frac{1}{k_{N+1}r}\chi_l(k_{N+1}r)[D_{N+1}+a_{N+1MH}(r'_{N+1})], \tag{39}$$

$$\mathbf{H}_{sc} = \sum_{l,m}(\frac{1}{\mu_{N+1}})\mathbf{\Phi}_{lm}(\theta,\phi)\frac{1}{k_{N+1}r}\chi_l(k_{N+1}r)[B_{N+1}+a_{N+1EH}(r'_{N+1})]$$
$$+\sum_{l,m}(\frac{in_{N+1}}{\mu_{N+1}})\frac{1}{k_{N+1}r}\chi_l^{'}(k_{N+1}r)\mathbf{\Psi}_{lm}[D_{N+1}+a_{N+1MH}(r'_{N+1})]. \tag{40}$$

Note that in arriving at the above equation, we have used Eqs. (2), (9), and (10) and $j_l(kr)\to 0$ as $r\to\infty$. The total scattered power through a sphere of radius r can then be calculated by

$$P_{\text{total}} = r^2\int \mathbf{S}_{sc}.\hat{\mathbf{r}}d\Omega = \frac{c}{8\pi\mu_{N+1}}r^2\int(\mathbf{E}_{sc}\times\mu_{N+1}\mathbf{H}_{sc}^*).\hat{\mathbf{r}}d\Omega$$
$$= \frac{c}{8\pi\mu_{N+1}}\sum_{l,m}\Big(\frac{-\mathrm{i}}{n_{N+1}k_{N+1}^2}\Big)\chi_l^{'}k_{N+1}r\chi_l^*(k_{N+1}r)\left|B_{N+1}+a_{N+1EH}(r'_{N+1})\right|^2$$
$$+\mathrm{i}\frac{n_{N+1}}{k_{N+1}^2}\chi_l(k_{N+1}r)\chi_l^{*'}(k_{N+1}r)\left|D_{N+1}+a_{N+1MH}(r'_{N+1})\right|^2, \tag{41}$$

where we have used the orthonormal properties of $\mathbf{\Psi}_{lm}(\theta,\phi)$ and $\mathbf{\Phi}_{lm}(\theta,\phi)$ functions given in Eq. (68) through (70). Note that in the limit of $r\to\infty$, $\chi_l(z)\to zh_l^{(1)}(z)\to \mathrm{i}^{-l-1}e^{\mathrm{i}z}$ and $\chi_l^{'}(z)\to \mathrm{i}^{-l}e^{\mathrm{i}z}$ [2], and hence

$$P_{\text{total}} = \frac{c}{8\pi}\sqrt{\frac{\varepsilon_{N+1}}{\mu_{N+1}}}\frac{1}{k_{N+1}^2}\sum_{l,m}[\Big(\frac{1}{n_{N+1}^2}\Big)\left|B_{N+1}+a_{N+1EH}(r'_{N+1})\right|^2+\left|D_{N+1}+a_{N+1MH}(r'_{N+1})\right|^2]. \tag{42}$$

Equation (42) is general, where B_{N+1}, D_{N+1}, $a_{N+1EH}(r'_{N+1})$ and $a_{N+1MH}(r'_{N+1})$ can be calculated based on Eqs. (31), (33), (15), and (16) respectively. Note that if there is no dipole in the outermost region, then $a_{N+1EH}(r'_{N+1}) = a_{N+1MH}(r'_{N+1}) = 0$.

2.6. A dipole in one layer

In this section, we assume that there exists only one dipole in the layer j, where $j = 1,\ldots,N+1$. Then, according to Scenario 2 of Section 2.3,

$$A_1 = -\frac{(-S_{21}S_{12}+S_{11}S_{22})}{S_{22}}D_1, \quad C_1 = \frac{(S_{43}S_{34}-S_{33}S_{44})}{S_{44}}D_3,$$
$$B_{N+1} = D_2+\frac{S_{21}}{S_{22}}D_1, \qquad D_{N+1} = D_4+\frac{S_{43}}{S_{44}}D_3. \tag{43}$$

Then, using Eqs. (15), (27), and (29), we get

$$\mathbf{D} = T(N+1,j)(1-\delta_{j,N+1})\mathbf{a}_{jH}-T(N+1,j)(1-\delta_{j,1})a_{jL}$$
$$= \begin{pmatrix} T_{12}^j(1-\delta_{j,N+1})a_{jEH}-T_{11}^j(1-\delta_{j,1})a_{jEL} \\ T_{22}^j(1-\delta_{j,N+1})a_{jEH}-T_{21}^j(1-\delta_{j,1})a_{jEL} \\ T_{34}^j(1-\delta_{j,N+1})a_{jMH}-T_{33}^j(1-\delta_{j,1})a_{jML} \\ T_{44}^j(1-\delta_{j,N+1})a_{jMH}-T_{43}^j(1-\delta_{j,1})a_{jML} \end{pmatrix}, \tag{44}$$

based on which we can find

$$B_{N+1}+a_{N+1EH}(r'_{N+1}) =$$
$$(T^j_{22}+\frac{S_{21}}{S_{22}}T^j_{12})(1-\delta_{j,N+1})a_{jEH}(r'_j)-(T^j_{21}+\frac{S_{21}}{S_{22}}T^j_{11})(1-\delta_{j,1})a_{jEL}(r'_j)+\delta_{j,N+1}a_{jEH}(r'_j)$$
$$=\alpha_l a_{jEH}(r'_j)-\beta_l a_{jEL}(r'_j), \tag{45}$$
$$\text{where } \alpha_l=(T^j_{22}+\frac{S_{21}}{S_{22}}T^j_{12})(1-\delta_{j,N+1})+\delta_{j,N+1} \text{ and } \beta_l=(T^j_{21}+\frac{S_{21}}{S_{22}}T^j_{11})(1-\delta_{j,1}) \tag{46}$$

and

$$D_{N+1}+a_{N+1MH}(r'_{N+1}) =$$
$$(T^j_{44}+\frac{S_{43}}{S_{44}}T^j_{34})(1-\delta_{j,N+1})a_{jMH}(r'_j)-(T^j_{43}+\frac{S_{43}}{S_{44}}T^j_{33})(1-\delta_{j,1})a_{jML}(r'_j)+\delta_{j,N+1}a_{jMH}(r'_j)$$
$$=\gamma_l a_{jMH}(r'_j)-\zeta_l a_{jML}(r'_j), \tag{47}$$
$$\text{where } \gamma_l=(T^j_{44}+\frac{S_{43}}{S_{44}}T^j_{34})(1-\delta_{j,N+1})+\delta_{j,N+1} \text{ and } \zeta_l=(T^j_{43}+\frac{S_{43}}{S_{44}}T^j_{33})(1-\delta_{j,1}) \tag{48}$$

Equations (45) and (47) are also general, and can be applied to a dipole in any layer j, including the innermost layer 1 or the outermost layer $N+1$. Considering Eqs. (16) and (17), we can rewrite $B_{N+1}+a_{N+1EH}(r'_{N+1})$ and $D_{N+1}+a_{N+1MH}(r'_{N+1})$, which appear in the total scattered power in Eq. (42), as

$$B_{N+1}+a_{N+1EH}(r'_{N+1})=4\pi k_j^2\sqrt{\frac{\mu_j}{\varepsilon_j}}\mathbf{P}.\nabla'_j\times\{[\alpha_l j_l(k_j r'_j)-\beta_l h_l^{(1)}(k_j r'_j)]\mathbf{\Phi}^*_{lm}(\theta'_j,\phi'_j)\}, \tag{49}$$
$$D_{N+1}+a_{N+1MH}(r'_{N+1})=4\pi \mathrm{i}k_j^3\frac{1}{\varepsilon_j}[\gamma_l j_l(k_j r'_j)-\zeta_l h_l^{(1)}(k_j r'_j)]\mathbf{P}.\mathbf{\Phi}^*_{lm}(\theta'_j,\phi'_j). \tag{50}$$

Using the properties of orthonormal functions $\mathbf{Y}_{lm}$, $\mathbf{\Psi}_{lm}$, and $\mathbf{\Phi}_{lm}(\theta,\phi)$, and Eq (70), we note the forms of $B_{N+1}+a_{N+1EH}(r'_{N+1})=\mathbf{P}.[f_l(r'_j)\mathbf{Y}_{lm}+g_l(r'_j)\mathbf{\Psi}_{lm}]$ and $D_{N+1}+a_{N+1MH}(r'_{N+1})=\mathbf{P}.k_l(r'_j)\mathbf{\Phi}^*_{lm}$, where $f_l(r'_j), g_l(r'_j)$, and $k_l(r'_j)$ are functions of r'_j, as in Eqs. (49) and (50). Hence we can use the properties of the dyadic products of $\mathbf{Y}_{lm}$, $\mathbf{\Psi}_{lm}$, and $\mathbf{\Phi}_{lm}$, Eq. (71), to perform the summation over m and simplify $\sum_{l,m}\left|B_{N+1}+a_{N+1EH}(r'_{N+1})\right|^2$ and $\sum_{l,m}\left|D_{N+1}+a_{N+1MH}(r'_{N+1})\right|^2$, which appear in Eq. (42),

$$\sum_{l,m}\left|B_{N+1}+a_{N+1EH}(r'_{N+1})\right|^2 =$$
$$16\pi^2k_j^6(\frac{\mu_j}{\varepsilon_j})\sum_l\{\frac{2l+1}{4\pi}l(l+1)\frac{\left|[\alpha_l j_l(k_j r'_j)-\beta_l h_l^{(1)}(k_j r'_j)]\right|^2}{k_j^2 r'^2}|\mathbf{P}_r|^2$$
$$+\frac{2l+1}{8\pi}\frac{\left|\{\alpha_l\frac{\mathrm{d}}{\mathrm{d}r'_j}[r'_j j_l(k_j r'_j)]-\beta_l\frac{\mathrm{d}}{\mathrm{d}r'_j}[r'_j h_l(k_j r'_j)]\}\right|^2}{k_j^2 r'^2_j}(|\mathbf{P}_\theta|^2+\left|\mathbf{P}_\phi\right|^2)\}, \tag{51}$$
$$\sum_{l,m}\left|D_{N+1}+a_{N+1MH}(r'_{N+1})\right|^2 =$$
$$16\pi^2k_j^6(\frac{1}{\varepsilon_j^2})\sum_l\frac{2l+1}{8\pi}\left|[\gamma_{lm}j_l(k_j r'_j)-\zeta_{lm}h_l^{(1)}(k_j r'_j)]\right|^2(|\mathbf{P}_\theta|^2+\left|\mathbf{P}_\phi\right|^2). \tag{52}$$

Here, $\mathbf{P}_r$, $\mathbf{P}_\theta$, and $\mathbf{P}_\phi$ are the polar components of the polarization vector $\mathbf{P}$. Based on the above equation, we can find the total scattered power from a sphere as the sum of powers due to normal and transverse components of $\mathbf{P}$,

$$P_{total} = P_\perp + P_\parallel = \frac{c}{2}\sqrt{\frac{\varepsilon_{N+1}}{\mu_{N+1}}}\frac{k_j^4 n_j^2}{n_{N+1}^2}\frac{1}{\varepsilon_j^2}\sum_l (2l+1)\Bigg\{(\frac{n_j^2}{n_{N+1}^2})l(l+1)\frac{\left|[\alpha_l j_l(k_j r'_j)-\beta_l h_l^{(1)}(k_j r'_j)]\right|^2}{k_j^2 r'^2_j}|\mathbf{P}_r|^2$$
$$+\Bigg[\Big(\frac{n_j^2}{n_{N+1}^2}\Big)\frac{\left|\{\alpha_l \frac{\mathrm{d}}{\mathrm{d}r'_j}[r'_j j_l(k_j r'_j)]-\beta_l \frac{\mathrm{d}}{\mathrm{d}r'_j}[r'_j h_l(k_j r'_j)]\}\right|^2}{k_j^2 r'^2_j}+\left|[\gamma_l j_l(k_j r'_j)-\zeta_l h_l^{(1)}(k_j r'_j)]\right|^2\Bigg]\Bigg[\frac{|\mathbf{P}_\theta|^2+|\mathbf{P}_\phi|^2}{2}\Bigg]\Bigg\}. \tag{53}$$

One can normalize the powers $P_\perp$ and $P_\parallel$ to powers radiated by a dipole in a bulk material with $(n_j, \varepsilon_j, \mu_j)$, i.e. $P_\perp^0 = ck_j^4|\mathbf{P}_r|^2/(3\varepsilon_j n_j)$ and $P_\parallel^0 = ck_j^4(|\mathbf{P}_\theta|^2+|\mathbf{P}_\phi|^2)/(3\varepsilon_j n_j)$ to obtain

$$\frac{P_\perp}{P_\perp^0} = \frac{1}{2}\sqrt{\frac{\varepsilon_{N+1}}{\mu_{N+1}}}\frac{n_j^2}{n_{N+1}^2}\frac{3n_j}{\varepsilon_j}\sum_l(\frac{n_j^2}{n_{N+1}^2})(2l+1)l(l+1)\frac{\left|[\alpha_l j_l(k_j r'_j)-\beta_l h_l^{(1)}(k_j r'_j)]\right|^2}{k_j^2 r'^2_j} \tag{54}$$

$$\frac{P_\parallel}{P_\parallel^0} = \frac{1}{4}\sqrt{\frac{\varepsilon_{N+1}}{\mu_{N+1}}}\frac{n_j^2}{n_{N+1}^2}\frac{3n_j}{\varepsilon_j}\times$$
$$\sum_l(2l+1)\Bigg\{\Bigg[\Big(\frac{n_j^2}{n_{N+1}^2}\Big)\frac{\left|\{\alpha_l \frac{\mathrm{d}}{\mathrm{d}r'_j}[r'_j j_l(k_j r'_j)]-\beta_l \frac{\mathrm{d}}{\mathrm{d}r'_j}[r'_j h_l(k_j r'_j)]\}\right|^2}{k_j^2 r'^2_j}+\left|[\gamma_l j_l(k_j r'_j)-\zeta_l h_l^{(1)}(k_j r'_j)]\right|^2\Bigg]\Bigg\} \tag{55}$$

2.7. One active layer

In this section, we consider a multilayer structure where one of the layers consists of active material. In this context, we add randomly oriented and uniformly distributed dipoles, with density $\rho(r'_j)=1$, into that layer. As a result, one must integrate Eqs. (54) and (55) with respect to r'_j, which is located within the layer j. Since dipoles are randomly oriented in the layer, we can write $\left\langle P_{total}/P^0\right\rangle = \frac{1}{3}\left\langle P_\perp/P_\perp^0\right\rangle + \frac{2}{3}\left\langle P_\parallel/P_\parallel^0\right\rangle$, where

$$\left\langle\frac{P_\perp}{P_\perp^0}\right\rangle = \frac{1}{2}\sqrt{\frac{\varepsilon_{N+1}}{\mu_{N+1}}}\frac{n_j^2}{n_{N+1}^2}\frac{3n_j}{\varepsilon_j}\sum_l(\frac{n_j^2}{n_{N+1}^2})(2l+1)l(l+1)\int_j\frac{\left|[\alpha_l j_l(k_j r'_j)-\beta_l h_l^{(1)}(k_j r'_j)]\right|^2}{k_j^2 r'^2_j}d^3r'_j\Big/\int_j d^3r'_j \tag{56}$$

$$= \frac{1}{2}\sqrt{\frac{\varepsilon_{N+1}}{\mu_{N+1}}}\frac{n_j^2}{n_{N+1}^2}\frac{3n_j}{k_j^2\varepsilon_j V_{j\mathrm{shell}}}4\pi\sum_l(\frac{n_j^2}{n_{N+1}^2})l(l+1)I_l^{(1)}, \tag{57}$$

$$I_l^{(1)} = (2l+1)\int_j\left|[\alpha_l j_l(k_j r'_j)-\beta_l h_l^{(1)}(k_j r'_j)]\right|^2 dr'_j, \tag{58}$$

where the volume of the shell is $V_{j\mathrm{shell}} = 4\pi(r'^2_j - r'^2_{j-1})$. If $j=1$, then by convention, r_0 is set to zero, as in that case the volume is simply the sphere bounded by the innermost radius.

Similarly,

$$\left\langle \frac{P_{\parallel}}{P_{\parallel}^0} \right\rangle = \frac{1}{4}\sqrt{\frac{\varepsilon_{N+1}}{\mu_{N+1}}}\frac{n_j^2}{n_{N+1}^2}\frac{3n_j}{k_j^2\varepsilon_j}(\frac{n_j^2}{n_{N+1}^2})4\pi\sum_l(2l+1)\left\{\left[\int_j(\frac{n_j^2}{n_{N+1}^2})\left|\{\alpha_l\frac{\mathrm{d}}{\mathrm{d}r_j'}[r_j' j_l(k_j r_j')]\right.\right.\right.$$
$$\left.\left.\left. -\beta_l\frac{\mathrm{d}}{\mathrm{d}r_j'}[r_j' h_l(k_j r_j')]\}\right|^2 + k_j^2 r_j'^2\left|[\gamma_l j_l(k_j r_j') - \zeta_l h_l^{(1)}(k_j r_j')]\right|^2 dr_j' / \int_j d^3 r_j'\right]\right\}, \quad (59)$$

$$= \frac{1}{4}\sqrt{\frac{\varepsilon_{N+1}}{\mu_{N+1}}}\frac{n_j^2}{n_{N+1}^2}\frac{3n_j}{k_j^2\varepsilon_j V_{j\mathrm{shell}}}4\pi\sum_l(\frac{n_j^2}{n_{N+1}^2})I_l^{(2)} + I_l^{(3)}, \quad (60)$$

$$I_l^{(2)} = (2l+1)\int_{j\mathrm{shell}}\left|\{\alpha_l\frac{\mathrm{d}}{\mathrm{d}r_j'}[r_j' j_l(k_j r_j')] - \beta_l\frac{\mathrm{d}}{\mathrm{d}r_j'}[r_j' h_l(k_j r_j')]\}\right|^2 dr_j', \quad (61)$$

$$I_l^{(3)} = (2l+1)\int_{j\mathrm{shell}} k_j^2 r_j'^2\left|[\gamma_l j_l(k_j r_j') - \zeta_l h_l^{(1)}(k_j r_j')]\right|^2 dr_j'. \quad (62)$$

The total power is then

$$\left\langle \frac{P_{total}}{P^0} \right\rangle = \frac{1}{3}\left\langle \frac{P_{\perp}}{P_{\perp}^0} \right\rangle + \frac{2}{3}\left\langle \frac{P_{\parallel}}{P_{\parallel}^0} \right\rangle$$
$$= \frac{1}{2}\sqrt{\frac{\varepsilon_{N+1}}{\mu_{N+1}}}\frac{n_j^2}{n_{N+1}^2}\frac{n_j}{k_j^2\varepsilon_j V_{j\mathrm{shell}}}4\pi\sum_l\left[(\frac{n_j^2}{n_{N+1}^2})l(l+1)I_l^{(1)} + (\frac{n_j^2}{n_{N+1}^2})I_l^{(2)} + I_l^{(3)}\right]. \quad (63)$$

Defining a functional form

$$\Psi[p_l q_l](z) = \int p_l(z)q_l(z)dz = \text{constant} + \frac{1}{2}\{[z - \frac{l(l+1)}{z}]p_l q_l - \frac{1}{2}(p_l q_l' + p_l' q_l) + z p_l' q_l'\}, \quad (64)$$

where $p_l(z)$ and $q_l(z)$ can be any of $\psi(x) = x j_l(x)$ or $\chi(x) = x h_l^{(1)}(x)$, one can then find

$$\left[l(l+1)I_l^{(1)} + I_l^{(2)}\right] =$$
$$\frac{1}{k_j}\Big\{|\alpha_l|^2(l+1)\big(\Psi[|\psi_{l-1}|^2](k_j r_j) - \Psi[|\psi_{l-1}|^2(k_j r_{j-1})\big) + |\alpha_l|^2 l\big(\Psi[|\psi_{l+1}|^2](k_j r_j) - \Psi[|\psi_{l+1}|^2](k_j r_{j-1})\big)$$
$$+ |\beta_l|^2(l+1)\big(\Psi[|\chi_{l-1}|^2](k_j r_j) - \Psi[|\chi_{l-1}|^2](k_j r_{j-1})\big) + |\beta_l|^2 l\big(\Psi[|\chi_{l+1}|^2](k_j r_j) - \Psi[|\chi_{l+1}|^2](k_j r_{j-1})\big)$$
$$- (l+1)\Big(\alpha_l\beta_l^*\big(\Psi[\psi_{l-1}\chi_{l-1}^*](k_j r_j) - \Psi[\psi_{l-1}\chi_{l-1}^*\big)(k_j r_{j-1})]$$
$$+ \alpha_l^*\beta_l\big(\Psi[\psi_{l-1}^*\chi_{l-1}](k_j r_j) - \Psi[\psi_{l-1}^*\chi_{l-1}](k_j r_{j-1})\big)\Big)$$
$$- l\Big(\alpha_l\beta_l^*\big(\Psi[\psi_{l+1}\chi_{l+1}^*](k_j r_j) - \Psi[\psi_{l+1}\chi_{l+1}^*](k_j r_{j-1})\big)$$
$$+ \alpha_l^*\beta_l\big(\Psi[\psi_{l+1}^*\chi_{l+1}](k_j r_j) - \Psi[\psi_{l+1}^*\chi_{l+1}](k_j r_{j-1})\big)\Big)\Big\}, \quad (65)$$

where r_j and r_{j-1} are the radii of the upper and lower interfaces of the region j, respectively. Similarly, we can calculate

$$I_l^{(3)} = (2l+1)\int_{j\text{shell}} k_j^2 r_j'^2 \left|[\gamma_l j_l(k_j r_j') - \zeta_l h_l^{(1)}(k_j r_j')]\right|^2 dr_j' =$$
$$\frac{1}{k_j}(2l+1)\Big\{|\gamma_l|^2\big(\Psi[|\psi_l|^2](k_j r_j) - \Psi[|\psi_l|^2](k_j r_{j-1})\big) + |\zeta_l|^2\big(\Psi[|\chi_l|^2](k_j r_j) - \Psi[|\chi_l|^2](k_j r_{j-1})\big)$$
$$-\Big(\gamma_l\zeta_l^*\big(\Psi[\psi_l\chi_l^*](k_j r_j) - \Psi[\psi_l\chi_l^*](k_j r_{j-1})\big) + \gamma_l^*\zeta_l\big(\Psi[\psi_l^*\chi_l](k_j r_j) - \Psi[\psi_l^*\chi_l](k_j r_{j-1})\big)\Big)\Big\}. \tag{66}$$

With $\left[l(l+1)I_l^{(1)} + I_l^{(2)}\right]$ and $I_l^{(3)}$ now known, the total averaged power can be calculated from Eq. (63).

3. Demonstration and discussion

We now consider several scenarios of interest that can be uniquely treated using this model. First, we examine the behavior of the WGM spectrum of a silica microsphere (with dispersion included [52]) coated with a single high refractive index layer ($N = 2$) surrounded by water, as the thickness of the coating d is changed from 5 nm to 15 nm. Figure 2 shows the results for an electric dipole placed just outside the surface, with an orientation perpendicular or parallel to the surface of the sphere. A range of wavelengths 0.59–0.61 μm is simulated, and the outer diameter is kept fixed at 25 μm. It is found that there is a systematic shift in the prominent WGM peaks towards higher wavelengths, as the thickness of the layer is increased. The free spectral range, however, remains largely unchanged over this range of wavelength values. In the limit $d \to 0$, the results match the simple case of the Chew model, as anticipated [20].

The *thin* vertical lines marking the position of the resonances, with the corresponding mode numbers and labels, are obtained from the structure resonance positions in Eqs. (36) and (37) for a two-layer microsphere, by setting $N = 2$ in our general formalism. This can be done in a straightforward way in the code associated with this paper (see footnote on pg. 10). The *thick* vertical lines indicate the resonance positions obtained from the Arnold formalism [24, 26], which agree exactly. Note that in the case of the parallel excitation in Fig. 2(b), there is a small contribution from the TM mode as well, as expected from Eq. (55).

A silica microsphere of the same size, 25 μm, is then modeled as being coated with a polymer (PMMA) with dispersion incorporated through the Sellmeier equations for both materials [52, 53], as shown in Fig. 3. PMMA is simulated in this example because it can act as an active layer [47] and is a straightforward way of testing the functionality of the model. At the diameter considered, higher order modes are not strongly coupled to, and so both the TE and TM modes remain distinct, as can be seen in Fig. 3(a). The refractive index contrast between silica and PMMA is relatively small, and so the dependence of the mode positions on the thickness of the coating is more mild. A close-up view of the plot is shown in Fig. 3(b). The vertical lines indicate the full-width at half-maximum positions for a variety of peaks, from which Q-factors can be extracted. Q-factors corresponding to a selection of TM and TE modes are also shown above each peak. Note that for the TM modes (the left three peaks) there is a decrease in the Q-factor as d increases, but for the TE modes there is an apparent increase in the Q-factor.

The sensitivity of the WGM peaks can be examined by varying the refractive index of the surrounding medium, n_3. In Fig. 4(a), $d = 10$ nm, the mean TE peak shift leads to a sensitivity of $S \equiv d\lambda/dn_3 = 60.0$ nm/R.I.U. For a surrounding index of 1.36 and above, the index contrast is sufficiently low that the TM mode is suppressed, and only the TE mode appears. We also

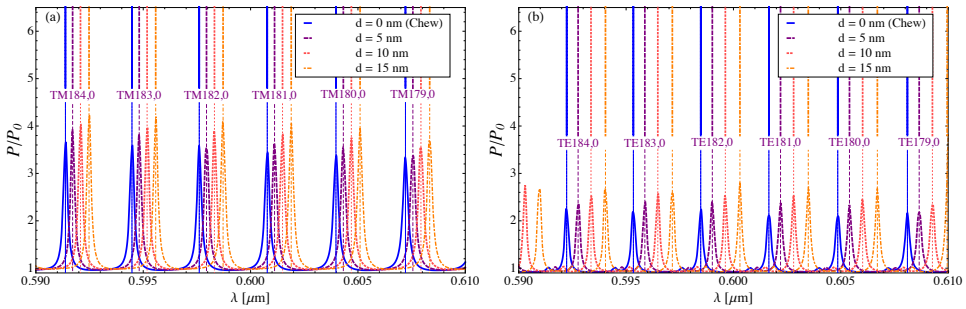

Fig. 2. Spectra obtained from a simulated silica microsphere, incorporating dispersion, coated with a high refractive index layer ($n_2 = 1.7$) with a diameter of 25 μm, surrounded by water. A single electric dipole is oriented (a) in the radial direction and (b) in the tangential direction.

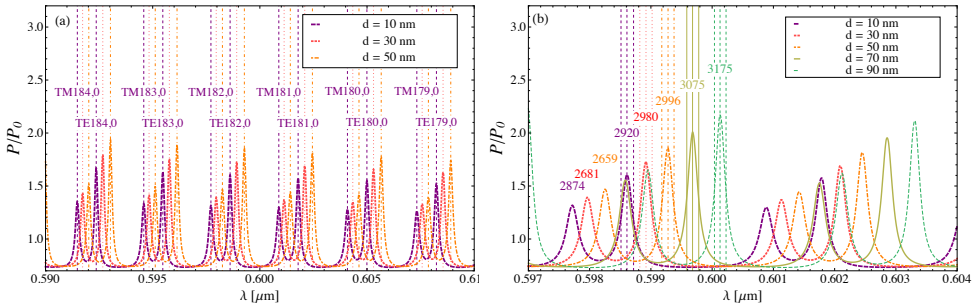

Fig. 3. Spectra for a silica microsphere coated with a polymer layer (PMMA), both of which include dispersion. The polymer layer functions as an active layer. (a) Both TE and TM modes are excited. (b) A zoomed in plot showing the FWHM of several peaks and their Q-factors.

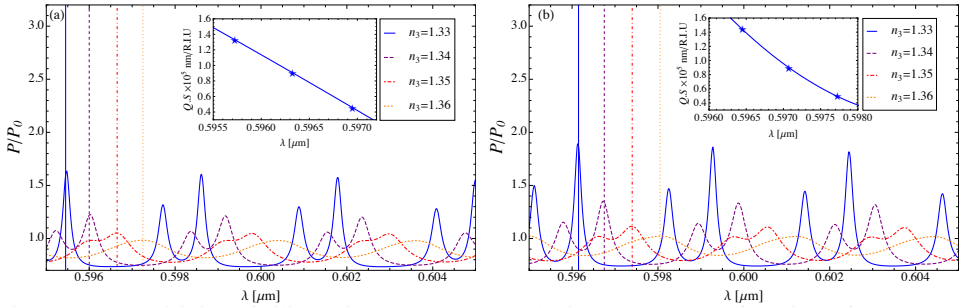

Fig. 4. The sensitivity of silica microspheres coated with PMMA as a function of the surrounding refractive index, for two example layer thicknesses. (a) $d = 10$ nm, (b) $d = 50$ nm. *Inset:* the figure of merit (FOM), $Q.S$, in units of 10^5 nm/R.I.U., as a function of λ.

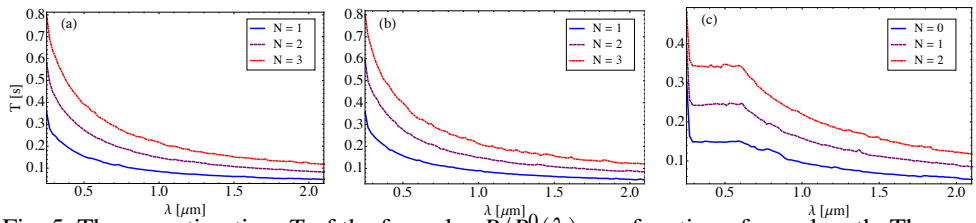

Fig. 5. The execution time T of the formulae $P/P^0(\lambda)$ as a function of wavelength. The results are shown for a numbers of layers $N = 1, 2$ and 3. The results for a single-dipole excitation oriented (a) parallel, and (b) perpendicular to the surface of the sphere are similar in magnitude. (c) The results of a single uniform distribution of dipoles within the center of the sphere begin to plateau as the wavelength becomes small. The tolerance selected is $\tau = 1 \times 10^{12}$.

calculate a figure of merit (FOM), defined as $Q.S$ [43], to assess the sensing performance of the microspheres. The inset of Fig. 4(a) shows a decrease in the FOM as a function of λ. In Fig. 4(b), $d = 50$ nm, both the sensitivity and the FOM are larger, with $S = 63.3$ nm/R.I.U.

The implementation of the algorithm for the calculation of $P/P^0(\lambda)$ is presented in the supplementary information. The summation, $\sum_{l=1}^{\infty}$, is calculated to an upper bound, l_{max}, determined by a prescribed tolerance τ, so that

$$\frac{|(P/P^0)_{l=l_{max}+1} - (P/P^0)_{l=l_{max}}|}{(P/P^0)_{l=l_{max}+1}} < \tau. \tag{67}$$

This prescription is sufficient so long as the behavior of P/P^0 is convergent, which is usually the case, except for unstable parameter regions, described below. At each value of $l > 1$, the spherical Bessel and Hankel functions are calculated using the recursion relations, and function calls are minimized to improve the efficiency of the calculation.

Examples of the scaling behavior of the execution times (T) for the functions $P/P^0(\lambda)$, with respect to wavelength, for numbers of layers $N = 1, 2$ and 3 are shown in Fig. 5 for a fixed outer diameter of 25 μm. The results are fairly insensitive to the layer thickness, allowing Fig. 5 to be a fairly accurate measure of the execution time for a given number of layers and prescribed tolerance, τ. It was found that the implementation of the recursion relations resulted in an improvement of approximately one order of magnitude in the execution time compared to function-call methods.

4. Conclusion

A method for the modeling of whispering gallery modes in optical resonators, including various excitation scenarios that closely mirror experimental techniques, is an important step toward facilitating the design and analysis of novel resonator architectures. We developed an algorithm based on the solutions of the boundary value problem for multilayer spherical resonators, with improved execution times compared to standard functional methods. The model is able to handle an arbitrary number of concentric, spherical dielectric layers, and extract the resonance positions from the characteristic equation. Formulae for the power spectrum are derived for the case of a single dipole or an active layer source, and the behavior of the mode positions are examined for several different scenarios. Estimates of the computation time for the normalized emitted power at a single wavelength, and improvements to stability issues inherent in the transfer-matrix approach, have been discussed. The spectrum simulator reported represents an important step towards a general, fast and efficient method for extracting the underlying parameters and properties of a given resonator purely from its spectrum, simulating spectra over a wide parameter space, and predicting features of novel resonator designs for photonic band-gap devices and biosensing applications.

5. Acknowledgements

The authors acknowledge the support of an Australian Research Council (ARC) Georgina Sweet Laureate Fellowship (T. M. M.), and the ARC Centre for Nanoscale BioPhotonics.

6. Appendix A: Properties of Vector Spherical Harmonics (VSH)

The VSH are orthogonal in the usual three-dimensional sense,

$$\mathbf{Y}_{lm} \cdot \mathbf{\Psi}_{lm} = \mathbf{\Phi}_{lm} \cdot \mathbf{\Psi}_{lm} = \mathbf{\Phi}_{lm} \cdot \mathbf{Y}_{lm} = 0, \tag{68}$$

and also orthonormal in the Hilbert space

$$\int \mathbf{Y}_{lm}\cdot\mathbf{Y}^*_{l'm'}d\Omega=\int \mathbf{\Psi}_{lm}\cdot\mathbf{\Psi}^*_{l'm'}d\Omega=\int \mathbf{\Phi}_{lm}\cdot\mathbf{\Phi}^*_{l'm'}d\Omega=\delta_{ll'}\delta_{mm'},$$
$$\int \mathbf{Y}_{lm}\cdot\mathbf{\Psi}^*_{l'm'}d\Omega=\int \mathbf{\Psi}_{lm}\cdot\mathbf{\Phi}^*_{l'm'}d\Omega=\int \mathbf{Y}_{lm}\cdot\mathbf{\Phi}^*_{l'm'}d\Omega=0. \tag{69}$$

In addition, it can be shown that

$$\nabla\times(f(r)\mathbf{Y}_{lm})=\frac{1}{r}f(r)\mathbf{\Phi}_{lm};\quad \nabla\times(f(r)\mathbf{\Psi}_{lm})=\left(\frac{df}{dr}+\frac{1}{r}f(r)\right)\mathbf{\Phi}_{lm},$$
$$\nabla\times(f(r)\mathbf{\Phi}_{lm})=-\frac{\sqrt{l(l+1)}}{ir}f\mathbf{Y}_{lm}-\left(\frac{df}{dr}+\frac{1}{r}f\right)\mathbf{\Psi}_{lm}. \tag{70}$$

The following summation rules apply to dyadic products of the VSH:

$$\sum_{m=-l}^{m=l}\mathbf{\Phi}_{lm}\mathbf{\Phi}^*_{lm}=\sum_{m=-l}^{m=l}\mathbf{\Psi}_{lm}\mathbf{\Psi}^*_{lm}=\frac{2l+1}{8\pi}(\mathbf{e}_\theta\mathbf{e}_\theta+\mathbf{e}_\phi\mathbf{e}_\phi);\ \sum_{m=-l}^{m=l}\mathbf{Y}_{lm}\mathbf{Y}^*_{lm}=\frac{2l+1}{4\pi}(\mathbf{e}_r\mathbf{e}_r);$$
$$\sum_{m=-l}^{m=l}\mathbf{\Phi}_{lm}\mathbf{Y}^*_{lm}=\sum_{m=-l}^{m=l}\mathbf{\Phi}_{lm}\mathbf{\Psi}^*_{lm}=\sum_{m=-l}^{m=l}\mathbf{Y}_{lm}\mathbf{\Psi}^*_{lm}=0. \tag{71}$$

7. Appendix B: Relation between conventions

Depending on the application, different definitions have been used for the VSH. The following functions have been used in the literature

$$\mathbf{X}_{lm}(\theta,\phi)=(\frac{1}{\mathrm{i}})(\frac{1}{\sqrt{l(l+1)}})\mathbf{r}\times\nabla Y_{lm}(\theta,\phi)\ [23,51] \tag{72}$$

$$\mathbf{Y}_{llm}(\theta,\phi)=(\frac{1}{\mathrm{i}})(\frac{1}{\sqrt{l(l+1)}})\mathbf{r}\times\nabla Y_{lm}(\theta,\phi)\text{Eq. (5.9.14) of [54]} \tag{73}$$

$$\mathbf{Y}^{(m)}_L=(\frac{1}{\mathrm{i}})(\frac{1}{\sqrt{l(l+1)}})\mathbf{r}\times\nabla Y_{lm}(\theta,\phi);\ \ \mathbf{Y}^{(e)}_L=-(\frac{1}{\mathrm{i}})(\frac{1}{\sqrt{l(l+1)}})r\nabla Y_{lm}(\theta,\phi);$$
$$(\frac{-1}{\mathrm{i}})Y_{lm}(\theta,\phi)\hat{\mathbf{r}}=\mathbf{Y}^{(o)}_L\ [2] \tag{74}$$

Comparing these equations with the orthonormal functions used here, Eqs. (1), we find,

$$\mathbf{Y}_{llm}=\mathbf{X}_{lm}=\mathbf{Y}^{(m)}_L=\mathbf{\Phi}_{lm},\qquad \mathbf{Y}^{(e)}_L=-\mathbf{\Psi}_{lm},\qquad (\frac{1}{\mathrm{i}})\mathbf{Y}^{(o)}_L=\mathbf{Y}_{lm}. \tag{75}$$

8. Appendix C: Examples

8.1. Example 1: A microsphere

For a microsphere, we set $N=1$, and then using Eq. (23), the T matrix is

$$T(2,1)=M_2^{-1}(r_1)M_1(r_1), \tag{76}$$

and hence we can use Eq. (25) and (26) with $j=1$ to find

$$T_{11} = \frac{i}{n_2\mu_1} G_{11} = \frac{i}{n_2\mu_1}\frac{k_2}{k_1}\frac{n_2}{n_1}[n_2\mu_1\psi_l'(k_1r_1)\chi_l(k_2r_1) - n_1\mu_2\psi_l(k_1r_1)\chi_l'(k_2r_1)], \tag{77}$$

$$T_{33} = \frac{i}{n_2\mu_1}\frac{k_2}{k_1} G_{33} = \frac{i}{n_2\mu_1}\frac{k_2}{k_1}[n_1\mu_2\psi_l'(k_1r_1)\chi_l(k_2r_1) - n_2\mu_1\psi_l(k_1r_1)\chi_l'(k_2r_1)]. \tag{78}$$

By assuming $\mu_1 = \mu_2$, the TM and TE resonance conditions, $T_{11} = 0$ and $T_{33} = 0$, lead to

$$n_2\frac{\psi_l^{'}(k_1r_1)}{\psi_l(k_1r_1)} = n_1\frac{\chi_l^{'}(k_2r_1)}{\chi_l(k_2r_1)} \text{ TM resonance condition,} \tag{79}$$

$$n_1\frac{\psi_l^{'}(k_1r_1)}{\psi_l(k_1r_1)} = n_2\frac{\chi_l^{'}(k_2r_1)}{\chi_l(k_2r_1)} \text{ TE resonance condition.} \tag{80}$$

Eqs. (79) and (80) exactly match Eqs. (19) and (13) in [25] and Eq. (4.53) in [27], respectively. It should be noted that in Eq. (33) of [2] the TE and TM modes are interchanged.

8.1.1. Special case: A dipole in the outer region

Let us assume a dipole source is located in the outermost region, i.e., $j = N+1 = 2$. Then $\mathbf{D}$ from Eqs. (27) and (23) becomes

$$\mathbf{D} = -T^2(2,2)a_{2L} = -I_{4\times4}\mathbf{a}_{2L} \tag{81}$$

Using Eq. (45) and (47), we can find $B_2 + a_{2EH}(r_j')$ and $D_2 + a_{2MH}(r_j')$ in

$$B_2 + a_{2EH}(r_2') = \alpha_l a_{2EH} - \beta_l a_{2EL}; \text{ where } \alpha_l = 1 \text{ and } \beta_l = (T_{21}^2 + \frac{S_{21}}{S_{22}}T_{11}^2) = \frac{S_{21}}{S_{22}} \tag{82}$$

$$D_2 + a_{2MH}(r_2') = \gamma_l a_{2MH} - \zeta_l a_{2ML}; \text{ where } \gamma_l = 1 \text{ and } \zeta_l = (T_{43} + \frac{S_{43}}{S_{44}}T_{33}) = \frac{S_{43}}{S_{44}} \tag{83}$$

Having identified the coefficient $\alpha_l, \beta_l, \gamma_l, \zeta_l$, we can find the power due to normal and transverse components using Eq. (54) and (55) as

$$\frac{P_\perp}{P_\perp^0} = \frac{3}{2}\sum_l (2l+1)l(l+1)\frac{\left|[j_l(k_2r_2') + \frac{S_{21}}{S_{22}}h_l^{(1)}(k_2r_2')]\right|^2}{k_2^2r_2'^2}, \tag{84}$$

$$\frac{P_\parallel}{P_\parallel^0} = \frac{3}{4}\sum_l (2l+1)\left\{\left[\frac{\left|\{\frac{\mathrm{d}}{\mathrm{d}r_2'}[r_2'j_l(k_2r_2')] + \frac{S_{21}}{S_{22}}\frac{\mathrm{d}}{\mathrm{d}r_2'}[r_2'h_l(k_2r_2')]\}\right|^2}{k_2^2r_2'^2} + \left|[j_l(k_2r_2') + \frac{S_{43}}{S_{44}}h_l^{(1)}(k_2r_2')]\right|^2\right]\right\}. \tag{85}$$

Now since $S = T^{-1}$, Eq. (29), then $\frac{S_{21}}{S_{22}} = -\frac{T_{21}}{T_{11}}$ and $\frac{S_{43}}{S_{44}} = -\frac{T_{43}}{T_{33}}$. In addition, $T(2,1) = M_2^{-1}(r_1)M_1(r_1)$ and hence we can use Eq. (25) and (26) to find

$$\frac{S_{21}}{S_{22}} = -\frac{[n_1\mu_2\psi_l'(k_2r_1)\psi_l(k_1r_1) - n_2\mu_1\psi_l(k_2r_1)\psi_l'(k_1r_1)]}{[n_2\mu_1\psi_l'(k_1r_1)\chi_l(k_2r_1) - n_1\mu_2\psi_l(k_1r_1)\chi_l'(k_2r_1)]} \tag{86}$$

$$= \frac{[(\varepsilon_2/n_2)\psi_l(k_2r_1)\psi_l'(k_1r_1) - (\varepsilon_1/n_1)\psi_l'(k_2r_1)\psi_l(k_1r_1)]}{[(\varepsilon_2/n_2)\psi_l'(k_1r_1)\chi_l(k_2r_1) - (\varepsilon_1/n_1)\psi_l(k_1r_1)\chi_l'(k_2r_1)]}, \tag{87}$$

$$\frac{S_{43}}{S_{44}} = -\frac{n_2\mu_1\psi_l'(k_2r_1)\psi_l(k_1r_1) - n_1\mu_2\psi_l(k_2r_1)\psi_l'(k_1r_1)}{n_1\mu_2\psi_l'(k_1r_1)\chi_l(k_2r_1) - n_2\mu_1\psi_l(k_1r_1)\chi_l'(k_2r_1)} \tag{88}$$

$$= \frac{(\varepsilon_1/n_1)\psi_l(k_2r_1)\psi_l'(k_1r_1) - (\varepsilon_2/n_2)\psi_l'(k_2r_1)\psi_l(k_1r_1)}{(\varepsilon_1/n_1)\psi_l'(k_1r_1)\chi_l(k_2r_1) - (\varepsilon_2/n_2)\psi_l(k_1r_1)\chi_l'(k_2r_1)}. \tag{89}$$

Having found the coefficients $\frac{S_{21}}{S_{22}}$ and $\frac{S_{43}}{S_{44}}$, we can find $\frac{P_\perp}{P_\perp^0}$ and $\frac{P_\parallel}{P_\parallel^0}$. Equations (86) and (88) are the same as Eqs. (6) and (7) of Chew [20].

8.1.2. Special case: A dipole in the inner region

Let us assume a dipole in the innermost region, then $N = 1$, $j = 1$ and from Eqs. (15), (23) and (27) we find $\mathbf{D} = T(2,1)\mathbf{a}_{jH} = (T_{12}a_{1EH}, T_{22}a_{1EH}, T_{34}a_{1MH}, T_{44}a_{1MH})$. Using Eq. (45) and (47), we can find $B_2 + a_{2EH}(r_1')$ and $D_2 + a_{2MH}(r_1')$,

$$B_{N+1} + a_{N+1EH}(r_2') = (T_{22} + \frac{S_{21}}{S_{22}}T_{12})a_{jEH} \tag{90}$$

$$= \alpha_l a_{_1EH} - \beta_l a_{1EL}; \text{ where } \alpha_l = (T_{22} + \frac{S_{21}}{S_{22}}T_{12}) \text{ and } \beta_l = 0 \tag{91}$$

$$D_{N+1} + a_{N+1MH}(r_2') = (T_{44} + \frac{S_{43}}{S_{44}}T_{34})a_{1MH} \tag{92}$$

$$= \gamma_l a_{1MH} - \zeta_l a_{1ML}; \text{ where } \gamma_l = (T_{44} + \frac{S_{43}}{S_{44}}T_{34}) \text{ and } \zeta_l = 0 \tag{93}$$

According to Eq. (27), $S = T^{-1}(2,1)$ hence $(S_{22}T_{22} + S_{21}T_{12}) = (S_{44}T_{44} + S_{43}T_{34}) = 1$ and as a result, $\alpha_l = \frac{1}{S_{22}}$ and $\gamma_l = \frac{1}{S_{44}}$. Now, since $S = T^{-1}(2,1)$, then $S_{22} = \det(T^{\mathrm{TM}})^{-1}T_{11}$ and $S_{44} = \det(T^{\mathrm{TE}})^{-1}T_{33}$ and hence we can use Eqs. (25) and (26) to find

$$S_{22} = [\det(M_2)^{-1}\det(M_1)]^{-1}\frac{\mathrm{i}}{n_2\mu_1}\frac{k_2}{k_1}\frac{n_2}{n_1}[n_2\mu_1\psi_l'(k_1r_1)\chi_l(k_2r_1) - n_1\mu_2\psi_l(k_1r_1)\chi_l'(k_2r_1)], \tag{94}$$

$$= -\mathrm{i}\frac{k_1n_1}{\varepsilon_2\varepsilon_1}\sqrt{\frac{\varepsilon_2}{\mu_2}}\frac{n_1}{n_2}[\varepsilon_1r_1j_l(k_1r_1)\chi'(k_2r_1) - \varepsilon_2\psi_l'(k_1r_1)rh_l(k_2r_1)]. \tag{95}$$

Similarly, we find

$$S_{44} = [\det(M_2)^{-1}\det(M_1)]^{-1}\frac{\mathrm{i}}{n_2\mu_1}\frac{k_2}{k_1}[n_1\mu_2\psi_l'(k_1r_1)\chi_l(k_2r_1) - n_2\mu_1\psi_l(k_1r_1)\chi_l'(k_2r_1)], \tag{96}$$

$$= \mathrm{i}(\frac{n_1}{\mu_2})[\frac{n_2}{\varepsilon_2}\psi_l'(k_1r_1)\chi_l(k_2r_1) - \frac{n_1}{\varepsilon_1}\psi_l(k_1r_1)\chi_l'(k_2r_1)]. \tag{97}$$

Thus, we can find $\frac{P_\perp}{P_\perp^0}$ and $\frac{P_\parallel}{P_\parallel^0}$ as

$$\frac{P_\parallel}{P_\parallel^0} = \frac{1}{4}\sqrt{\frac{\varepsilon_2}{\mu_2}}\frac{3n_1\varepsilon_1}{(k_1r_1)^2}\sum_l(2l+1)\left\{\frac{\left|\frac{\mathrm{d}}{\mathrm{d}r_1'}[r_j' j_l(k_1r_1')]\right|^2}{k_1^2r_1'^2\left|D_l\right|^2}+\frac{\mu_1\mu_2}{\varepsilon_2\varepsilon_1}\frac{\left|j_l(k_1r_1')\right|^2}{\left|D_l'\right|^2}\right\}, \tag{98}$$

$$\frac{P_\perp}{P_\perp^0} = \frac{1}{2}\sqrt{\frac{\varepsilon_2}{\mu_2}}\frac{3n_1\varepsilon_1}{(k_1r_1)^2}\sum_l(2l+1)l(l+1)\frac{\left|j_l(k_1r_1')\right|^2}{k_1^2r_1'^2\left|D_l\right|^2}, \tag{99}$$

$$\text{for}\quad D_l=[\varepsilon_1 j_l(k_1r_1)\chi_l'(k_2r_1)-\varepsilon_1\psi_l'(k_1r_1)h_l(k_2r_1)],\quad D_l'=D_l(\varepsilon\leftrightarrow\mu). \tag{100}$$

These are exactly the same as Eqs. (1, 3a) and Eq. (2,3) of Chew [9].

8.1.3. Special case: A microsphere with an active inner region

Now assume that the inner region is filled with randomly oriented dipoles. Then, we can use Eqs. (63), (65), and (66) together with $\alpha_l=\frac{1}{S_{22}}$, $\beta_l=0$, $\zeta=0$, and $\gamma_l=\frac{1}{S_{44}}$, calculated in the previous section, to find

$$\frac{1}{(2l+1)}\left[l(l+1)I_l^{(1)}+I_l^{(2)}\right]=\frac{\alpha_l^2}{(2l+1)k_1}\{(l+1)\Psi[\psi_{l-1}^2](k_1r_1)+l^2\Psi[\psi_{l+1}^2](k_1r_1)\}. \tag{101}$$

Note that r_1 and r_0, which would be the radii of the higher and lower interfaces of inner region for a microsphere, means that r_0 is set to zero, and all functional forms $\Psi[\cdot](k_1r_0)=0$. Similarly, we can also find

$$I_l^{(3)}=\frac{1}{k_1}(2l+1)\gamma_l^2\Psi[\psi_l^2](k_1r_1) \tag{102}$$

Having $\frac{1}{(2l+1)}\left[l(l+1)I_l^{(1)}+I_l^{(2)}\right]$ and $I_l^{(3)}$, we find

$$\left\langle\frac{P_{total}}{P^0}\right\rangle=\frac{1}{3}\left\langle\frac{P_\perp}{P_\perp^0}\right\rangle+\frac{2}{3}\left\langle\frac{P_\parallel}{P_\parallel^0}\right\rangle=\frac{3}{2}\sqrt{\frac{\varepsilon_2}{\mu_2}}\frac{n_1^2}{n_2^2}\frac{n_1}{k_1^2\varepsilon_1r_1^3}\sum_l\left[l(l+1)I_l^{(1)}+I_l^{(2)}+I_l^{(3)}\right]. \tag{103}$$

8.2. Example 2: A shell

If $N=2$, i.e., a microsphere coated by a single layer, then using Eqs. (23), (25), and (26), we have the following $T(3,1)$ matrix:

$$T=M_3^{-1}(r_2)M_2(r_2)M_2^{-1}(r_1)M_1(r_1)=\frac{ik_3}{n_2\mu_2}\frac{ik_2}{n_1\mu_1}G(3,2)G(2,1). \tag{104}$$

One can find the TM and TE resonances of the structure by setting $T_{11}=0$ and $T_{33}=0$, respectively, from Eqs. (36) and (37)

$$T_{11}=\frac{ik_3}{n_2\mu_2}\frac{ik_2}{n_1\mu_1}[G_{11}(3,2)G_{11}(2,1)+G_{12}(3,2)G_{21}(2,1)]=0 \tag{105}$$

$$T_{33}=\frac{ik_3}{n_2\mu_2}\frac{ik_2}{n_1\mu_1}[G_{33}(3,2)G_{33}(2,1)+G_{34}(3,2)G_{43}(2,1)]=0 \tag{106}$$

which results in the following resonances

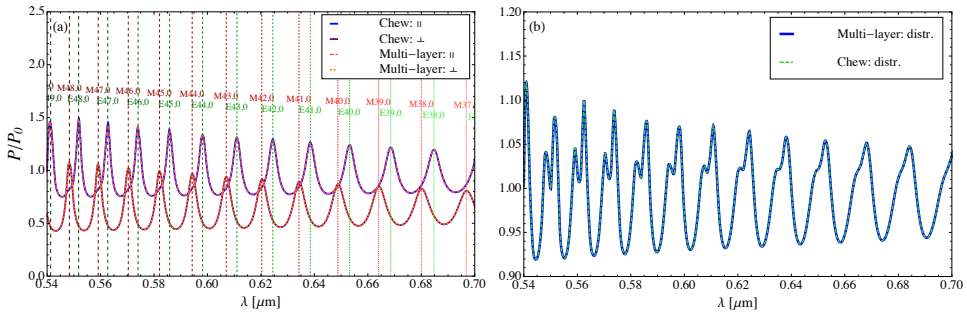

Fig. 6. Demonstration that the multilayer model reproduces the microsphere model results, for $D = 6\ \mu$m, $n_1 = 1.59$, and $n_2 = 1.33$. (a) Spectra for single-dipole excitation in both tangential and radial orientations. (b) Spectra for a uniform distribution of dipoles are also shown.

$$\frac{\mu_2 n_3 \chi_l(k_3 r_2)}{n_2 \mu_3 \chi_l'(k_3 r_2)} = \frac{\frac{C}{D}\psi_l(k_2 r_2) + \chi_l(k_2 r_2)}{\frac{C}{D}\psi_l'(k_2 r_2) + \chi_l'(k_2 r_2)\}} \quad \text{(TM)} \tag{107}$$

and

$$\frac{n_2 \mu_3 \chi_l(k_3 r_2)}{n_3 \mu_2 \chi_l'(k_3 r_2)} = \frac{\frac{E}{F}\psi_l(k_2 r_2) + \chi_l(k_2 r_2)}{\frac{E}{F}\psi_l'(k_2 r_2) + \chi_l'(k_2 r_2)} \quad \text{(TE)} \tag{108}$$

where

$$\frac{C}{D} = \frac{[n_2 \mu_1 \psi_l'(k_1 r_1)\chi_l(k_2 r_1) - n_1 \mu_2 \psi_l(k_1 r_1)\chi_l'(k_2 r_1)]}{[n_1 \mu_2 \psi_l'(k_2 r_1)\psi_l(k_1 r_1) - n_2 \mu_1 \psi_l(k_2 r_1)\psi_l'(k_1 r_1)]} \tag{109}$$

$$\frac{E}{F} = \frac{[n_1 \mu_2 \psi_l'(k_1 r_1)\chi_l(k_2 r_1) - n_2 \mu_1 \psi_l(k_1 r_1)\chi_l'(k_2 r_1)]}{[n_2 \mu_1 \psi_l'(k_2 r_1)\psi_l(k_1 r_1) - n_1 \mu_2 \psi_l(k_2 r_1)\psi_l'(k_1 r_1)]}. \tag{110}$$

Eqs. (107) and (108) exactly match Eq. (7) in [26] and Eq. (10) in [24], respectively.

A numerical comparison is shown in Fig. 6. The multilayer model for a single layer converges to the microsphere case for a vanishingly small layer coating, or a vanishingly small internal sphere size. It was found that both the limits converge to within numerical precision.

Appendix D

MATLAB Code for Generating the Whispering Gallery Mode Spectra of Active Multilayer Microspherical Resonators

Active Multilayer Microsphere WGM Spectrum Simulator

Matthew R Henderson, Jonathan M M Hall, Tess Reynolds Shahraam Afshar V. and Nicholas Riesen.

MLStest.m is an example spectrum calculator, and may be modified to save, print or plot spectra across a range of wavelength values, for any number of layers, refractive index values and radii. The excitation method is established by assigning the dipole layer, and calling the routine 'calculateSpectrum1Dipole.m' or 'calculateSpectrumDipoleLayer.m'. The output of each of these routines is a spectrum.

Website: http://www.photonicssimulation.net/microsphere

MLStest.m

```
%MLSTEST: An example testing file. Given multilayer microsphere
parameters, output a spectrum within a given wavelength range.
%Matthew Henderson, Jonathan Hall, Tess Reynolds, Shahraam Afshar.
%(2015)
%University of Adelaide, Australia.

clear all
format long e

%Set the number of layers:
Nlayers=2;

%Set the refractive indices of each layer, and the outer medium:
n(1)=1.00;
n(2)=1.59;
n(3)=1.33;

%Set the radii values (in units of micron):
rad(1)=3.0-0.5;
rad(2)=3.0;

%Set the dipole position (for calculateSpectrum1Dipole case):
dpos(1)=rad(2)-10^-10;
dpos(2)=0;
```

```
dpos(3)=0;

%Obtain the layer the dipole sits in, from dpos:
dlayer=1;
for ilayer=1:Nlayers
  if rad(ilayer)<norm(dpos)
      dlayer=ilayer+1;
  end
end

%Set the dipole orientation:
Pr=1; Ptheta=0; Pphi=0;

%Set the wavelength range:
lamlo=0.60;
lamup=0.60;

%Define the wavelength array, for a given coarseness:
lambda0_vect=(lamlo:0.002:lamup);

%Set the buffer size and convergence tolerance:
buff=0.2;
tol=1e-5;

%Create a multilayer sphere:
s=createMLSphere(lamlo, lamup, buff, [rad], [n], [dpos], [Pr Ptheta
Pphi], dlayer);

%Calculate the spectrum:
P=calculateSpectrum1Dipole(lambda0_vect,tol,s);
%P=calculateSpectrumDipoleLayer(lambda0_vect,tol,s);
```

createMLSphere.m

```
function sphere = createMLSphere(wavelengthLow, wavelengthHigh,
wavelengthBuffer, radii, refractiveIndices, dipolePosition,
dipoleVector, dipoleLayer)
```

```
%createMLSphere creates a data structure for storing the geometric
%parameters of a multilayer sphere.

%Matthew Henderson, Jonathan Hall, Tess Reynolds, Shahraam Afshar.
%(2015)
%University of Adelaide, Australia.

%INPUT CHECKS
if length(refractiveIndices) ~= length(radii) + 1
    error('MLWGMSolver:refractiveIndexRadiiLengthMismatch', 'There
must be N+1 refractive indices for N radii, check input vector
lengths.');
end

if wavelengthLow > wavelengthHigh
    error('MLWGMSolver:wavelengthLimitsOutOfBounds', 'The high limit
of wavelength must be larger than the low limit.');
end

sphere.wavelengthRange = [wavelengthLow wavelengthHigh];
sphere.radii = radii;
sphere.refractiveIndices = refractiveIndices;
sphere.permeabilities = ones(length(refractiveIndices), 1);
sphere.permittivities = refractiveIndices.^2;

sphere.dipolePosition = dipolePosition;
sphere.dipoleVector = dipoleVector;
sphere.dipoleLayer = dipoleLayer;

end
```

calculateSpectrum1Dipole.m

```
function [Ptotal] =
calculatesSpectrum1Dipole(lambda,tol,sphereStruct)
%CALCULATES SPECTRUM for 1 dipole placed in/on a layer of a
multilayer microshell.

%Matthew Henderson, Jonathan Hall, Tess Reynolds, Shahraam Afshar.
%(2015)
%University of Adelaide, Australia.

%Definitions of the properties of the medium:
nList = sphereStruct.refractiveIndices; %refractive indices
ep = sphereStruct.permittivities; %the electric permittivities
mu = sphereStruct.permeabilities; %the magnetic permeabilities
r = sphereStruct.radii; %the radii of the layers
dl = sphereStruct.dipoleLayer; %the layer in which the dipole sits
dpos = sphereStruct.dipolePosition(1); %dipole position

%Initialise the loop variables:
Ptotal(length(lambda)) = 0;
lMax=10000;

%Loop over wavelength lambda:
for i_lambda = 1:length(lambda)

    %Initialse the total power:
    PSum = 0;
    PSum_prev=Inf;

    %Set the wave number values:
    for j=1:length(nList)
        k(j) = 2.*pi.*nList(j)./lambda(i_lambda);
    end
```

```
    %Loop over the azimuthal quantum number, l:
    for l = 1:lMax

        %Set the wave number in the dipole layer:
        kj = k(dl);

        %Set the wave number in the outermost medium:
        kend = k(length(nList));

        %Set the initial values of the Bessel/Hankel functions
needed:
        if l==1

            %Nl: need only the lower and upper boundaries of each
layer:
            for Nl=1:2

                %NN: loop over the number of layers:
                for NN=1:length(r)
                    jv(Nl,NN)=besseljsph(l, k(Nl+NN-1).*r(NN));
                    jvm(Nl,NN)=besseljsph(l-1, k(Nl+NN-1).*r(NN));

                    hv(Nl,NN)=h1sph(l, k(Nl+NN-1).*r(NN));
                    hvm(Nl,NN)=h1sph(l-1, k(Nl+NN-1).*r(NN));
                end
            end

  %Set the Bessel/Hankel functions that occur at the dipole location:
            jlkj = besseljsph(l, kj.*dpos);
            jlkjm = besseljsph(l-1, kj.*dpos);

            hlkj = h1sph(l, kj.*dpos);
            hlkjm = h1sph(l-1, kj.*dpos);
        end

        %Use recursion relations to update the Bessel/Hankel
```

```
functions:
        for Nl=1:2
            for NN=1:length(r)
                jvp(Nl,NN)=(2.*l+1)./(k(Nl+NN-1).*r(NN)).*jv(Nl,NN) -
jvm(Nl,NN);
                hvp(Nl,NN)=(2.*l+1)./(k(Nl+NN-1).*r(NN)).*hv(Nl,NN) -
hvm(Nl,NN);
            end
        end

%Use recursion relations to update the Bessel/Hankel functions that
occur at the dipole location:
        jlkjp=(2.*l+1)./(kj.*dpos).*jlkj -  jlkjm;
        hlkjp=(2.*l+1)./(kj.*dpos).*hlkj -  hlkjm;

%Use the function 'primesphf' to obtain the Riccati-Bessel
derivatives:
        jlprimekj=primesphf(kj.*dpos,jlkjp,jlkj,jlkjm);
        hlprimekj=primesphf(kj.*dpos,hlkjp,hlkj,hlkjm);


 %Use the function 'recurseMatrixMultiplicationNRange' to obtain
 the TM block of the matrix t=T(N+1,j) defined in Eq.(X):
        t_TM =
recurseMatrixMultiplicationNRange(0,0,lambda(i_lambda),length(r),dl,l
,r,nList,ones(length(nList),1),jvp,jv,jvm,hvp,hv,hvm);

 %Obtain the TM block of the matrix t=T(N+1,j):
        t_TE =
recurseMatrixMultiplicationNRange(0,1,lambda(i_lambda),length(r),dl,l
,r,nList,ones(length(nList),1),jvp,jv,jvm,hvp,hv,hvm);

 %Obtain the TM block of the matrix S defined in Eq.(X):
        S_TM =
recurseMatrixMultiplicationNRange(1,0,lambda(i_lambda),length(r),1,l,
r,nList,ones(length(nList),1),jvp,jv,jvm,hvp,hv,hvm);
```

```
%Obtain the TE block of the matrix S:
        S_TE =
recurseMatrixMultiplicationNRange(1,1,lambda(i_lambda),length(r),1,l,
r,nList,ones(length(nList),1),jvp,jv,jvm,hvp,hv,hvm);

%Define the polarisabilities that specify the coefficients in the
outermost layer, and the total power:
        alpha = t_TM(2,2) + t_TM(1,2).*S_TM(2,1)./S_TM(2,2);
        beta = t_TM(2,1) + t_TM(1,1).*S_TM(2,1)./S_TM(2,2);
        gamma = t_TE(2,2) + t_TE(1,2).*S_TE(2,1)./S_TE(2,2);
        zeta = t_TE(2,1) + t_TE(1,1).*S_TE(2,1)./S_TE(2,2);

%Construct the perpendicular-to-tangent (R direction) and parallel-
to-tangent (Theta or Phi direction) parts of the power:
        R_coeff = nList(dl).^2./nList(end).^2.*l.*(l +
1).*abs(alpha.*jlkj - beta.*hlkj).^2./kj.^2./dpos.^2;
        TPhi_coeff =
nList(dl).^2./nList(end).^2.*abs(alpha.*jlprimekj -
beta.*hlprimekj).^2./kj.^2./dpos.^2 + abs(gamma.*jlkj -
zeta.*hlkj).^2;

%Define the normalisation factors to the medium of the layer that
contains the dipole:
        fac0=(kj.^4)./(3.*ep(dl).*nList(dl));

%Define the normalised components of the power:
        R_coeffnorm= R_coeff./fac0;
        TPhi_coeffnorm= TPhi_coeff./fac0;

%Define the total power, which is summed iteratively:
        PSum = PSum + (2.*l + 1).*(R_coeffnorm + TPhi_coeffnorm./2);

%State the escape clause, prescribed by the preset tolerance, tol:
        if abs(PSum-PSum_prev)<tol*abs(PSum)
            break;
        end
```

```
 %Update the total power inside the loop:
        PSum_prev = PSum;

 %Update the Bessel functions inside the loop:
        jvm=jv;
        jv=jvp;

        hvm=hv;
        hv=hvp;

        jlkjm=jlkj;
        jlkj=jlkjp;

        hlkjm=hlkj;
        hlkj=hlkjp;
    end

 %Define the final coefficient to be premultiplied:
    finalcoeff =
(1.0/2.0)*sqrt(ep(end)/mu(end))*((kj)^4*nList(dl)^2)/(nList(end)^2*ep
(dl)^2);

 %The total power is written the same way as Eq.(X):
    Ptotal(i_lambda) = finalcoeff.*PSum;

    disp(lambda(i_lambda));
    disp(Ptotal(i_lambda));
end
end
```

calculateSpectrumDipoleLayer.m

```
function [Ptotal] =
calculateSpectrumDipoleLayer(lambda,tol,sphereStruct)
%CALCULATES SPECTRUM for a uniform distribution of dipoles in/on a
layer of a multilayer microshell.

%Matthew Henderson, Jonathan Hall, Tess Reynolds, Shahraam Afshar.
%(2015)
%University of Adelaide, Australia.

%Definitions of the properties of the medium:
nList = sphereStruct.refractiveIndices; %refractive indices
ep = sphereStruct.permittivities; %the electric permittivities
mu = sphereStruct.permeabilities; %the magnetic permeabilities
r = sphereStruct.radii; %the radii of the layers
dl = sphereStruct.dipoleLayer; %the layer that contains the
distribution of dipoles

%the volume of the layer that contains the distribution of dipoles
if dl == 1
    VShell=(4*pi/3).*(r(dl).^3);
else
    VShell=(4*pi/3).*(r(dl).^3-r(dl-1).^3);
end

%Initialise the loop variables:
Ptotal(length(lambda)) = 0;
lMax=10000;

%Loop over wavelength lambda:
for i_lambda = 1:length(lambda)

    %Initialse the total power:
    PSum = 0;
    PSum_prev=Inf;
```

```
    %Set the wave number values:
    for j=1:length(nList)
        k(j) = 2.*pi.*nList(j)./lambda(i_lambda);
    end

    %Loop over the azimuthal quantum number, l:
    for l = 1:lMax

        %Set the wave number in the dipole layer:
        kj = k(dl);

        %Set the wave number in the outermost medium:
        kend = k(length(nList));

%Set the initial values of the Bessel/Hankel functions needed:
        if l==1

%Nl: need only the lower and upper boundaries of each layer:
            for Nl=1:2

                %NN: loop over the number of layers:
                for NN=1:length(r)
                    jv(Nl,NN)=besseljsph(l, k(Nl+NN-1).*r(NN));
                    jvm(Nl,NN)=besseljsph(l-1, k(Nl+NN-1).*r(NN));

                    hv(Nl,NN)=h1sph(l, k(Nl+NN-1).*r(NN));
                    hvm(Nl,NN)=h1sph(l-1, k(Nl+NN-1).*r(NN));
                end
            end

%Set the Bessel/Hankel functions in the dipole layer, at l-2, which
are needed for the variable PSI:
        jlkjmm=besseljsph(l-2, kj.*r(dl));
        hlkjmm=h1sph(l-2, kj.*r(dl));
```

```
        if dl ~= 1
            jlkjm1mm=besseljsph(l-2, kj.*r(dl-1));
            hlkjm1mm=h1sph(l-2, kj.*r(dl-1));
        end
      end

%Use recursion relations to update the Bessel/Hankel functions:
        for Nl=1:2
            for NN=1:length(r)
                jvp(Nl,NN)=(2.*l+1)./(k(Nl+NN-1).*r(NN)).*jv(Nl,NN) -
jvm(Nl,NN);
                hvp(Nl,NN)=(2.*l+1)./(k(Nl+NN-1).*r(NN)).*hv(Nl,NN) -
hvm(Nl,NN);
            end
        end

%Use recursion relations to update the Bessel/Hankel functions that
occur in the dipole layer:
        jlkjpp=(2.*l+3)./(kj.*r(dl)).*jvp(1,dl) - jv(1,dl);
        hlkjpp=(2.*l+3)./(kj.*r(dl)).*hvp(1,dl) - hv(1,dl);

%Use recursion relations to update the Bessel/Hankel functions in the
layer below the dipole layer:
        if dl ~= 1
          jlkjm1pp=(2.*l+3)./(kj.*r(dl-1)).*jvp(2,dl-1) - jv(2,dl-1);
          hlkjm1pp=(2.*l+3)./(kj.*r(dl-1)).*hvp(2,dl-1) - hv(2,dl-1);
        end

%Use the function 'primesphf' to obtain the Riccati-Bessel
derivatives:
        jlprimekjm=primesphf(kj.*r(dl),jv(1,dl),jvm(1,dl),jlkjmm);
        hlprimekjm=primesphf(kj.*r(dl),hv(1,dl),hvm(1,dl),hlkjmm);

        jlprimekj=primesphf(kj.*r(dl),jvp(1,dl),jv(1,dl),jvm(1,dl));
        hlprimekj=primesphf(kj.*r(dl),hvp(1,dl),hv(1,dl),hvm(1,dl));
```

```
        jlprimekjp=primesphf(kj.*r(dl),jlkjpp,jvp(1,dl),jv(1,dl));
        hlprimekjp=primesphf(kj.*r(dl),hlkjpp,hvp(1,dl),hv(1,dl));

%Use the function 'primesphf' to obtain the Riccati-Bessel
derivatives in the layer below the dipole layer:
        if dl ~= 1
        jlm1primekjm=primesphf(kj.*r(dl-1),jv(2,dl-1),jvm(2,dl-
1),jlkjm1mm);
        hlm1primekjm=primesphf(kj.*r(dl-1),hv(2,dl-1),hvm(2,dl-
1),hlkjm1mm);

        jlm1primekj=primesphf(kj.*r(dl-1),jvp(2,dl-1),jv(2,dl-
1),jvm(2,dl-1));
        hlm1primekj=primesphf(kj.*r(dl-1),hvp(2,dl-1),hv(2,dl-
1),hvm(2,dl-1));

        jlm1primekjp=primesphf(kj.*r(dl-1),jlkjm1pp,jvp(2,dl-
1),jv(2,dl-1));
        hlm1primekjp=primesphf(kj.*r(dl-1),hlkjm1pp,hvp(2,dl-
1),hv(2,dl-1));
        end

%Use the function 'recurseMatrixMultiplicationNRange' to obtain
%the TM block of the matrix t=T(N+1,j) defined in Eq.(X):
        t_TM =
recurseMatrixMultiplicationNRange(0,0,lambda(i_lambda),length(r),dl,l
,r,nList,ones(length(nList),1),jvp,jv,jvm,hvp,hv,hvm);

%Obtain the TM block of the matrix t=T(N+1,j):
        t_TE =
recurseMatrixMultiplicationNRange(0,1,lambda(i_lambda),length(r),dl,l
,r,nList,ones(length(nList),1),jvp,jv,jvm,hvp,hv,hvm);

 %Obtain the TM block of the matrix S defined in Eq.(X):
        S_TM =
recurseMatrixMultiplicationNRange(1,0,lambda(i_lambda),length(r),1,l,
```

```
r,nList,ones(length(nList),1),jvp,jv,jvm,hvp,hv,hvm);

%Obtain the TE block of the matrix S:
        S_TE =
recurseMatrixMultiplicationNRange(1,1,lambda(i_lambda),length(r),1,l,
r,nList,ones(length(nList),1),jvp,jv,jvm,hvp,hv,hvm);

%Define the polarisabilities that specify the coefficients in the
outermost layer, and the total power:
        alpha = t_TM(2,2) + t_TM(1,2).*S_TM(2,1)./S_TM(2,2);
        beta = t_TM(2,1) + t_TM(1,1).*S_TM(2,1)./S_TM(2,2);
        gamma = t_TE(2,2) + t_TE(1,2).*S_TE(2,1)./S_TE(2,2);
        zeta = t_TE(2,1) + t_TE(1,1).*S_TE(2,1)./S_TE(2,2);

%Define the size parameter at the upper dipole layer boundary:
        rho1=kj*r(dl);

%Special case: dipole layer is the innermost layer
        if dl == 1

%Obtain the quantities T1-T6 defined in Eqs.(X) - (X):
      T1=PSI(l-
1,rho1,rho1*jvm(1,dl),jlprimekjm,rho1*jvm(1,dl),jlprimekjm);

      T2=PSI(l+1,rho1,rho1*jvp(1,dl),jlprimekjp,rho1*jvp(1,dl),jlprim
      ekjp);

      T3=PSI(l-
1,rho1,rho1*hvm(1,dl),hlprimekjm,rho1*hvm(1,dl),hlprimekjm);

      T4=PSI(l+1,rho1,rho1*hvp(1,dl),hlprimekjp,rho1*hvp(1,dl),hlprim
      ekjp);

      T5=PSI(l-
1,rho1,rho1*jvm(1,dl),jlprimekjm,rho1*hvm(1,dl),hlprimekjm);
```

```
T6=PSI(l+1,rho1,rho1*jvp(1,dl),jlprimekjp,rho1*hvp(1,dl),hlprimekjp);
        else

%Define the size parameter at the upper dipole layer boundary:
        rhom1=kj*r(dl-1);

%Obtain the quantities T1-T6 defined in Eqs.(X) -(X):
        T1=PSI(l-
1,rho1,rho1*jvm(1,dl),jlprimekjm,rho1*jvm(1,dl),jlprimekjm)-...
            PSI(l-1,rhom1,rhom1*jvm(2,dl-
1),jlm1primekjm,rhom1*jvm(2,dl-1),jlm1primekjm);


T2=PSI(l+1,rho1,rho1*jvp(1,dl),jlprimekjp,rho1*jvp(1,dl),jlprimekjp)-
...
            PSI(l+1,rhom1,rhom1*jvp(2,dl-
1),jlm1primekjp,rhom1*jvp(2,dl-1),jlm1primekjp);

        T3=PSI(l-
1,rho1,rho1*hvm(1,dl),hlprimekjm,rho1*hvm(1,dl),hlprimekjm)-...
            PSI(l-1,rhom1,rhom1*hvm(2,dl-
1),hlm1primekjm,rhom1*hvm(2,dl-1),hlm1primekjm);


T4=PSI(l+1,rho1,rho1*hvp(1,dl),hlprimekjp,rho1*hvp(1,dl),hlprimekjp)-
...
            PSI(l+1,rhom1,rhom1*hvp(2,dl-
1),hlm1primekjp,rhom1*hvp(2,dl-1),hlm1primekjp);

        T5=PSI(l-
1,rho1,rho1*jvm(1,dl),jlprimekjm,rho1*hvm(1,dl),hlprimekjm)-...
            PSI(l-1,rhom1,rhom1*jvm(2,dl-
1),jlm1primekjm,rhom1*hvm(2,dl-1),hlm1primekjm);
```

```
T6=PSI(l+1,rho1,rho1*jvp(1,dl),jlprimekjp,rho1*hvp(1,dl),hlprimekjp)-
...
            PSI(l+1,rhom1,rhom1*jvp(2,dl-
1),jlm1primekjp,rhom1*hvp(2,dl-1),hlm1primekjp);
        end

%Obtain the quantity I1PlusI2 from Eq.(X):
        I1PlusI2 = (1./kj).*(abs(alpha).^2*((l+1).*T1+l.*T2)+...
                abs(beta).^2*((l+1).*T3+l.*T4)-...
                2*abs(alpha).*abs(beta)*((l+1).*T5+l.*T6));


%Special case: dipole layer is the innermost layer
    if dl == 1

%Obtain the quantities T7-T9 defined in Eqs.(X) - (X):

T7=PSI(l,rho1,rho1*jv(1,dl),jlprimekj,rho1*jv(1,dl),jlprimekj);

T8=PSI(l,rho1,rho1*hv(1,dl),hlprimekj,rho1*hv(1,dl),hlprimekj);

T9=PSI(l,rho1,rho1*jv(1,dl),jlprimekj,rho1*hv(1,dl),hlprimekj);

    else

%Re-define the size parameter at the upper dipole layer boundary:
    rhom1=kj*r(dl-1);

%Obtain the quantities T7-T9 defined in Eqs.(X) - (X):
   T7=PSI(l,rho1,rho1*jv(1,dl),jlprimekj,rho1*jv(1,dl),jlprimekj)-...
       PSI(l,rhom1,rhom1*jv(2,dl-1),jlm1primekj,rhom1*jv(2,dl-
1),jlm1primekj);

   T8=PSI(l,rho1,rho1*hv(1,dl),hlprimekj,rho1*hv(1,dl),hlprimekj)-...
       PSI(l,rhom1,rhom1*hv(2,dl-1),hlm1primekj,rhom1*hv(2,dl-
1),hlm1primekj);
```

```
   T9=PSI(l,rho1,rho1*jv(1,dl),jlprimekj,rho1*hv(1,dl),hlprimekj)-...
       PSI(l,rhom1,rhom1*jv(2,dl-1),jlm1primekj,rhom1*hv(2,dl-
1),hlm1primekj);

    end

        %Obtain the quantity I3 from Eq.(X):
        I3 =(1./kj).*(2*l+1).*(abs(gamma)^2.*T7+...
            abs(zeta).^2.*T8-...
            2*abs(gamma).*abs(zeta).*T9);

        %Define the total power, which is summed iteratively:
        PSum = PSum +
(((nList(dl)).^2)./(nList(end).^2)).*I1PlusI2+I3;


  %State the escape clause, prescribed by the preset tolerance, tol:
        if abs(PSum-PSum_prev)<tol*abs(PSum)
            break;
        end

        %Update the total power inside the loop:
        PSum_prev = PSum;

        %Update the Bessel functions inside the loop:
        jlkjmm=jvm(1,dl);
        hlkjmm=hvm(1,dl);

        if dl ~= 1
          jlkjm1mm=jvm(2,dl-1);
          hlkjm1mm=hvm(2,dl-1);
        end

        jvm=jv;
        jv=jvp;
```

```
        hvm=hv;
        hv=hvp;
    end

    %Define the final coefficient to be premultiplied:
    finalcoeff =
1.0/2.0*sqrt(ep(end)./mu(end))*nList(dl)^2/nList(end)^2*nList(dl)/(kj
^2*ep(dl)*VShell)*4*pi;

    %The total power is written the same way as Eq.(X):
    Ptotal(i_lambda) = finalcoeff.*abs(PSum);

    disp(lambda(i_lambda));
    disp(Ptotal(i_lambda));

end
end
```

recurseMatrixMultiplicationNRange.m

```
function M = recurseMatrixMultiplicationNRange(invert,TE,lambdaGuess,
n, nLow, l, radiusList, nList, muList,jvp,jv,jvm,hvp,hv,hvm)

%RECURSEMATRIXMULTIPLICATION Returns the transfer matrix of an n-
layer sphere. Calculates the 2x2 submatrix of the transfer matrix of
the nth layer, and then multiplies this by the n-1th layer by calling
itself again. Generates all of the transfer matrices down to the 1st
layer and multiplies them all together with recursive calls.

%Matthew Henderson, Jonathan Hall, Tess Reynolds, Shahraam Afshar.
%(2015)
%University of Adelaide, Australia.

%Sphere layers nomenclature:
%n=1 | n=2 | .... | n=N+1
%    r(1)  r(2)   r(N)


if n > 0

    %Define the momenta for the two neighbouring layers:
    k = 2*pi*nList(n)./lambdaGuess;
    npk = 2*pi*nList(n+1)./lambdaGuess;

    %Define the size parameters for the two neighbouring layers:
    rho = k.*radiusList(n);
    nprho = npk.*radiusList(n);

    %Assign the refractive indices:
    nn=nList(n);
    nnp=nList(n+1);

    %Assign the magnetic permeabilities:
    mu=muList(n);
    mup=muList(n+1);
```

```
 %Assign the Riccati-Bessel/Hankel functions, and their  derivatives:
    psip = rho*jvp(1,n);
    psi = rho*jv(1,n);
    psim = rho*jvm(1,n);
    chip = rho*hvp(1,n);
    chi = rho*hv(1,n);
    chim = rho*hvm(1,n);
    psiprime = primesphf(rho,jvp(1,n),jv(1,n),jvm(1,n));
    chiprime = primesphf(rho,hvp(1,n),hv(1,n),hvm(1,n));

    nppsip = nprho*jvp(2,n);
    nppsi = nprho*jv(2,n);
    nppsim = nprho*jvm(2,n);
    npchip = nprho*hvp(2,n);
    npchi = nprho*hv(2,n);
    npchim = nprho*hvm(2,n);
    nppsiprime = primesphf(nprho,jvp(2,n),jv(2,n),jvm(2,n));
    npchiprime = primesphf(nprho,hvp(2,n),hv(2,n),hvm(2,n));

end

%'invert' controls whether we calculate elements of the matrix T or S
if invert~=1

    %This part calculates the TE and TM blocks of the G matrix
    if n > 0
        coef = i/(nnp*mu)*npk/k;

        if TE == 1
            GcoefL=nn*mup;
            GcoefR=nnp*mu;
        else
            GcoefL=nnp^2/nn*mu;
            GcoefR=nnp*mup;
        end
```

```
            Gmatrix = [...
            (GcoefL*psiprime*npchi - GcoefR*psi*npchiprime) ...
            (GcoefL*chiprime*npchi - GcoefR*chi*npchiprime);
            (GcoefR*nppsiprime*psi - GcoefL*nppsi*psiprime) ...
            (GcoefR*nppsiprime*chi - GcoefL*nppsi*chiprime);
            ].*coef;
        disp(GcoefL*psiprime*npchi);
    end

    %Multiply down the series from N+1 to 1
    if n == nLow - 1
%Finished, so just return the identity matrix so that the recursion
ends.
        M = eye(2);
    else
            M = Gmatrix*recurseMatrixMultiplicationNRange(0, TE,
lambdaGuess, n-1, nLow, l, radiusList, nList,
muList,jvp,jv,jvm,hvp,hv,hvm);
    end


else
%This part calculates the TE and TM blocks of the inverted G matrix.
    if n > 0
        coef = i/(nn*mup)*k/npk;

        if TE == 1
            GcoefL=nnp*mu;
            GcoefR=nn*mup;
        else
            GcoefL=nn^2/nnp*mup;
            GcoefR=nn*mu;
        end

        Gmatrix = [...
            (GcoefL*nppsiprime*chi - GcoefR*nppsi*chiprime) ...
```

```
            (GcoefL*npchiprime*chi - GcoefR*npchi*chiprime);
            (GcoefR*psiprime*nppsi - GcoefL*psi*nppsiprime) ...
            (GcoefR*psiprime*npchi - GcoefL*psi*npchiprime);
            ].*coef;
    end

    if n == nLow - 1
%Finished, so just return the identity matrix so that the recursion
ends.
        M = eye(2);
    else
            M = recurseMatrixMultiplicationNRange(1, TE, lambdaGuess,
n-1, nLow, l, radiusList, nList,
muList,jvp,jv,jvm,hvp,hv,hvm)*Gmatrix;
    end

end

end
```

besseljsph.m

```
%Spherical Bessel Function

%Matthew Henderson, Jonathan Hall, Tess Reynolds, Shahraam Afshar.
%(2015)
%University of Adelaide, Australia.

function[C]=besseljsph(m,x)

C = sqrt(pi./(2*x))*besselj(m+1/2,x);

end
```

h1sph.m

```
%Spherical Hankel Function

%Matthew Henderson, Jonathan Hall, Tess Reynolds, Shahraam Afshar.
%(2015)
%University of Adelaide, Australia.

function[C]=h1sph(m,x)

C = sqrt(pi./(2*x))*besselh(m+1/2,1,x);

end
```

primesphf.m

```
%Provides the form for a derivative of a Bessel-like function, for
%Bessel-like function inputs.

% Matthew Henderson, Jonathan Hall, Tess Reynolds, Shahraam Afshar.
% (2015)
% University of Adelaide, Australia.

function[C]=primesphf(x,jp,j,jm)

C = (j + x*(jm-jp))./2;

end
```

PSI.m

```
%The function PSI, defined in Eq.(X) of the publication doi:///

% Matthew Henderson, Jonathan Hall, Tess Reynolds, Shahraam Afshar.
% (2015)
% University of Adelaide, Australia.

function out = PSI(m,x,f1,f1p,f2,f2p)
out=(1/2)*((x-m*(m+1)./x).*f1.*f2-...
    (1/2)*(f1.*f2p+f1p.*f2)+...
    x.*f1p.*f2p);
end
```